REPORT DOCUMENTATION PAGE

Public reporting burden for this collection of information is estimated to average 1 hour per response, including the time for reviewing instructions, searching existing data sources, gathering and maintaining the data needed, and completing and reviewing the collection of information. Send comments regarding this burden estimate or any other aspect of this collection of information, including suggestions for reducing this burden, to Washington Headquarters Services, Directorate for Information Operations and Reports, 1215 Jefferson Davis Highway, Suite 1204, Arlington, VA 22202-4302, and to the Office of Management and Budget, Paperwork Reduction Project (0704-0188), Washington, DC 20503.

1. AGENCY USE ONLY (Leave blank)	2. REPORT DATE 10 Sep 95	3. REPORT TYPE AND DATES COVERED

4. TITLE AND SUBTITLE
A Study of Polar Cap Electron Precipitation Events
To Determine Source Region Parameters

5. FUNDING NUMBERS

6. AUTHOR(S)

Steven Edward Cahanin

7. PERFORMING ORGANIZATION NAME(S) AND ADDRESS(ES)

AFIT Students Attending:

Utah State University

8. PERFORMING ORGANIZATION REPORT NUMBER

95-109

9. SPONSORING/MONITORING AGENCY NAME(S) AND ADDRESS(ES)

DEPARTMENT OF THE AIR FORCE
AFIT/CI
2950 P STREET, BLDG 125
WRIGHT-PATTERSON AFB OH 45433-7765

10. SPONSORING/MONITORING AGENCY REPORT NUMBER

11. SUPPLEMENTARY NOTES

12a. DISTRIBUTION/AVAILABILITY STATEMENT

Approved for Public Release IAW AFR 190-1
Distribution Unlimited
BRIAN D. GAUTHIER, MSgt, USAF
Chief of Administration

12b. DISTRIBUTION CODE

13. ABSTRACT (Maximum 200 words)

Accesion For		
NTIS CRA&I		☒
DTIC TAB		☐
Unannounced		☐
Justification		
By		
Distribution /		
Availability Codes		
Dist	Avail and/or Special	
A-1		

19951017 170

DTIC QUALITY INSPECTED 5

14. SUBJECT TERMS	15. NUMBER OF PAGES 204
	16. PRICE CODE

17. SECURITY CLASSIFICATION OF REPORT	18. SECURITY CLASSIFICATION OF THIS PAGE	19. SECURITY CLASSIFICATION OF ABSTRACT	20. LIMITATION OF ABSTRACT

A STUDY OF POLAR CAP ELECTRON PRECIPITATION EVENTS

TO DETERMINE SOURCE REGION PARAMETERS

by

Steven Edward Cahanin

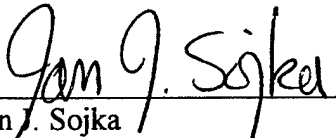A thesis submitted in partial fulfillment
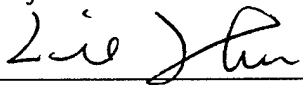of the requirements for the degree
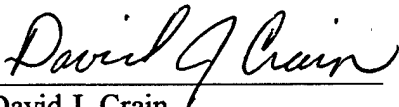
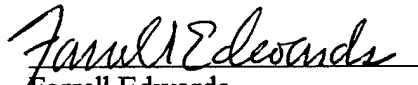of

MASTER OF SCIENCE

in

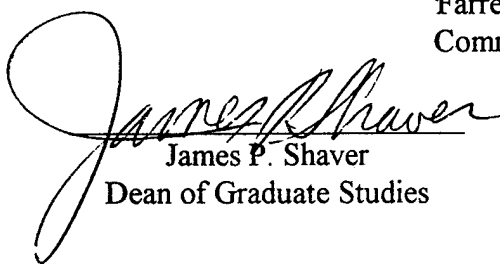Physics
(Upper Atmospheric Physics)

Approved:

Jan J. Sojka
Major Professor

Lie Zhu
Committee Member

David J. Crain
Committee Member

Farrell Edwards
Committee Member

James P. Shaver
Dean of Graduate Studies

UTAH STATE UNIVERSITY
Logan, Utah

1995

To my beautiful and loving wife, Kathy Charlotte Cahanin,

and to my wonderful daughter, Allison Louise Cahanin.

ACKNOWLEDGMENTS

I wish express my thanks to thank Dr. Jan J. Sojka for his teaching, research assistance, and above all, his patience. He gave me the confidence to complete this thesis when I needed it most.

A special thanks to Kim Marshall and Don Thompson who provided me with technical assistance used to complete this thesis. Kim assisted in reading archaic data tapes, and Don's plotting routines were quite useful.

Finally, I wish to express my greatest thanks to my parents, Joseph Theodore Cahanin and Valerie Hattie Cahanin. Without their love and encouragement, I could have never come this far.

Steven E. Cahanin

CONTENTS

LIST OF TABLES

LIST OF FIGURES

ABSTRACT

A Study of Polar Cap Electron Precipitation Events to

Determine Source Region Parameters

by

Steven E. Cahanin, Master of Science

Utah State University, 1995

Major Professor: Dr. Jan J. Sojka
Department: Physics

A thorough understanding of polar cap electron precipitation and the source region

of these particles is essential for producing accurate models of the near-earth space

environment. Although this phenomenon received considerable attention during the

1980s, most researchers have now focused their attention on one specific form of polar

cap electron precipitation, the sun-aligned arc. By examining energy flux/time series plots

from 976 passes of the Defense Meteorological Satellite Program (DMSP) F-8 SSJ/4

polar cap satellite from 1 November 1989 through 31 December 1989, enormous variety

of structures was found. These structures, regardless of their respective energy flux, are

the focus of this research and will be referred to as polar cap electron precipitation events.

By selecting only those events that occurred under northward IMF conditions and

at magnetic latitude greater than 80°, the events were then sorted by the collecting energy

channel and by different total energy flux categories. By assuming the source region

particles have a Maxwellian distribution, proceed down open field lines, are accelerated by a potential drop, and obey Liouville's Theorem, the source region parameters are described. In particular, the source region kT temperature (energy) is found to be generally invariant while the electron number density varies by an order of magnitude.

(215 pages)

CHAPTER I

INTRODUCTION

Along with the advent of space exploration and space-borne telecommunications, and the development of a permanent space station, inevitably humans beings will live and travel in the space environment for extended periods of time. Therefore, the need for understanding this environment is essential. Since the first satellites were launched, our ability to understand the space environment and eventually produce "space forecasts" has grown significantly. However, the difficulty in understanding this environment is similar to when tropospheric meteorology was in its infancy--we simply do not have enough detailed information. The problem is compounded by the fact that it is quite expensive to collect data using satellites. Furthermore, data from satellites are collected only at one point in time. This challenge will eventually be overcome as groups of smaller, less expensive satellites are used to collect data at numerous locations simultaneously. As the volume of data increases, theoreticians and modelers will continue to improve numerical forecast models of the space environment. Eventually "space forecasts" with significant accuracy, similar to weather forecasts, will be available. The research presented here will provide the research community with significant information about the polar cap electron precipitation and the source region of these particles.

This thesis begins with Chapter II presenting the subject of polar cap electron precipitation with a literature review on this subject. Polar cap electron precipitation is a crucial component of modeling the high latitude near-earth space environment. Chapter III presents the Defense Meteorological Satellite Program (DMSP) and the SSJ-4

Electrostatic Analyzer. Chapter IV presents the data reduction methods of the DMSP

SSJ/4 electron count data and describes the interplanetary magnetic field (IMF) database.

These two databases are merged and the final database is described. Chapter V discusses

data analysis. Theoretical data analysis as well as applied data analysis is presented.

Finally, Chapter VI will summarize the results of this research.

CHAPTER II

POLAR CAP ELECTRON PRECIPITATION

2.1 Theoretical Introduction

As a first approximation, the earth's magnetic field closely resembles a dipole magnet with the magnetic field lines leaving the south pole and connecting at the north pole. In reality however, the earth's magnetic field is generated by a quite complicated process. The resultant structure is a distorted and tilted magnetic field with the geomagnetic poles currently located at 79° N, 70° W, and 79° S, 70° E (they move about slightly over time) [*Hargreaves*, 1992]. The distortion is caused by the solar wind as it streams past the earth as seen in Figure 2.1 [*Tascione*, 1988].
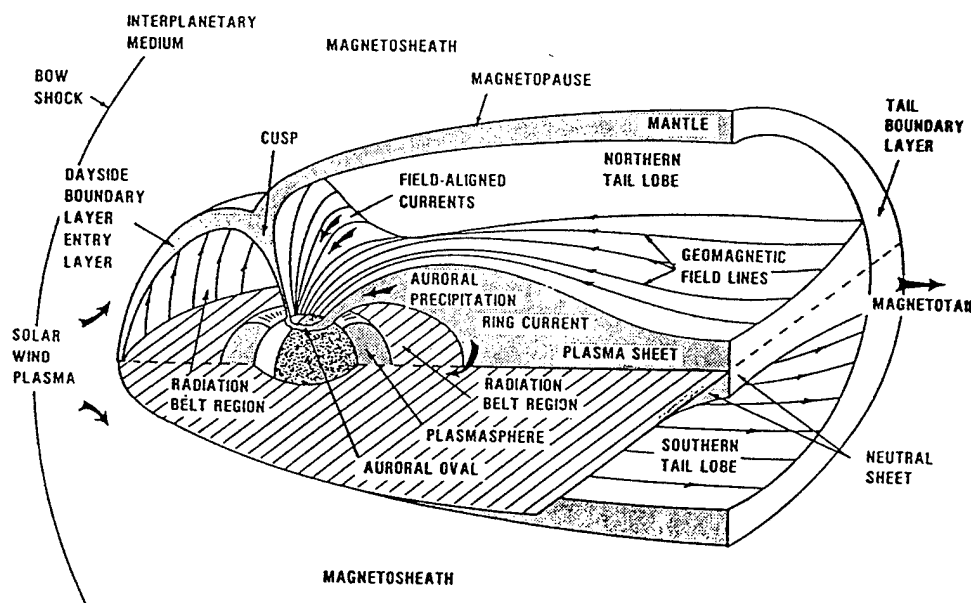
Figure 2.1. Cross section of the magnetosphere [*Tascione*, 1988].

The sun's magnetic field is pulled toward the planets by the solar wind. This process generates the interplanetary magnetic field (IMF). Interactions between the solar wind, IMF, and the earth's magnetic field result in this complicated model of the earth's magnetosphere. There are conditions under which the earth's magnetic field lines connect with the IMF [*Whalen et al.*, 1971]. These are referred to as open field lines. This interaction with the solar wind allows the magnetosheath to become populated with solar wind particles. Figure 2.1 shows the magnetospheric structures as well as the principal particle populations. The different populations have significantly different energies, and therefore it has been suggested that electrons precipitating from different populations would create different forms of aurora [*Winningham and Heikkila*, 1974].

The interplanetary magnetic field has a three component vector orientation. It has been shown by *Berkey et al.* [1976], *Ismail et al.* [1977], *Gussenhoven* [1982], and *Hardy et al.* [1982], among others, that significant polar cap electron precipitation is clearly correlated to a northward IMF condition ($B_z > 0$). Figure 2.2 shows the difference of magnetic field configuration for northward ($B_z > 0$) and southward ($B_z < 0$) IMF. This difference in connection would suggest different magnetospheric circulation patterns, which in turn will affect electron precipitation.

2.2 Historical Background

The magnetospheric area of interest in this research is the northern polar cap. This region is defined as the area nothrward of the auroral oval (see Figure 2.1). Although occurrence of auroral phenomena well poleward of the auroral oval was documented by
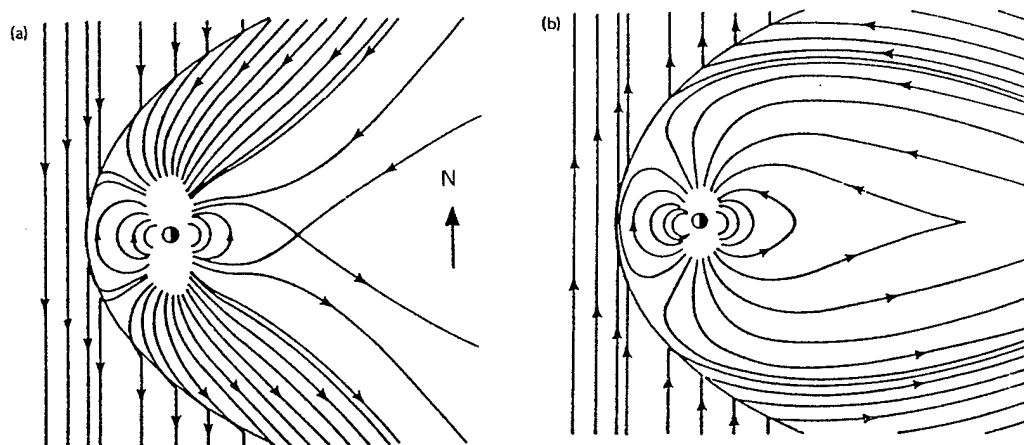
Figure 2.2. Earth's magnetic field interaction with IMF under (a) southward ($B_z < 0$) and (b) northward ($B_z > 0$) conditions [*Potemra*, 1983].

Davis [1962], *Sanford* [1964, 1968], *Lassen* [1969], *Eather and Akasofu* [1969], and *Romick and Brown* [1971], the history of classifying these polar cap auroral phenomena began with the first research showing that it is possible to distinguish between the auroral oval and polar cap aurora [*Akasofu*, 1972]. Using all-sky cameras and ground-based photometers, *Akasofu* displayed the difference between the midday aurora associated with the noon sector of the auroral oval and polar cap aurora. He determined the sun-earth alignment of the polar cap aurora and showed these phenomena tend to occur under low geomagnetic activity. Additionally, the photometers enabled *Akasofu* to find that there existed a "subvisual red belt" of [OI] 630 nm and that the electron population of the magnetosheath was sufficient to produce these aurora. This allowed him to suggest that the magnetic field lines from the magnetosheath map down to the high latitude polar caps, creating polar cap aurora.

The next major study of polar cap electron precipitation used different flux levels to classify these phenomena [*Winningham and Heikkila*, 1974]. This research used particle precipitation data from the particle spectrometer on the ISIS 1 satellite. Using this data, *Winningham and Heikkila* defined the terminology of "polar rain," "polar showers," and "polar squalls" as indicated in Table 2.1. However, they only allude to the possible source region for these particles, citing research done by *Bame et al.* [1971] and *Akasofu et al.* [1973] who report magnetotail measurements from Vela observations. These measurements allowed *Winningham and Heikkila* to suggest the magnetosheath as the source region, but note that this is probably the source only for polar rain.

Winningham and Heikkila [1974] plotted some differential spectra for polar rain and polar squalls (see Figure 2.3). In addition to the spectra, they showed energy/time series spectrograms for polar rain, polar showers, and squalls. Figure 2.4 (a) shows a typical polar cap satellite pass displaying the broad structureless flux of electrons they called polar rain. Figure 2.4 (b) shows the structures imbedded in the polar rain termed

Table 2.1. Energy flux and electron energy versus nomenclature for polar cap electron precipitation.

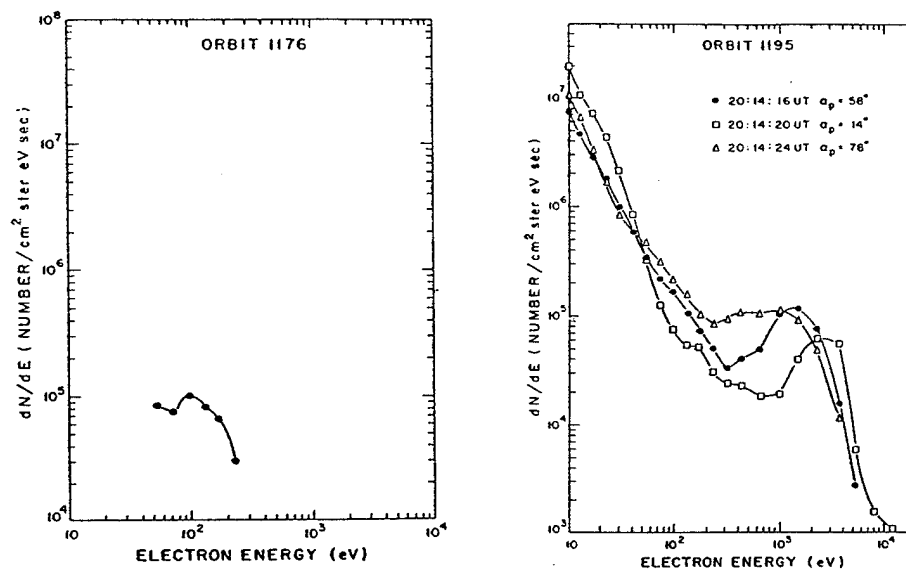|	Energy Flux	Electron Energy
Polar rain	$10^{-3} > 10^{-2}$ ergs/cm^2·sec^1	~ 100 eV
Polar shower	$10^{-2} > 10^{-1}$ ergs/cm^2·sec^1	~ 200 to 1000 eV
Polar squall	$10^{-1} > 10$ ergs/cm^2·sec^1	~ few KeV

Figure 2.3. Typical differential spectra for polar rain (left), and for polar squall (right) [*Winningham and Heikkila*, 1974].

polar showers. *Winningham and Heikkila* stated they noticed this type of electron precipitation "often" but had no occurrence frequency of these phenomena. Finally, Figure 2.4 (c) shows an example of a polar squall. *Winningham and Heikkila* stated that the polar rain surrounding the squall has the same phase space density and suggested the squall could be caused by energized polar rain.

The next step in polar cap auroral research came with the launch of satellites carrying auroral imagers. These imagers allowed the classification of large-scale polar cap structures [*Ismail et al.*, 1977; *Ismail and Meng*, 1982]. *Ismail et al.* [1977] first used the auroral scanning photometer on board the ISIS 2 satellite to describe the characteristic of polar cap sun-aligned arcs. Figure 2.5 shows the observed location of these arcs.

8
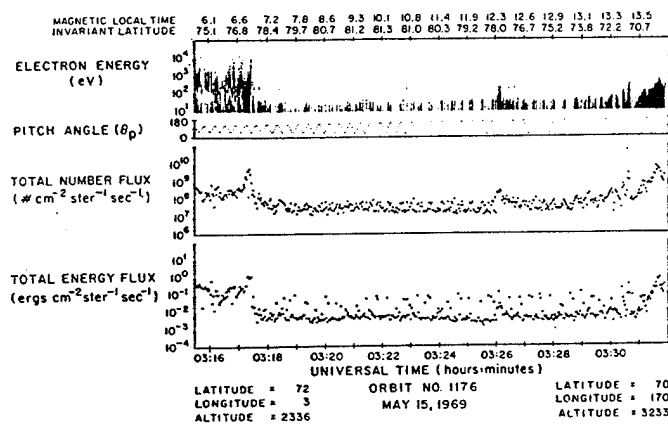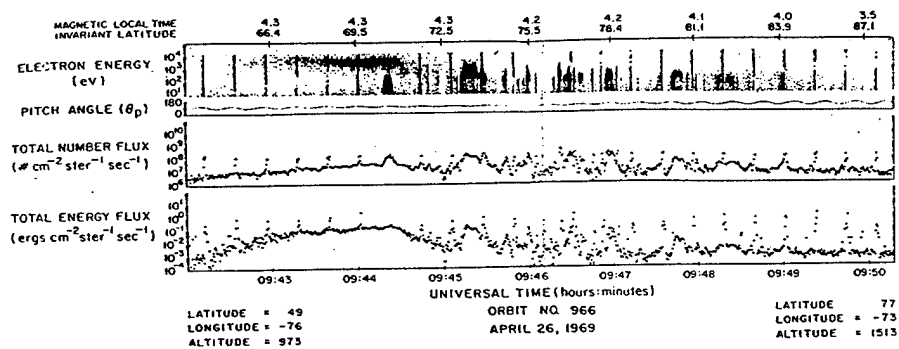
Figure 2.4. Energy/time series spectrograms for (a) polar rain, (b) polar showers, and (c) polar squall [*Winningham and Heikkila*, 1974].
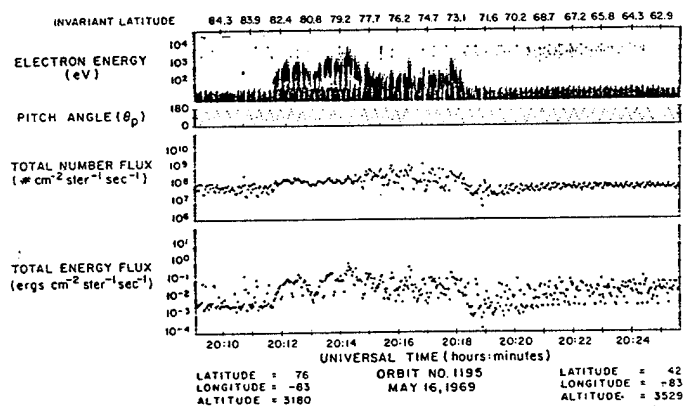
Although the arcs were generally sun-earth aligned, many of them have significant curvature. *Ismail et al.* suggested that these arcs might be classified further since their large-scale structure indicated significant differences. For example, some arcs in Figure 2.5 were connected to the auroral oval differently.

The electron precipitation data for these arcs showed general agreement with the particle measurements by *Winningham and Heikkila* [1974] for being associated with polar showers. Citing an earlier study by *Berkey et al.* [1976] showing 16 of 18 sun-aligned arcs occurred with a northward IMF component, *Ismail et al.* [1977] showed a strong correlation between the occurrence of the arcs in Figure 2.5 and northward IMF.
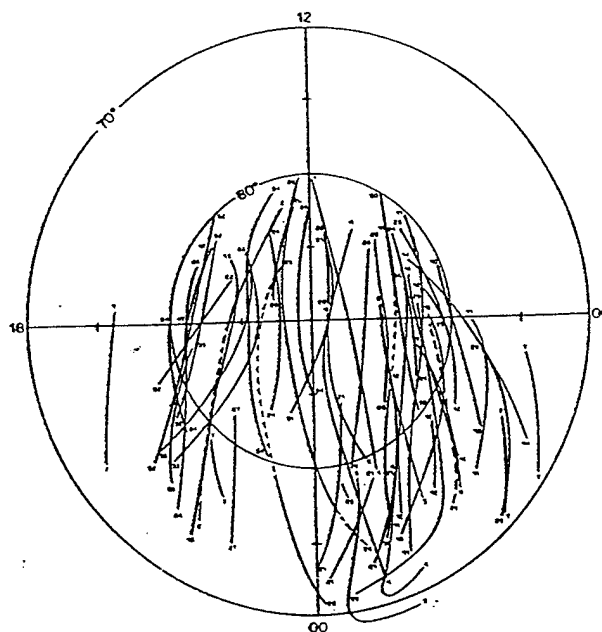

Figure 2.5. Observed location of sun-aligned polar cap arcs plotted on a corrected geomagnetic latitude-time grid [*Ismail et al.*, 1977].

This relationship has since been established by *Ismail and Meng* [1982], *Gussenhoven* [1982], and others. Finally, *Ismail et al.* [1977] discussed the possible source of these particles and suggested they are from open field lines proposed in the reconnection model described by *Whalen et al.* [1971].

Ismail and Meng [1982] further classified polar cap sun-aligned arcs using auroral images collected by the DMSP satellites from 1972-1979. These arcs were classified as Type I, II, or III. The Type I arcs were described as being distinctly sun-aligned and completely separate from the auroral oval. Type II arcs were described as curved arcs expanded from the morning and evening sectors of the oval. Finally, Type III arcs were described as being attached to the midnight oval. All of these different types can be seen in Figure 2.5. However, it was not until 1986 that the first complete images of polar cap arcs extending from the midnight sector of the auroral oval to the noon sector were described by *Frank et al.* [1986]. They used images from the high altitude DE1 spacecraft to describe this phenomenon and named the arcs "theta aurora."

Hardy et al. [1982] did an extensive study on optical and electron precipitation measurements of polar cap arcs, including lower energy electron precipitation using DMSP satellite data. This study showed several important findings. The results appropriate to this research are as follows: (1) Only polar rain was present during extended periods of southward IMF. (2) During the onset of northward IMF conditions, structured electron precipitation occurred in both polar caps with the strongest precipitation in the northern polar cap. (3) The low energy electrons in the polar cap region are the result of two different distributions. The first distribution was

approximately Maxwellian with temperatures between 50 and 200 eV and number densities ranging from $0.03/cm^3$ to $4/cm^3$. The other distribution displayed a peak between 50 and 200 eV from an acceleration through a potential drop of approximately 100 V from a Maxwellian distribution. (4) Polar cap sun-aligned arcs had electron distributions peaked at approximately 1 KeV, which is the result of a electron population accelerated through a potential drop of approximately 750 V. (5) Some of the electron distributions in the polar cap can be explained by an acceleration through a potential of approximately 50 V of magnetosheath electrons.

Hardy et al. [1982] also produced time series plots of electron precipitation over the polar cap. Figures 2.6 and 2.7 display the shift between southward IMF conditions showing only polar rain, then to northward conditions and the subsequent development of polar showers and polar cap arcs.

Hardy [1984] revisited the low energy electron precipitation at high latitudes of the polar cap. Using the definitions of polar rain and polar showers described by *Winningham and Heikkila* [1974], his research showed that the occurrence frequency of polar showers is approximately 50%, indicating that polar showers are much more frequent than previously thought. He also showed that these polar showers are accompanying all visual and sub-visual forms in the polar cap. Among other conclusions, he suggested three results pertinent to this thesis. First he suggested these electrons likely are coming from the same source region. Secondly, he showed that the observed number flux is independent of the solar wind flux or the flux gated by northward IMF shifts.
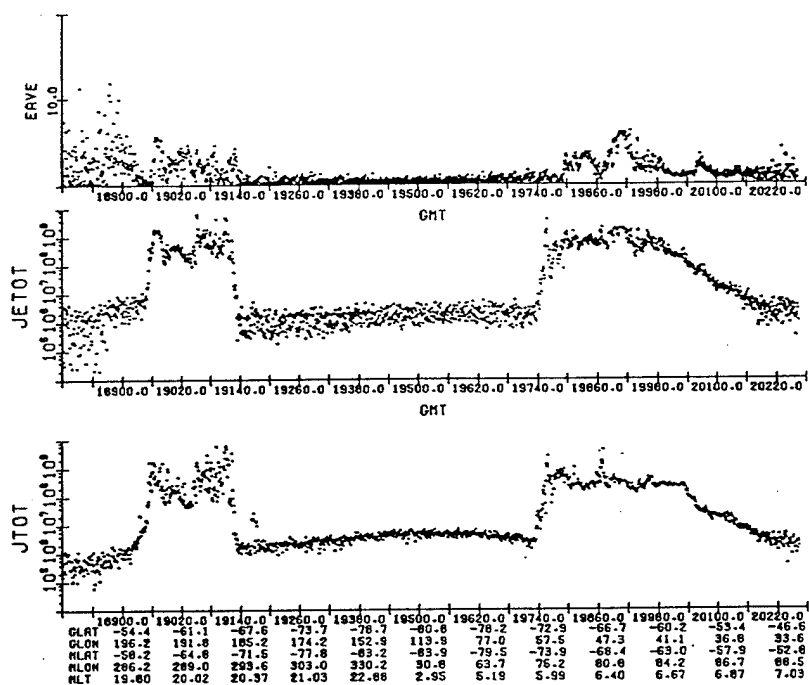
Figure 2.6. Electron precipitation time series for polar rain under southward IMF conditions [*Hardy et al.*, 1982]. Dec. 12, 1977.
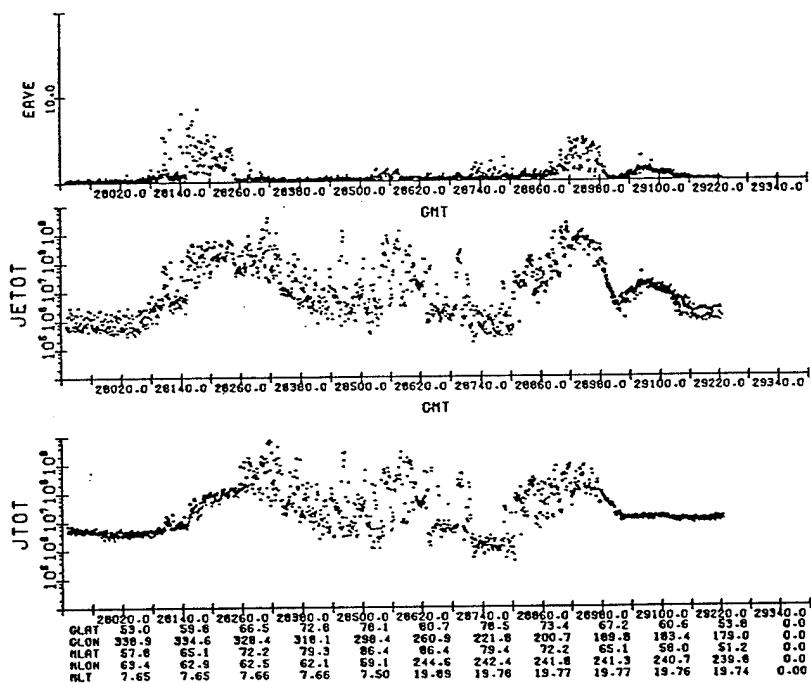

Figure 2.7. Electron precipitation time series for structured polar showers and polar cap arcs after the shift to northward IMF [*Hardy et al.*, 1982]. Dec. 12, 1977.

Finally, he concluded the particles are accelerated by processes between the magnetopause and ionosphere.

After 1985 it appears that most of the research is focused on studying intense visual sun-aligned arcs or modeling of these phenomena [*Hoffman et al.*, 1985; *Valladares and Carlson*, 1991; *Crain et al.*, 1993; *Zhu et al.*, 1993]. This thesis and associated research resume the study of all forms of polar cap electron precipitation. Using a large DMSP database, I will show the source of these different phenomena is in the magnetosheath. Additionally, I will show the number density of the source region is variable by at least an order of magnitude while the kT temperature is generally invariant.

CHAPTER III

INSTRUMENTATION

3.1 Defense Meteorological Satellite Program

The Defense Meteorological Satellite Program (DMSP) is a US Air Force-sponsored program primarily used to provide data for terrestrial weather forecasting and data about the near-space environment. The program calls for two polar orbiting satellites to be operational at all times. One is in a dawn-dusk orbit while the other is in a noon-midnight orbit (actually 1030-2230). Occasionally there may be as many as four or as few as one, depending on launch scheduling.

The DMSP satellites fly in circular polar orbits ranging from ~840-860 km altitude in a dawn-dusk meridional plane (F6 and F8), or in a 1030-2230 meridional plane (F7 and F9). The orbital period is approximately 101 minutes and the orbital inclination is 98.3°. Although the satellites are in sun-synchronous orbits, their spatial coverage in magnetic local time (MLT) and geomagnetic latitude (MLAT) is wide. This is due to the diurnal rotation of the geomagnetic pole about the geographic pole. Figure 3.1 shows the extensive coverage of the polar cap regions and most of the auroral oval. The auroral oval circles the magnetic north pole and spans a magnetic latitude varying between 60° and 75°. The DMSP F8 satellite used for this research is in a dawn-dusk orbit and carries the SSJ/4 Precipitating Ion and Electron Detector. This detector is described in detail in the next section.
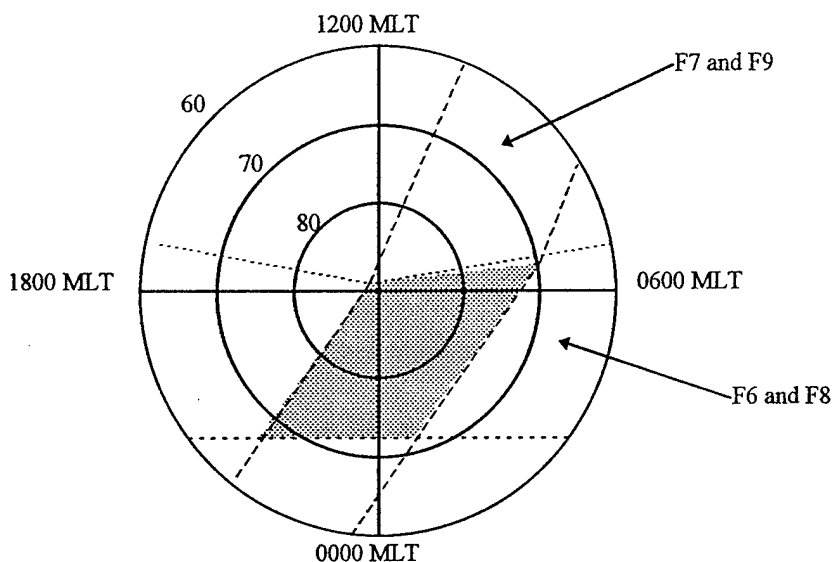
Figure 3.1. Combined north pole coverage for DMSP F8 and F9 plotted in a corrected geomagnetic latitude/magnetic local time coordinate system.

3.2 The SSJ/4 Precipitating Ion and Electron Detector

3.2.1 Description

Since 1974 the DMSP satellites have carried several different versions of precipitating particle detectors. The first version had only had six channels and measured only precipitating electrons with energy levels ranging from 0.2 KeV to 20 KeV. The instrument was improved over the years and the latest version has 20 channels, measuring precipitating electrons and ions with energies logarithmically spaced from 30 eV to 30 KeV. The DMSP F8 carries this latest version of this instrument, the SSJ/4 Precipitating Ion and Electron Detector.

The satellite is three-axis stabilized; therefore, the aperture of the SSJ/4 collecting the particles is always looking to the local zenith. The detector collects these particles

using a set of four cylindrically curved plate electrostatic analyzers arranged in two pairs. The radii of curvatures of the plates are 127° for the low energy pair (30 eV to 1 KeV) and 60° for the high energy pair (1 KeV to 30 KeV). The voltage on the two sets of plates is stepped through ten levels from high voltage to low such that the low energy (high energy) analyzer samples the energy flux from 1 KeV to 30 eV (30 KeV to 1 KeV). The time at which the detector dwells in each channel is 98 milliseconds with a 2-millisecond period between each step to stabilize the voltage [*Schumaker et al.*, 1988]. The electrons or ions entering the apertures are only collected if their energy is such that the particle can complete the path between the curved plates under the applied voltage. For example, if the particle's energy is too low it will make contact with the inner plate and is not counted. If the energy is too high, the particle makes contact with the outer plate and is not counted. The ion detector is essentially the same as the electron detector except the aperture is slightly larger and the plate voltage is opposite.

3.2.2 Calibration

The SSJ/4 instrument was calibrated at the Phillips Laboratory located at Hanscom AFB, Massachusetts. The instrument is calibrated by mounting it on a platform that has the ability to scan in azimuth and elevation. An electron beam source, coupled with a computer system to control the energy level, performs the calculations. This system produces a nearly monoenergetic, uniform electron beam with a radius of about 15 centimeters. The beam can be tuned to produce an electron beam ranging in energy from 10 eV to 50 KeV [*Schumaker et al.*, 1988]. The entire system is placed in a set of

Helmholtz coils to cancel out the effects of the earth's magnetic field. At the end of each

scan, the computer calculates the energy dependent geometric factor G(E) and a response

curve is generated for each channel by determining G(E) at a series of energy levels (see
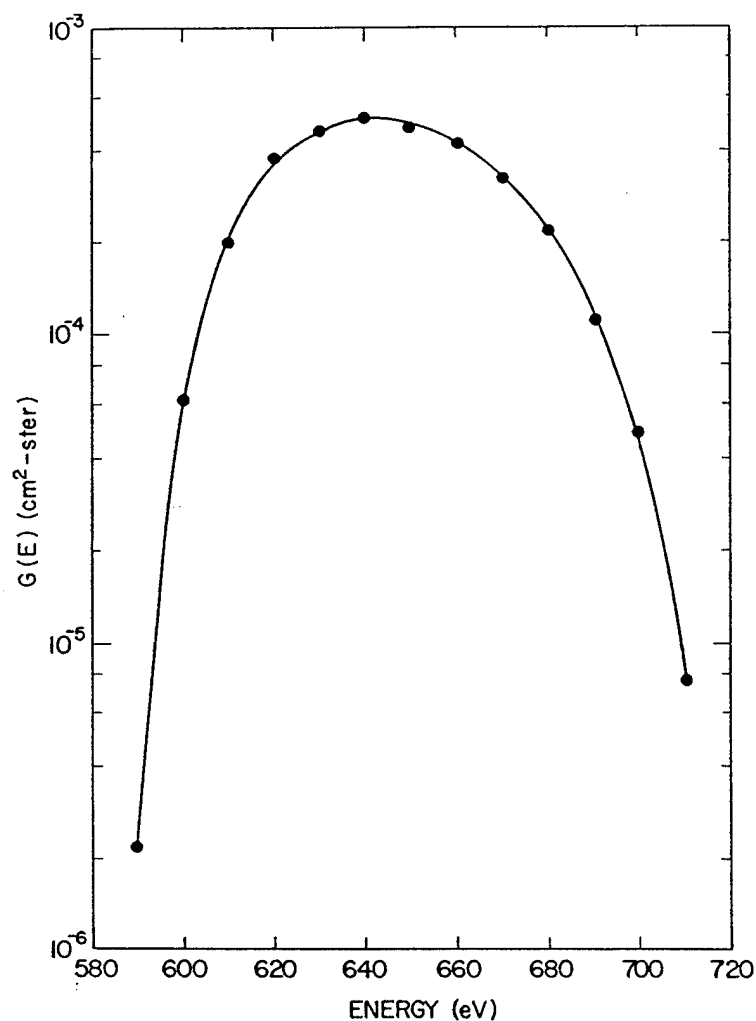
Figure 3.2).

Figure 3.2. The energy dependent geometric factor G(E) plotted as a function
of energy for channel 8 of the F8 SSJ/4 detector [*Schumaker et al.*, 1988].

The energy independent geometric factor is then calculated by integrating over the response curve such that

$$j(E) = C / (\Delta T \cdot G)$$

where j(E) is the differential flux (particles/cm^2·sec·ster·eV) in the channel with energy threshold E, C is the count level observed in that channel, and ΔT is the accumulation interval for these counts (98 milliseconds). Finally, G is the energy independent geometric factor [*Schumaker et al.*, 1988].

Because of time constraints and beam distortion problems at lower energies, some of the channels of the F8 SSJ/4 were not calibrated experimentally as discussed in this section. These channels are indicated with an asterisk in Table 3.1. The energy dependent geometric factors for the uncalibrated channels were determined as follows: the high energy channel geometric factors were found by logarithmic interpolation while the low energy channel factors were set to the experimentally determined value for channels 11 and 12. *Schumaker et al.* checked this assumption for the low energy channels and found the values to be in error by no more than a few percent from calculated values using a Gaussian line shape where $G \approx 1.065(\Delta E \cdot G(E))$.

After injection into orbit, the instruments aboard the F6-F9 were cross calibrated in flight. The conversion constants resulting from the cross calibration are presented in Table 31. The constants listed include only those for the F8 satellite. Figure 3.3 shows a graphical depiction of the channel pass bands for the SSJ/4 electron detector. The energy

Table 3.1. Conversion constants for the DMSP F8 SSJ/4 detector.

Ch	E	ΔE	G	KJETOT	KJTOT	CDIST
20	31.3	3050	3.26E-04	9.99E+06	3.19E+05	1.60E-34
19	21.1	2000	2.75E-04	6.65E+06	3.15E+05	2.82E-34
18	14.3	1330	2.30E-04	3.61E+06	2.52E+05	4.97E-34 *
17	9.72	860	1.85E-04	2.06E+06	2.12E+05	9.10E-34
16	6.61	615	1.52E-04	1.16E+06	1.75E+05	1.63E-33 *
15	4.50	430	1.18E-04	6.93E+05	1.54E+05	3.08E-33
14	3.05	284	8.99E-05	4.21E+05	1.38E+05	5.97E-33 *
13	2.07	184	7.30E-05	2.39E+05	1.15E+05	1.08E-32
12	1.40	125	5.39E-05	1.48E+05	1.06E+05	2.17E-32
11	.950	88	4.27E-05	8.63E+04	9.08E+04	4.03E-32
10	.950	85	3.20E-05	1.15E+05	1.21E+05	5.38E-32
9	.640	63	2.43E-05	6.85E+04	1.07E+05	1.05E-31
8	.440	42	1.94E-05	3.82E+04	8.68E+04	1.92E-31
7	.310	29	1.26E-05	2.89E+04	9.31E+04	4.19E-31 *
6	.210	20	8.84E-06	2.01E+04	9.58E+04	8.81E-31
5	.144	13	5.63E-06	1.46E+04	1.01E+05	2.02E-30 *
4	.098	9.1	3.30E-06	1.15E+04	1.18E+05	5.06E-30 *
3	.068	6.3	1.94E-06	9.48E+03	1.39E+05	1.24E-29 *
2	.045	4.2	1.07E-06	7.94E+03	1.76E+05	3.40E-29 *
1	.031	2.9	5.53E-07	8.01E+03	2.58E+05	9.54E-29 *

E is the energy in KeV, ΔE is the bandwidth in eV of the channel, G is the geometric factor in $cm^2 \cdot ster \cdot KeV$, KJETOT is the energy flux conversion constant in $KeV/cm^2 \cdot sec \cdot ster$, KJTOT is the number flux conversion constant in $electrons/cm^2 \cdot sec \cdot ster$, and CDIST is the distribution function conversion constant in $electrons \cdot sec^3/cm^6$.

resolution depicted in Figure 3.3 will play an important role in the data analysis. Further

discussion about the resolution effects will be discussed in Chapter V.

The constants in Table 3.1 are used to convert the electron counts from the SSJ/4

data into useable information such as the total energy flux, total number flux, and

distribution function for each channel. The procedure for this is outlined in detail in the

next chapter, which discusses the databases used for this research.
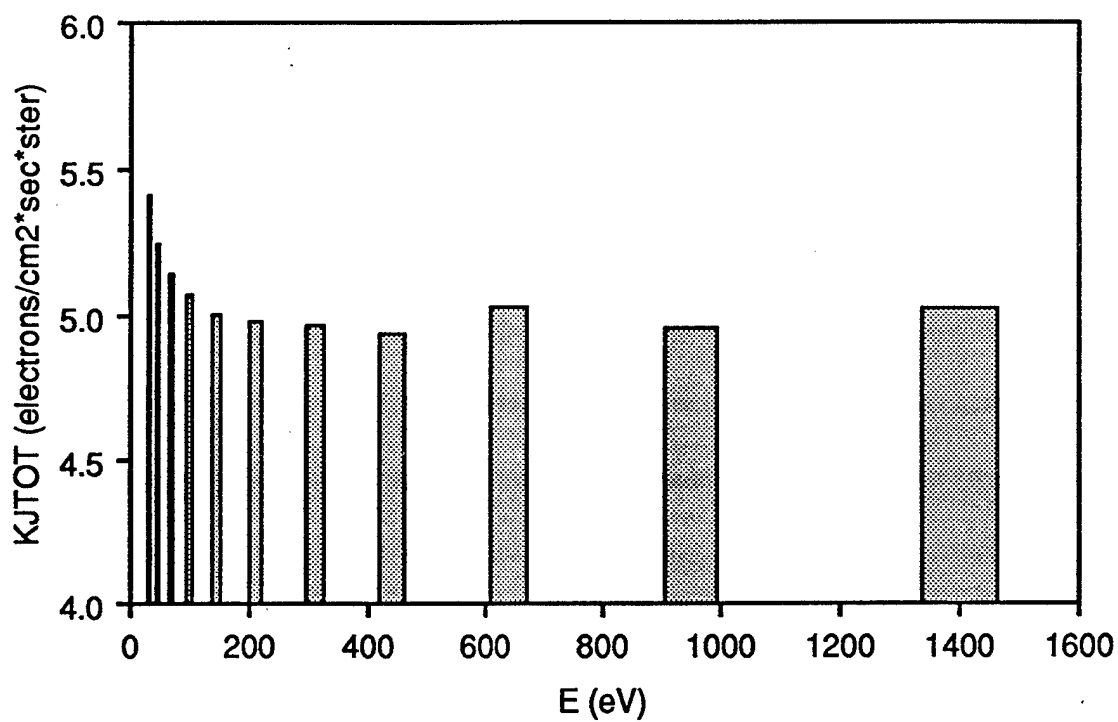
Figure 3.3. Channel pass bands for channels 1 (31 eV) through 12 (1.4 KeV) for the SSJ/4 electron detector.

CHAPTER IV

DATABASES

4.1 Precipitating Electron Count Database

4.1.1 Data Format

The SSJ/4 detector simply counts precipitating ions and electrons. These counts must be converted into useable information such as energy flux, number flux, and the distribution function. The data were collected through previous research and stored on magnetic tape (6250 bpi). These tapes were read into files in the format shown in Table 4.1. The raw data shown in Table 4.1 include all the information to extract the energy flux and number flux, and plot the distribution function, using the channel response characteristics and calibration constants shown in Table 3.2. In addition to the counts, the exact time and location of the satellite are provided in these files.

Table 4.1. Sample precipitating electron data from the SSJ/4 F8 detector.

YR	MODA	HHMMSS	LAT	LONG	(TIME)	ALT	TYPE		30.0 EV	44.0 EV	64.6 EV	94.9 EV	139.2 EV	204.4 EV	300.0 EV	440.0 EV	646.0 EV	948.0 EV	0.948 KEV	1.39 KEV	2.04 KEV	3.00 KEV	4.40 KEV	6.46 KEV	9.48 KEV	13.92 KEV	20.00 KEV	30.00 KEV
89	1216	4422	-45.1	333.4	180002	860	DMSP-F8	ELECTRON																				
		1	1	2	1	1	1	0	0	0	0	1	3	1	0	0	0	0	0	0	0
		2	0	2	1	1	1	1	0	0	0	1	1	0	1	0	1	0	0	0	0
		1	2	0	3	0	0	0	0	0	0	0	0	2	0	0	0	0	0	1	1
		1	3	1	0	0	0	0	0	0	0	0	0	0	0	0	2	0	1	1
89	1216	4426	-45.3	333.4	180008	860	DMSP-F8	ELECTRON																				
		3	1	1	1	1	0	0	0	0	0	1	0	2	0	0	1	1	0	1
		1	0	0	1	0	0	1	1	1	0	1	0	0	0	0	0	0	0	1
		3	0	0	1	0	0	0	1	0	0	1	0	1	1	0	0	0	0	1
		4	2	1	1	1	1	0	0	0	0	0	0	0	0	0	2	0	0
89	1216	4430	-45.5	333.4	180013	860	DMSP-F8	ELECTRON																				
		3	1	1	1	1	1	0	1	0	0	0	1	0	1	0	1	0	0	0
		1	0	0	1	1	0	1	0	0	0	0	1	1	1	1	0	0	0	1
		4	1	0	1	1	0	0	0	0	0	0	0	1	0	0	0	1	0	1
		2	3	1	1	1	0	0	1	0	0	1	0	1	1	0	0	1	0
89	1216	4434	-45.7	333.4	180019	860	DMSP-F8	ELECTRON																				
		2	1	1	1	0	0	0	0	0	0	1	0	1	0	0	1	1	0	0
		2	0	1	1	1	0	0	0	0	0	0	0	0	0	1	1	0	2	3
		3	1	0	2	0	1	0	0	1	0	1	0	0	0	0	1	1	0	3
		2	1	1	1	0	0	1	1	0	1	0	0	0	0	0	1	1	0
89	1216	4438	-45.9	333.4	180025	860	DMSP-F8	ELECTRON																				
		4	1	0	0	4	1	1	2	2	0	1	1	0	0	0	1	0	0	0
		2	1	1	0	0	0	0	1	0	0	1	0	1	0	2	2	0	0	3
		3	1	2	0	0	0	0	1	0	0	0	2	1	0	0	0	1	1	1
		1	1	0	2	1	0	0	0	1	0	0	0	0	0	1	1	1
89	1216	4442	-46.1	333.4	180031	860	DMSP-F8	ELECTRON																				
		3	2	1	1	0	1	0	1	0	0	0	1	0	0	0	1	0	0
		6	0	1	0	3	0	0	1	0	0	1	1	1	0	2	0	0	1
		1	0	0	2	1	0	0	0	0	2	0	0	1	0	0	0	0	1
		4	0	0	0	0	1	0	0	0	0	0	1	0	0	0	0	0
89	1216	4446	-46.2	333.4	180038	860	DMSP-F8	ELECTRON																				
		0	0	0	2	2	0	0	0	1	0	0	0	0	0	0	1	0	0
		1	0	0	1	0	1	2	0	0	0	0	0	0	1	0	0	0	0
		2	2	0	1	0	1	0	0	0	0	0	1	0	0	0	0	2	0
		3	0	0	1	0	1	0	0	0	0	1	0	0	0	0	1	0	0

21

4.1.2 Data Selection Criteria

The data used include all satellite orbits from 1 November 1989 through 31 December 1989 (976 passes). I selected only those satellite passes that attained a geomagnetic latitude of 80° in the northern hemisphere (488 passes). This ensured only events classified as polar cap phenomena would be included. This subset of data was further reduced to one second resolution columnar data including the following;

   a. Year, Month, Day (YYMMDD)

   b. Hour, Minute, Second (HHMMSS)

   c. Universal time (UT)

   d. Magnetic latitude (MLAT)

   e. Magnetic local time (MLT)

   d. Total energy flux (JETOT)

   e. Total number flux (JTOT)

   f. Integer number count for each channel

All of the quantities except the total energy and number fluxes can be directly read from the original files. The fluxes were calculated as follows:

$$JETOT = \sum_{i=1}^{9} K_{JETOT}(E_i) \cdot C_i + 1/2 \sum_{i=10}^{11} K_{JETOT}(E_i) \cdot C_i + \sum_{i=12}^{20} K_{JETOT}(E_i) \cdot C_i$$

$$JTOT = \sum_{i=1}^{9} K_{JTOT}(E_i) \cdot C_i + 1/2 \sum_{i=10}^{11} K_{JTOT}(E_i) \cdot C_i + \sum_{i=12}^{20} K_{JTOT}(E_i) \cdot C_i$$

where E_i is the central energy of channel i and C_i is the electron precipitation count in the respective channel. $K_{JETOT}(E_i)$ and $K_{JTOT}(E_i)$ are calibration coefficients for each channel. The numerical values for these coefficients and central energies were presented in Table 3.1.

4.2 Interplanetary Magnetic Field Database

I collected the interplanetary magnetic field data from the public OMNI database accessed through the internet at nssdca.gsfc.nasa.gov. This database included the available IMF components direction and magnitude and the KP index for every hour during the time period 1 November 1989 to 31 December 1989. The hourly IMF components in the OMNI database are calculated from IMF data with a higher time resolution than one hour. For example, the first hour of each day would be an average of the higher time resolution points throughout the first hour (from 00:00 UT through 01:00 UT). This hour would be indicated as 00:00 UT on the OMNI database.

However, data are not always available. The month of November and December had 14 and 16 days of IMF data, respectively. The OMNI database shown below in Table 4.2 is a sample from the actual data and shows that periods of data are occasionally missing. These missing periods of data correspond to the times when the IMF monitoring satellite was located in unsuitable locations relative to the solar wind for an IMF measurement. The available IMF data were merged with the electron precipitation data by using the hourly averaged IMF as close to or the hour preceding the pass. For example, if a particular day had only 5 hours of IMF data available, the whole day would be merged.

Table 4.2. Sample IMF data from the OMNI database.

Year	Day	Hour	B_x	B_y	B_z	$K_p \cdot 10$
89	339	0	0.0	0.0	0.0	53
89	339	1	0.0	0.0	0.0	53
89	339	2	0.0	0.0	0.0	53
89	339	3	0.0	0.0	0.0	33
89	339	4	0.0	0.0	0.0	33
89	339	5	0.0	0.0	0.0	33
89	339	6	3.6	-4.2	0.1	20
89	339	7	2.9	-4.5	0.3	20
89	339	8	4.3	-2.5	2.0	20
89	339	9	1.8	-4.5	-0.3	13
89	339	10	3.7	-3.8	0.9	13
89	339	11	3.2	-4.2	0.2	13

However, when examining the final database, the IMF was a selection criterion and an

entry of 0.0 would prohibit use of the particular event. This merged database was then

further reduced to its final form described in the following section.

4.3 Final Merged Database

The final merged database shows total integral energy fluxes on numerous

occasions, which would create visible auroral forms. Additionally, research shows that all

forms of visible polar cap aurora are sun-aligned. Therefore, many of the events in our

database are sun-aligned arcs. However, since there are several different nomenclatures

for polar cap electron precipitation, these events will be referred to here as polar cap

electron precipitation events.

Selection criteria were needed to locate and study the polar cap electron precipitation events. Two criteria were used to accomplish this task. First, by examining time series plots of JETOT, the data confirmed *Winningham and Heikkila*'s [1974] baseline "polar rain" total energy flux. By choosing several different energy levels to serve as "filtering" criteria, the data were separated into polar rain, polar showers, and polar squalls. The total energy flux levels used to separate the precipitation events are shown in Table 4.3. Secondly, I selected only those events which lasted for more than two seconds once a particular energy flux criterion was met. Requiring three second events raised our data set above the one second sampling rate of the count data, and ensured the data was not contaminated by "noise level" one second spikes.

The resultant database had only polar cap electron precipitation events described in detail by the information listed below in Table 4.4. Many of the listed descriptors are self explanatory or are simply read from the original database. However, width, peak fluxes, and average fluxes need additional explanation about how they were calculated.

Table 4.3. Total energy flux (JETOT) selection criteria.

			Visual forms
	> 0.16	ergs/cm²·sec·ster	Visual forms
0.16 <	0.08	"	
0.08 <	0.04	"	Polar Showers
0.04 <	0.02	"	
0.02 <	0.01	"	Polar Rain
0.01 <	0.005	"	
0.005 <	0.0025	"	

The width of the events was calculated assuming an orbital velocity of ~7.5 km/s, and multiplying this factor by the number of second the event lasted. The peak number and energy fluxes are the peak one second JTOT and JETOT, respectively, for any given event. Table 4.5 shows the number of events by different thresholds included in the final database.

Table 4.4. Data included in merged database for final analysis.

Year, Month, Day of the event	YYMMDD
Start UTS of the event	SUTS (sec)
Peak energy channel	peak Ch
Count in the peak channel	peak Count
Magnetic Latitude	MLAT
Magnetic Longitude	MLONG
Magnetic Local Time	MLT
Width of the event	width (km)
Peak number flux	peak J (e/cm^2·sec·ster)
Peak energy flux	peak JE (ergs/cm^2·sec·ster)
Average number flux	avg J (e/cm^2·sec·ster)
Average energy Flux	avg JE (ergs/cm^2·sec·ster)
3 Component IMF	B_x, B_y, B_z
K_p Index	KP
Counts at the peak energy channel	C

Table 4.5. Number of events included in the final merged database.

	> 0.16	ergs/cm^2·sec·ster		174	events
0.16	< 0.08	"		294	"
0.08	< 0.04	"		526	"
0.04	< 0.02	"		812	"
0.02	< 0.01	"		1087	"

The average number and energy fluxes were calculated as follows:

$$avgJ = \frac{\sum_{i=1}^{\text{\# seconds}} JTOT_i}{\text{\# seconds}} \qquad avgJE = \frac{\sum_{i=1}^{\text{\# seconds}} JETOT_i}{\text{\# seconds}} \ .$$

To illustrate a sample event from the final merged database, Table 4.6 shows the data associated with an actual event. Figure 4.1 shows the count rate spectra for each second included in the event. This event was selected using a threshold of 0.08 ergs/cm^2·sec·ster and would be classified as a "polar squall by *Winningham and Heikkila* [1974]. Furthermore, this event has a peak JE of .9 ergs/cm^2·sec·ster, which would cause visible auroral emissions indicative of a sun-aligned arc. Examining this event, the peak in the spectra moves higher in energy until the peak energy channel (peak Ch) and peak total integral energy flux (peak JE) are reached. Additionally, the count rate increases as the peak energy is reached. As the event decays, the peak Ch and peak JE collapse to the lower energy channels and counts. Although this is a high energy event to demonstrate the phenomenon, all the events in the database follow this pattern. Now that the database is sufficiently described, the following chapter will show in detail the theoretical and data analysis.

Table 4.6. Sample data for an actual event from the final merged database.

YYMODD	891115
SUTS	36712
MLAT	81.3
MLONG	68.8
Peak Ch	8
Peak Count	6111
Peak JE	0.9067 ergs/cm^2·sec·ster
Peak J	1.5E9 electrons/cm^2·sec·ster
Width	37.5 km
IMF	$B_x = -8.4$, $B_y = -1.8$, $B_z = 5.6$

Counts

sec 1:	167	69	111	431	783	687	335	107	22	9	3	5	1	0
sec 2:	19	159	187	279	511	3423	862	119	8	5	367	16	3	1
sec 3:	89	93	143	231	623	1951	4703	6111	1311	783	31	20	14	1
sec 4:	53	87	87	183	327	991	1311	575	35	22	13	5	1	4
sec 5:	41	37	77	2719	399	263	151	81	10	5	7	2	4	2
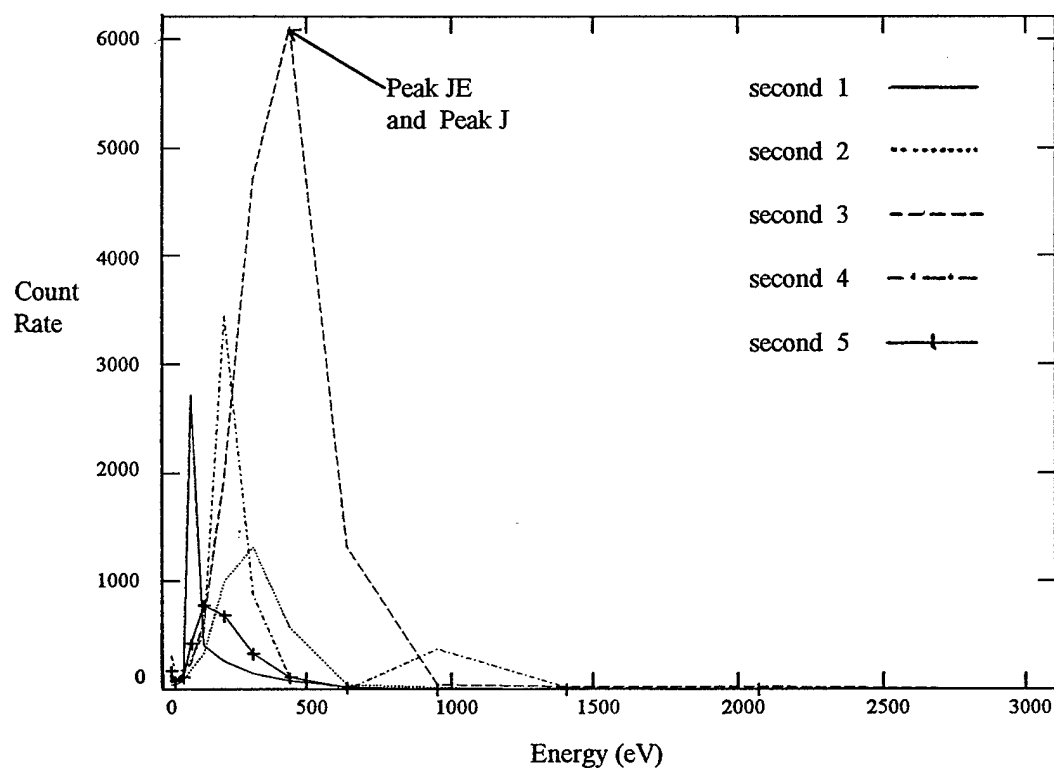
Figure 4.1. Five-second count rate spectra for sample event described in Table 4.6.

CHAPTER V

DATA ANALYSIS

5.1 Instrument and Physical Effects

Understanding the SSJ/4 instrument capabilities is an important part of the data analysis. The two effects related to this research are shown in Figure 5.1, which shows the entire database including one-second events. This figure shows a graph of peak JE (ergs/cm^2·sec·ster) versus peak J (electrons/cm^2·sec·ster) for all precipitation events in the entire database. The instrument effect is the striations seen in the lower portion of the figure. Section 5.1.1 discusses the cause of these low energy flux striations and the solution. The physical effect is the distinct positive slope and spread of the data points beginning at a peak J of approximately 10^7 electrons/cm^2·sec·ster. Section 5.1.2 presents
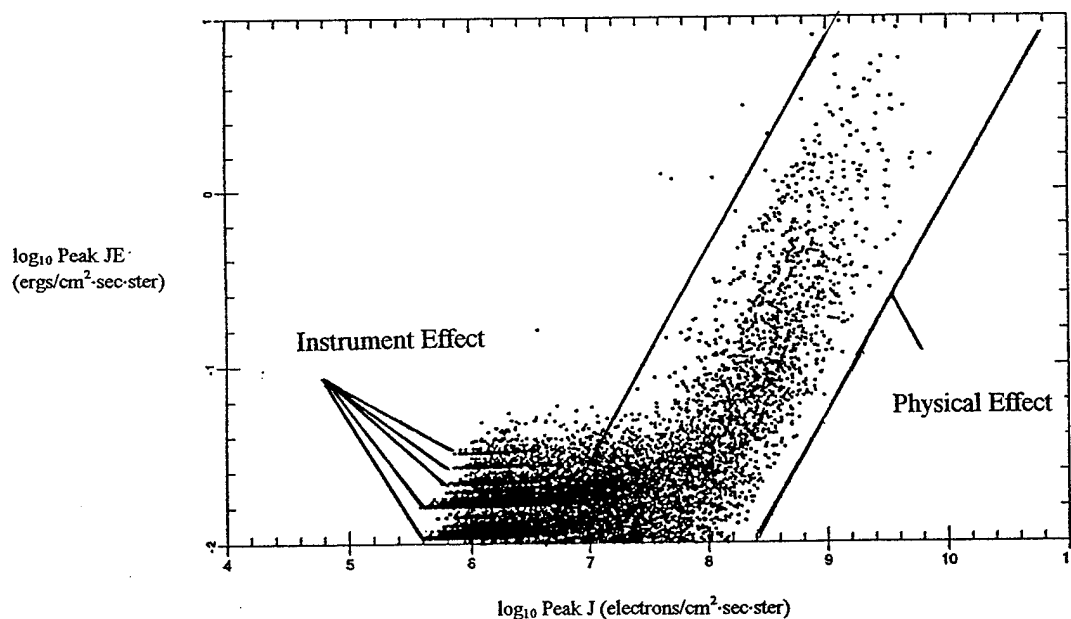
Figure 5.1. Peak JE versus peak J for entire database.

an understanding of the slope and spread of the high energy fluxes.

5.1.1 Horizontal Striations at Low Energy/Number Fluxes

Figure 5.1 shows approximately six striations in the lower left corner where the

peak JE is less than ~ 0.06 ergs/cm^2·sec·ster. The cause of these is electron counts of 1 or

2 in the high energy channels, while simultaneously the counts in the lower energy

channels are sufficient only for polar rain. This count arrangement has the effect of

moving the data points from the lowest portion of the sloped population (which extends

continuously below the x-axis of Figure 5.1) to these "striation" levels. A closer

examination shows a better view of this phenomenon (see Figure 5.2).
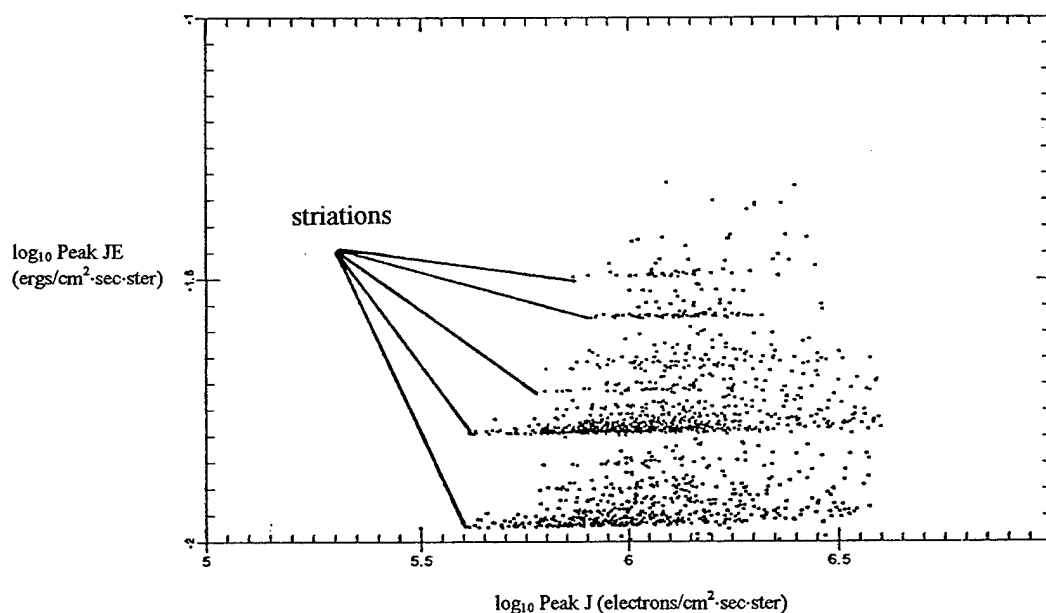
Figure 5.2. Closeup of horizontal striations for events t > 1 second.

In order to explain the striations, a set of theoretical count rate spectra was generated. These theoretical count rates had either a one count or zero count in each channel. The spectra were then analyzed using the conversion constants in Table 3.1 to calculate the peak J and peak JE such that the resulting values could be overlaid on Figure 5.2. Figure 5.3 shows two examples of 20 one-second theoretical spectra in the top and bottom panels. Each row on the matrices corresponds to a theoretical count rate spectrum for 20 energy channels starting with the lowest energy channel at the left.

In the top panel, all twenty spectra have a single count in channel 19, whereas the bottom panel has a single count in channel 20. Adding a count of one to the lowest channel and then systematically adding a count of one to the next higher energy channel will produce the matrices in Figure 5.3. Applying the same computer code used to generate Figure 5.2 on these matrices produced the events shown in the two panels of Figure 5.3. Overlaying Figure 5.3 and 5.2 clearly shows the phenomenon is created by low counts at the high energy channels while simultaneously there are sufficiently low counts at the lower energy channels.

For example, Figure 5.3 shows that a count of 1 in channel 20 will give a peak JE ~ 0.03 ergs/cm^2·sec·ster. However, a count of 1 in channels 1 (30 eV) through 14 (3.05 KeV) must be added before a significant increase in peak JE can be detected. Other count rate matrices can be created to produce similar results. To remove this effect, I selected only channels 1 through 14 to examine the polar cap electron precipitation. This choice is consistent with previous studies done by *Winningham and Heikkila* [1974],

log₁₀ Peak JE
(ergs/cm²·sec·ster)

```
0 0 0 0 0 0 0 0 0 0 0 0 0 0 0 0 0 0 1 0
1 0 0 0 0 0 0 0 0 0 0 0 0 0 0 0 0 0 1 0
1 1 0 0 0 0 0 0 0 0 0 0 0 0 0 0 0 0 1 0
1 1 1 0 0 0 0 0 0 0 0 0 0 0 0 0 0 0 1 0
1 1 1 1 0 0 0 0 0 0 0 0 0 0 0 0 0 0 1 0
1 1 1 1 1 0 0 0 0 0 0 0 0 0 0 0 0 0 1 0
1 1 1 1 1 1 0 0 0 0 0 0 0 0 0 0 0 0 1 0
1 1 1 1 1 1 1 0 0 0 0 0 0 0 0 0 0 0 1 0
1 1 1 1 1 1 1 1 0 0 0 0 0 0 0 0 0 0 1 0
1 1 1 1 1 1 1 1 1 0 0 0 0 0 0 0 0 0 1 0
1 1 1 1 1 1 1 1 1 1 0 0 0 0 0 0 0 0 1 0
1 1 1 1 1 1 1 1 1 1 1 0 0 0 0 0 0 0 1 0
1 1 1 1 1 1 1 1 1 1 1 1 0 0 0 0 0 0 1 0
1 1 1 1 1 1 1 1 1 1 1 1 1 0 0 0 0 0 1 0
1 1 1 1 1 1 1 1 1 1 1 1 1 1 0 0 0 0 1 0
1 1 1 1 1 1 1 1 1 1 1 1 1 1 1 0 0 1 0
1 1 1 1 1 1 1 1 1 1 1 1 1 1 1 1 0 0 1 0
1 1 1 1 1 1 1 1 1 1 1 1 1 1 1 1 1 1 1 0
```

log₁₀ Peak J (electrons/cm²·sec·ster)

log₁₀ Peak JE
(ergs/cm²·sec·ster)

```
0 0 0 0 0 0 0 0 0 0 0 0 0 0 0 0 0 0 0 1
1 0 0 0 0 0 0 0 0 0 0 0 0 0 0 0 0 0 0 1
1 1 0 0 0 0 0 0 0 0 0 0 0 0 0 0 0 0 0 1
1 1 1 0 0 0 0 0 0 0 0 0 0 0 0 0 0 0 0 1
1 1 1 1 0 0 0 0 0 0 0 0 0 0 0 0 0 0 0 1
1 1 1 1 1 0 0 0 0 0 0 0 0 0 0 0 0 0 0 1
1 1 1 1 1 1 0 0 0 0 0 0 0 0 0 0 0 0 0 1
1 1 1 1 1 1 1 0 0 0 0 0 0 0 0 0 0 0 0 1
1 1 1 1 1 1 1 1 0 0 0 0 0 0 0 0 0 0 0 1
1 1 1 1 1 1 1 1 1 0 0 0 0 0 0 0 0 0 0 1
1 1 1 1 1 1 1 1 1 1 0 0 0 0 0 0 0 0 0 1
1 1 1 1 1 1 1 1 1 1 1 0 0 0 0 0 0 0 0 1
1 1 1 1 1 1 1 1 1 1 1 1 0 0 0 0 0 0 0 1
1 1 1 1 1 1 1 1 1 1 1 1 1 0 0 0 0 0 0 1
1 1 1 1 1 1 1 1 1 1 1 1 1 1 0 0 0 0 0 1
1 1 1 1 1 1 1 1 1 1 1 1 1 1 1 0 0 0 0 1
1 1 1 1 1 1 1 1 1 1 1 1 1 1 1 1 0 0 0 1
1 1 1 1 1 1 1 1 1 1 1 1 1 1 1 1 1 0 0 1
1 1 1 1 1 1 1 1 1 1 1 1 1 1 1 1 1 1 0 1
1 1 1 1 1 1 1 1 1 1 1 1 1 1 1 1 1 1 1 1
```

log₁₀ Peak J (electrons/cm²·sec·ster)

Figure 5.3. Peak JE versus peak J for two different simulated matrices.

Hardy et al. [1982], *and Hardy* [1984]. These studies show the peak energy flux of electron precipitation over the polar cap should not normally exceed a few KeV except under strong sun-aligned arc conditions. Figure 5.4 shows the result of removing the highest 6 energy channels. Comparing Figures 5.4 and 5.5 shows this research has reproduced the work done by *Hardy* [1984]. Furthermore, the rest of this thesis continues where *Hardy* and others stopped and explains in detail the database shown in Figure 5.4.

5.1.2 Slope and Spread of Peak JE vs. Peak J

Figure 5.4 clearly shows a distinct positive slope and a significant spread in the data points. To examine this phenomenon, I separated the database by peak energy channels and peak JE baselines using the thresholds shown in Table 4.3. For example, the event described in Table 4.6 and Figure 4.1 would be placed in the bin Ch 8, > 0.08 ergs/cm^2·sec·ster. Since there are 14 channels and 7 energy thresholds, there are 98 bins. Some of the results from events binned in channels 6 (210 eV), 9 (640 eV) and 13 (2.07 KeV) are presented in Figures 5.6, 5.7, and 5.8, respectively. The trends shown in these plots are representative of all the channels, and only three are shown for the sake of brevity. The plots for the remaining channels are presented in Appendix A. To explain these graphs, for example, the baseline of 0.04 ergs/cm^2·sec·ster for channel 13 in Figure 5.8 means this graph would include all events exceeding a peak JE above 0.04 ergs/cm^2·sec·ster occurring at channel 13.
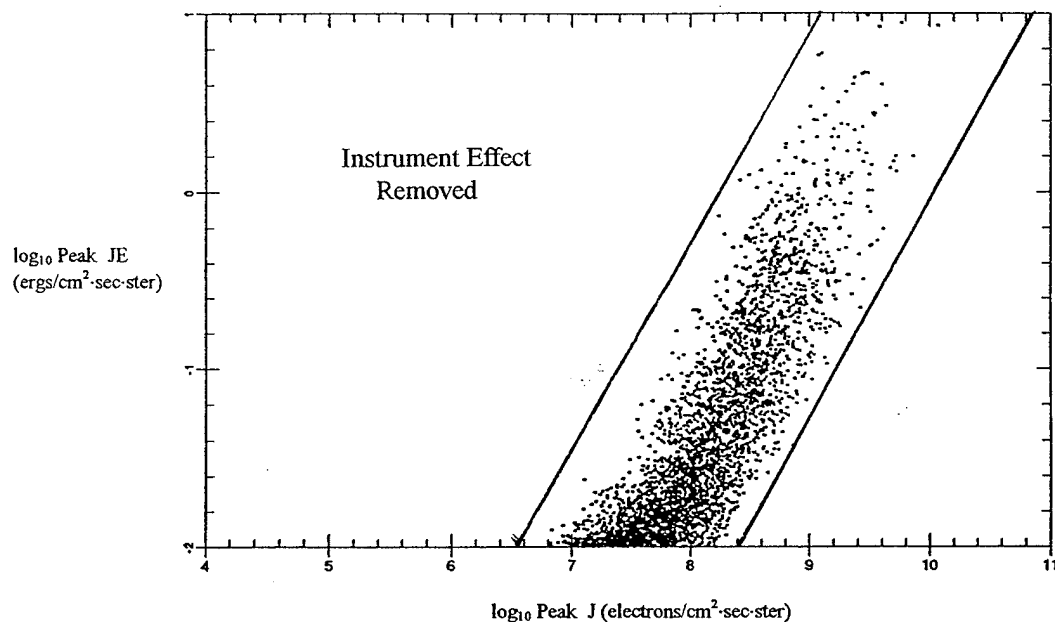
Figure 5.4. Population after removing channels 15 (4.4 KeV) through 20 (30 KeV). The dashed lines in Figure 5.5 below represent the solid lines above.
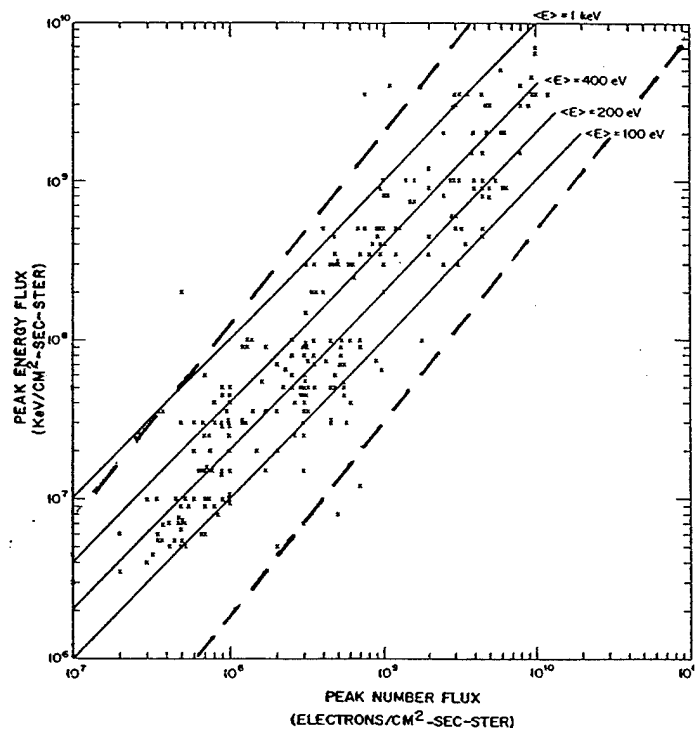
Figure 5.5. The peak energy flux observed above 85° geomagnetic latitude when the flux is above the level of polar rain, plotted as a function of the peak number [*Hardy*,1984]
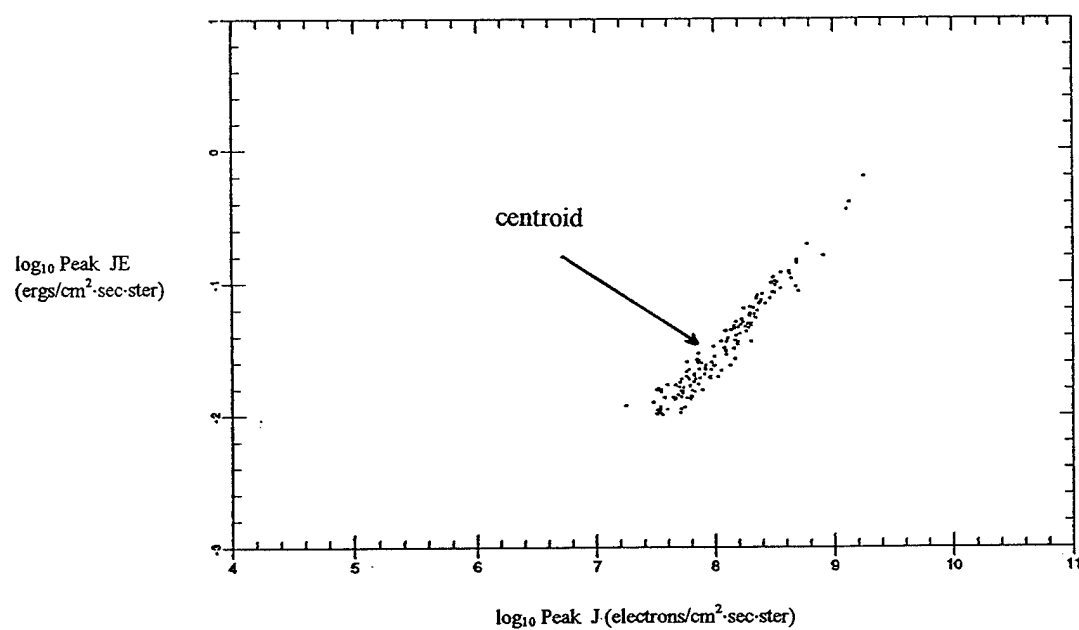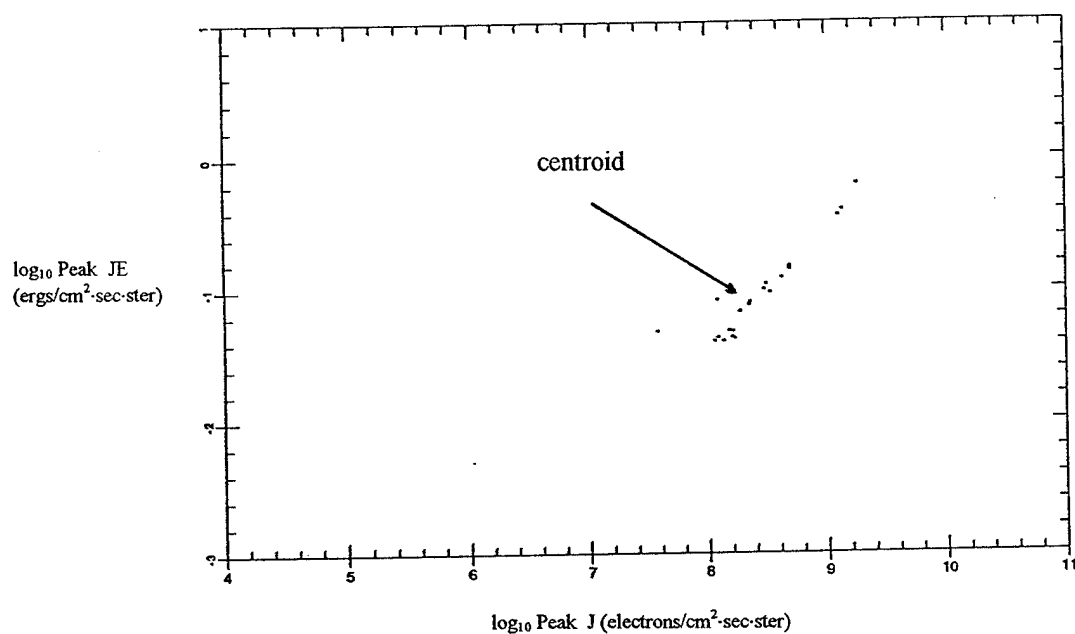
Figure 5.6. Peak JE versus peak J for two thresholds in channel 6 (210 eV). Top Figure is 0.04 ergs/cm^2·sec·ster and bottom Figure is 0.01 ergs/cm^2·sec·ster.
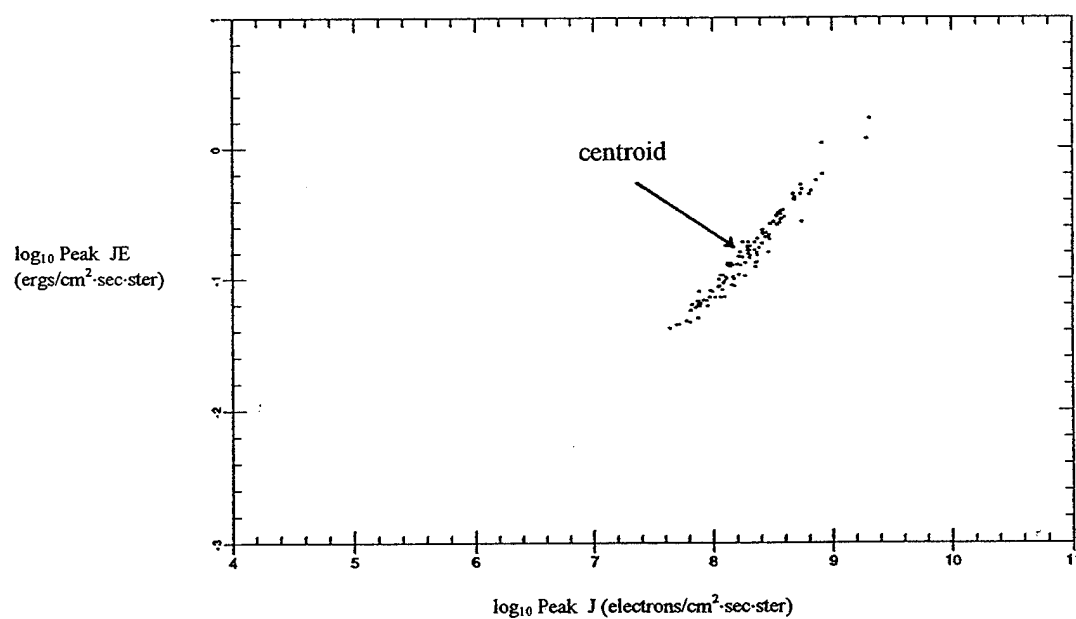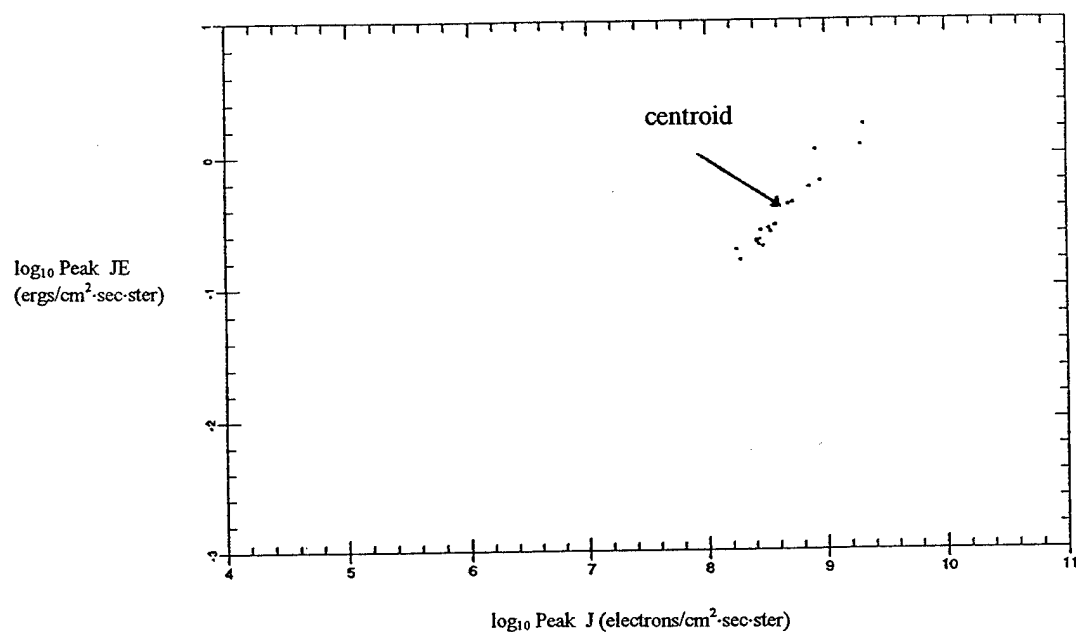
Figure 5.7. Peak JE versus peak J for two thresholds in channel 9 (640 eV).
Top Figure is 0.16 ergs/cm^2·sec·ster and bottom Figure is 0.04 ergs/cm^2·sec·ster.
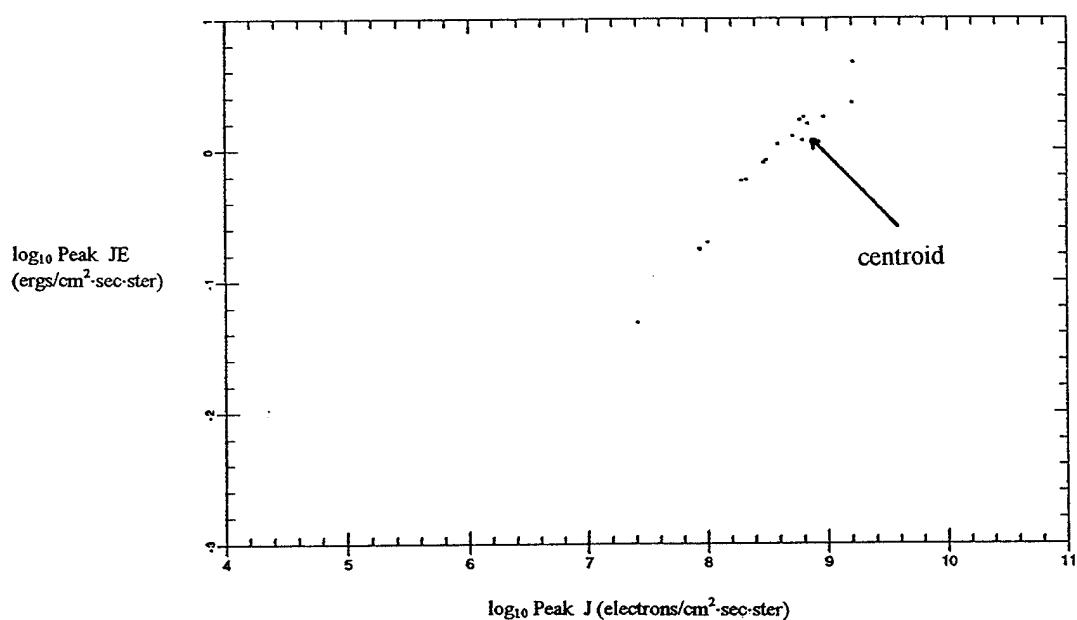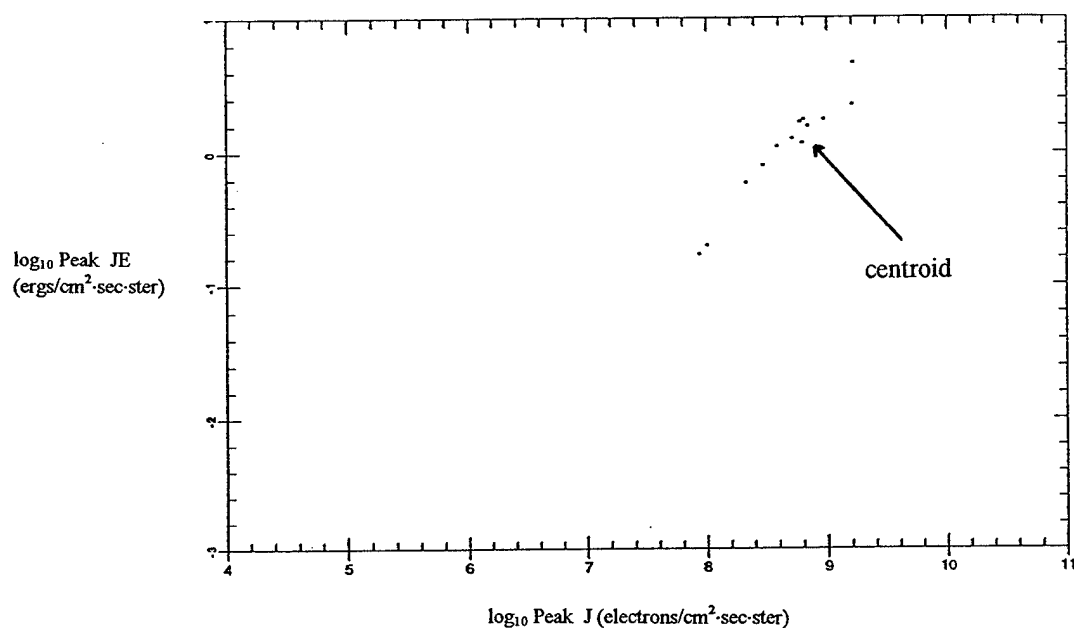
Figure 5.8. Peak JE versus peak J for two thresholds in channel 13 (2.07 KeV).
Top Figure is 0.16 ergs/cm^2·sec·ster and bottom Figure is 0.04 ergs/cm^2·sec·ster.

The partitioning of the channels displays three results: (1) The centroid of the population of events occurs at high energy fluxes for the higher energy channels and at low energy fluxes for the lower channels. (2) The population of events for each channel can be line fit on a log scale. As the peak energy channel increases, the line fit shifts to the left. This indicates the same energy flux can be accomplished with a lower number flux collected by higher energy channels. (3) The slope of the line fit increases as the peak energy channel increases. This is a manifestation of the movement of the centroid mentioned earlier. The centroid moves down the population shown in Figure 5.4 as the energy channel is lowered. This indicates the fit to the centroids of the entire database would be a curve passing through the population shown in Figure 5.4.

Figure 5.9 shows the line fit to each of the different energy channels. Comparing this figure to Figures 5.4 and 5.5 shows where the different energy channel populations lie within the entire database. This thorough examination of the database removed the "noise" that would have ultimately contaminated the data and additionally served the purpose of gaining an understanding of the sensitivity and possible misgivings of the SSJ/4 instrument.

5.2 Analysis of the Electron Precipitation Events at DMSP Altitudes

Using the separated datafiles discussed above, I determined basic statistics about the populations. Certain thresholds best describe each energy channel because of the moving centroid. To determine the best population of events for each channel, I plotted occurrence frequency histograms for each channel and threshold. Visual examination of
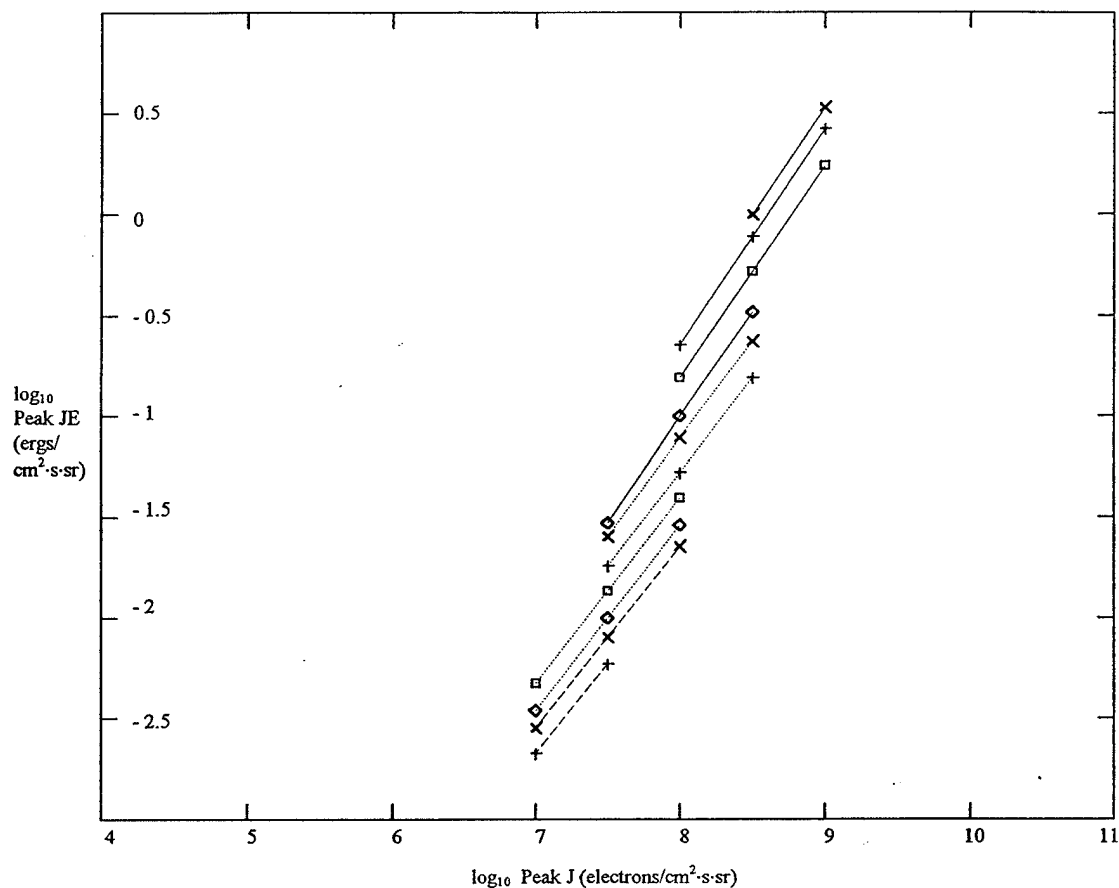
Figure 5.9. Line fit to the different channel populations.

all the histograms allows selection of the files which best describe each energy channel.

Those best describing the events occurring in channels 6, 9, and 13 are shown in Figures

5.10, 5.11, and 5.12. The core statistics for the selected populations are presented in

Table 5.1.
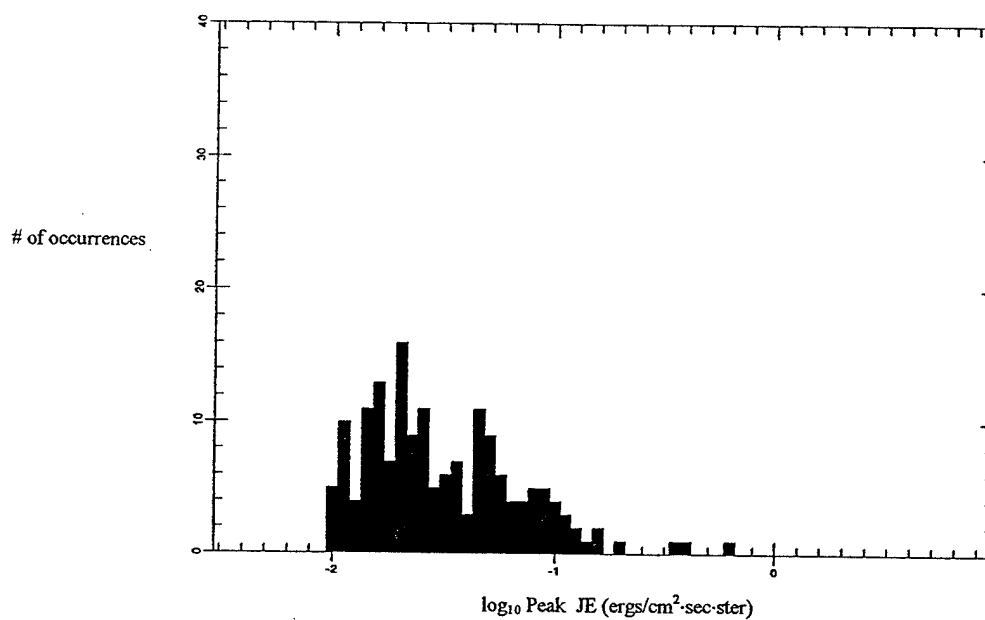
Figure 5.10. Histogram for channel 6 (210 eV) at threshold 0.01 ergs/cm^2·sec·ster.
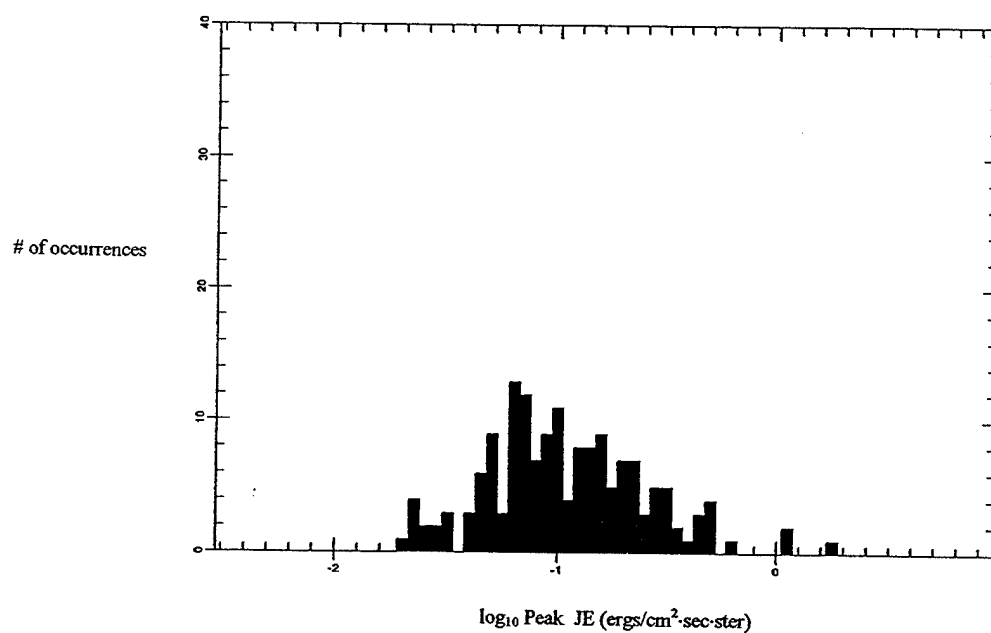
Figure 5.11. Histogram for channel 9 (640 eV) at threshold 0.02 ergs/cm^2·sec·ster.
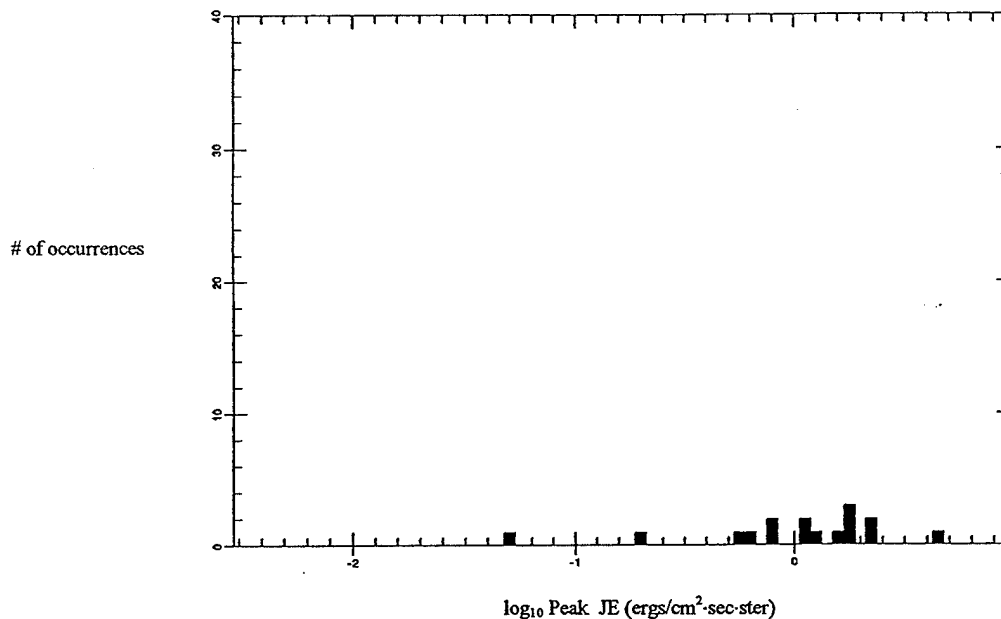
Figure 5.12. Histogram for channel 13 (2.07 KeV) at threshold 0.04 ergs/cm^2·sec·ster.

Table 5.1. Statistics for selected populations. Channel 10 is omitted because channel 11 has the same energy level and is most representative of the 950 eV energy population.

Ch.	Threshold	# points	Mean	Centroid (Median)	Std. dev.	Std. err. mean
14	0.16	6	1.923	1.324	0.376	0.154
13	0.04	16	0.982	1.019	0.466	0.117
12	0.04	47	0.484	0.441	0.332	0.048
11	0.04	108	0.188	0.190	0.372	0.036
10	omitted					
9	0.02	160	0.109	0.099	0.363	0.029
8	0.02	213	0.075	0.068	0.351	0.024
7	0.02	155	0.068	0.062	0.341	0.027
6	0.01	167	0.031	0.026	0.350	0.027
5	0.01	74	0.029	0.029	0.287	0.033
4	0.005	51	0.013	0.012	0.248	0.035
3	0.005	15	0.012	0.011	0.129	0.033

Using these statistics, I produced Figure 5.13 showing the median peak JE versus

energy channel. Figure 5.13 represents the populations of accelerated electrons detected

at ~ 840 km altitude by the DMSP SSJ/4 instrument. The ΔE resolution listed in Table

3.1 and shown in Figure 3.3 indicates the difficulty of determining at exactly what energy

level the peak JE occurs. For example, the ΔE in channel 13 (2.07 KeV) is 184 eV while

the ΔE in channel 6 (210 eV) is 20 eV. Therefore, the instrument cannot resolve the peak

JE as accurately at channel 13 compared to channel 6. Furthermore, although the

resolution is better at the lower energy channels, gaps still exist in the resolution. All of

this combined presents a challenge when determining the source population kT

temperature and number density for high energy precipitation events. This is because

often the peak of the spectra will fall between the energy channels. Further discussion

about the resulting effects from missing the peak will be presented at the end of this

chapter.

Figure 5.14 shows three different possible source population temperatures of 100,

200 and 400 eV. To produce this figure, I used two assumptions. I assumed the source

region electrons have a Maxwellian distribution and no precipitating electrons exist below

the energy level of the collecting channel. I then normalized the plot to Figure 5.13, which

compensates for the unknown source region number density.

Overlaying these plots shows the source temperature for precipitating electrons

with energy between 30 eV and 1.5 KeV ranges between 100 kT and 300 kT. However,

this result only appears to hold for the lower energy channels. This, once again, is the

result of missing the peak JE of the spectra. Therefore, a more in-depth analysis of the
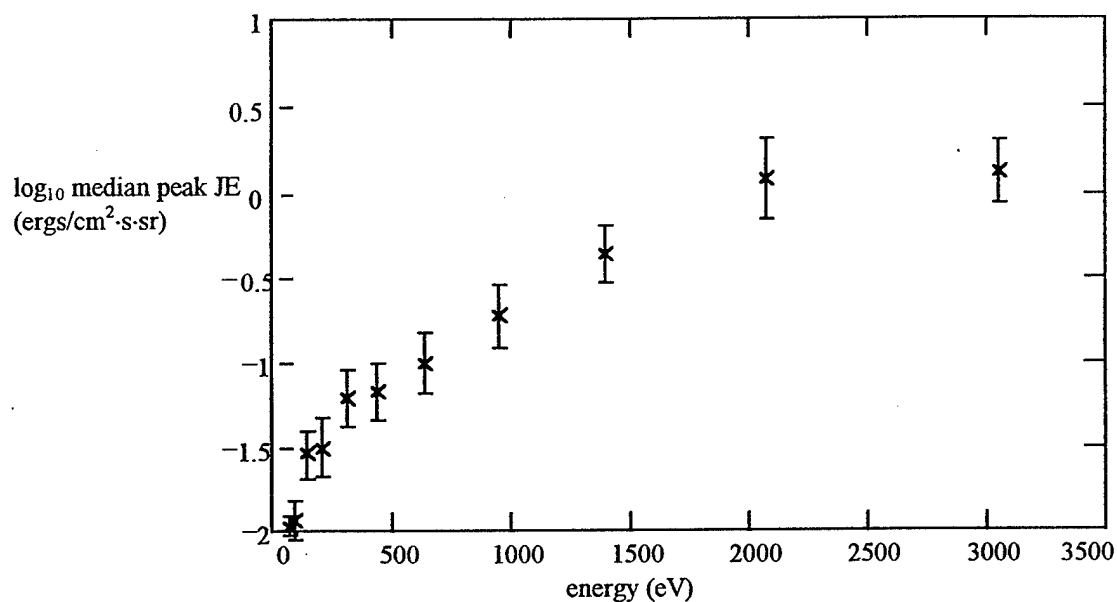
Figure 5.13. Median peak JE versus energy channel for electron precipitation events.
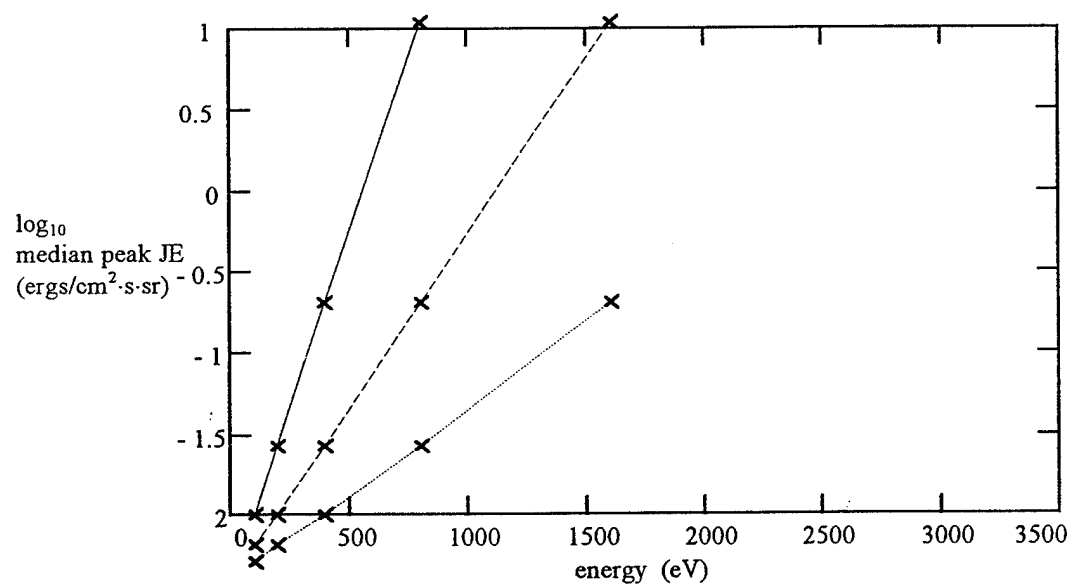
Figure 5.14. Possible accelerated source populations with varying kT temperatures versus energy channel. The temperature scale is normalized to Figure 5.13.

accelerating potential, electron number density, and the temperature must be pursued.

This will be accomplished by taking sample distribution function spectra from the

populations listed in Table 5.1 and determining the source region temperature and electron

number density using Liouville's Theorem. The methodology for this is discussed in the

next section.

5.3 Determining the Source Region Parameters Using Liouville's Theorem

5.3.1 Assumptions

Some assumptions are required to develop the process of determining the source

region temperature and electron number density. First, I assumed the source region is

located where open field lines lie along the magnetosheath [*Winningham and Heikkila,*

1974; *Hardy et al.,* 1982; *Hardy,* 1984] (see Figure 5.15).
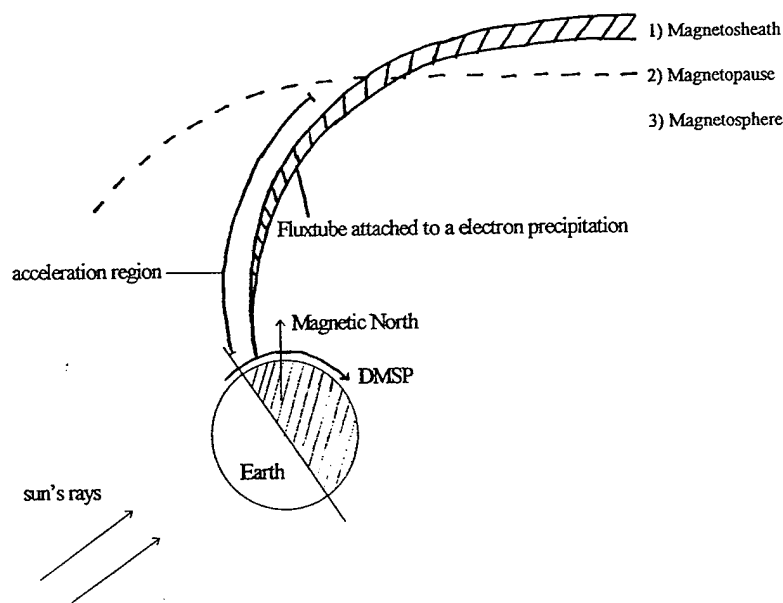
Figure 5.15. Simple polar cap electron precipitation model.

Second, I assumed these populations are accelerated into the ionosphere by a potential

drop. Third, I assumed the magnetosheath plasma is represented by a Maxwellian

distribution. Finally, I assumed Liouville's Theorem applies to the plasma acceleration

process.

Liouville's Theorem states that the phase space density of a plasma is conserved

when the plasma is accelerated or decelerated by an electric potential. This theory is

discussed further in section 5.3.2. Using these assumptions, I will present the method and

results of determining the source region temperature and electron number density from

data collected by the DMSP SSJ/4 instrument.

5.3.2. Liouville's Theorem

Let Φ represent an electric field potential extending from h to h + Δh. Then the

phase space density (or distribution function) between h and h + Δh is related by equation

(1)

$$D(E,h) = D(E',h+\Delta h) \tag{1}$$

where $E' = E + \Phi$ is the energy after acceleration. Assuming a Maxwellian distribution

permits the description of the magnetosheath plasma phase space density by the equation

$$D(E) = N \cdot \left[\frac{m}{2 \cdot \pi \cdot kT} \right]^{3/2} \cdot \exp\left[-\frac{E}{kT} \right] \tag{2}$$

where N is the plasma electron number density of the magnetosheath, kT is the plasma "temperature" and m is the mass of an electron. Applying Liouville's Theorem, the phase space density at DMSP altitude in the ionosphere can be obtained from the equation

$$D(E') = N \cdot \left[\frac{m}{2 \cdot \pi \cdot kT} \right]^{3/2} \cdot \exp\left[-\frac{E}{kT} \right] = N \cdot \left[\frac{m}{2 \cdot \pi \cdot kT} \right]^{3/2} \cdot \exp\left[-\frac{(E' - \Phi)}{kT} \right] \qquad (3)$$

where $E = E' - \Phi$. Here it is important to note that all collected electrons are accelerated by Φ volts, so theoretically we should not see any electrons precipitating with energy less than Φ. Therefore, to use equation (3) we must only consider the energy range $E' \geq \Phi$.

Since our detector does not measure the phase space density, we determine $D(E')$ using the differential electron number flux DNF(E') or differential electron energy flux DEF(E'). These quantities are readily determined from the electron count rates provided by the SSJ/4 instrument. The differential number flux in terms of phase space density is given by the equation

$$DNF(E') = \frac{2 \cdot E'}{m^2} \cdot D(E') \quad , \qquad (4)$$

and differential energy flux in terms of phase space density is given by the equation

$$DEF(E') = \frac{2 \cdot (E')^2}{m^2} \cdot D(E') \quad . \tag{5}$$

Either of these quantities can be used to determine $D(E')$. The spectra of $D(E')$ can be plotted and from these graphs one can determine the accelerating potential (Φ), the electron number density (N), and the temperature (kT).

5.3.3. Theoretical Analysis of the Distribution Function

The three quantities of interest are the accelerating potential, number density, and the temperature. First, the acceleration potential can be determined by converting the count rate to $DNF(E')$ or $DEF(E')$. The $DEF(E')$ spectrum has a peak E'_p, which can be located by setting the second derivative equal to zero as shown in the equation

$$\frac{d}{dE} DEF(E') = A \cdot \exp\left(\frac{\Phi}{kT}\right) \cdot \left[2 \cdot E'_p \cdot \exp\left(\frac{-E'_p}{kT}\right) - \frac{(E'_p)^2}{kT} \cdot \left(\frac{-E'_p}{kT}\right) \right] = 0 \;, \tag{6}$$

where

$$A = N \cdot \left(\frac{m}{2 \cdot \pi \cdot kT}\right)^{3/2} \cdot \frac{2}{m^2} \quad .$$

Solving equation (6) results in the peak energy

$$E_p' = 2 \cdot kT \; .$$
(7)

Since I already stated all the electrons are accelerated to an energy $E' \geq \Phi$, no electrons

exist with an energy less than Φ. Therefore, for equation (7) to be valid, the

condition

$$2 \cdot kT \geq \Phi$$
(8)

must always be satisfied. The kT temperatures in the magnetosheath theoretically range

from ~ 10 to 200 eV; therefore, 2kT ranges from 20 to 400 eV. However, some spectra

from DMSP SSJ/4 data show peaks at and above 1 KeV. So the assumption must be

made that there exist cases where

$$\Phi \gg 2 \cdot kT \; .$$
(9)

To illustrate finding Φ, Figure 5.16 shows a simple graph of $DEF(E')$ versus E_p'.

Note the function increases for $E' < 2kT$ and decreases for $E' > 2kT$. For cases where

$E' > 2kT$ the function for $DEF(E')$ is decreasing. Therefore, the accelerating potential will

always be at $E' = E_p' = \Phi$. For conditions where $E' < 2kT$, the accelerating potential is
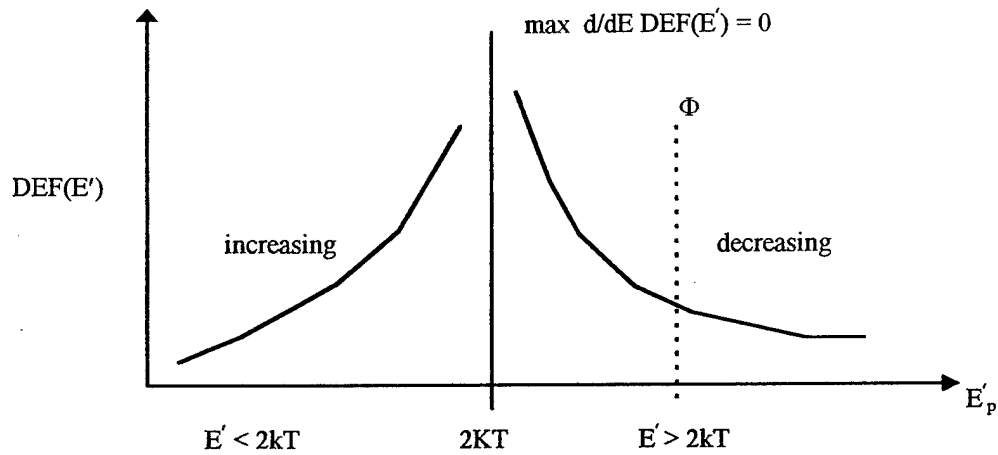
Figure 5.16. Locating the accelerating potential using differential energy flux spectra.

2kT. Therefore, to determine the potential when $E' < 2kT$, we must know the kT

temperature. This can be determined by

$$\ln(D(E)) = \text{constant} - \frac{E}{kT} \, , \tag{10}$$

and by plotting log[D(E)] versus E we produce a line with slope -1/kT. To find the

number density N, we solve the equation

$$\text{constant} = \ln\left[N \cdot \left[\frac{m}{2 \cdot \pi \cdot kT} \right]^{3/2} \exp\left[\frac{-(E - \Phi)}{kT} \right] \right] . \tag{11}$$

Everything in this equation is now known except the number density.

To demonstrate Liouville's Theorem, Figure 5.17 shows a plot of an unaccelerated ($\Phi = 0$) and accelerated ($\Phi = 200$) populations using the same number density of N = 1 electron/cm^2·sec and temperature = 100 eV. Note that the slope of the both D(E) and DACC(E) is -1/kT. From the slope we can determine the potential from equation (7) and then find the number density using equation (11).

5.3.4. Data Analysis Using the Distribution Function

The real-world data analysis often does not conform nicely to our theory. Keeping this in mind, I analyzed numerous data-generated distribution functions. The analysis used channels 3 (68 eV) through 8 (440 eV) from the files described in Chapter IV and listed in Table 5.2. Channels 1 and 2 were omitted because the very low collecting energy level
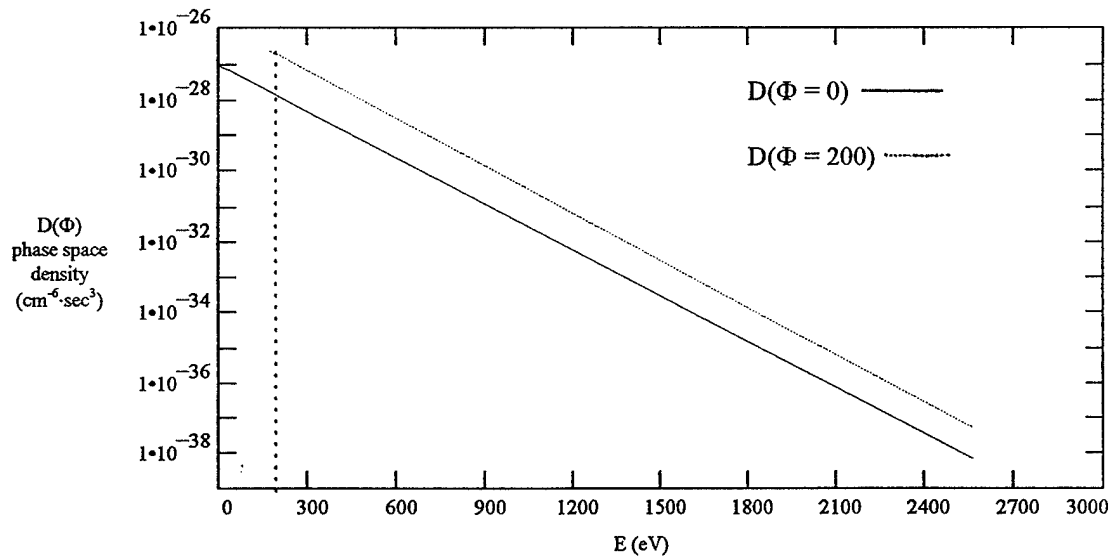
Figure 5.17. Distribution function (cm^{-6}·sec^3) for unaccelerated (D(E)), and accelerated Φ=200 eV (DACC(E)) source populations where N = 1 electron/cm^2·sec and kT = 100 eV.

Table 5.2 Energy channels and thresholds used in the data analysis.
Threshold units are in ergs/cm^2·sec·ster.

Channel	Thresholds	# Events
8 (440 eV)	> 0.16	15
	0.08 > 0.16	16
	0.04 > 0.08	20
	0.02 > 0.04	20
7 (310 eV)	> 0.16	2
	0.08 > 0.16	12
	0.04 > 0.08	20
	0.02 > 0.04	20
6 (210 eV)	0.08 > 0.16	3
	0.04 > 0.08	10
	0.02 > 0.04	20
5 (144 eV)	0.04 > 0.08	8
	0.02 > 0.04	20
	0.01 > 0.02	20
4 (98 eV)	0.02 > 0.04	6
	0.01 > 0.02	6
	0.005 > 0.01	17
3 (68 eV)	0.02 > 0.04	1
	0.01 > 0.02	6
	0.0050 > 0.010	4
	0.0025 > 0.005	4

would not add anything significant to this analysis. All the channels above 8 were omitted

since the energy resolution (ΔE) of these channels is near 100 eV (the approximate

expected temperature of the source region), and the gaps between these channels exceed

100 eV. Determining accurate temperatures from the distribution function at these high

energy channels would be difficult if not impossible. The distribution function is obtained

from the DMSP SSJ/4 counts using the equation

$$D(E) = count\ rate(E) \cdot cdist(E)\ .$$

The distribution function is then determined by using equation 10. Plotting log[D(E)]

versus energy channel will display the function. Sample distribution function plots from

channel 3 (68 eV) and channel 8 (440 eV) are presented in Figures 5.18 and 5.19. These

plots were analyzed as follows: (1) determine the y-intercept (y) at the peak of the

distribution function, (2) determine the slope of the function for one, two, and three points

past the peak and find the average of these slopes, (3) calculate the number density by

$$constant = \log\left[\frac{m}{2 \cdot \pi \cdot kT}\right]^{\frac{3}{2}} \tag{12}$$

and

$$N = 10^{(y-constant)}\ ; \tag{13}$$

finally, (4) the acceleration potential used in the analysis is the energy level ($\Phi = E'$) of the

collecting channel. This is reasonably valid for channels 3 through 8 for two reasons.

First, theory predicts $\Phi = E'$ when $E' > 2kT$, which is the case for many of the spectra

used in this research. Second, for the cases where $E' \leq 2kT$ the SSJ/4 energy level
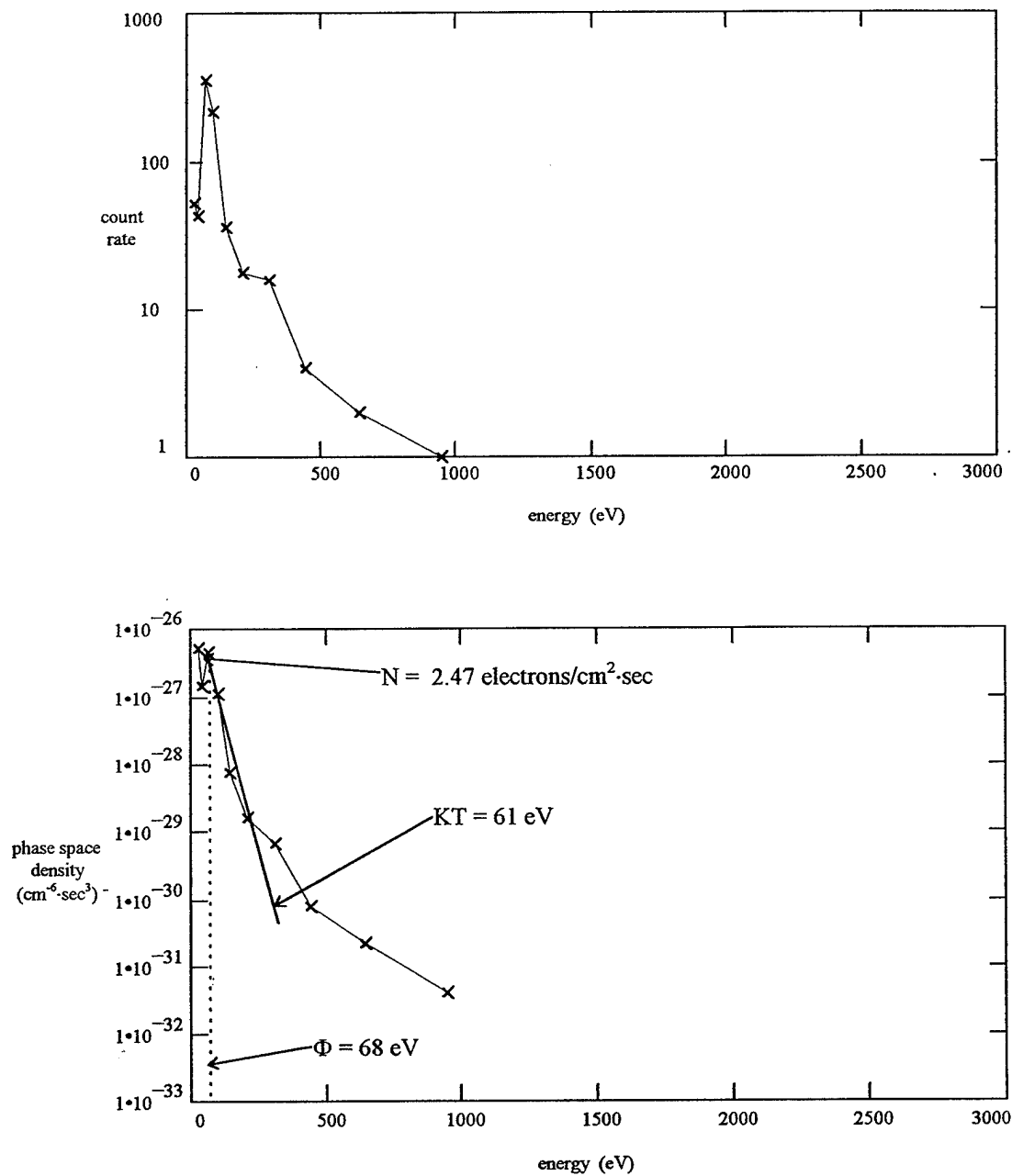
Figure 5.18. Sample count rate and distribution function for an event occurring with peak JE in channel 3 (68 eV).
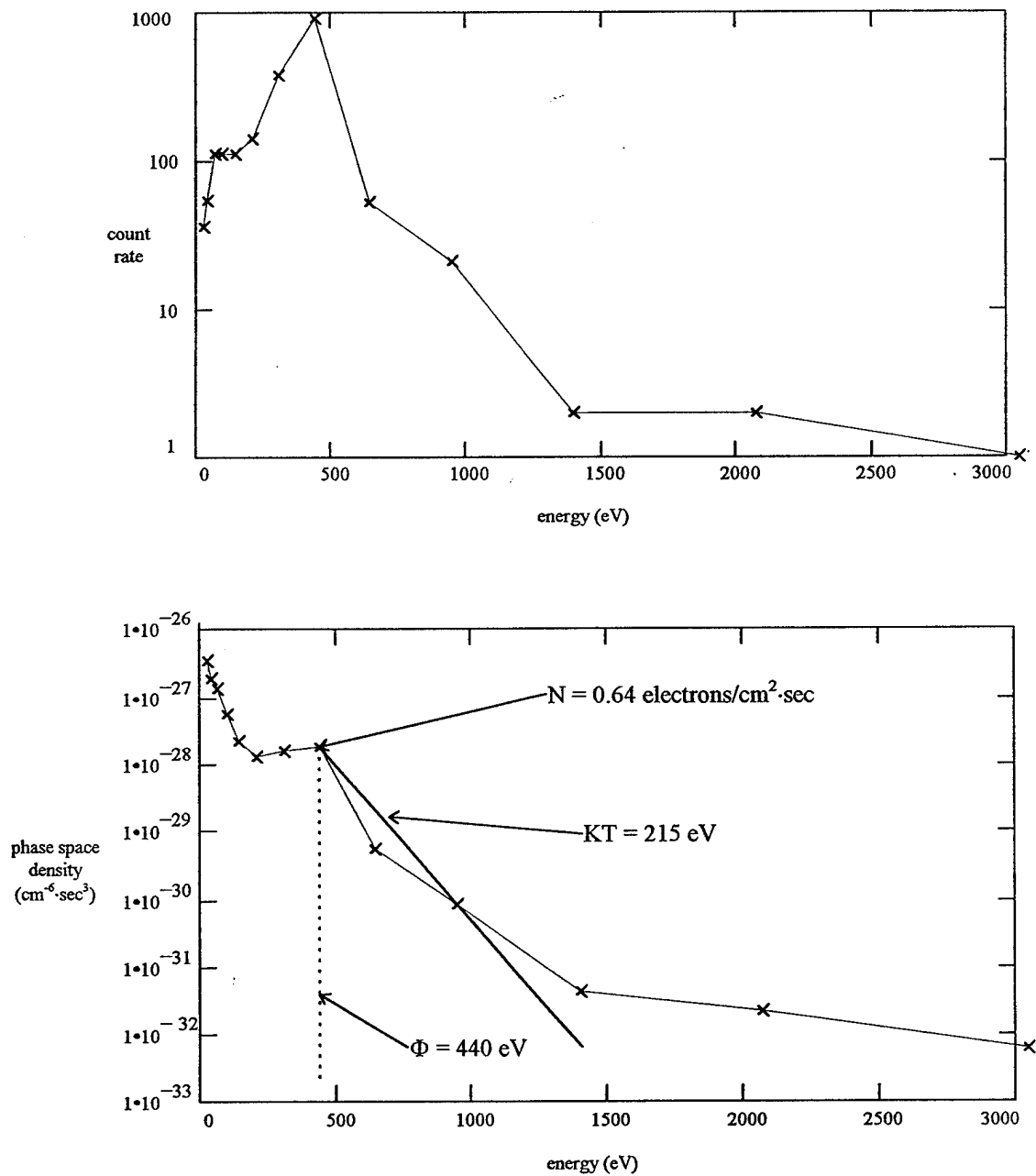
Figure 5.19. Sample count rate and distribution function for an event occurring with peak JE in channel 8 (440 eV).

resolution often does not enable one to resolve these peaks. For example, Figure 5.18 shows $\Phi = 68$ while $2kT = 122$. This is a result of the energy resolution of the SSJ/4 instrument, which allows the opportunity to miss the peak in the function while simultaneously overestimating the temperature. After analyzing the distribution functions for each event in Table 5.2, I plotted the mean temperature versus mean number density for each channel and threshold. The results are presented in Figure 5.20. These results display two phenomena. First, the mean temperature ranges between 50 eV and 250 eV for all the events. This is indicative of magnetosheath particles [*Wei et al.*, 1990]. Second, the number density ranges from $\sim 0.01 - 3.5$ cm^{-3}. This is also indicative of the magnetosheath as the source region [*Wei et al.*]. Table 5.3 shows the different electron number densities and temperatures for possible source regions.

Because each of the channels event thresholds is different, I plotted the mean temperature versus energy threshold (Figure 5.21) and mean number density versus energy threshold (Figure 5.22). The invariant temperature is again evident in Figure 5.21 as expected. However, Figure 5.22 shows the variation in number density by energy channel versus peak JE thresholds.

As a first estimate, these results indicate the magnetosheath as the source region. However, with some further examination of the instrument characteristics, the results show the range of electron number density and temperature are actually much tighter than shown in Figure 5.20, indicating definitively the magnetosheath as the source region.

Table 5.3. Different source region temperatures and electron number densities.

Solar Wind	$N \sim 0.1 - 50$ cm^{-3}	$kT \sim 10 - 50$ eV
Lobes	$N \sim \leq 0.01$ cm^{-3}	$kT \sim 100$ eV
Plasma sheet	$N \sim 0.1 - 2$ cm^{-3}	$kT \sim 200 - 2000$ eV
Magnetosheath	$N \sim 0.1 - 10$ cm^{-3}	$kT \sim 20 - 300$ eV
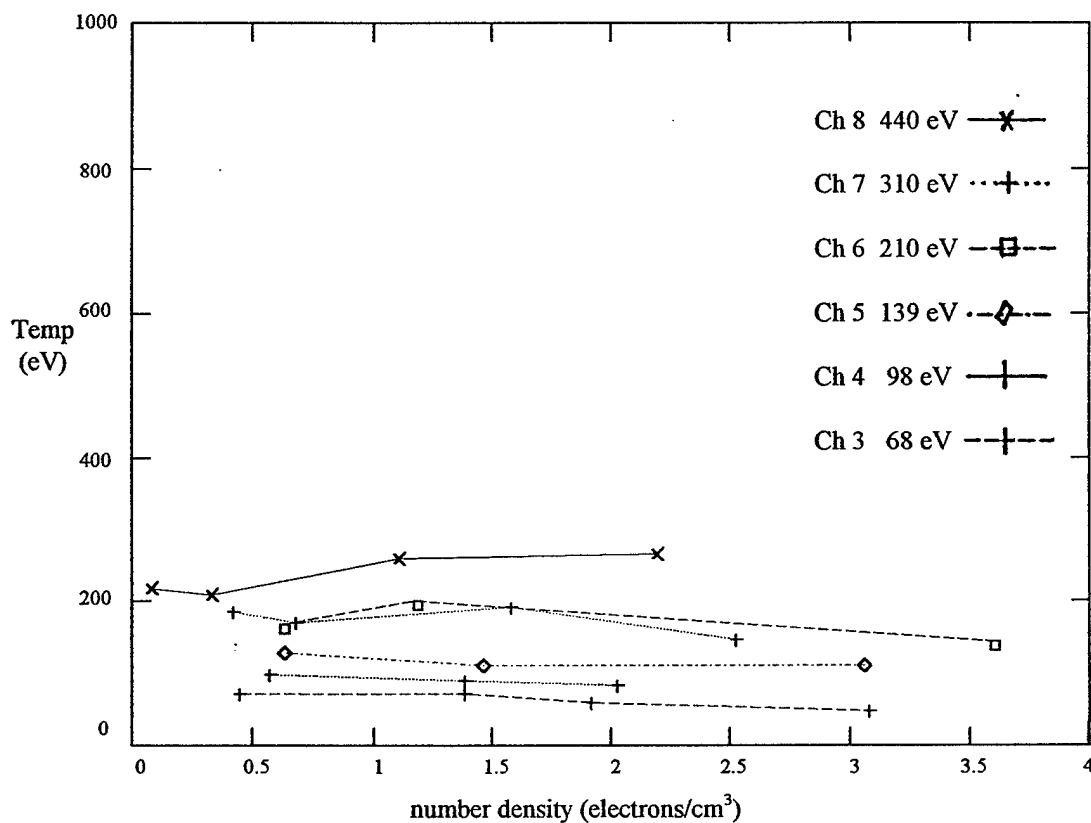
Figure 5.20. Mean kT temperature versus mean number density for all 8 channels listed in Table 5.2.
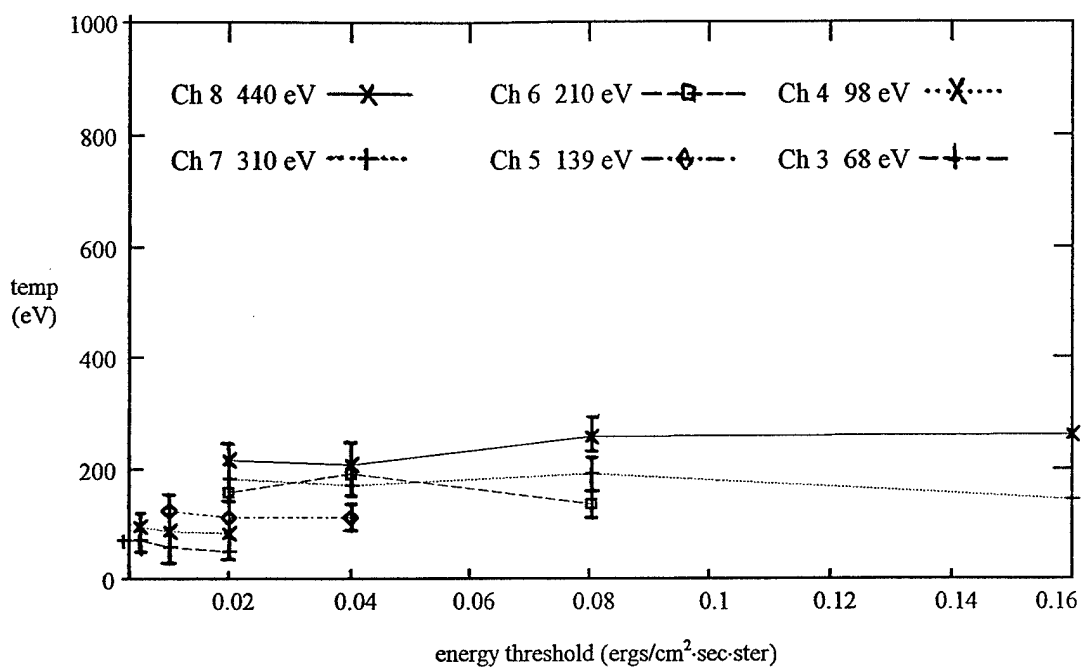
Figure 5.21. Mean kT temperature versus peak JE thresholds for channels 8 (440 eV) through 3 (68 eV).
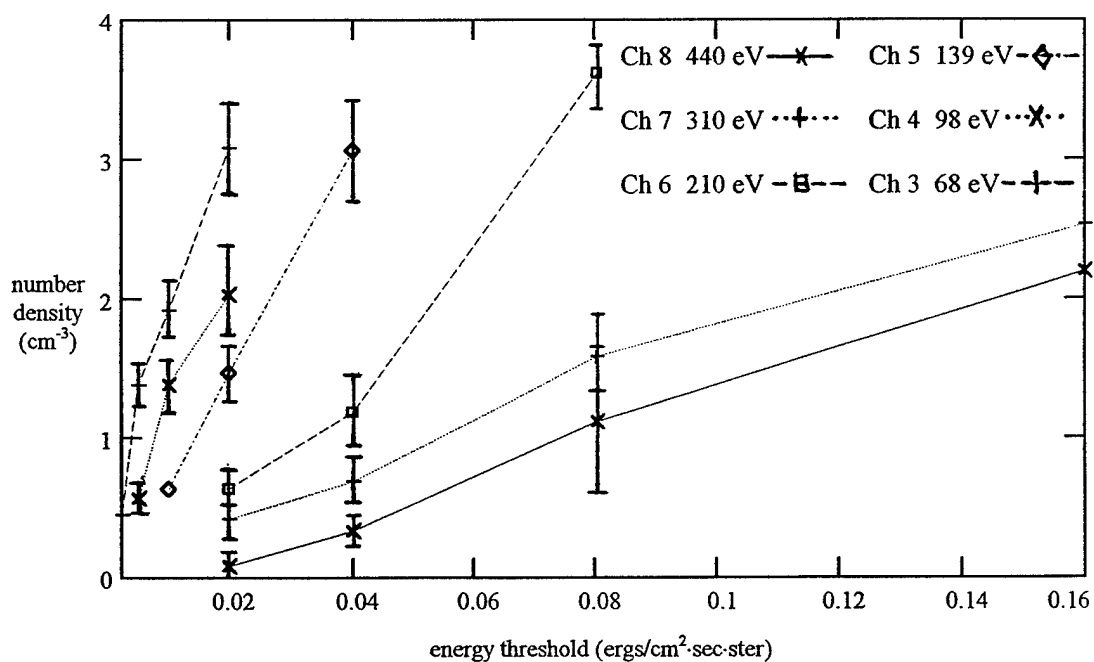
Figure 5.22. Mean number density versus peak JE thresholds for channels 8 (440 eV) through 3 (68 eV).

For example, Figure 5.23 shows at higher energy channels the peak of a spectra will often be between channels. This results in the peak being underestimated at the higher energy channels. This underestimation of the peak has two effects. First, the actual slope would be steeper and therefore the result is a colder temperature. Second, the actual y-intercept would be higher, which results in a higher number density. Thus, at the higher energy channels, the actual spectra are colder with a higher number density. This has the effect of collapsing the highest lines in Figure 5.15 to lower temperatures while simultaneously shifting them to higher number densities.
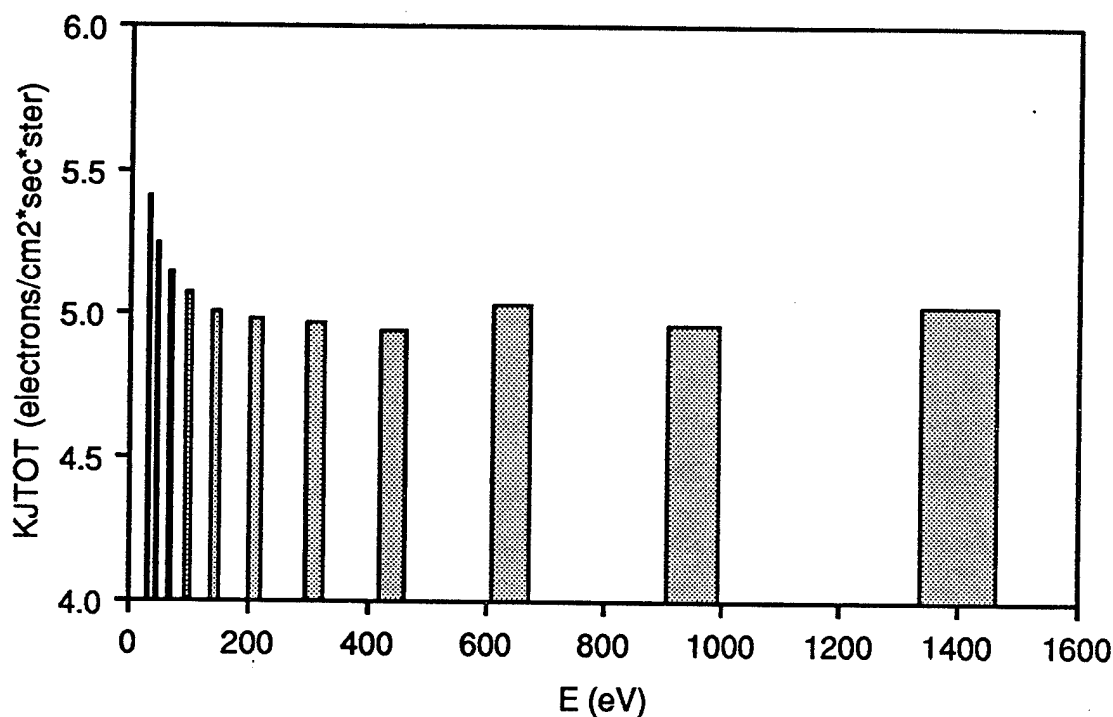
Figure 5.23. Channel pass bands for channels 1 (31 eV) through 12 (1.4 KeV) for the SSJ/4 electron detector.

The data presented here indicate that all the events occurring with energies from 68 eV through 440 eV are of magnetosheath origin and the particles are accelerated down open field lines into the ionosphere. The temperature of this source region is generally invariant while the number densities change by at least an order of magnitude. Finally, the data present the range magnetosheath parameters of kT temperature and electron number density.

CHAPTER VI

SUMMARY AND CONCLUSION

6.1. Discussion

This database used for this research included 488 DMSP polar cap satellite passes, which attained a geomagnetic latitude of 80°. At the 0.01 ergs/cm^2·sec·ster threshold level, 1087 electron precipitation events were included. By any standard, this is a sizable database. Although more data are available, they would not have contributed significantly.

The SSJ/4 instrument is a useful tool to examine these events, but the resolution of the energy channels could be tighter. As a meteorologist, however, I understand the need to balance the amount of information we might want versus the cost of the instrument. With this in mind, the lower energy channels (8 [440 eV] through 3 [68 eV]) served nicely for this research.

I made four assumptions about the source region plasma; the plasma has a Maxwellian distribution, it is connected to the ionosphere by open field lines, it is accelerated by a potential drop between the source region and the ionosphere, and finally, the plasma acceleration process obeys Liouville's Theorem. If all these assumptions hold, the kT temperature (energy) and number density of the source region electron population can be described. By accounting for the instrumental error at higher energy channels, the mean kT temperature of the events ranges from ~100 eV ± 50 eV. The mean electron number density ranges from ~0.1 - 5 electrons·cm^{-3}.

The results of this research lead to three conclusions.

1. The electrons precipitating over the polar cap under northward IMF conditions are of magnetosheath origin.

2. The variable for the numerical models is the number density N. The kT temperature must remain fixed.

3. The dim or nonvisible polar cap arcs occur under low magnetosheath number densities while the bright sun-aligned arcs occur under high magnetosheath number densities.

6.2 Suggestions for Further Research

The results presented here give the theoreticians and modelers a range of source region parameters for electron precipitation events. However, these results hold only for events occurring under northward IMF where electrons precipitate with energies between 68 eV and 440 eV over the northern hemisphere. Determining the source region for different IMF configurations, and for the southern hemisphere, would be a valuable addition to this research. Additionally, comparing data from solar maximum may provide further information about the source region parameter variablility.

Similar procedures could be accomplished using the AKEBONO satellite, which has an elliptical orbit attaining higher altitudes. The results from a different altitude may provide clues to the acceleration processes involved.

Furthermore, a detailed analysis of the instrument effect of missing the spectrum peak would be valuable. This would include theoretically modeling this effect to determine the temperature and density influence from higher acceleration potentials.

REFERENCES

Akasofu, S.-I., Midday auroras and polar cap auroras, *Geofysiske Publikasjoner*, *29*, 73, 1972.

Akasofu, S.-I., E. W. Hones, Jr., S. J. Bame, J. R. Asbridge, and A.T. Y. Lui, Magnetotail and boundary layer plasmas at a geocentric distance of $\sim 18\ R_E$: Vela 5 and 6 observations, *J. Geophys. Res.*, *78*, 7257, 1973.

Bame, S. J., E. W. Hones, Jr., S.-I. Akasofu, M. D. Montgomery, and J. R. Asbridge, Geomagnetic storm particles in the high latitude magnetotail, *J. Geophys. Res.*, *76*, 7566, 1971.

Berkey, F. T., L. L. Cogger, and S. Ismail, Evidence for a correlation between sun-aligned arcs and the interplanetary magnetic field direction, *Geophys. Res. Lett.*, *3*, 145, 1976.

Crain, D. J., J. J. Sojka, R. W. Schunk, and L. Zhu, Parameterized study of the ionospheric modification associated with sun-aligned polar cap arcs, *J. Geophys. Res.*, *98*, 6151, 1993.

Davis, T. N., The morphology of the auroral displays of 1957-1958, 2, detailed analysis of Alaska data and analyses of high latitude data, *J. Geophys. Res.*, *67*, 75, 1962.

Eather, R. H., and S.-I. Akasofu, Characteristics of polar cap auroras, *J. Geophys. Res.*, *74*, 4794, 1969.

Frank, L. A., J. D. Craven, D. A. Gurnett, and S. D. Shawhan, The theta aurora, *J. Geophys. Res.*, *91*, 3177, 1986.

Gussenhoven, M. S., Extremely high latitude auroras, *J. Geophys. Res.*, *87*, 2401, 1982.

Hardy, D. A., Intense fluxes of low-energy electrons at geomagnetic latitudes above 85°, *J. Geophys. Res.*, *89*, 3883, 1984.

Hardy, D. A., W. J. Burke, and M. S. Gussenhoven, DMSP optical and electron measurements in the vicinity of polar cap arcs, *J. Geophys. Res.*, *87*, 2413, 1982.

Hargreaves, J. K., The solar-terrestrial environment, *Cambridge Atmospheric and Space Sciences Series*, *5*, 150, 1992.

Hoffman, R. A., R. A. Heelis, and J. S. Prasad, A sun aligned arc observation by DMSP and AE-C, *J. Geophys. Res.*, *89*, 9697, 1985.

Ismail, S., D. D. Wallis, and L. L. Cogger, Characteristics of polar cap sun-aligned arcs, *J. Geophys. Res.*, *87*, 2401, 1977.

Ismail, S., and C. I. Meng, A classification of polar cap auroral arcs, *Planet. Space Sci.*, *30*, 319, 1982.

Lassen, K., Polar cap emissions, in *Atmospheric Emissions*, edited by B. M. McCormac, p. 63, Van Nostrand Reinhold, As, Norway, 1969.

Potemra, T. A., Magnetospheric currents, *Johns Hopkins APL Tech. Digest*, *4*, 276, 1983.

Romick, G. J., and N. B. Brown, Midday auroral observations in the oval, cusp region, and polar cap, *J. Geophys. Res.*, *76*, 8420, 1971.

Sanford, B. P., Aurora and airglow intensity variations with time and magnetic activity, *J. Atmos. Terr. Phys.*, *26*, 749, 1964.

Sanford, B. P., Variations of auroral emissions with time, magnetic activity, and the solar cycle, *J. Atmos. Terr. Phys.*, *30*, 1921, 1968.

Schumaker, T. L., D. A. Hardy, S. Moran, A. Huber, J. McGarity, and J. Pantazis, Precipitating ion and electron detectors (SSJ/4) for the block 5D/flight 8 DMSP satellite, *AFGL-TR-88-0030 Instrumentation Papers, No. 335*, Air Force Geophysical Laboratory, Hanscom AFB, Bedford, Mass., 1988.

Tascione T. F., *Introduction to the Space Environment*, Orbit Book Company, Malabar, Florida, 1988.

Valladares C. E., and H. C. Carlson, The electrodynamic, thermal, and energetic character of intense sun-aligned arcs in the polar cap, *J. Geophys. Res.*, *96*, 1379, 1991.

Wei, C. Q., L. C. Lee, and A. L. La Belle-Hamer, A simulation study of the vortex structure in the low latitude boundary layer, *J. Geophys. Res.*, *95*, 20793, 1990.

Whalen, B. A., J. R. Miller, and I. B. McDiarmid, Sounding rocket observations of particle precipitation in a polar-cap electron aurora, *J. Geophys. Res.*, *76*, 6847, 1971.

Winningham J. D., and W. J. Heikkila, Polar cap auroral electron fluxes observed with Isis 1, *J. Geophys. Res.*, *79*, 949, 1974.

Zhu, L., J. J. Sojka, R. W. Schunk, and D. J. Crain, A time dependent model of polar cap arcs, *J. Geophys. Res.*, *98*, 6139, 1993.

APPENDICES

Appendix A: Peak JE vs. Peak J Plots for all Channels and Thresholds

This appendix contains the peak JE versus Peak J plots for the entire database.

Plots included are channels 14 (3.05 KeV) through 3 (68 eV). The top plot of each page

is the average JE versus average J while the lower plot is peak JE versus peak J. The units

of JE are ergs/cm^2·sec·ster and the units of J are electrons/cm^2·sec·ster for both plots.

Threshold and channel are indicated at the top of each page.

Threshold 0.1600 Peak Ch 14 Bz +

log Avg JE (ergs/cm**2s*sr)

log Avg J (e/cm**2s*sr)

log Peak JE (ergs/cm**2s*sr)

log Peak J (e/cm**2s*sr)
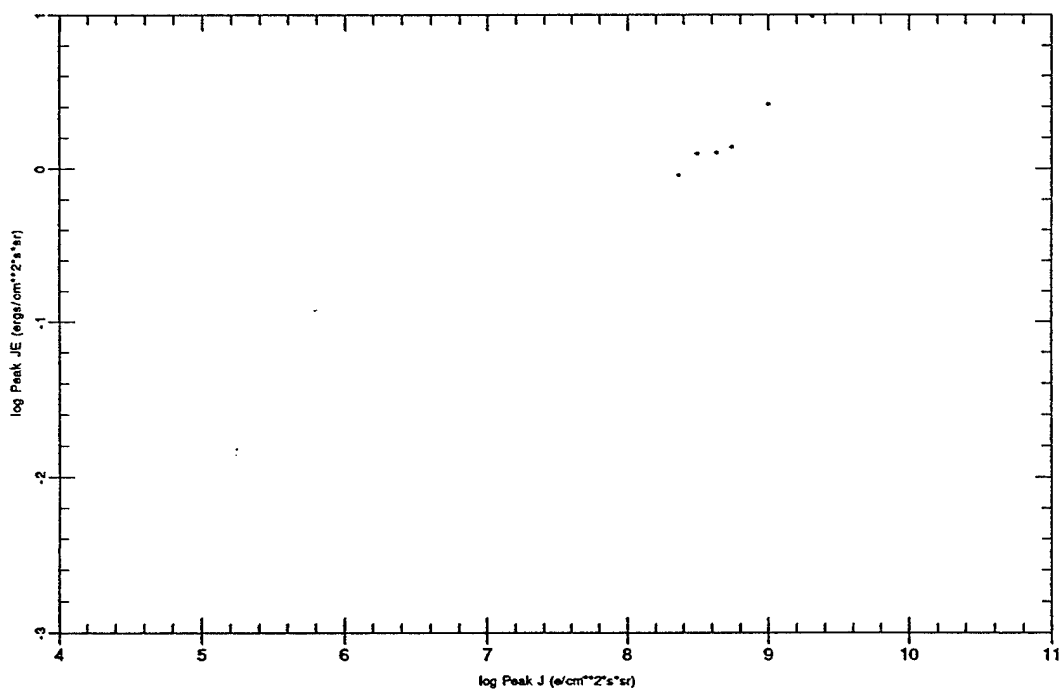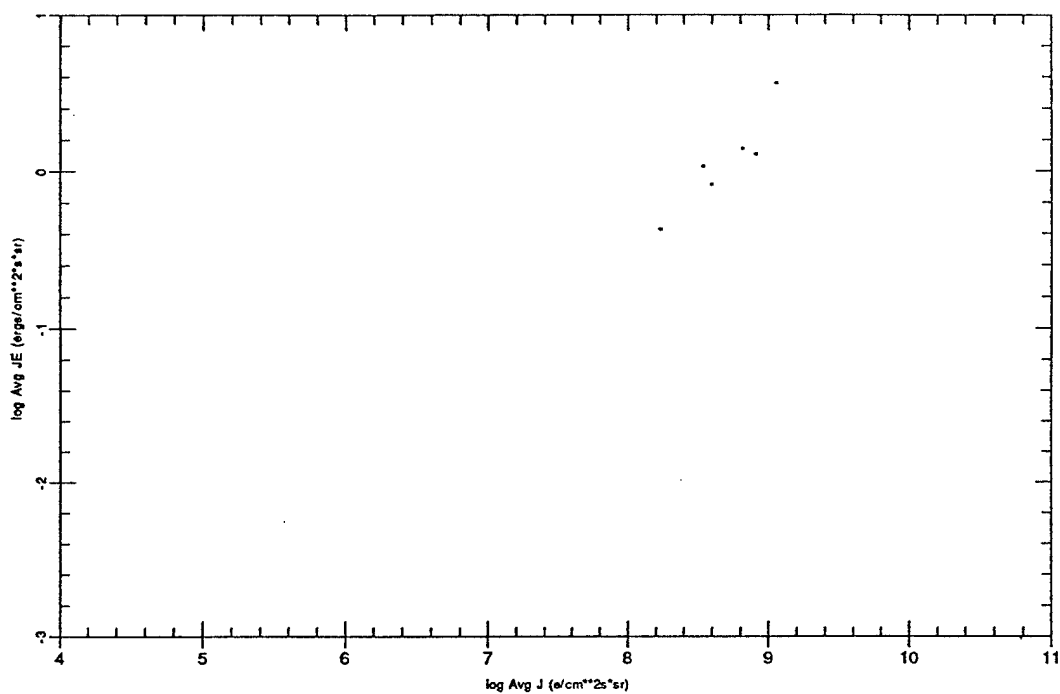
Threshold 0.0800 Peak Ch 14 Bz +
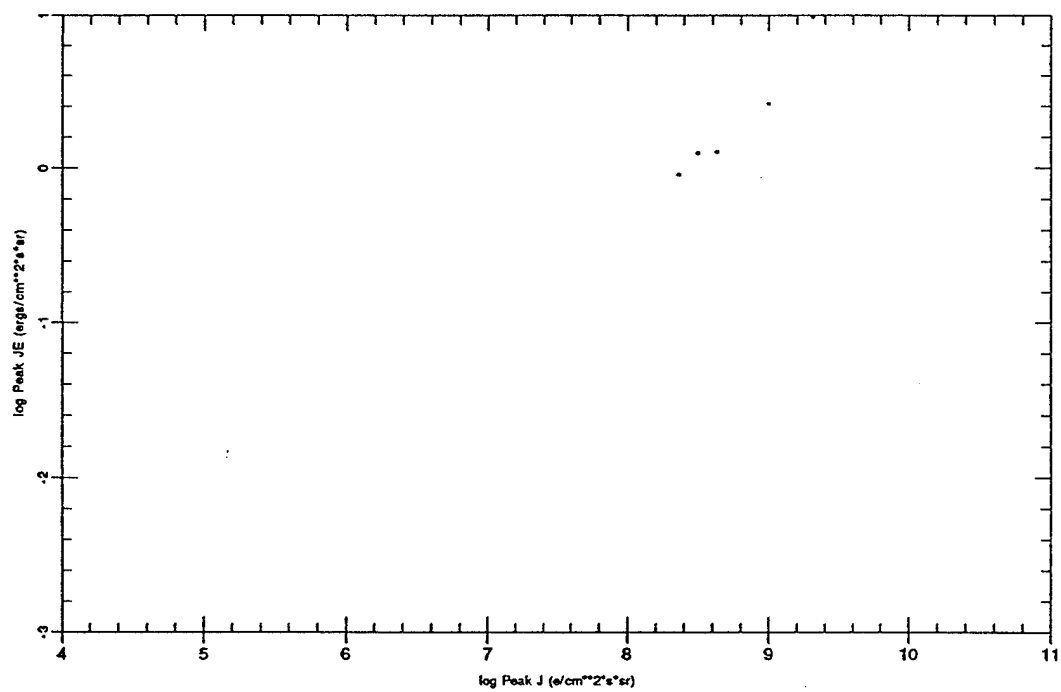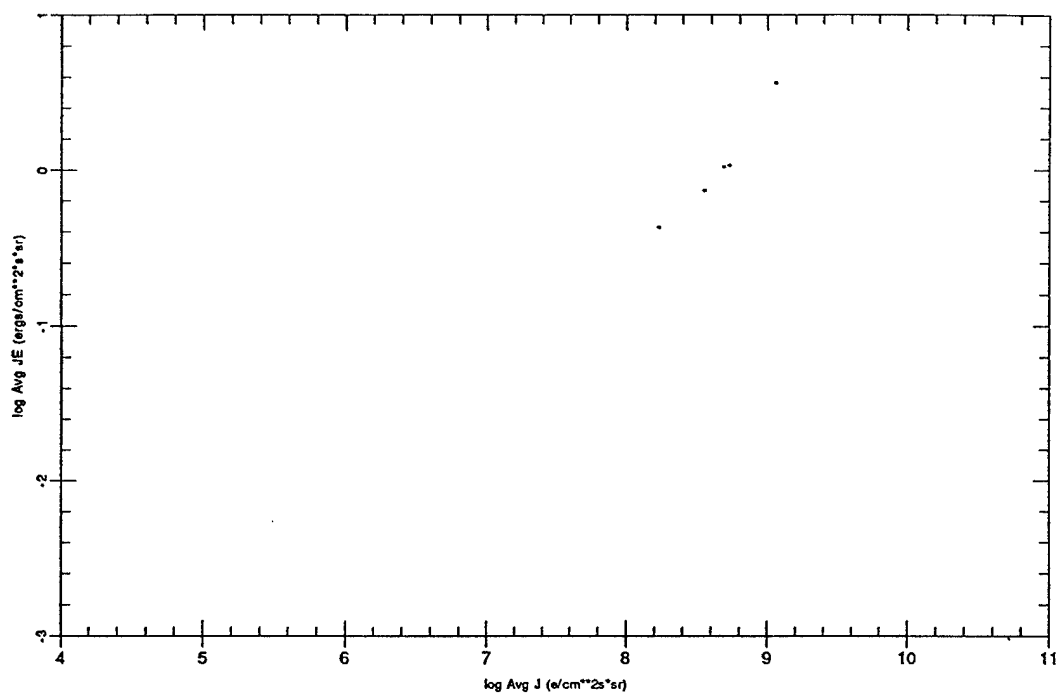
Threshold 0.0400 Peak Ch 14 Bz +
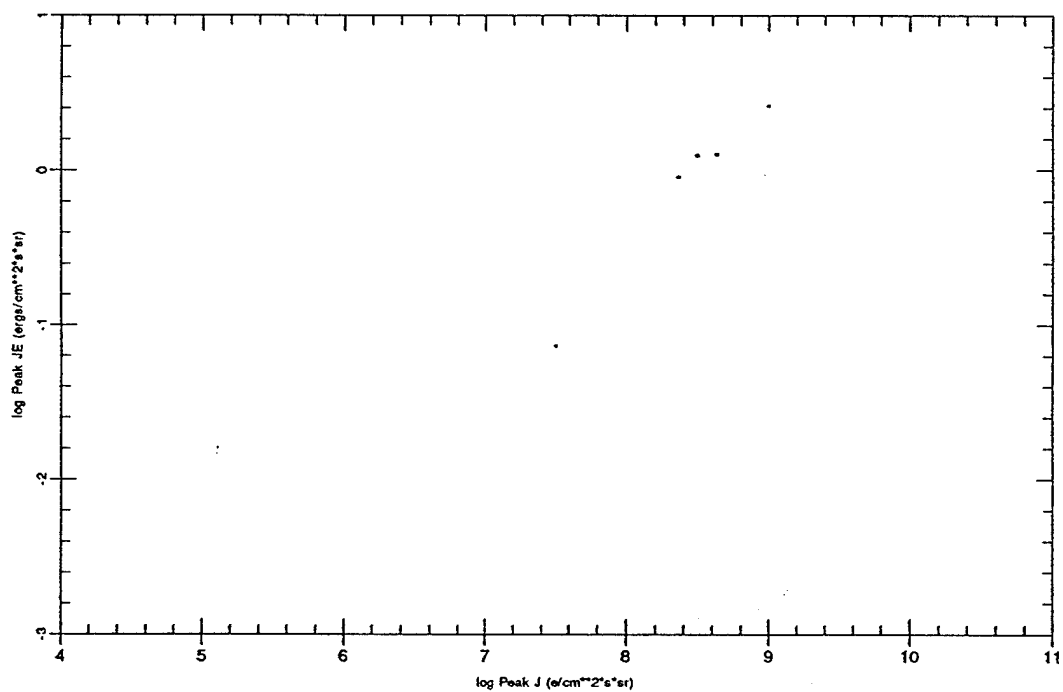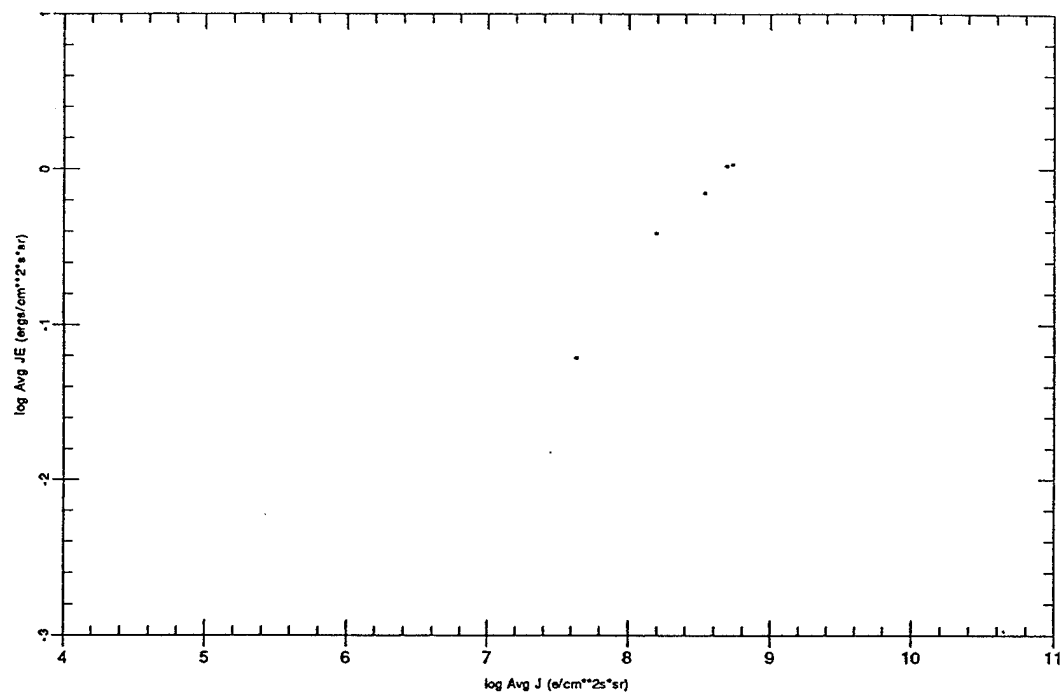
Threshold 0.0200 Peak Ch 14 Bz +
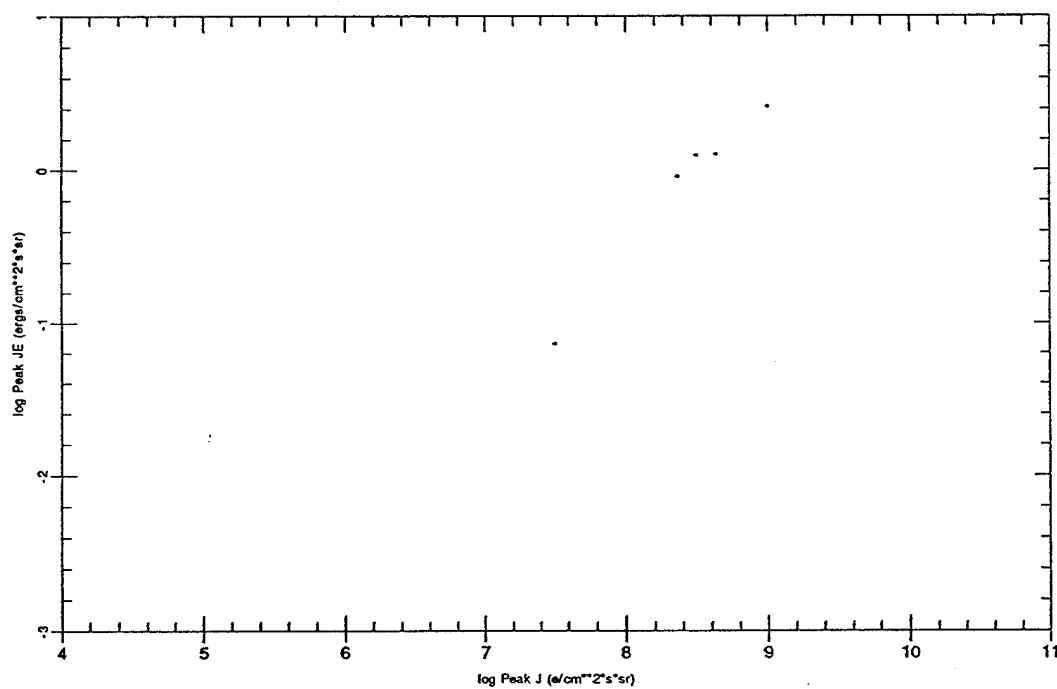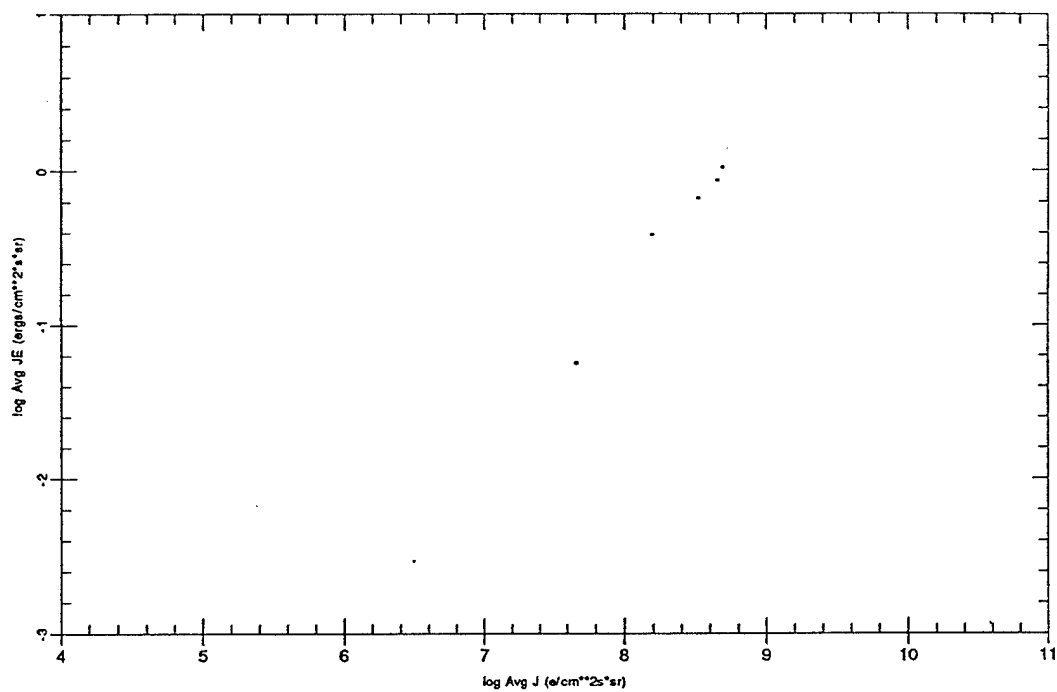
Threshold 0.0100 Peak Ch 14 Bz +
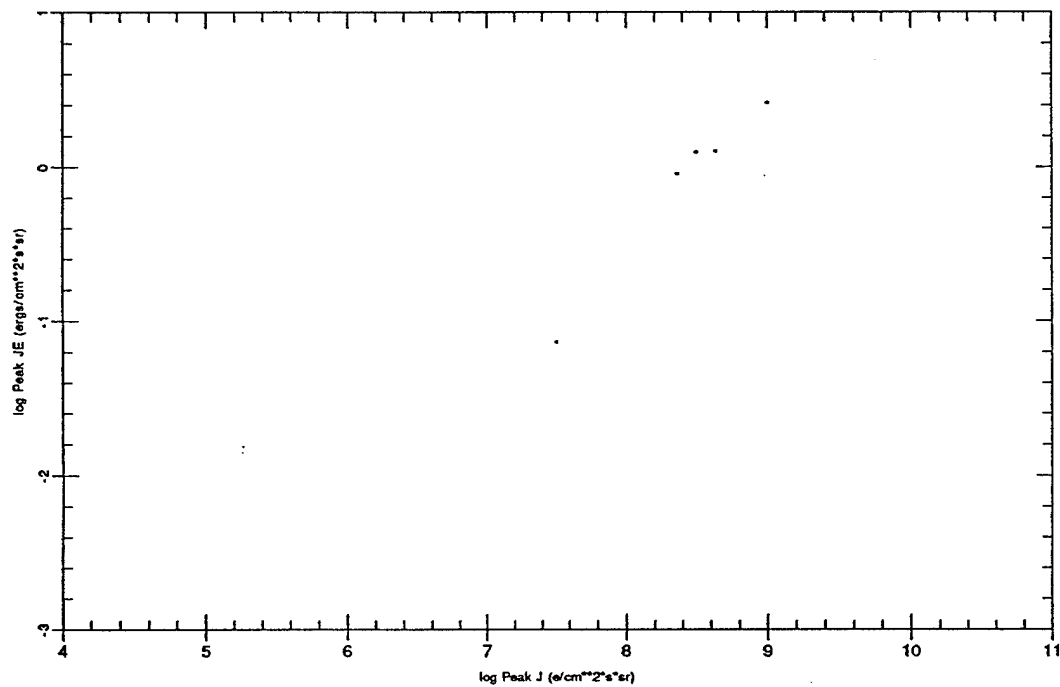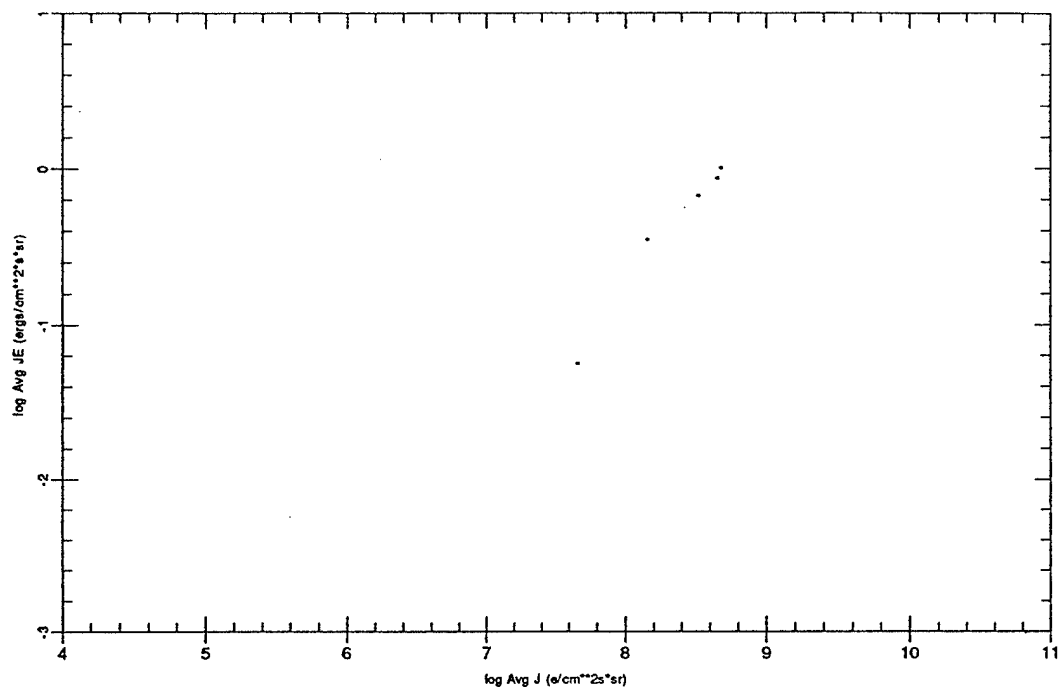
Threshold 0.0050 Peak Ch 14 Bz +
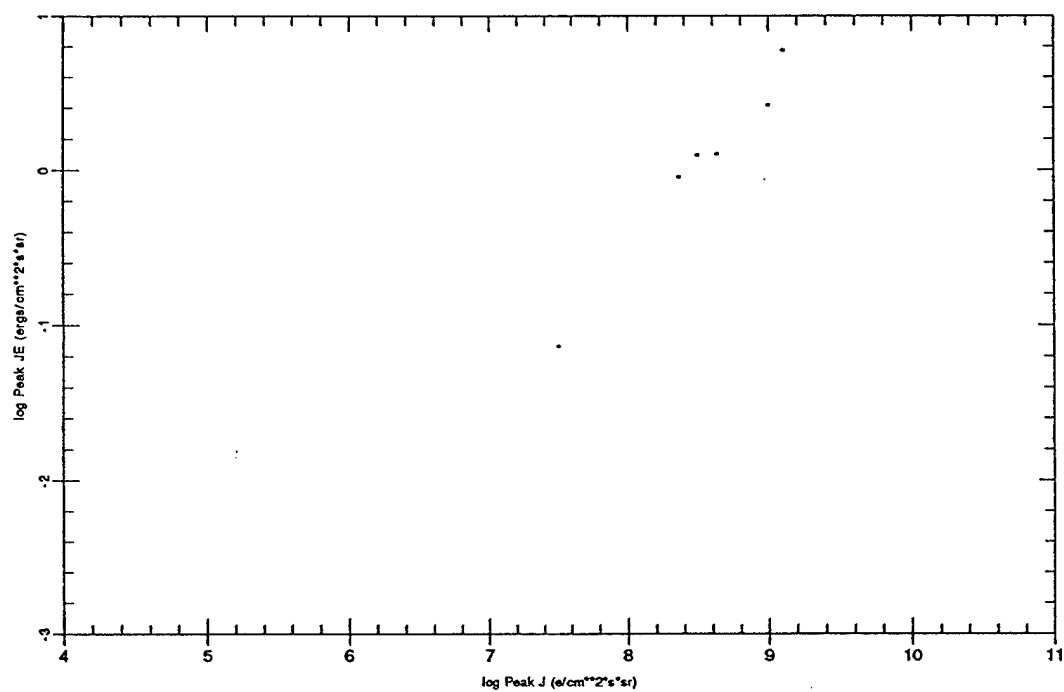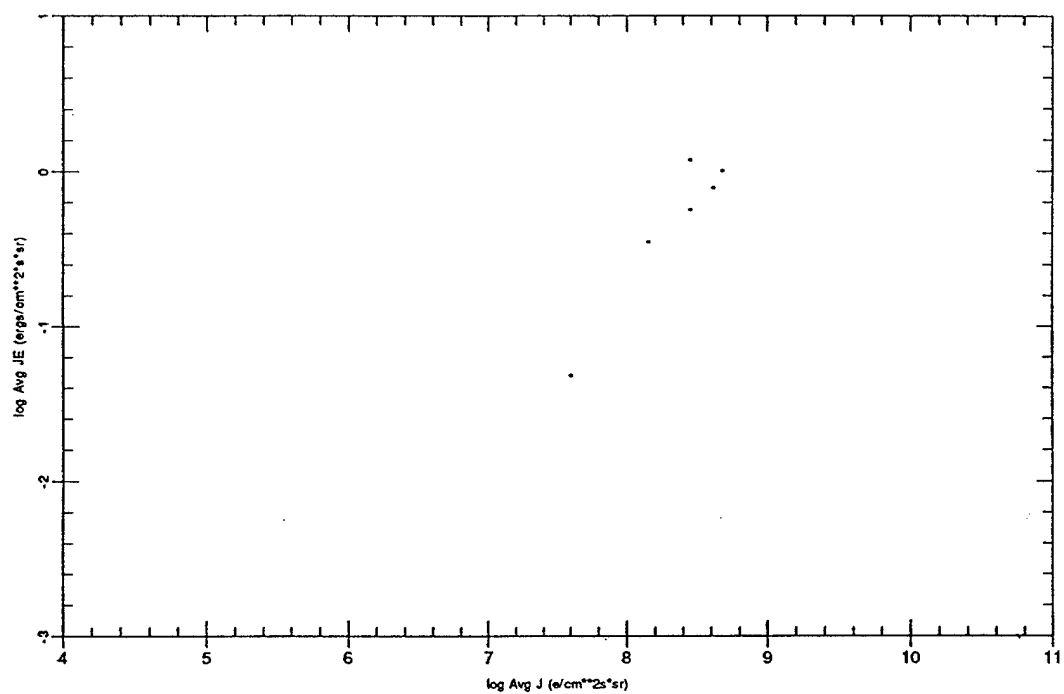
Threshold 0.0025 Peak Ch 14 Bz +
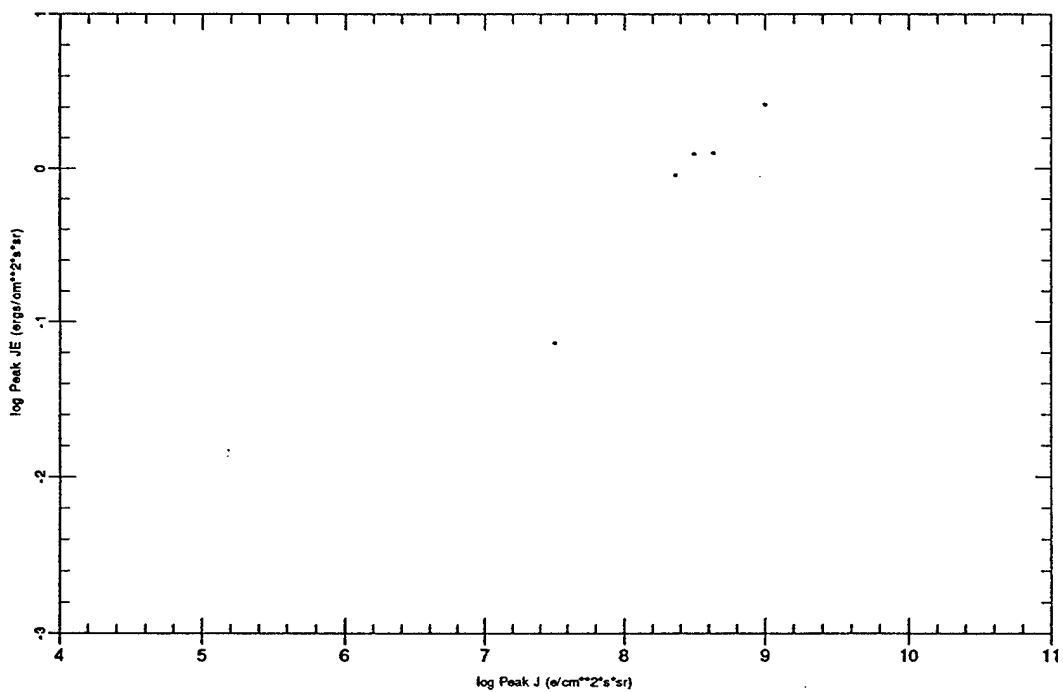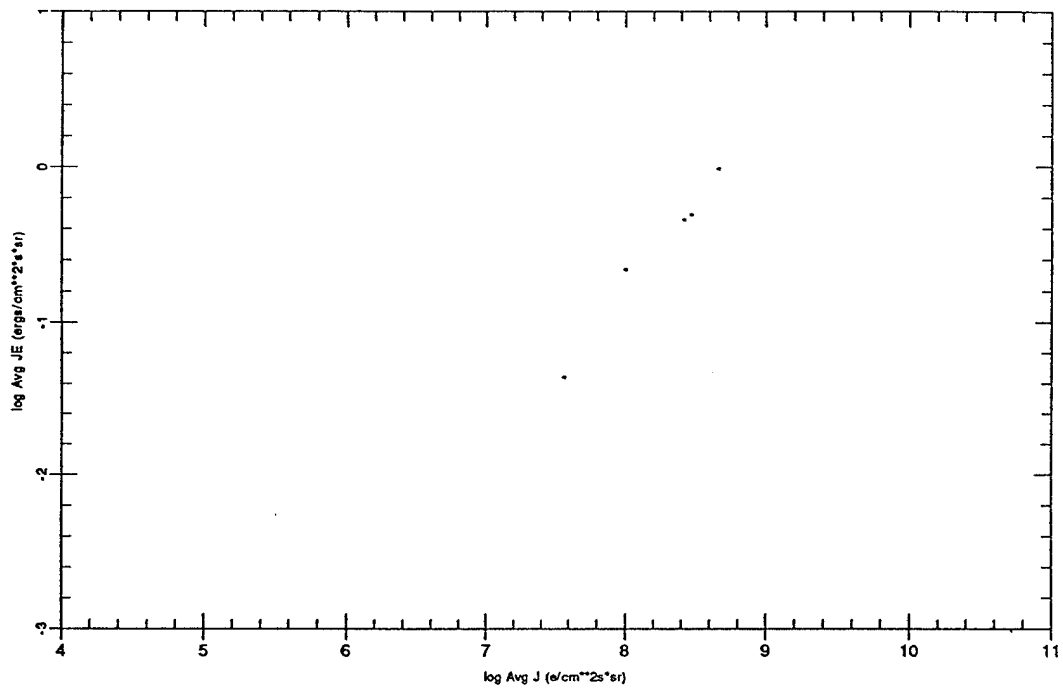
Threshold 0.1600 Peak Ch 13 Bz +

Threshold 0.0800 Peak Ch 13 Bz +

log Avg JE (ergs/cm**2*s*sr)

log Avg J (e/cm**2s*sr)

log Peak JE (ergs/cm**2*s*sr)

log Peak J (e/cm**2*s*sr)
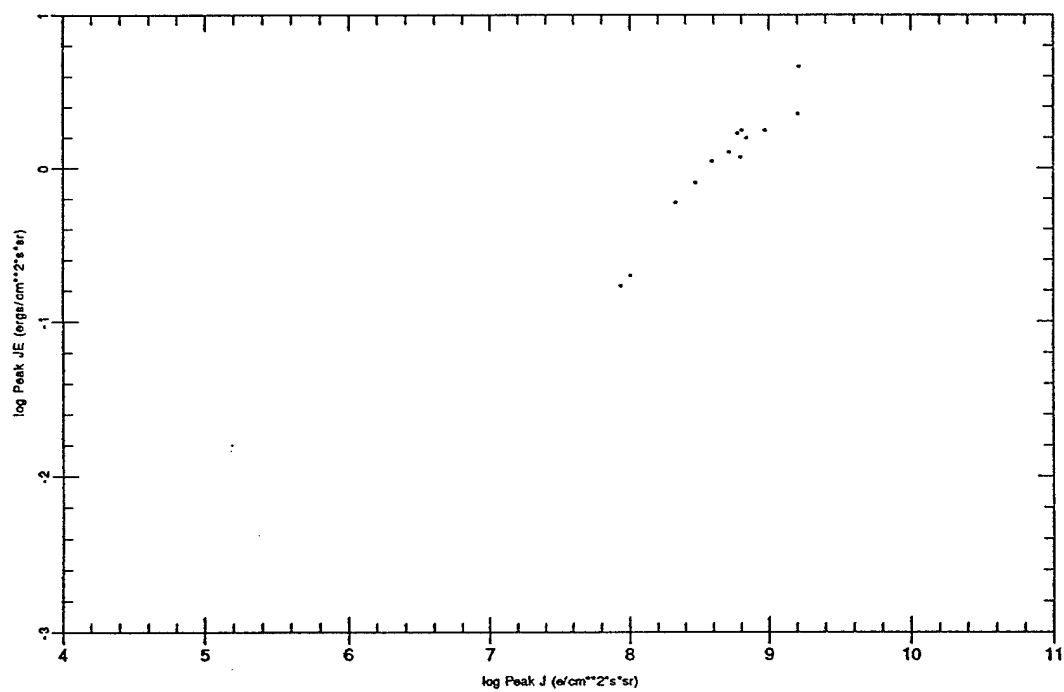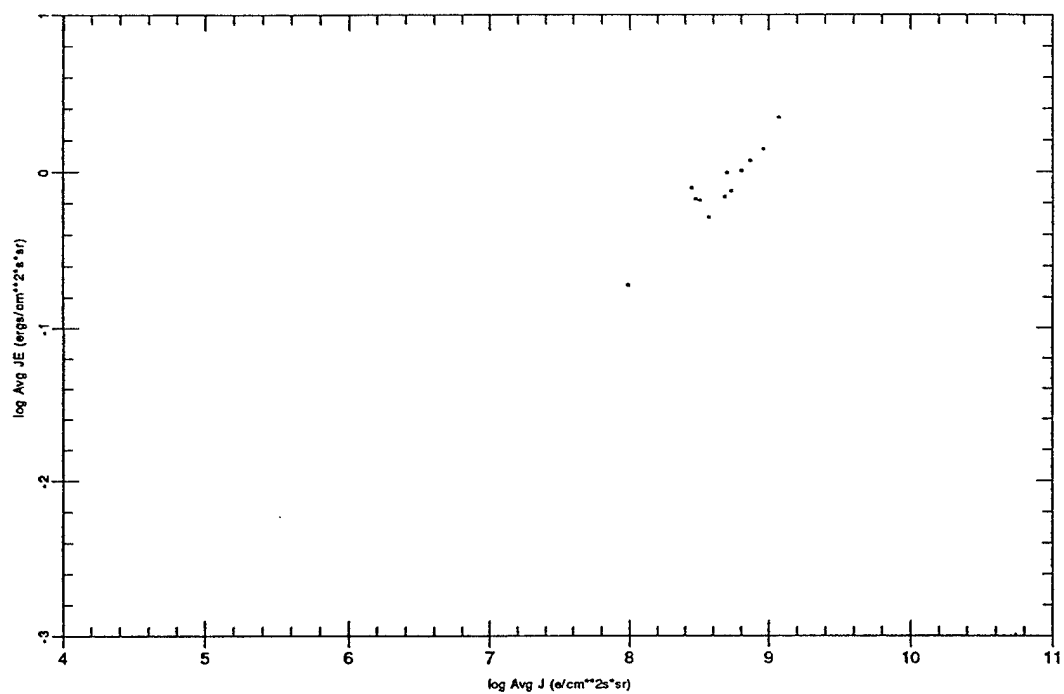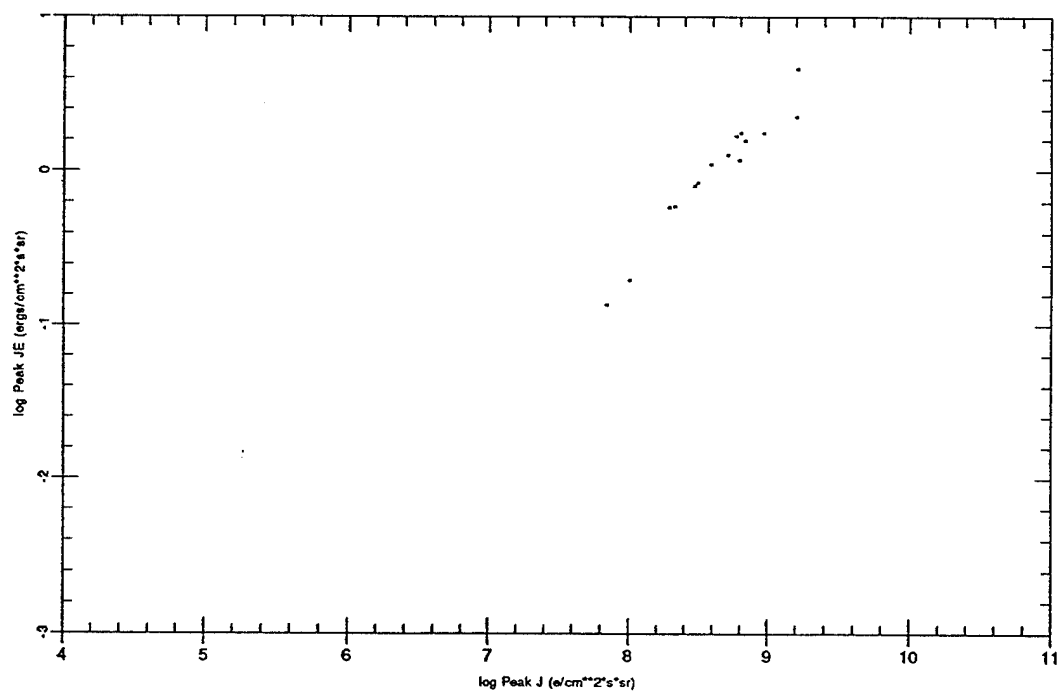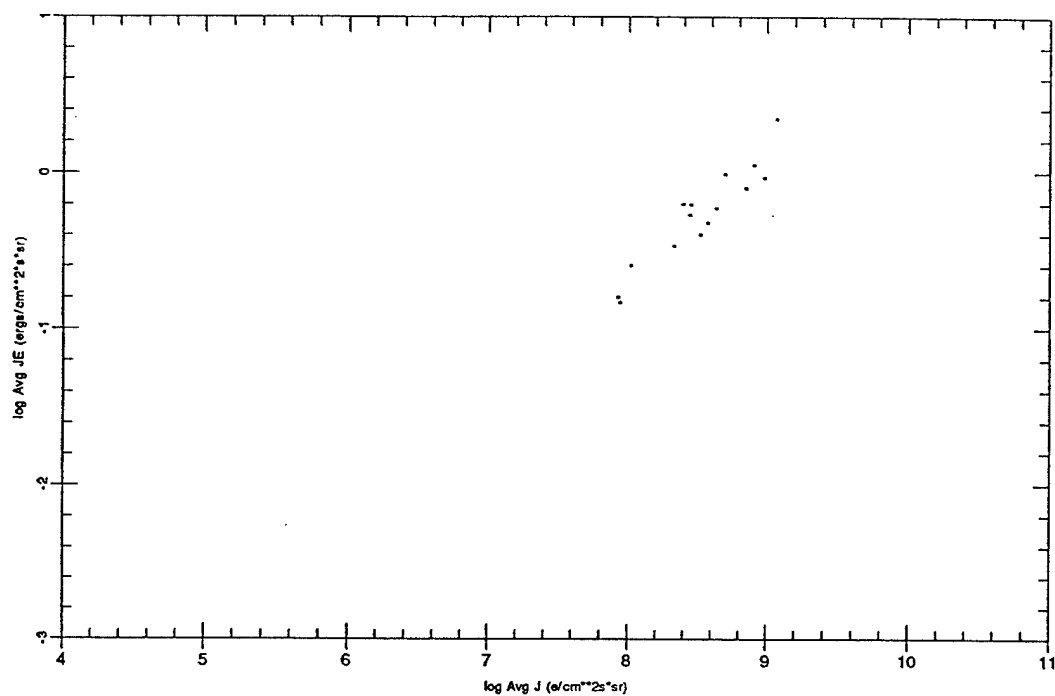
Threshold 0.0400 Peak Ch 13 Bz +
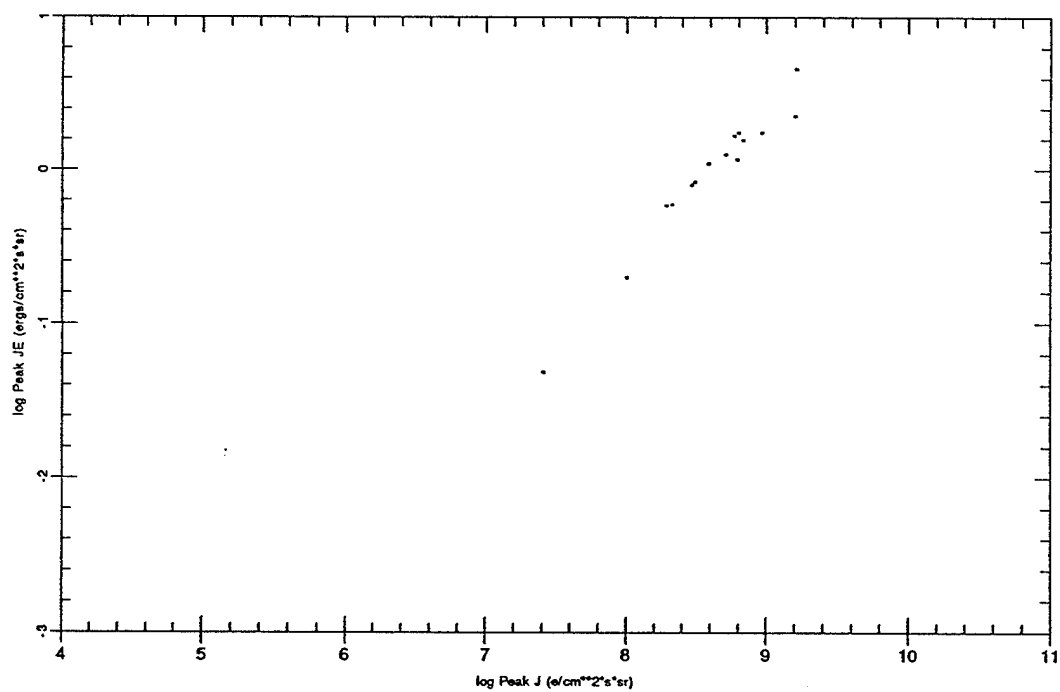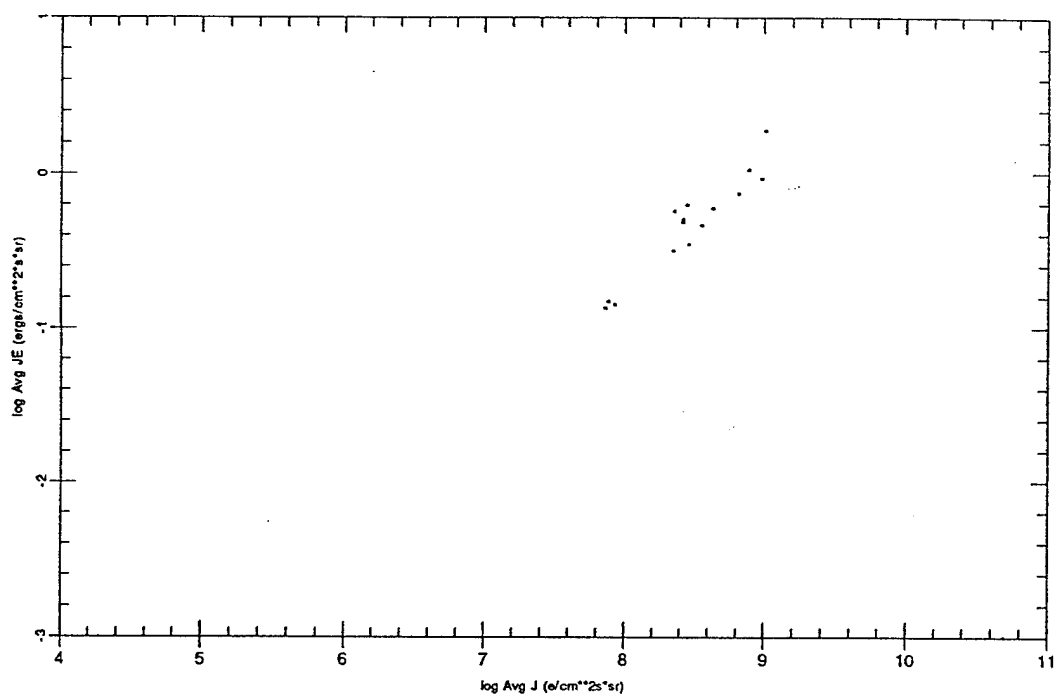
Threshold 0.0200 Peak Ch 13 Bz +
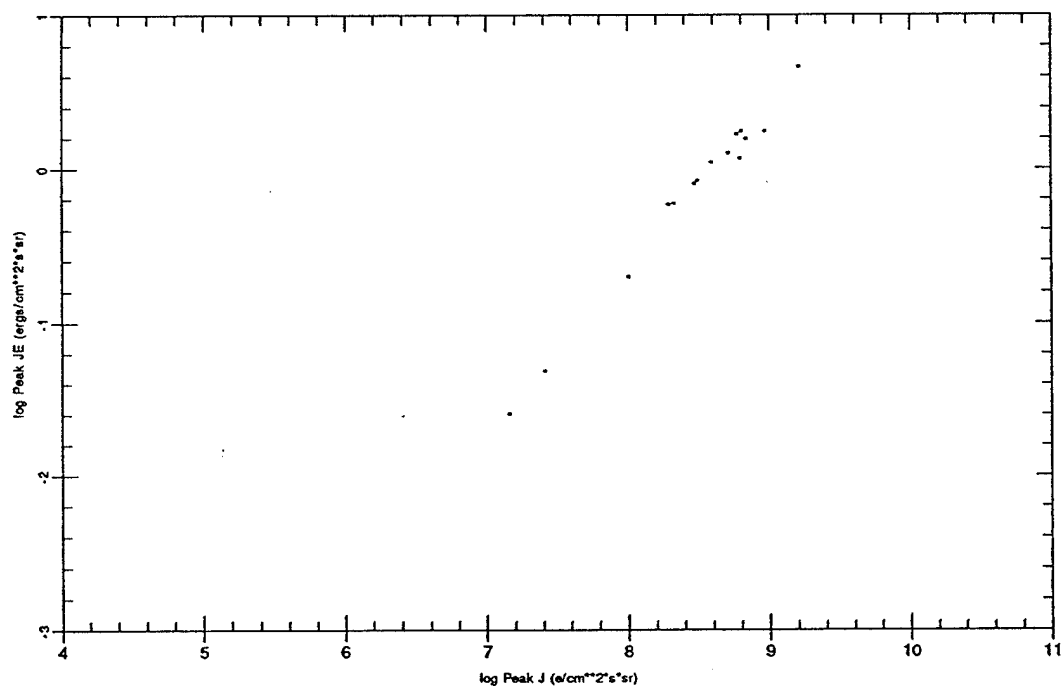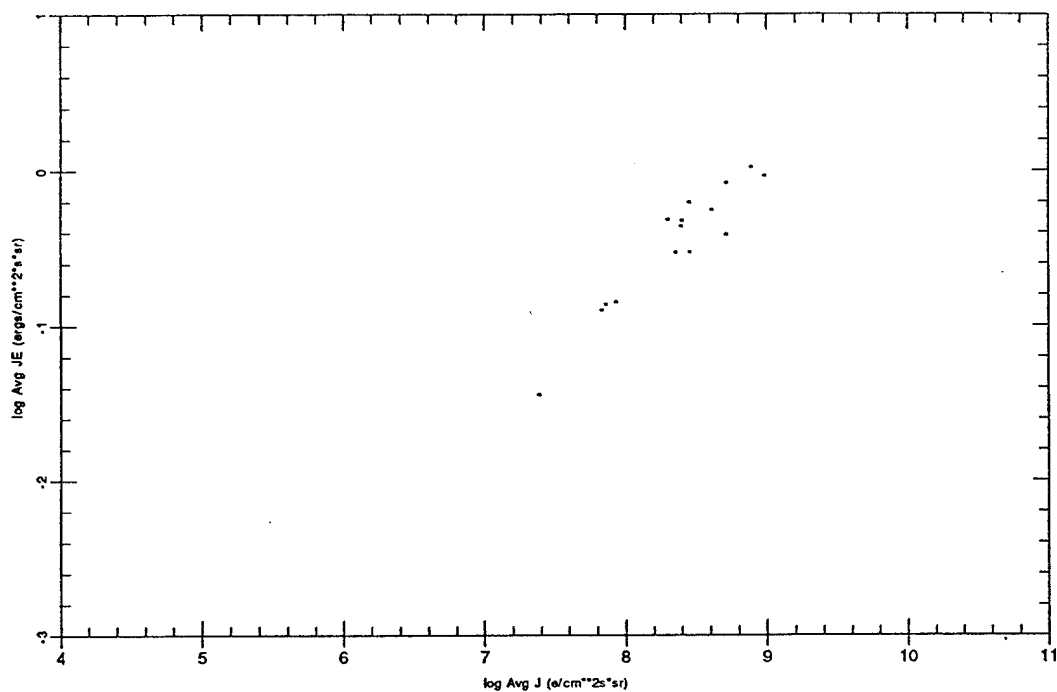
Threshold 0.0100 Peak Ch 13 Bz +
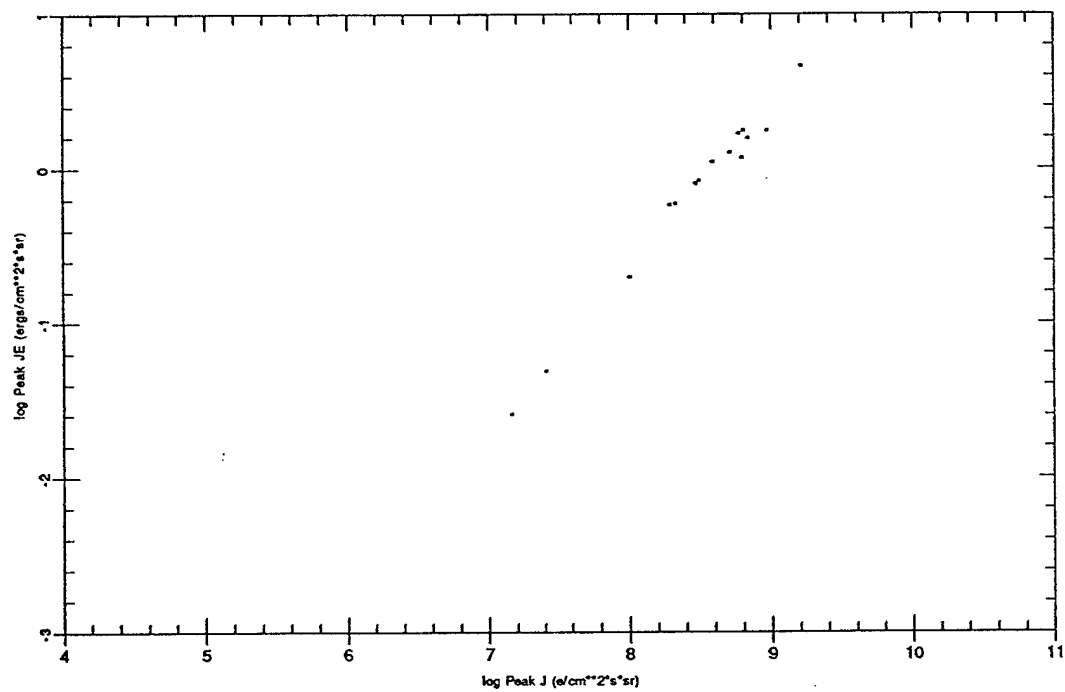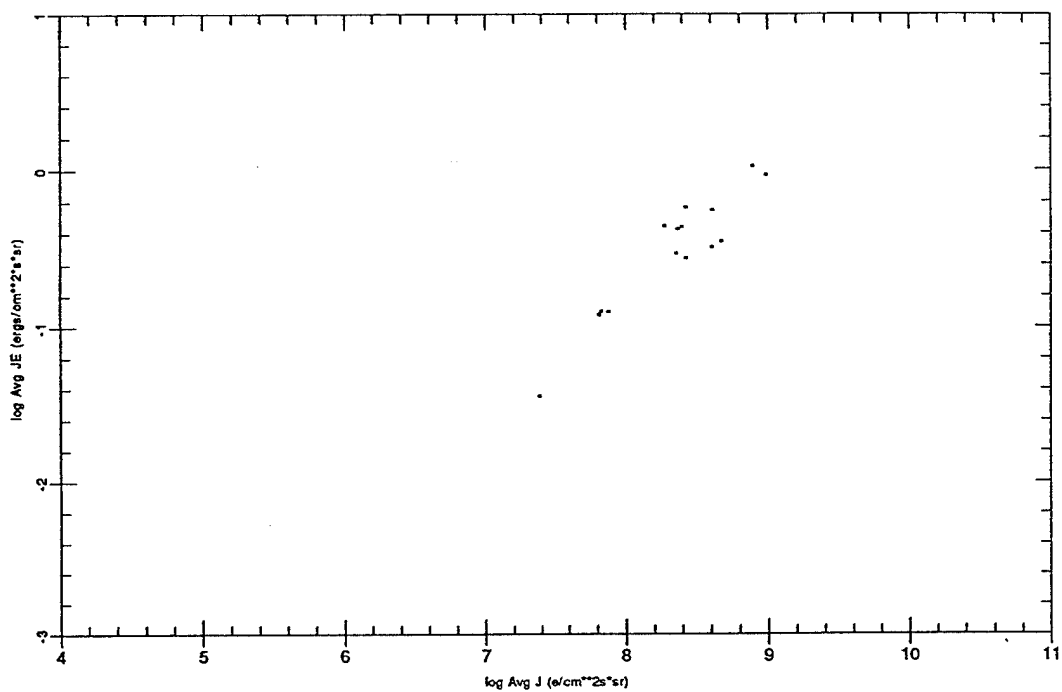
Threshold 0.0050 Peak Ch 13 Bz +
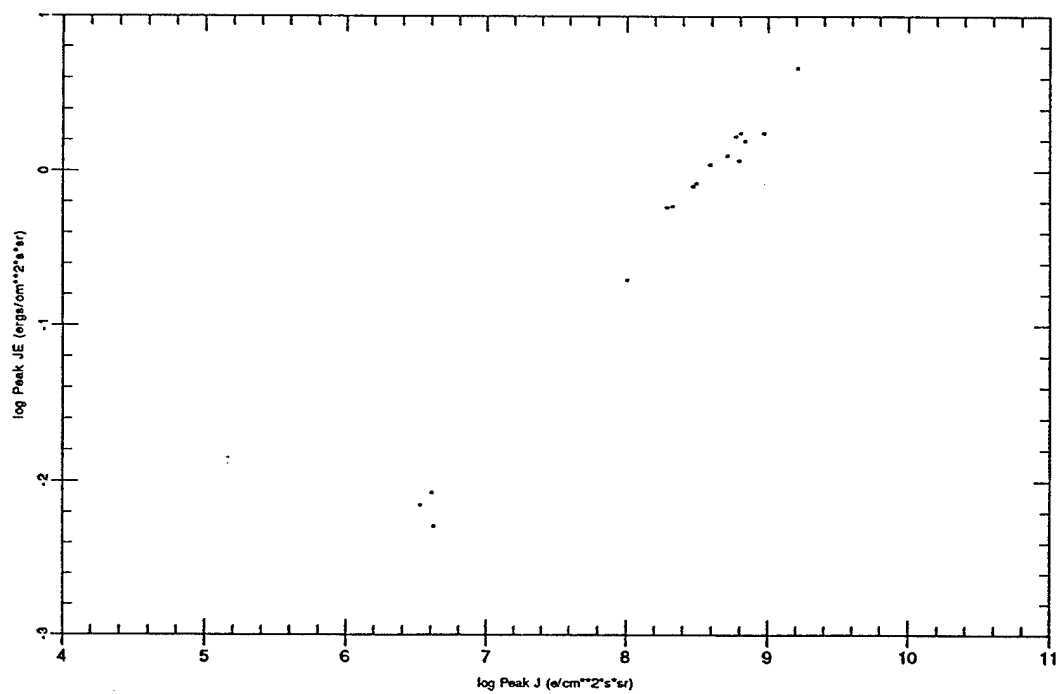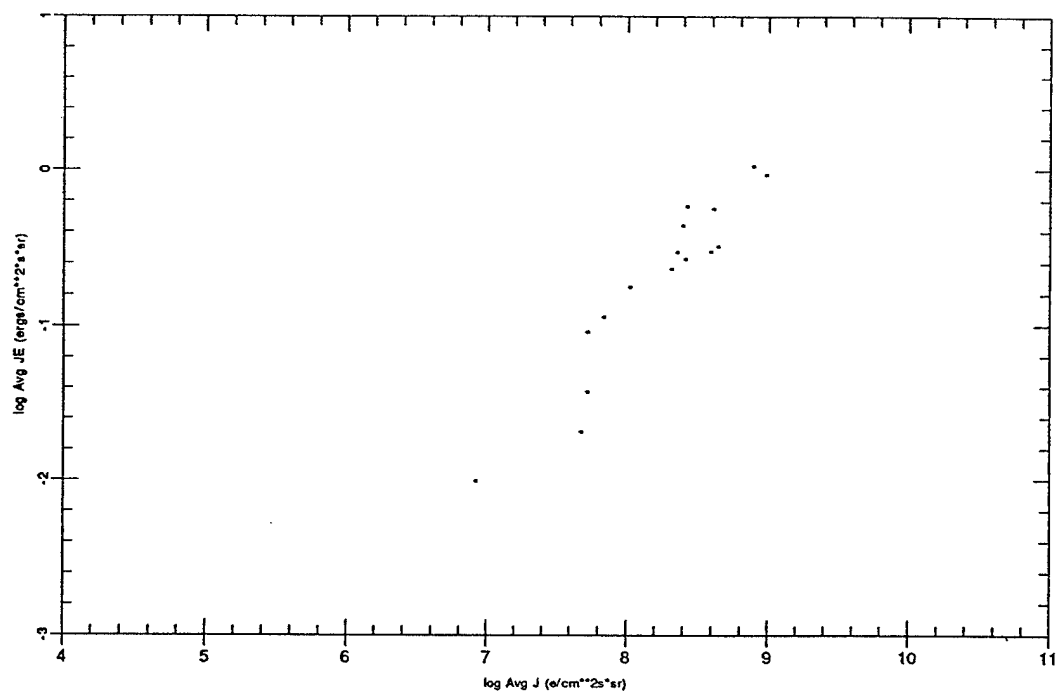
Threshold 0.0025 Peak Ch 13 Bz +
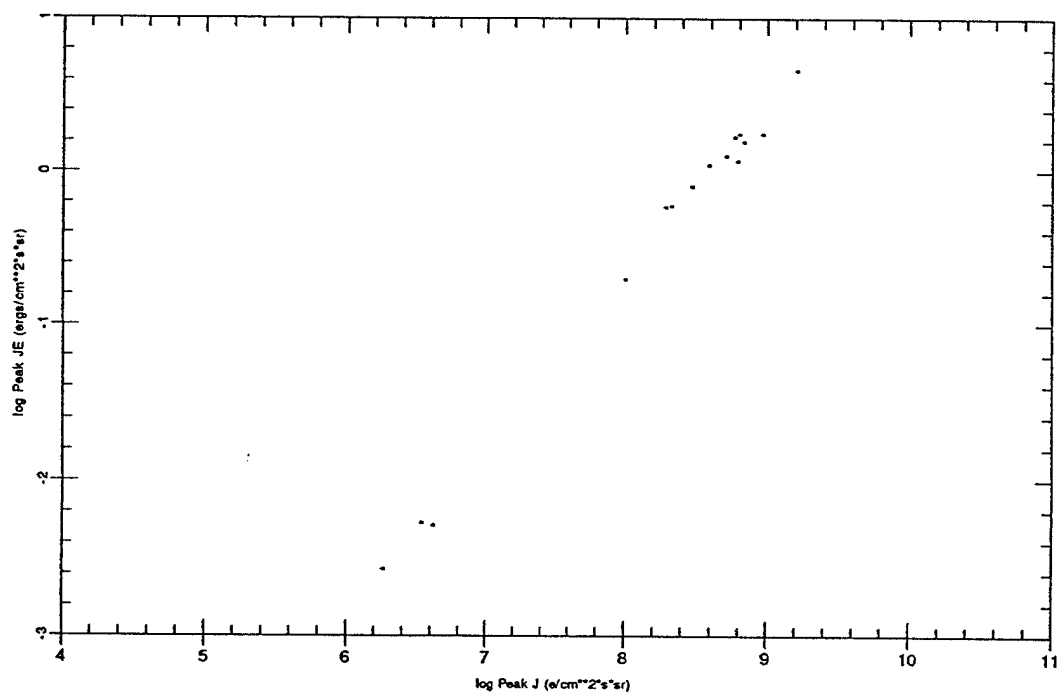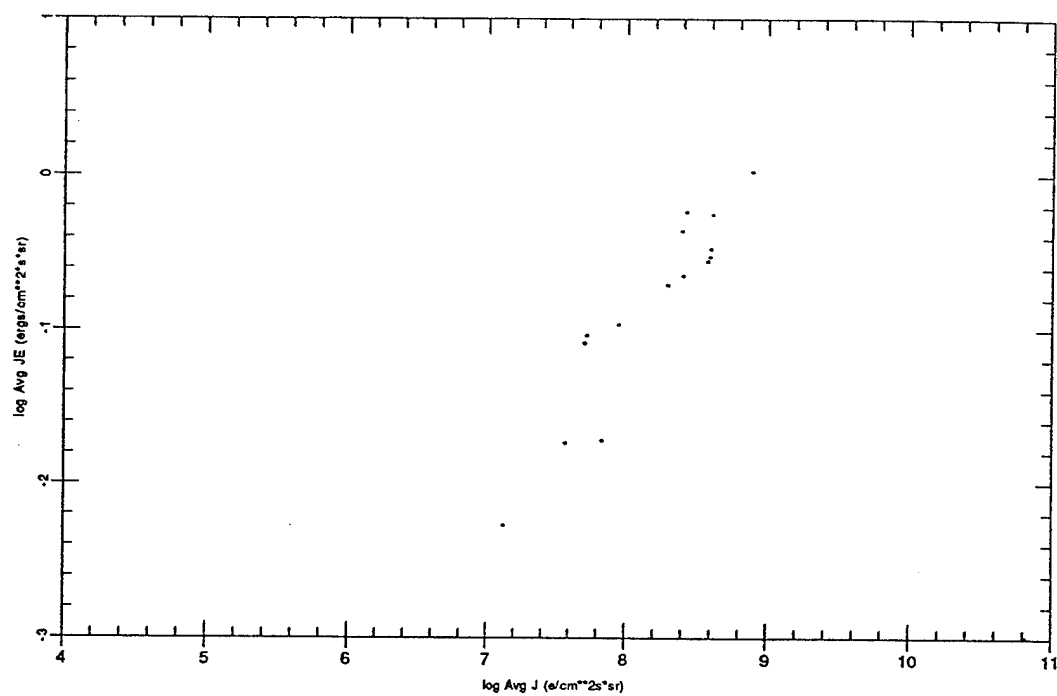
Threshold 0.1600 Peak Ch 12 Bz +
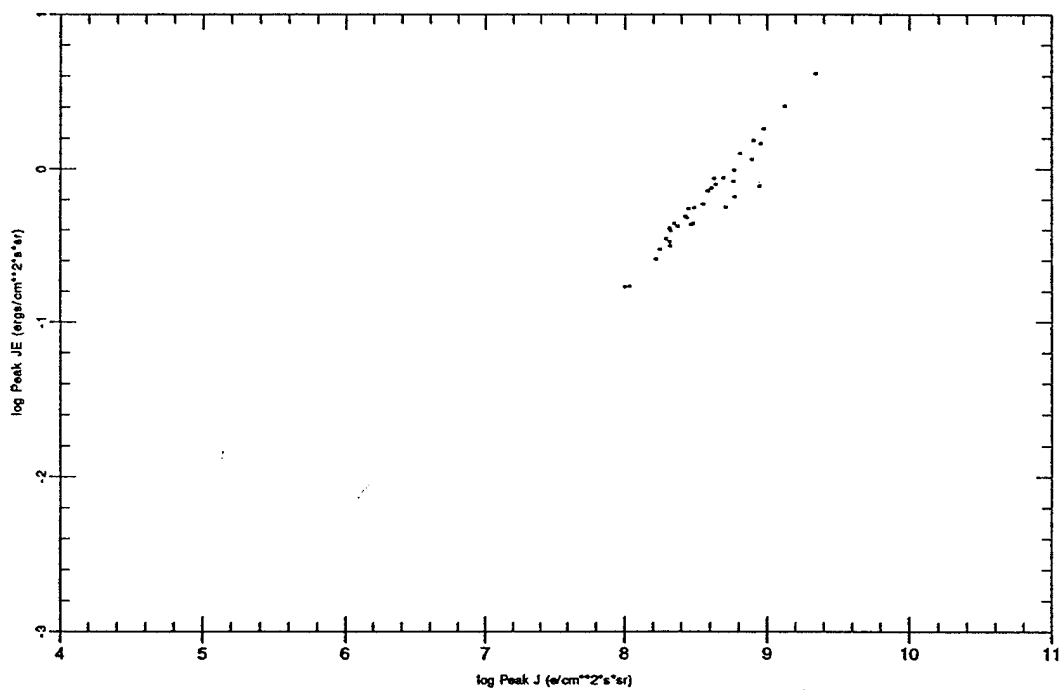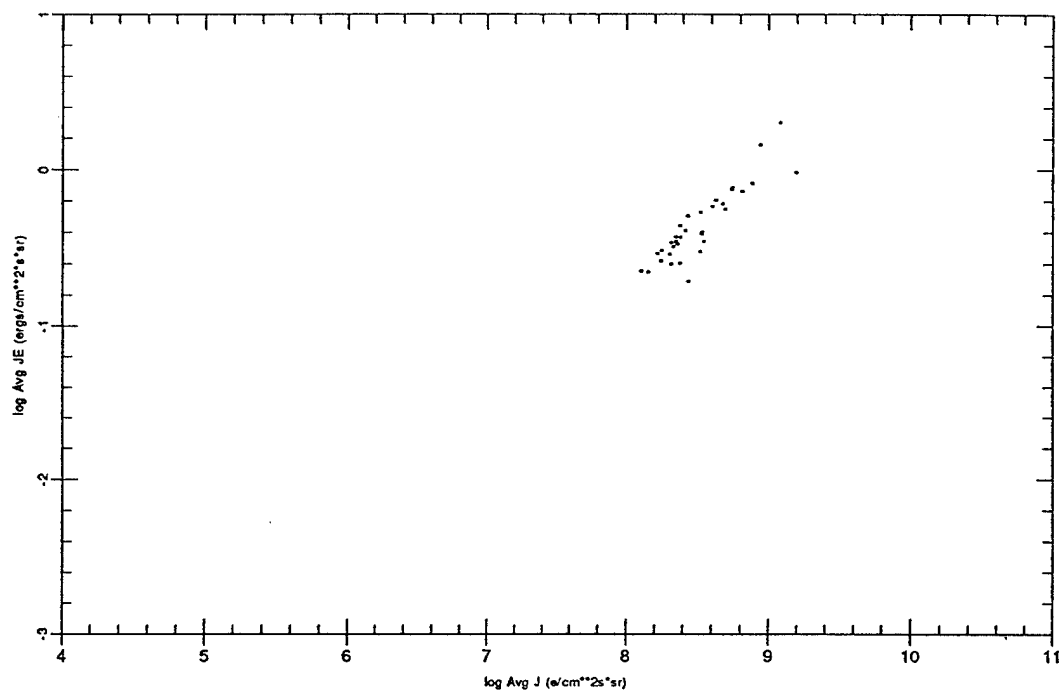
Threshold 0.0800 Peak Ch 12 Bz +
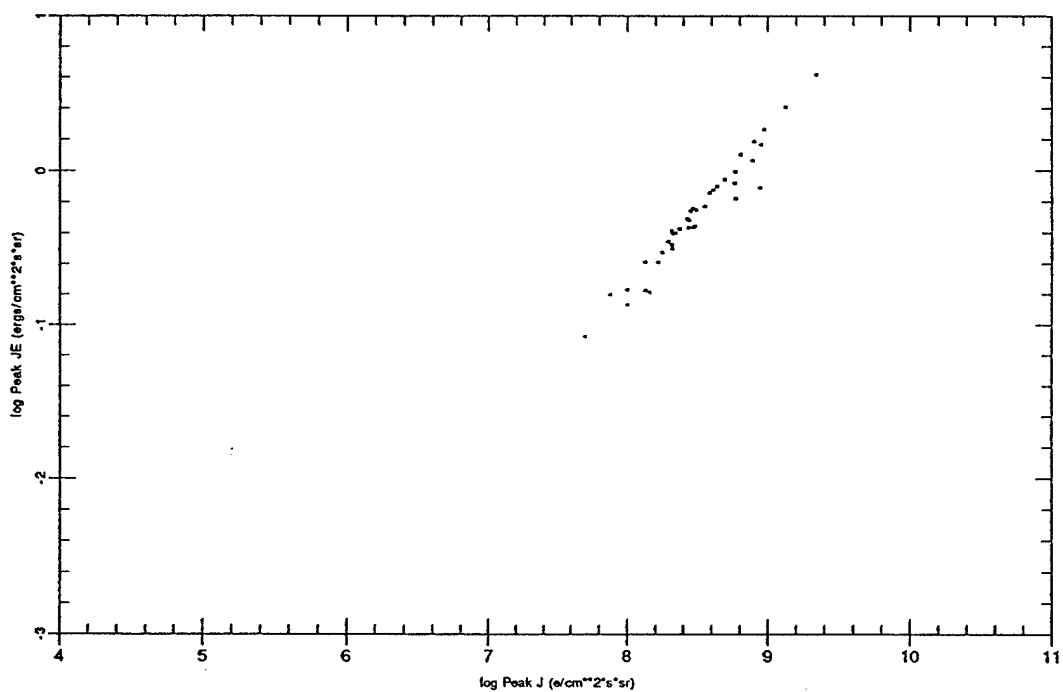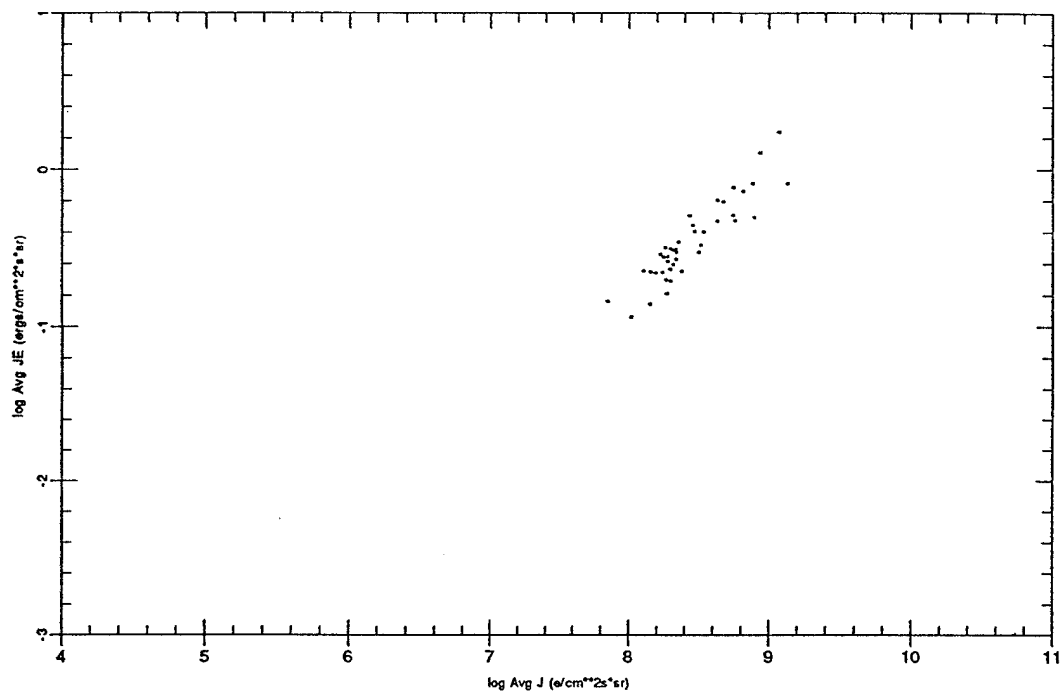
Threshold 0.0400 Peak Ch 12 Bz +
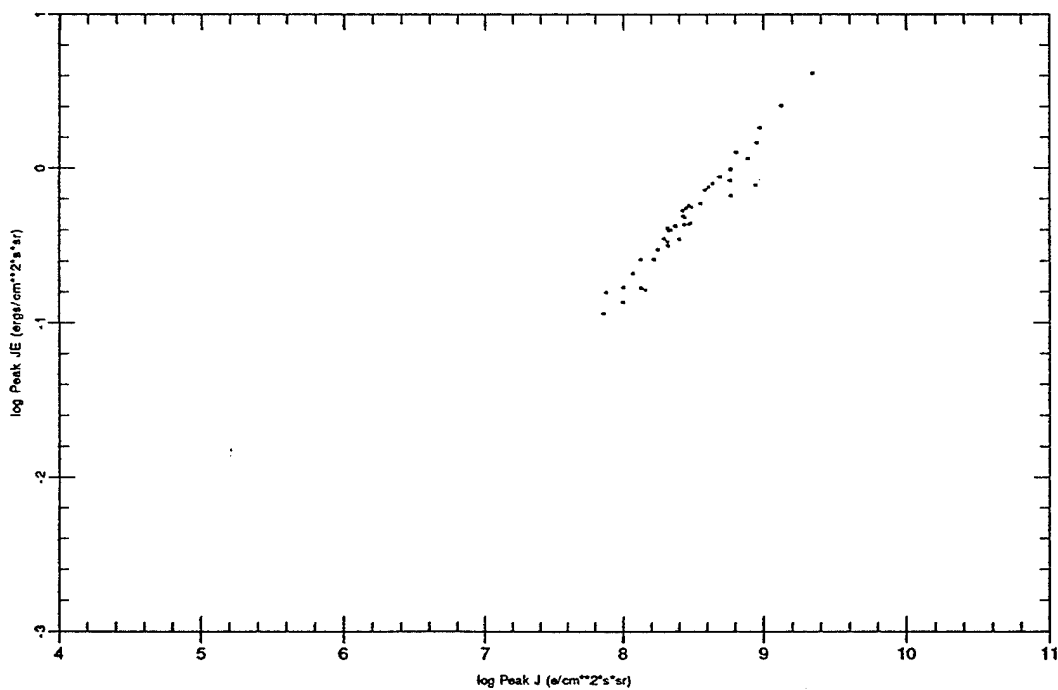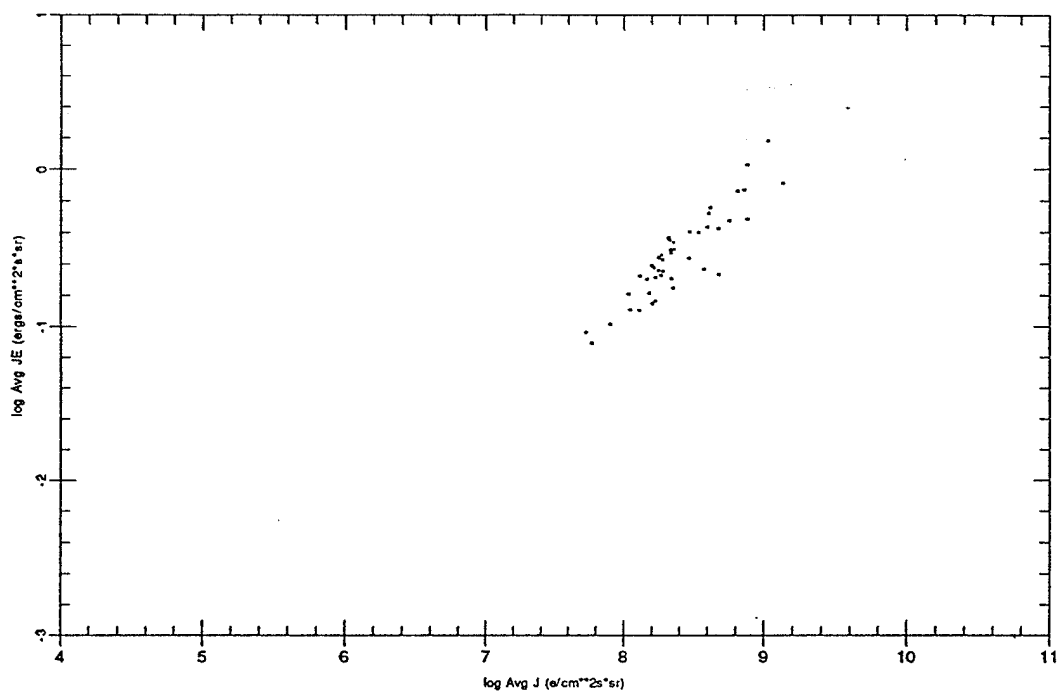
Threshold 0.0200 Peak Ch 12 Bz +
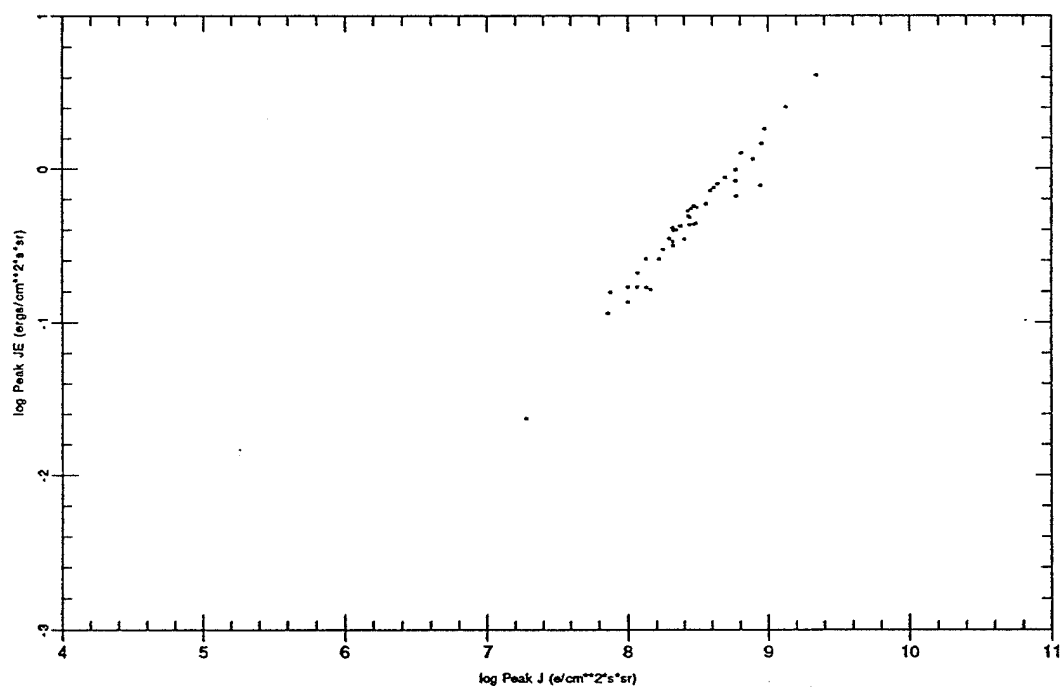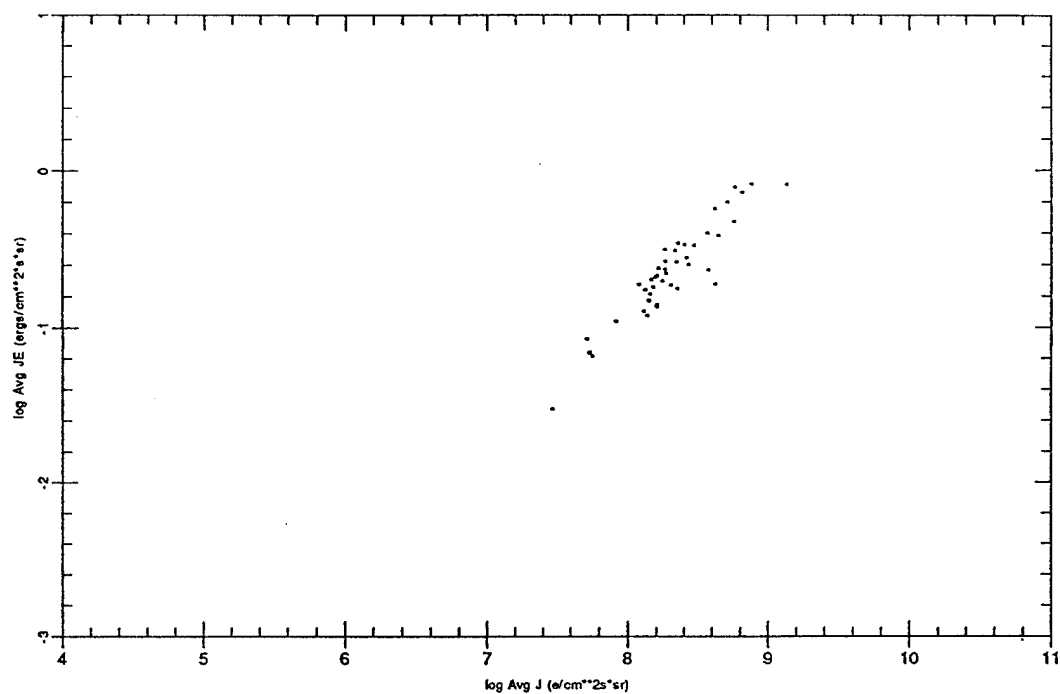
Threshold 0.0100 Peak Ch 12 Bz +
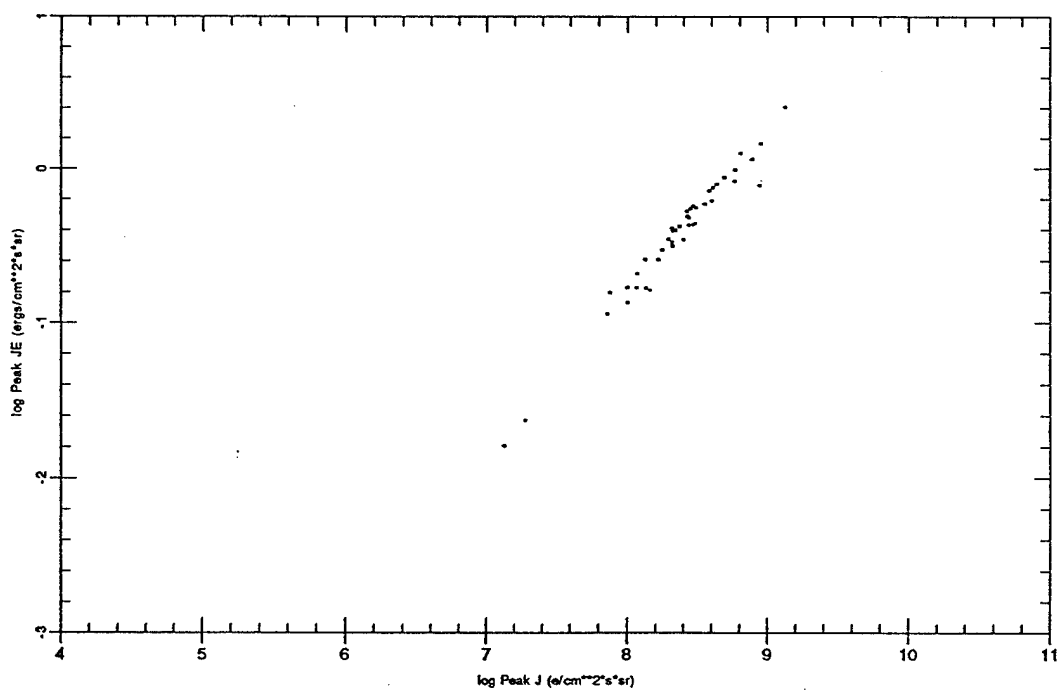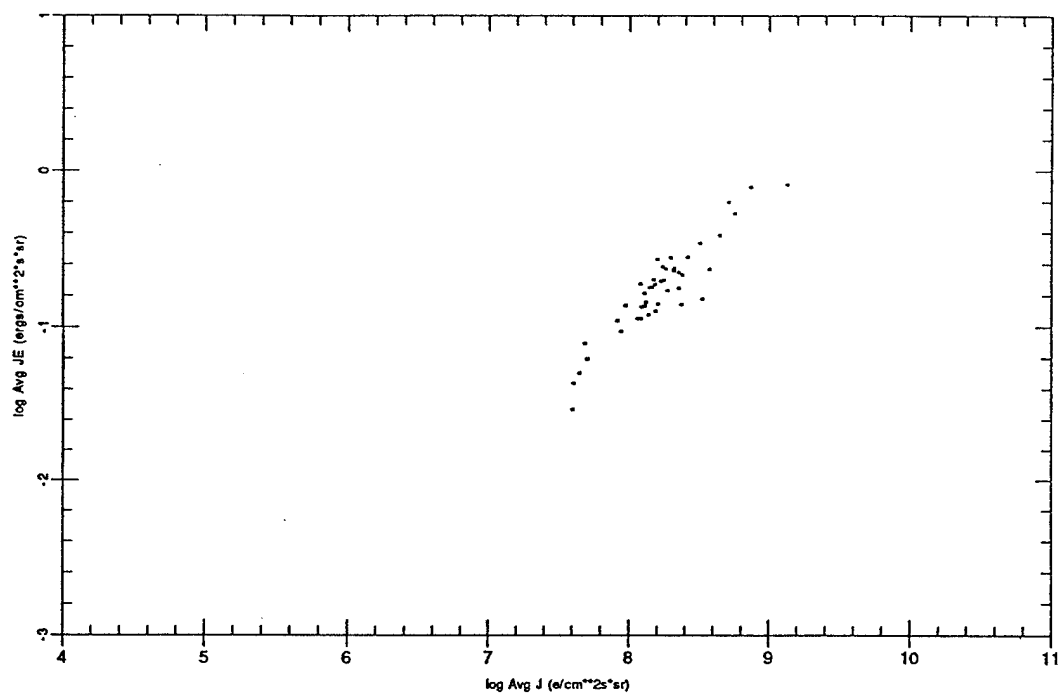
Threshold 0.0050 Peak Ch 12 Bz +

Threshold 0.0025 Peak Ch 12 Bz +

log Avg JE (ergs/cm**2*s*sr)

log Avg J (e/cm**2s*sr)

log Peak JE (ergs/cm**2*s*sr)

log Peak J (e/cm**2*s*sr)
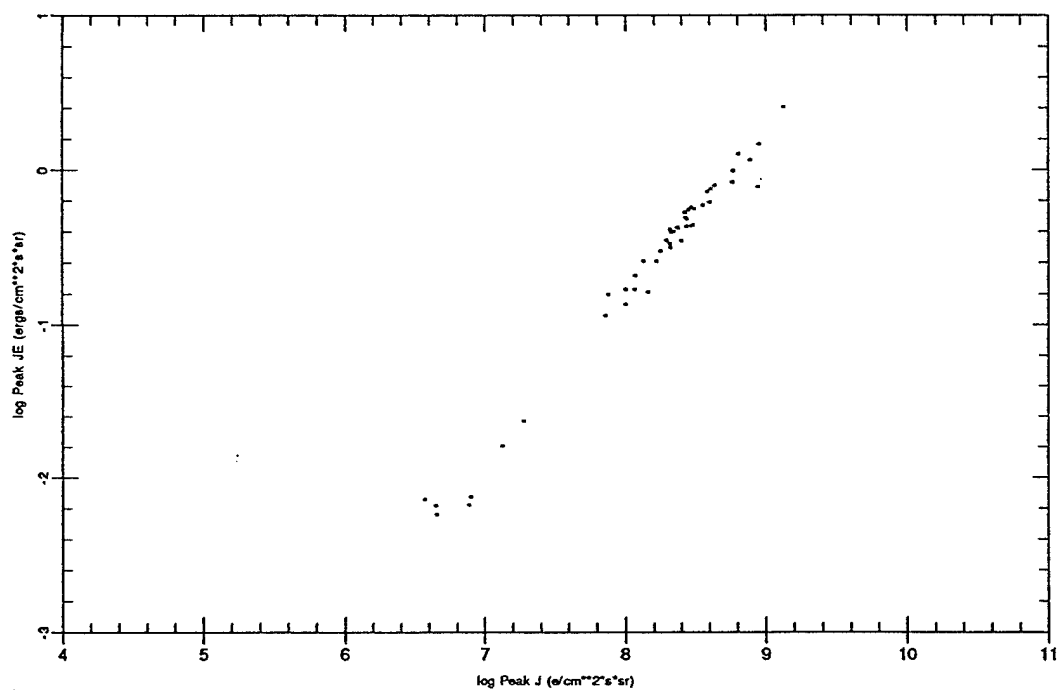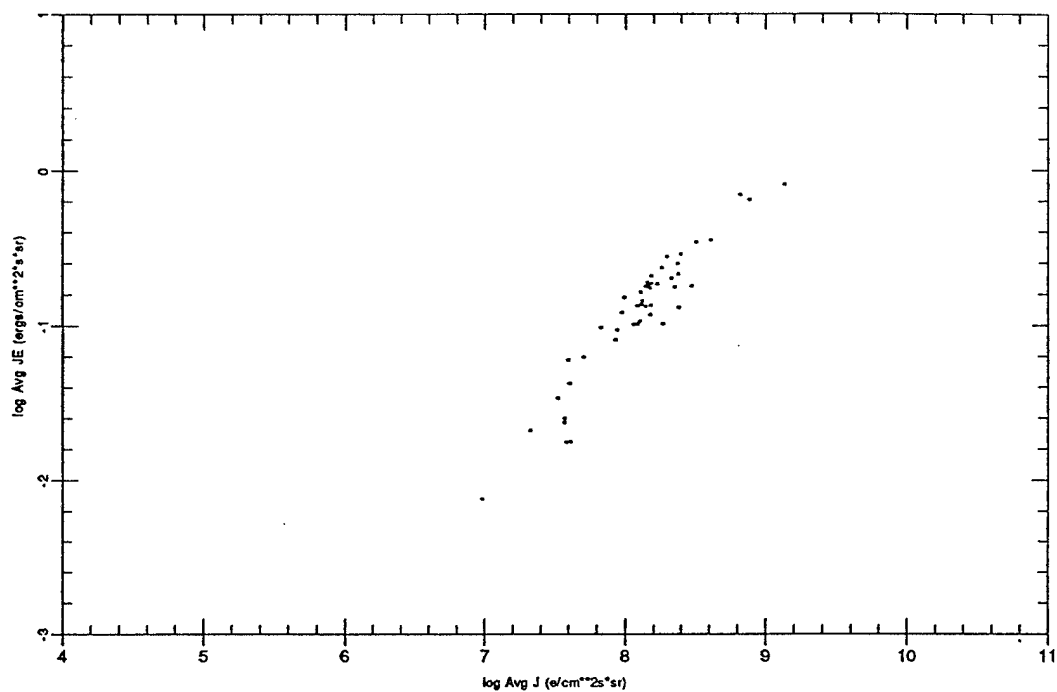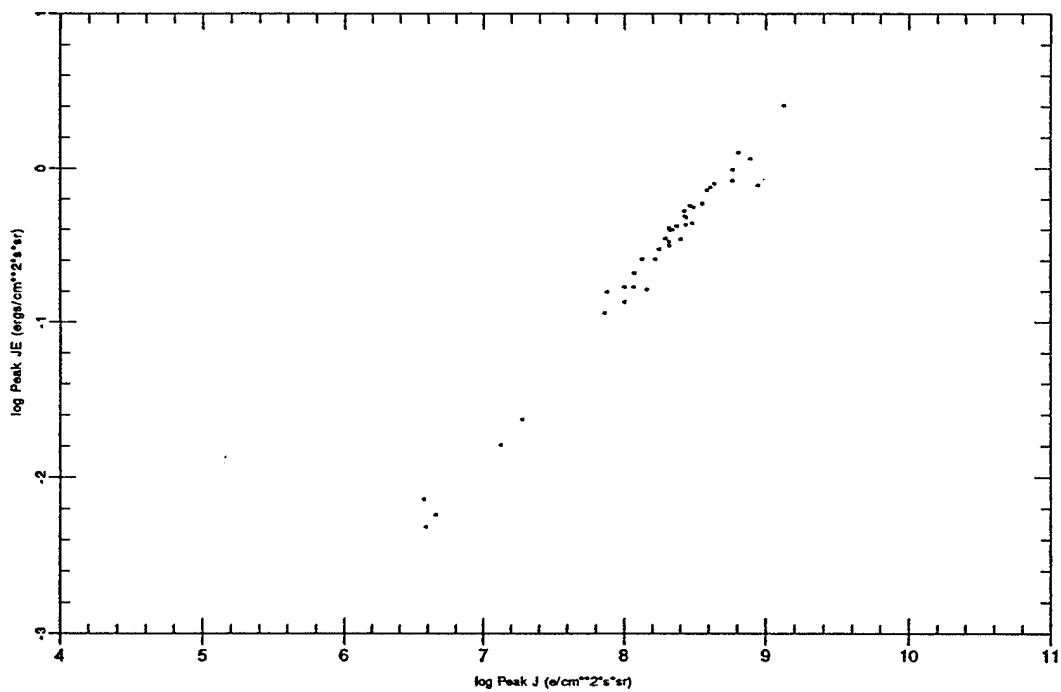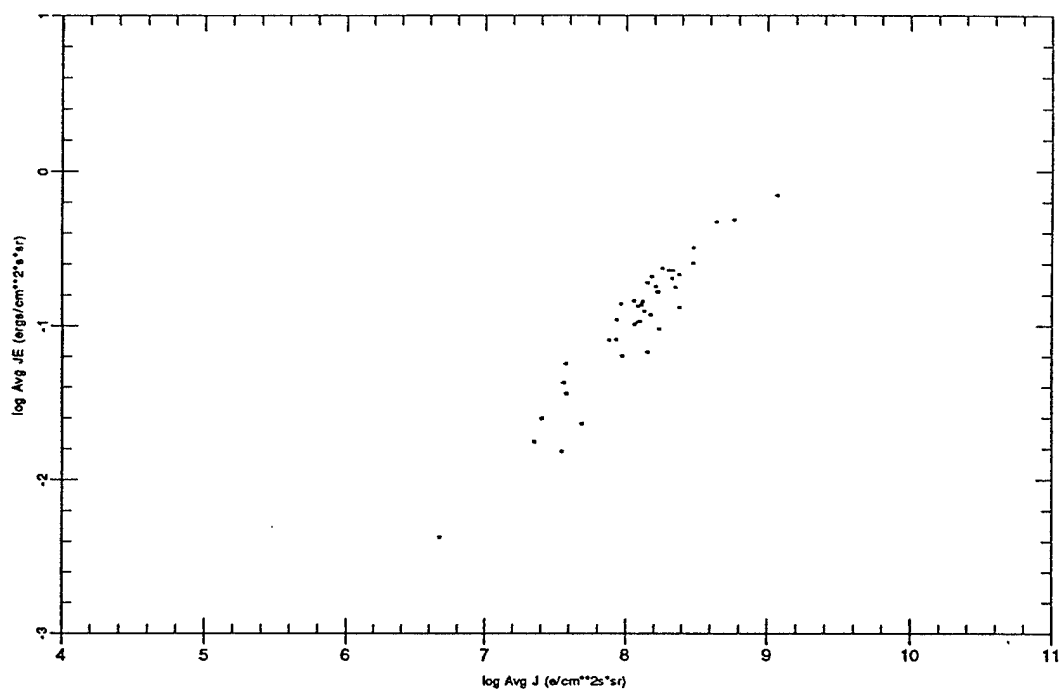
Threshold 0.1600 Peak Ch 11 Bz +
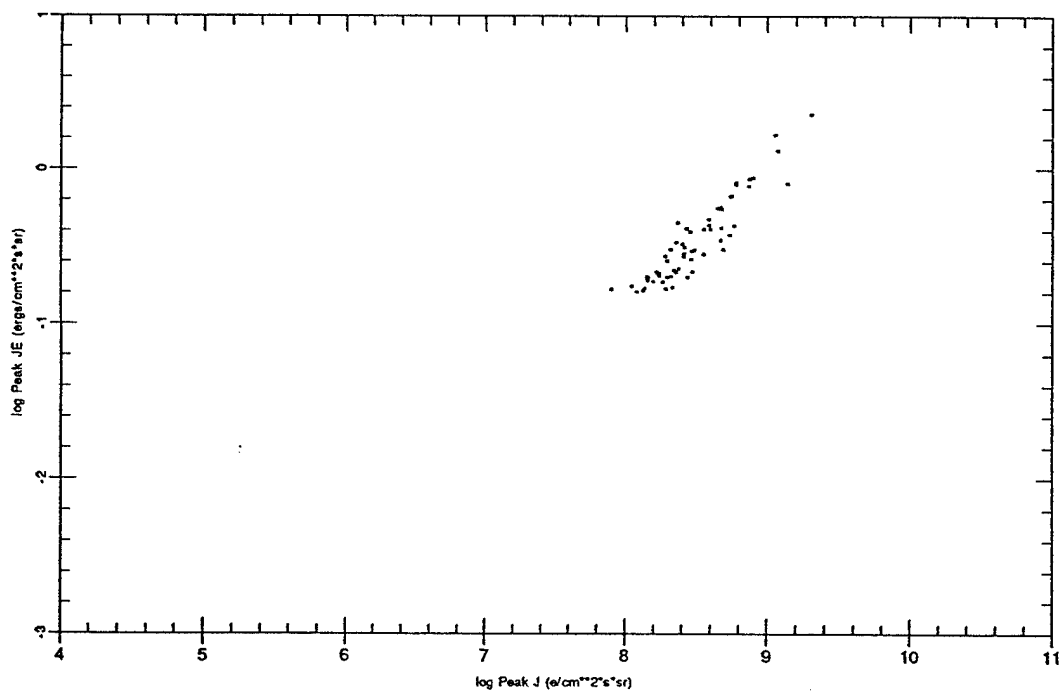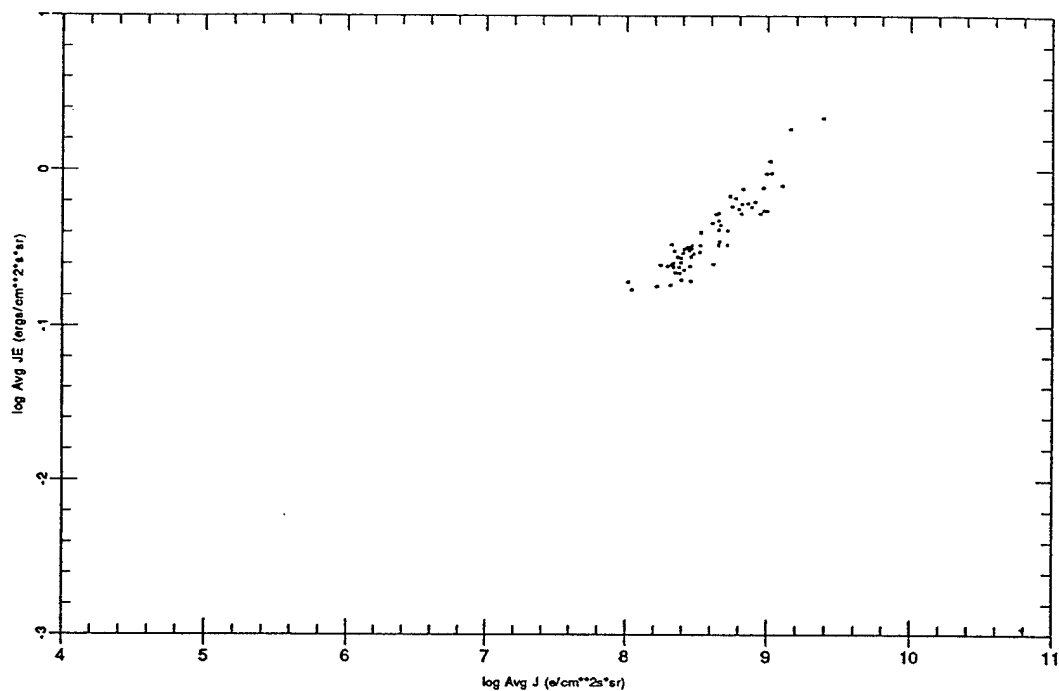
Threshold 0.0800 Peak Ch 11 Bz +

Threshold 0.0400 Peak Ch 11 Bz +

log Avg JE (ergs/cm**2*s*sr)

log Avg J (e/cm**2s*sr)

log Peak JE (ergs/cm**2*s*sr)

log Peak J (e/cm**2*s*sr)
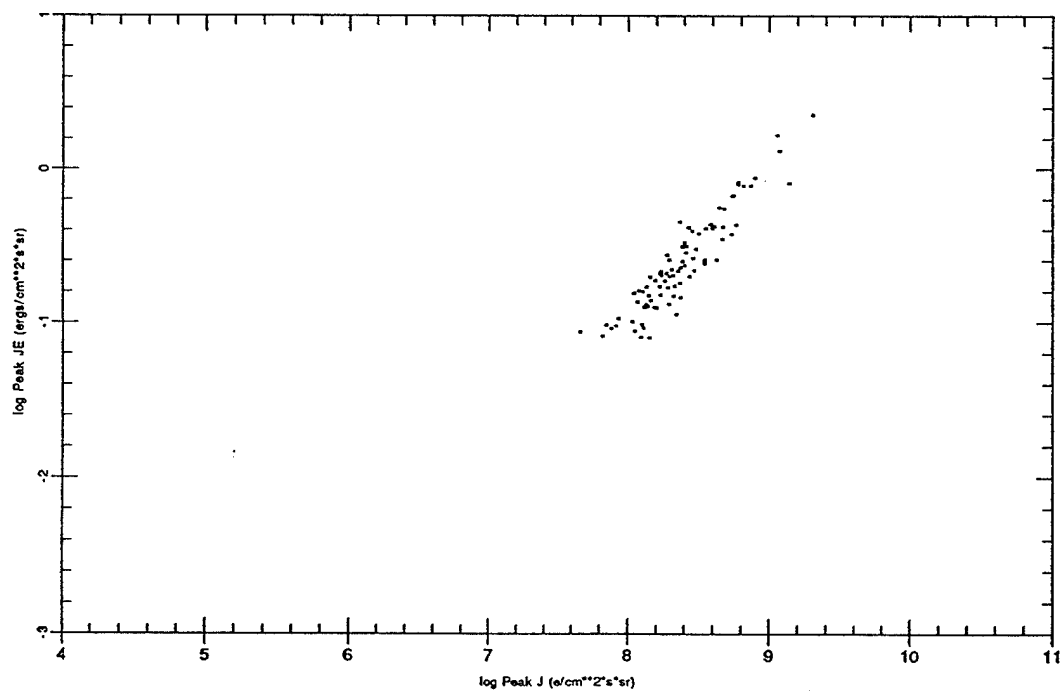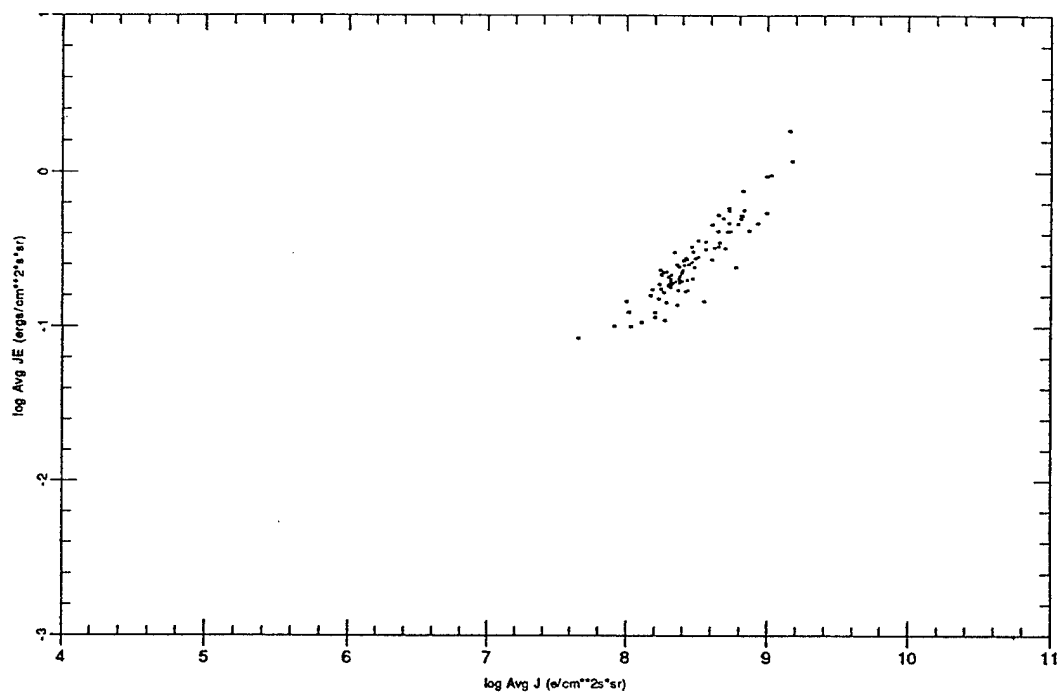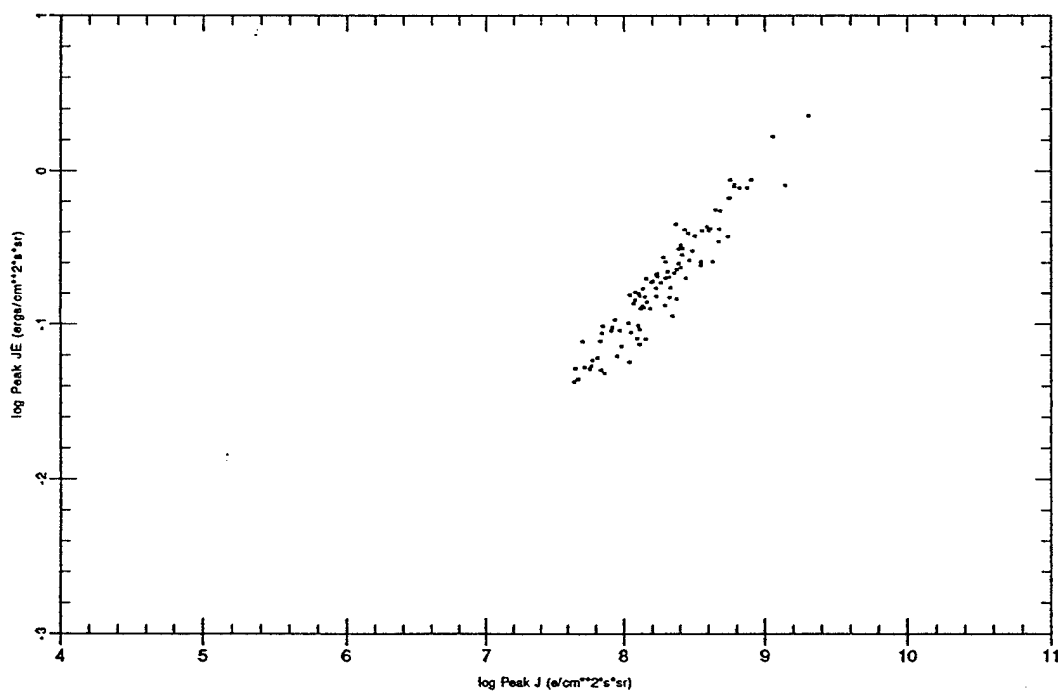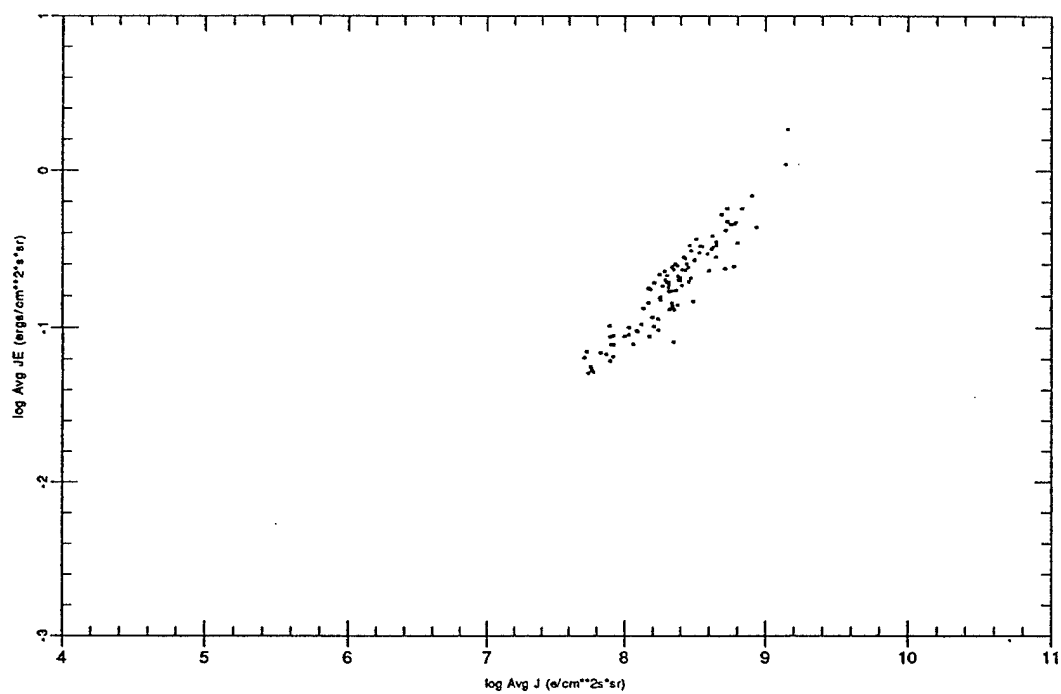
Threshold 0.0200 Peak Ch 11 Bz +
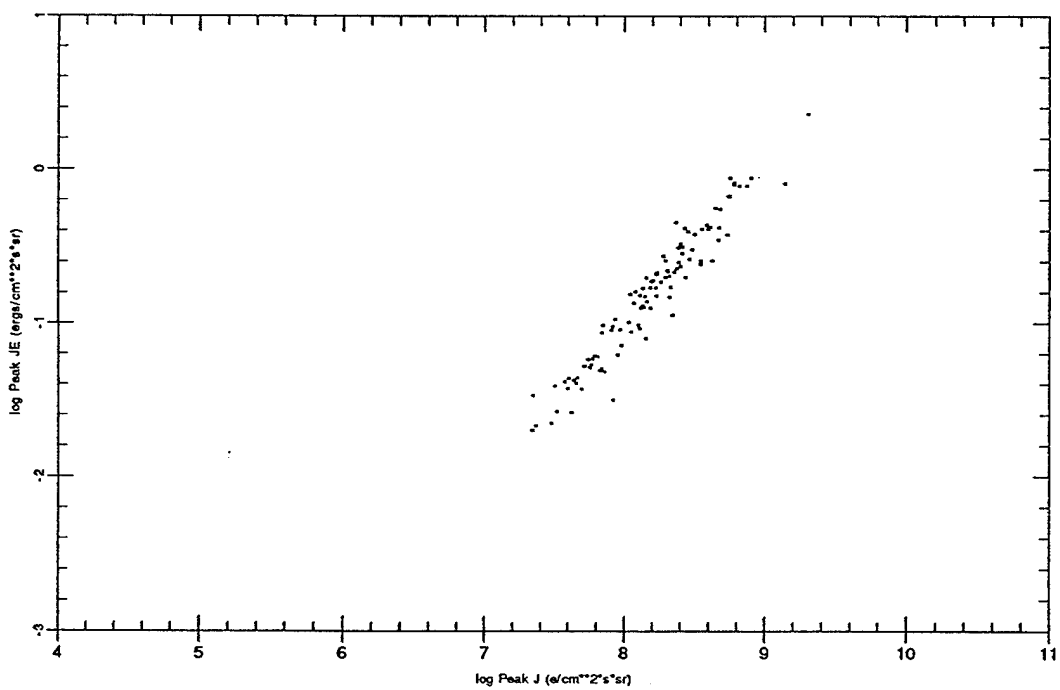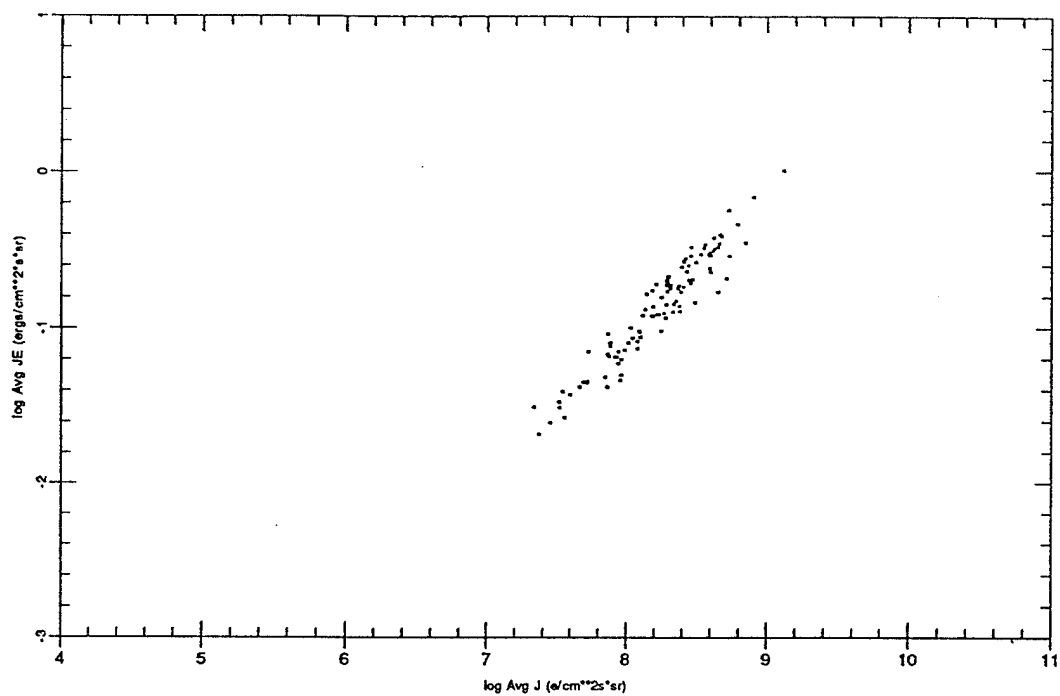
Threshold 0.0100 Peak Ch 11 Bz +
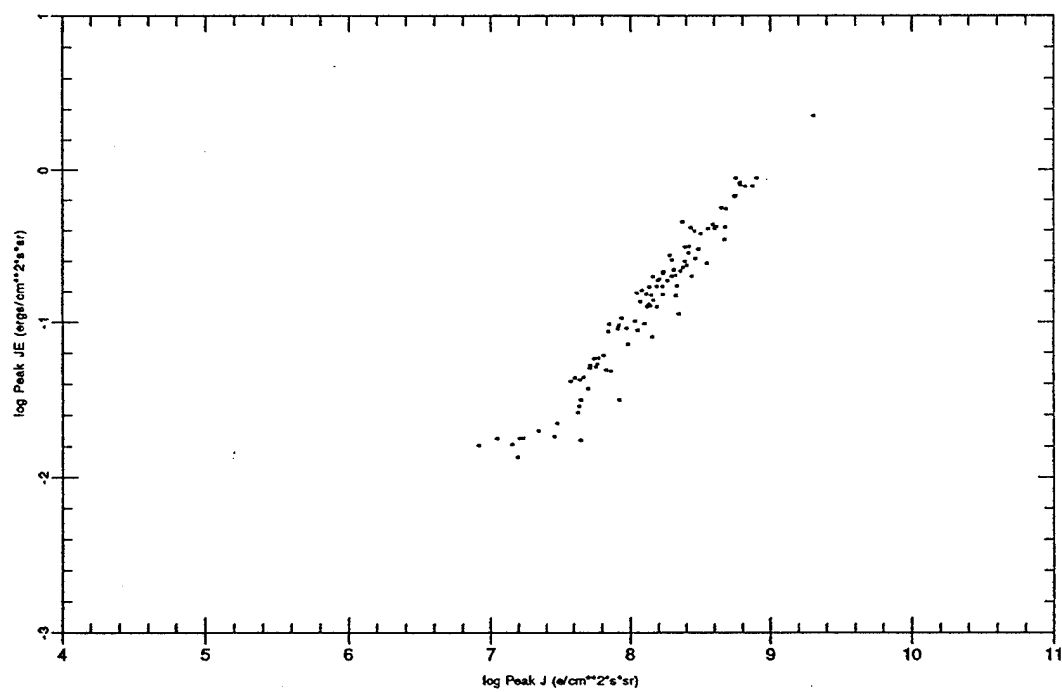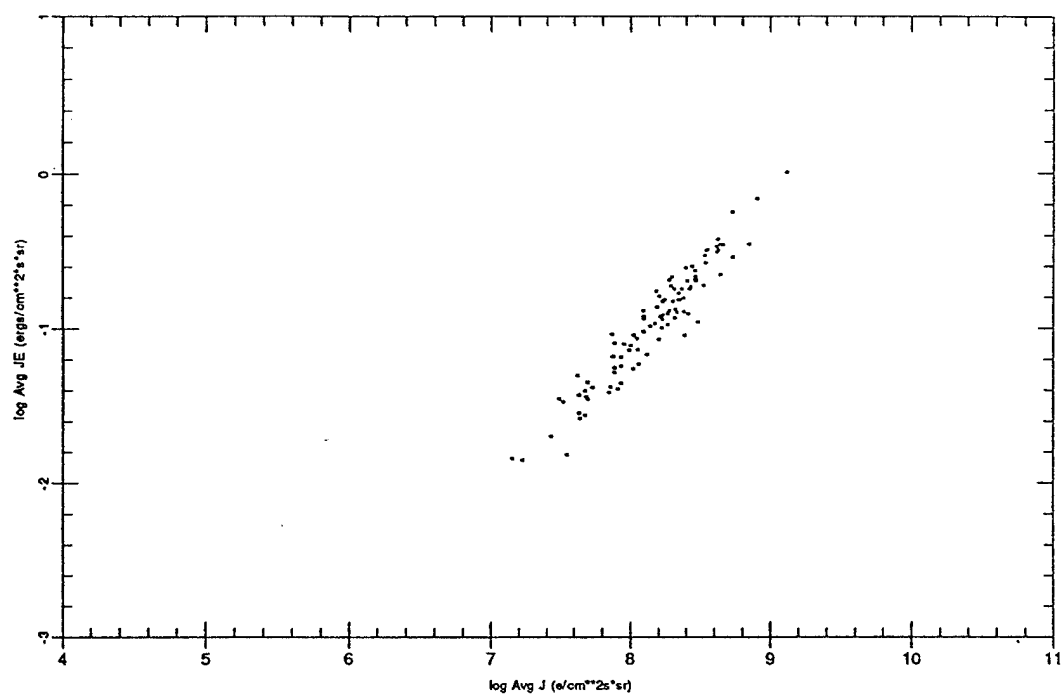
Threshold 0.0050 Peak Ch 11 Bz +
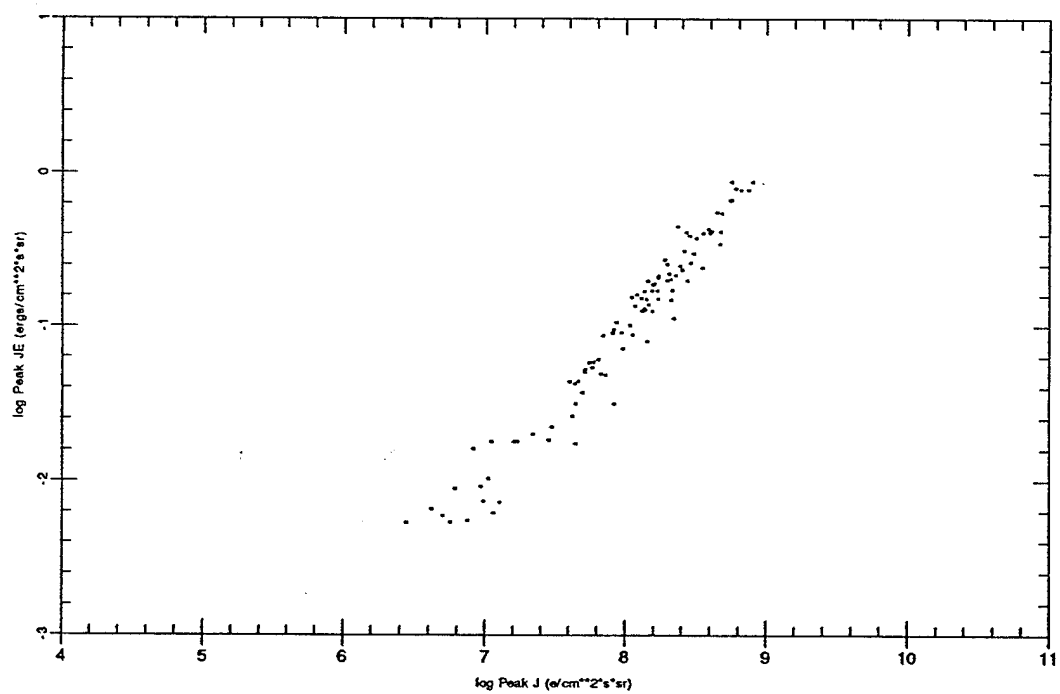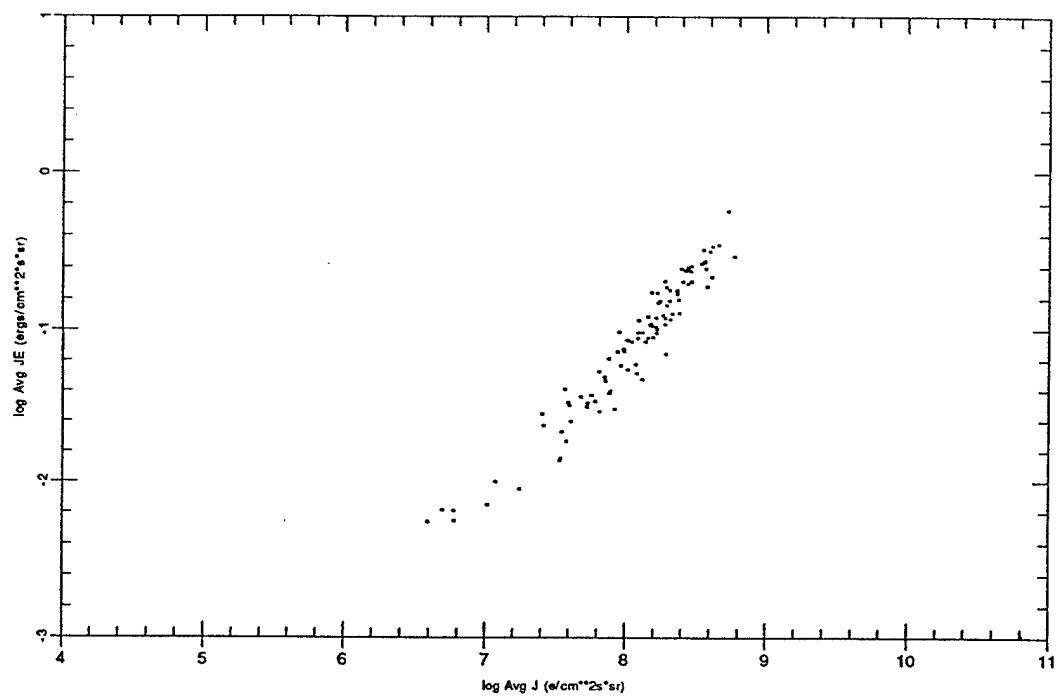
Threshold 0.0025 Peak Ch 11 Bz +
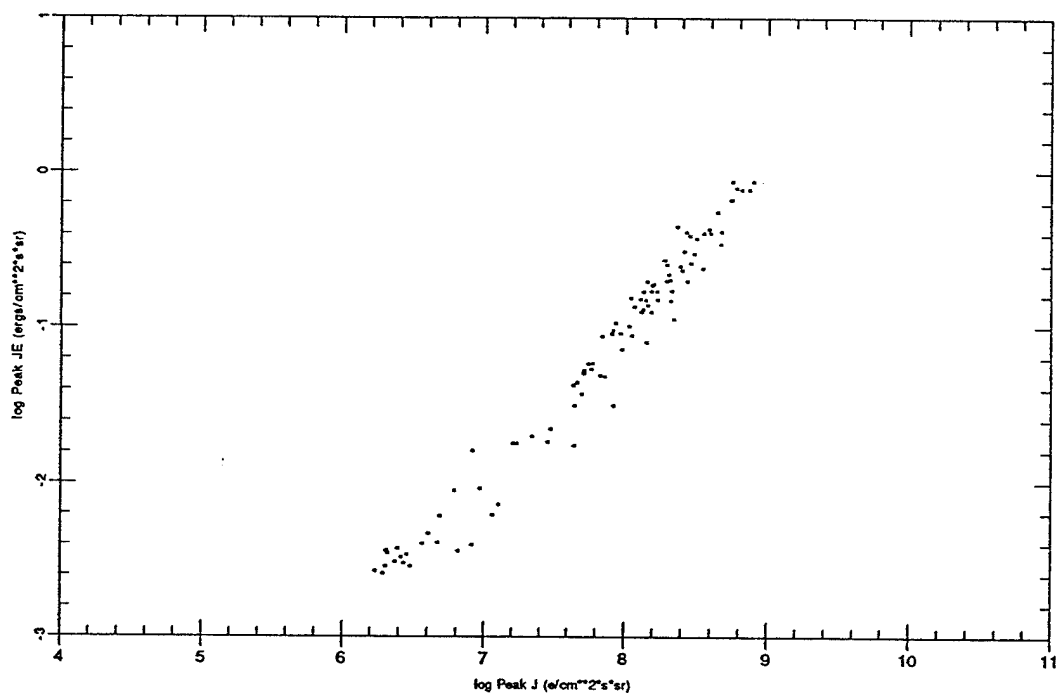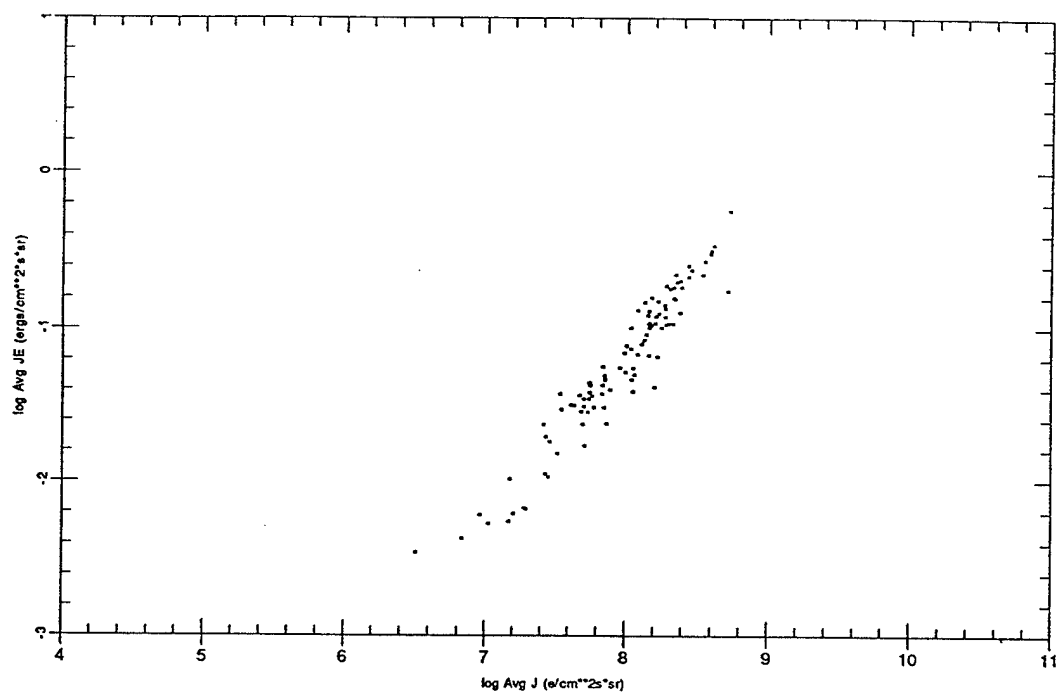
Threshold 0.1600 Peak Ch 9 Bz +
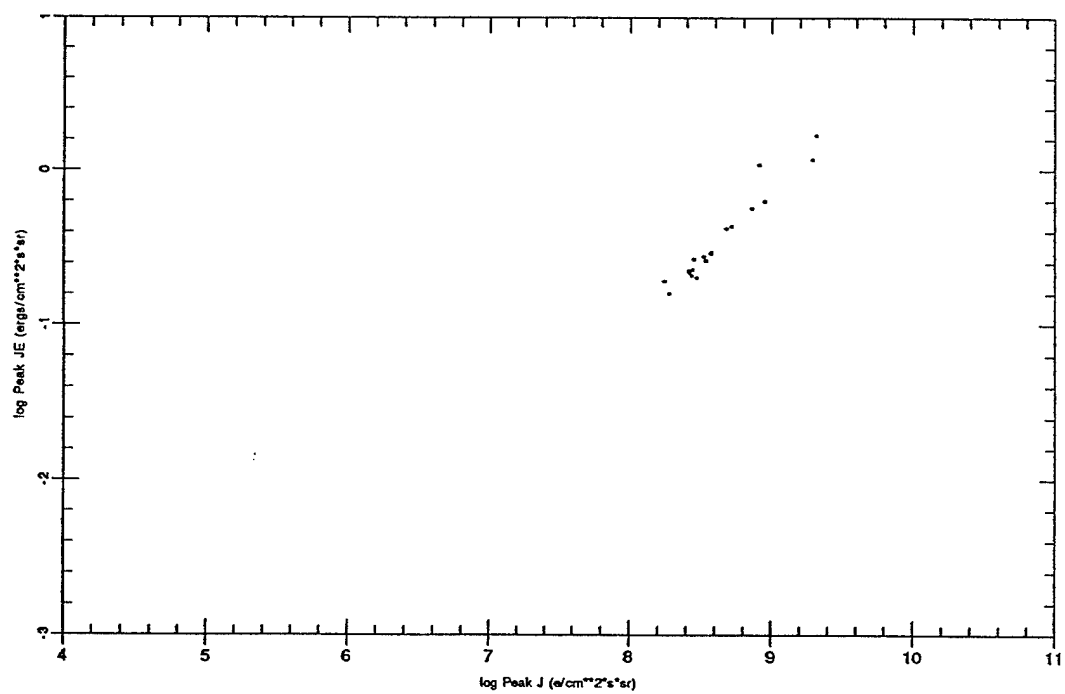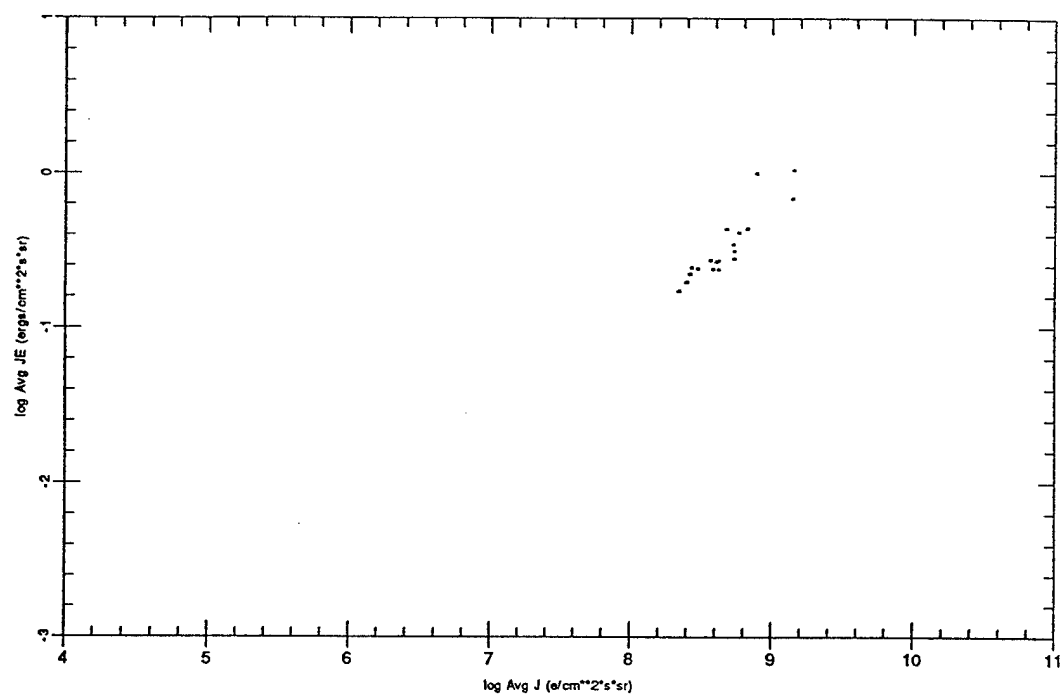
Threshold 0.0800 Peak Ch 9 Bz +
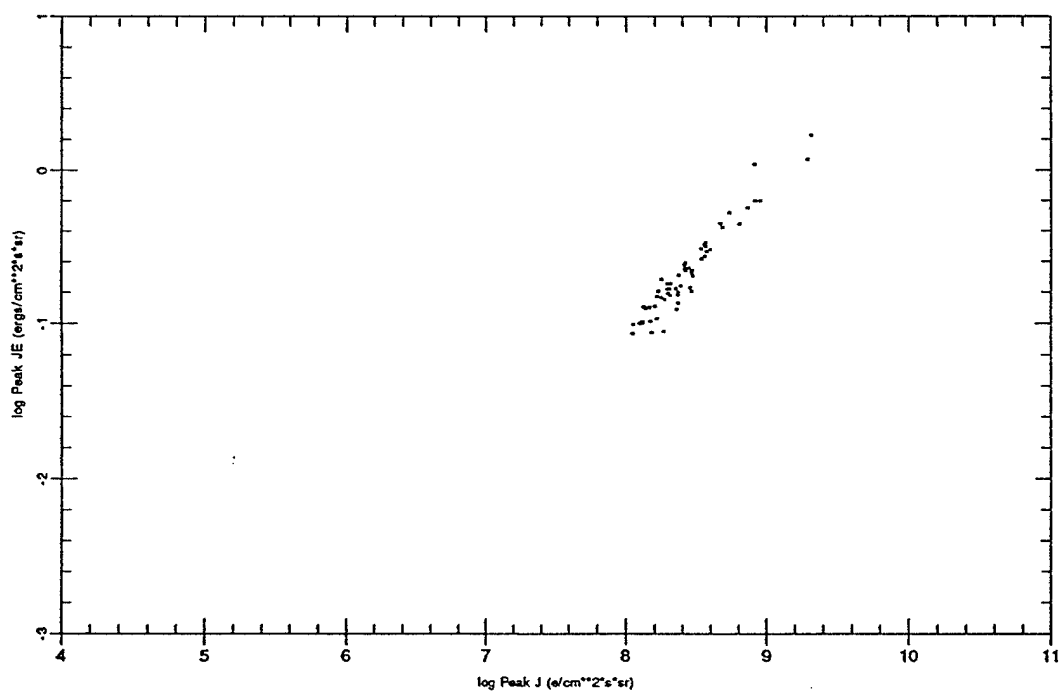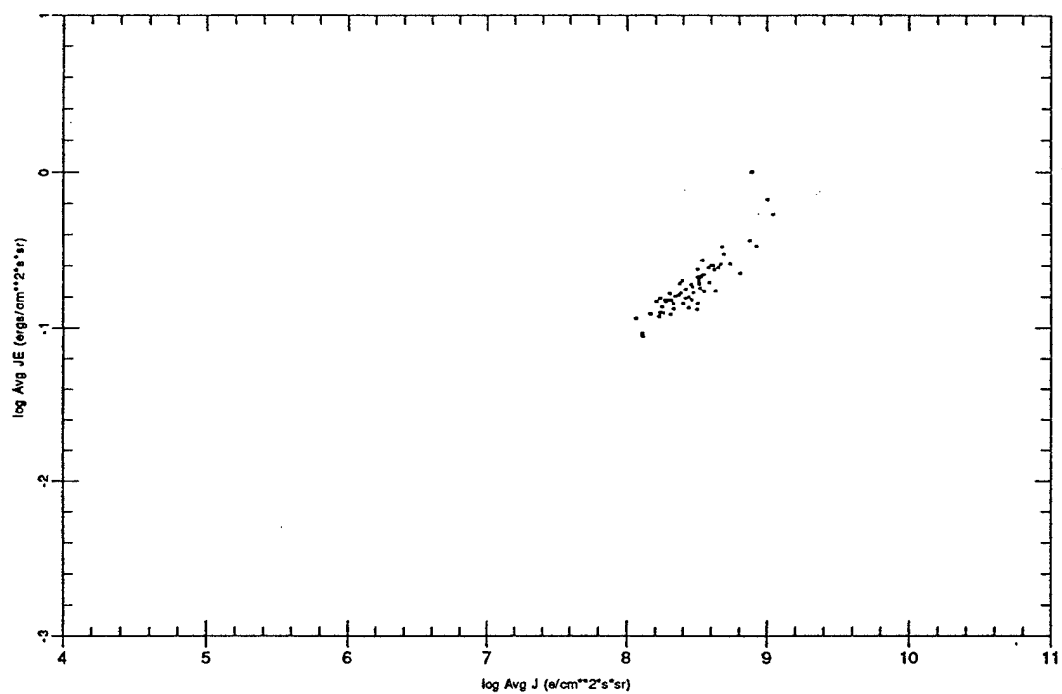
Threshold 0.0400 Peak Ch 9 Bz +
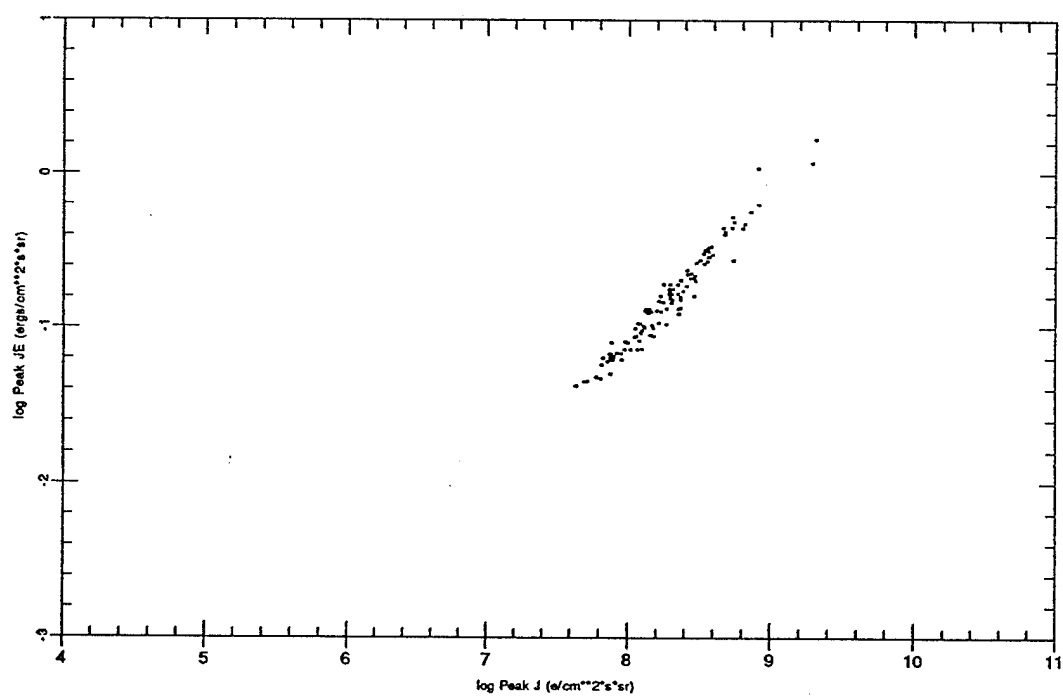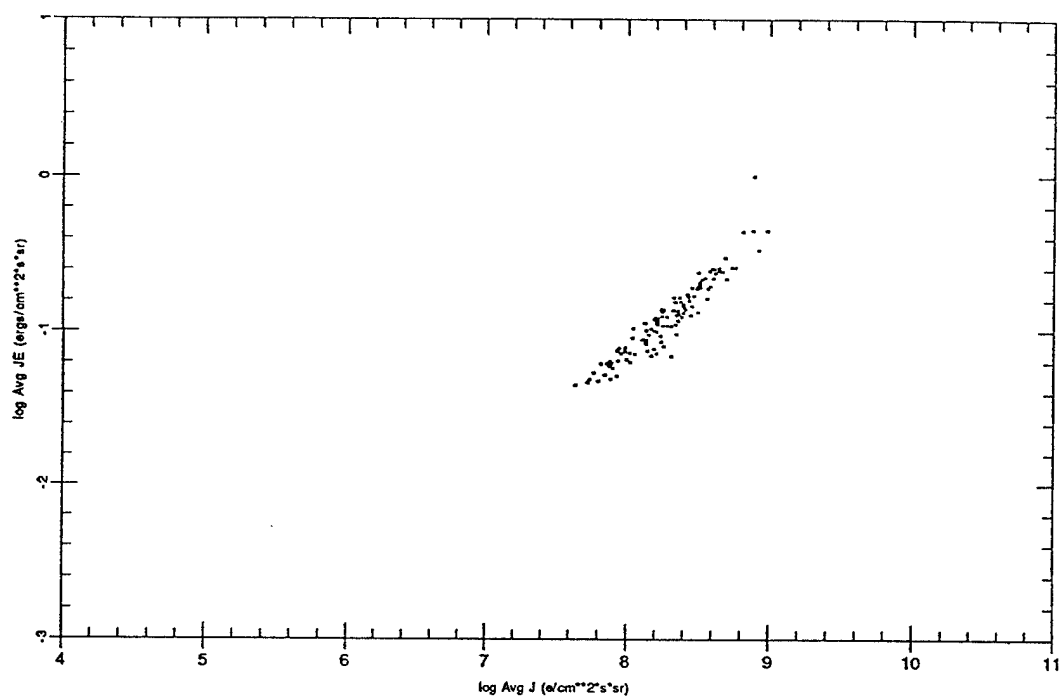
Threshold 0.0200 Peak Ch 9 Bz +
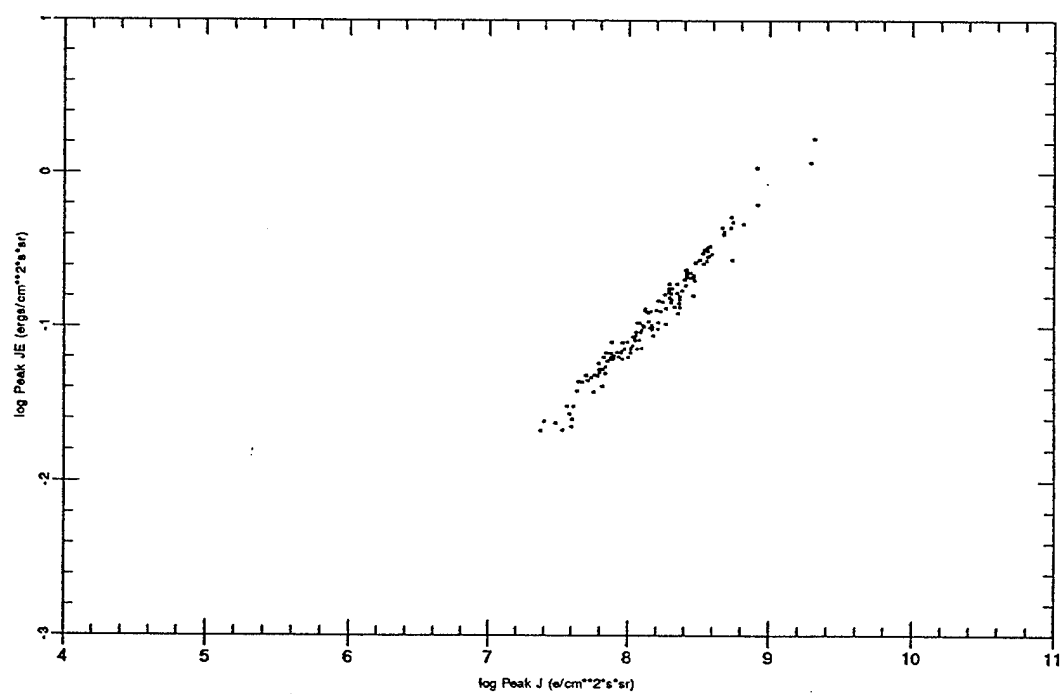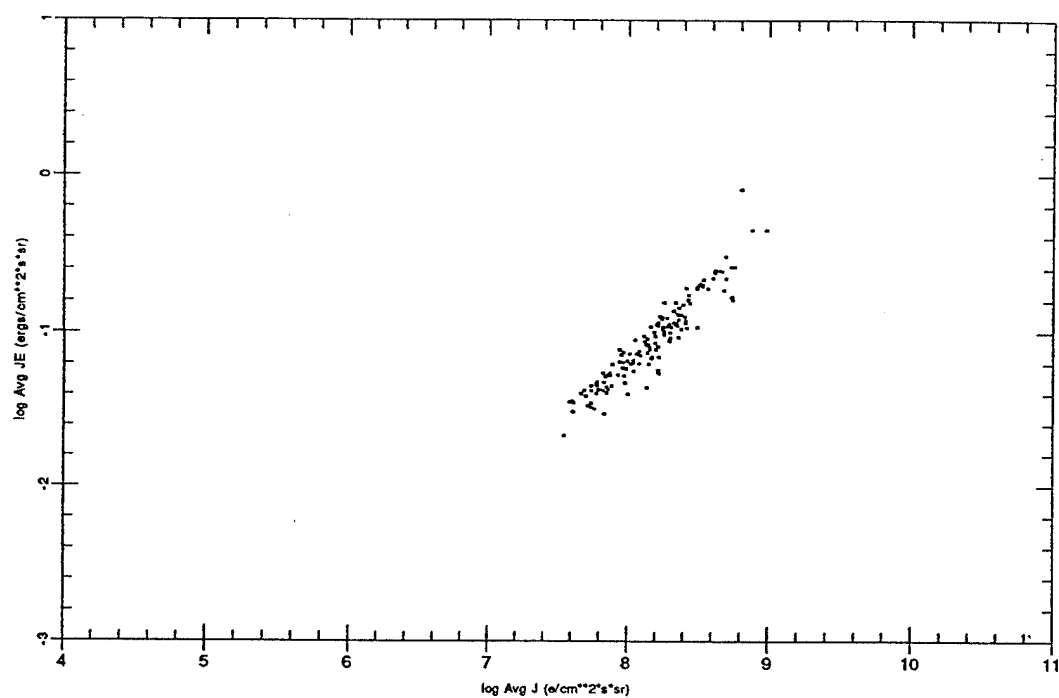
Threshold 0.0100 Peak Ch 9 Bz +
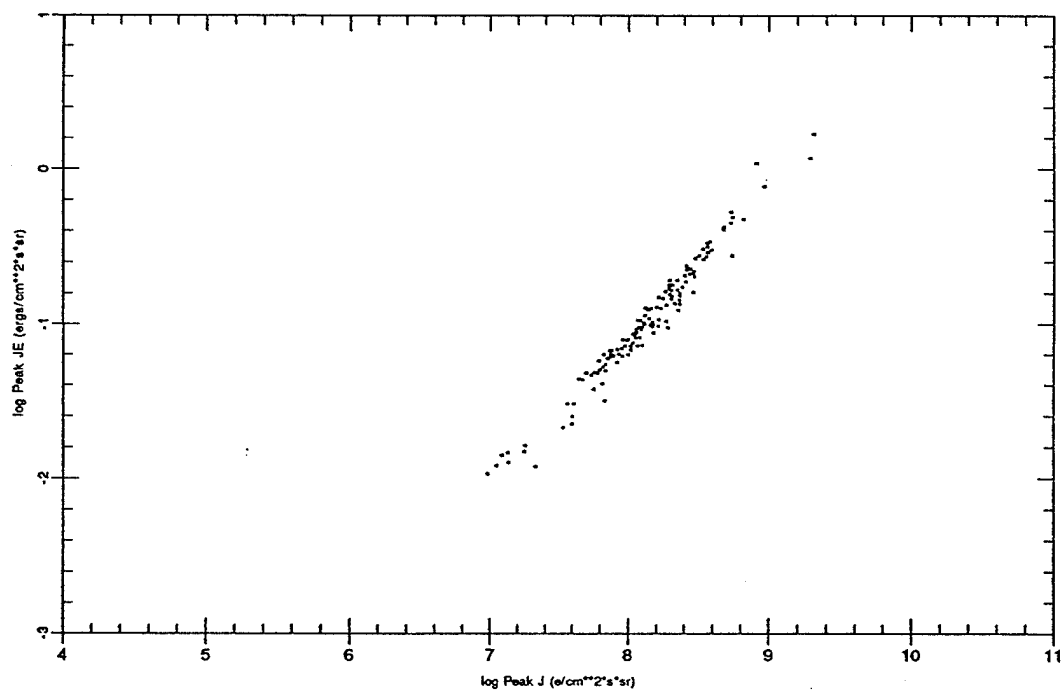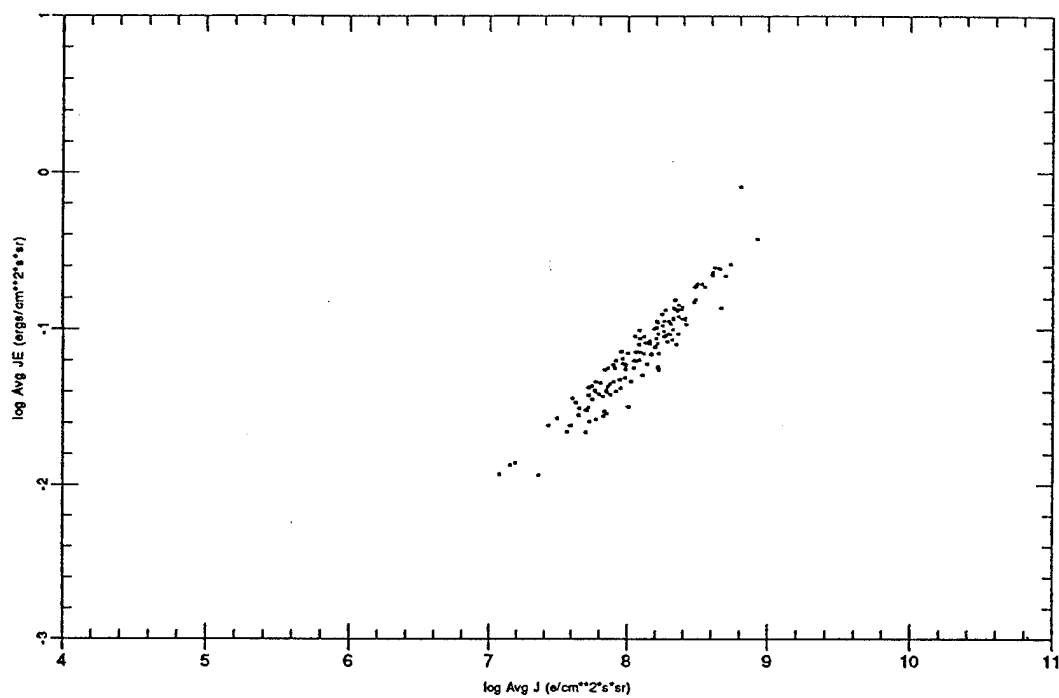
Threshold 0.0050 Peak Ch 9 Bz +
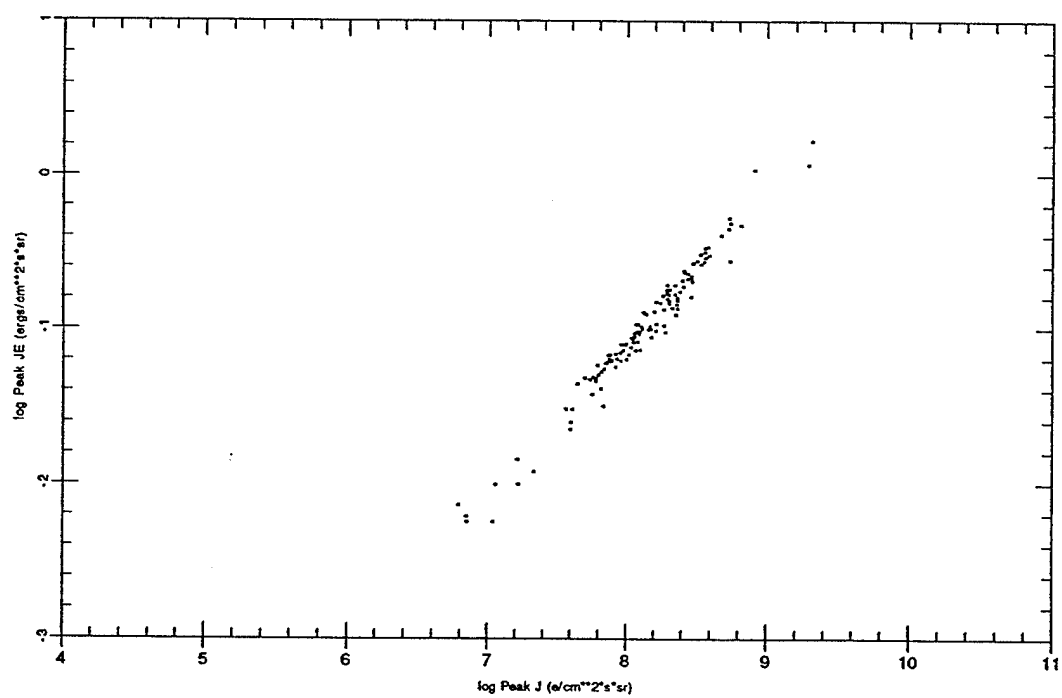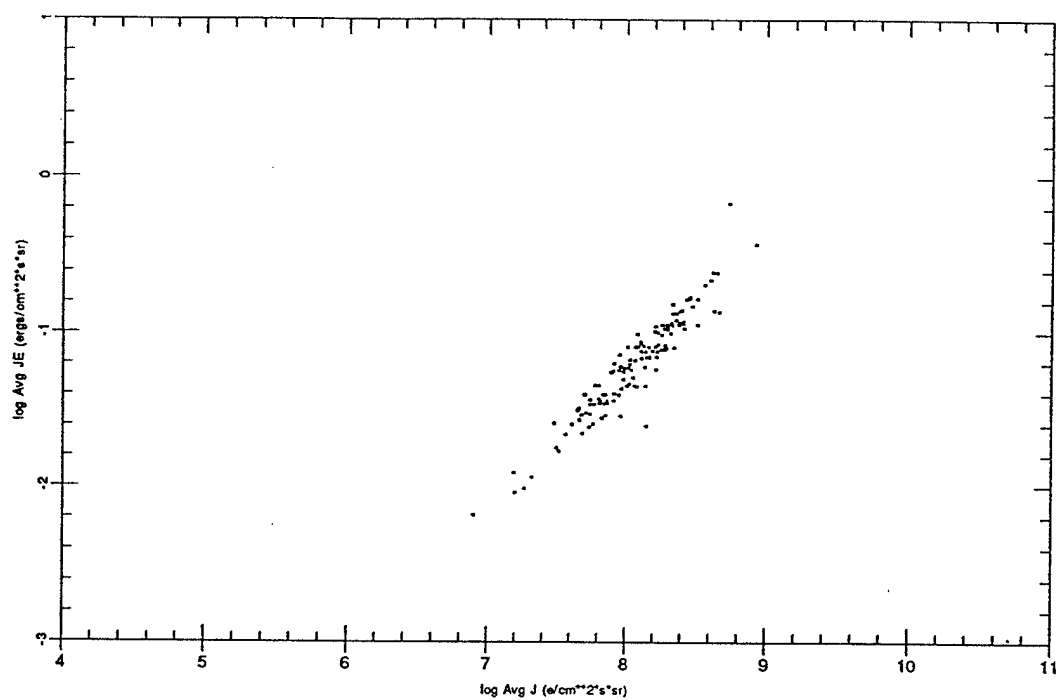
Threshold 0.0025 Peak Ch 9 Bz +
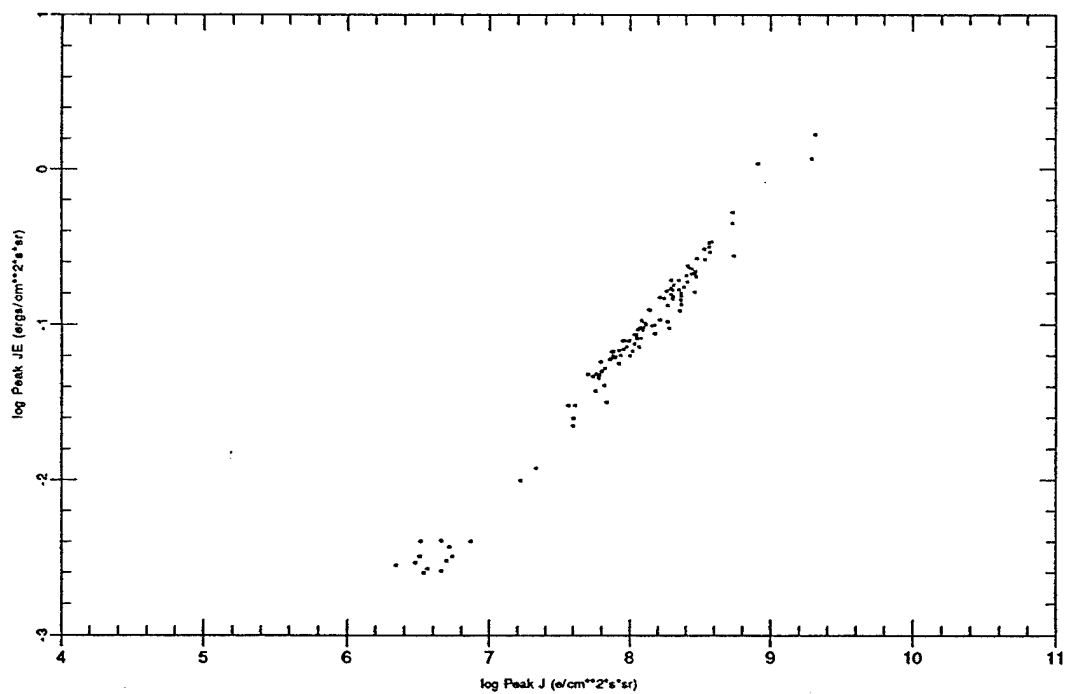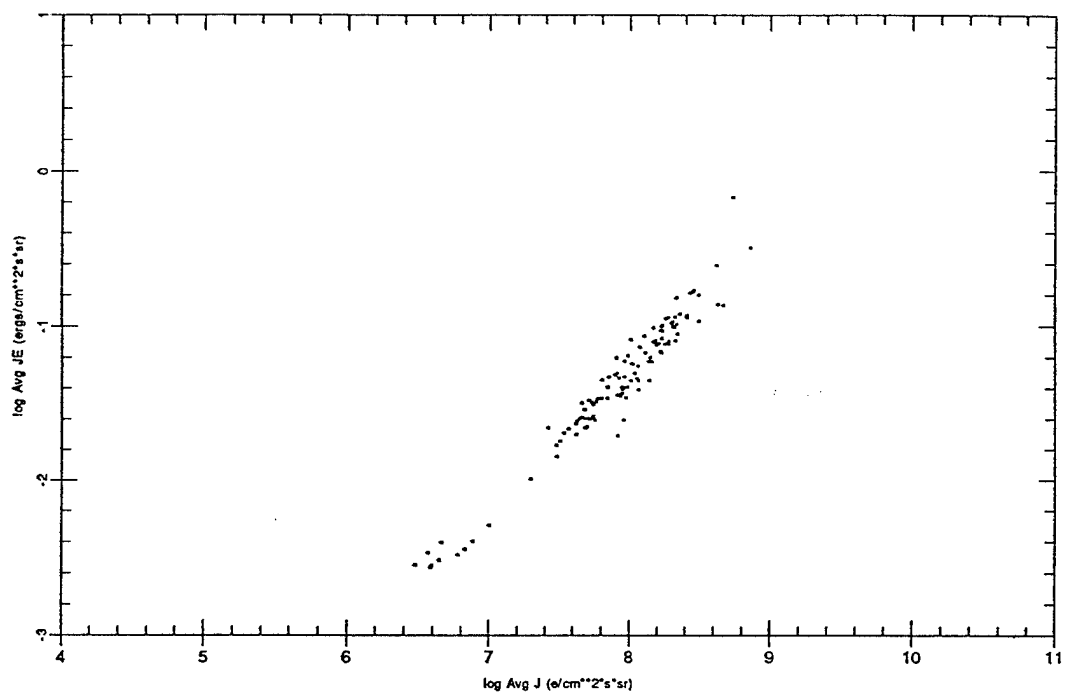
Threshold 0.1600 Peak Ch 8 Bz +
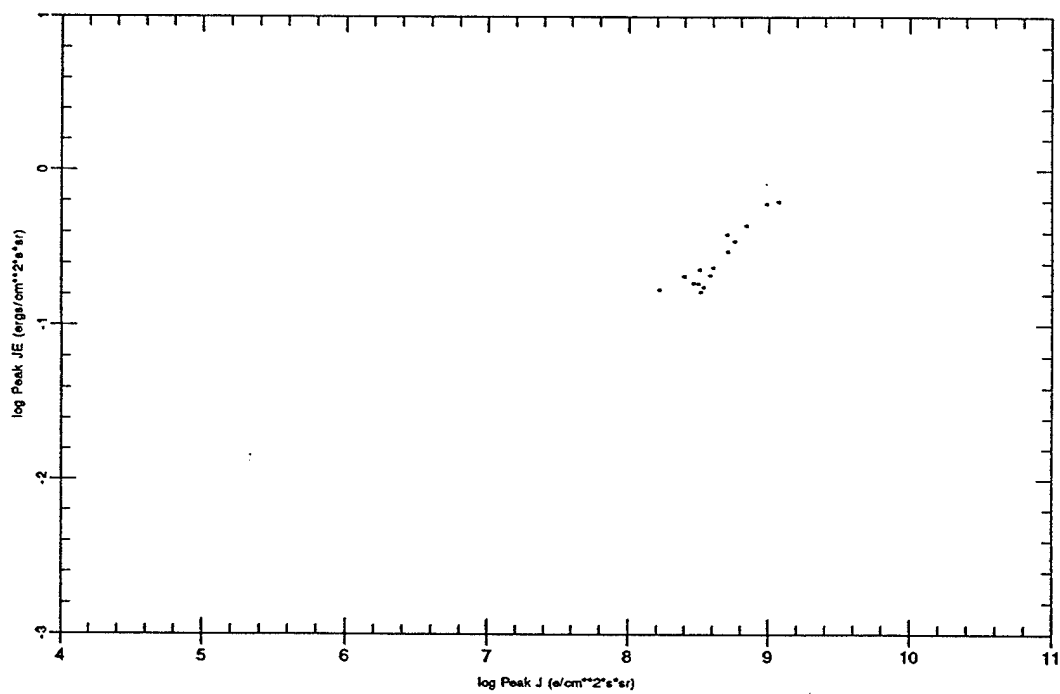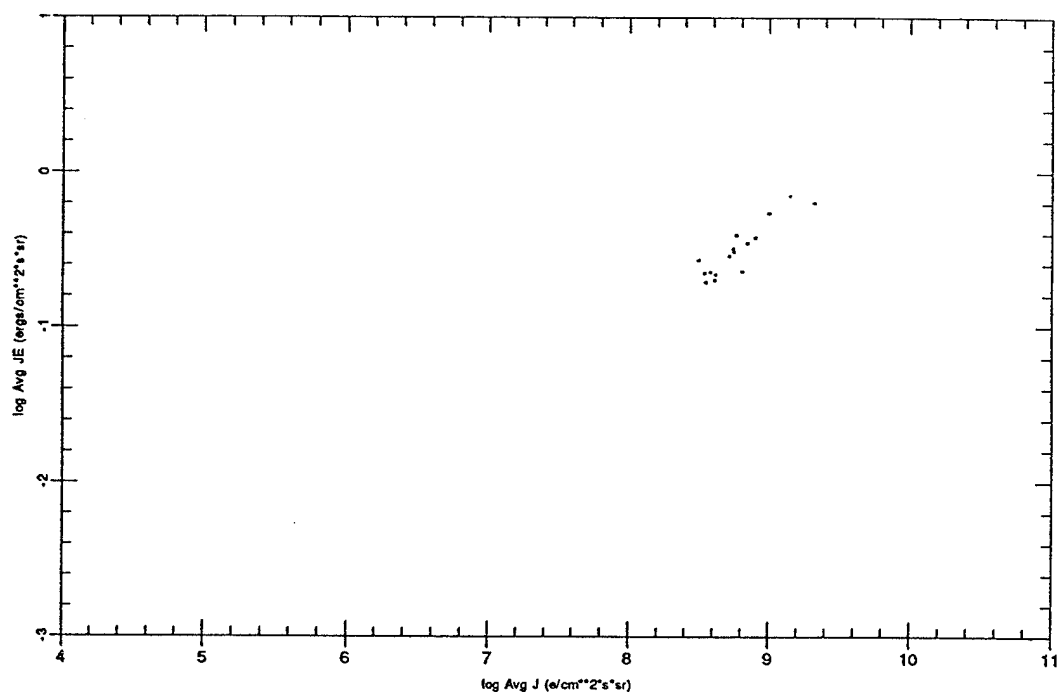
Threshold 0.0800 Peak Ch 8 Bz +
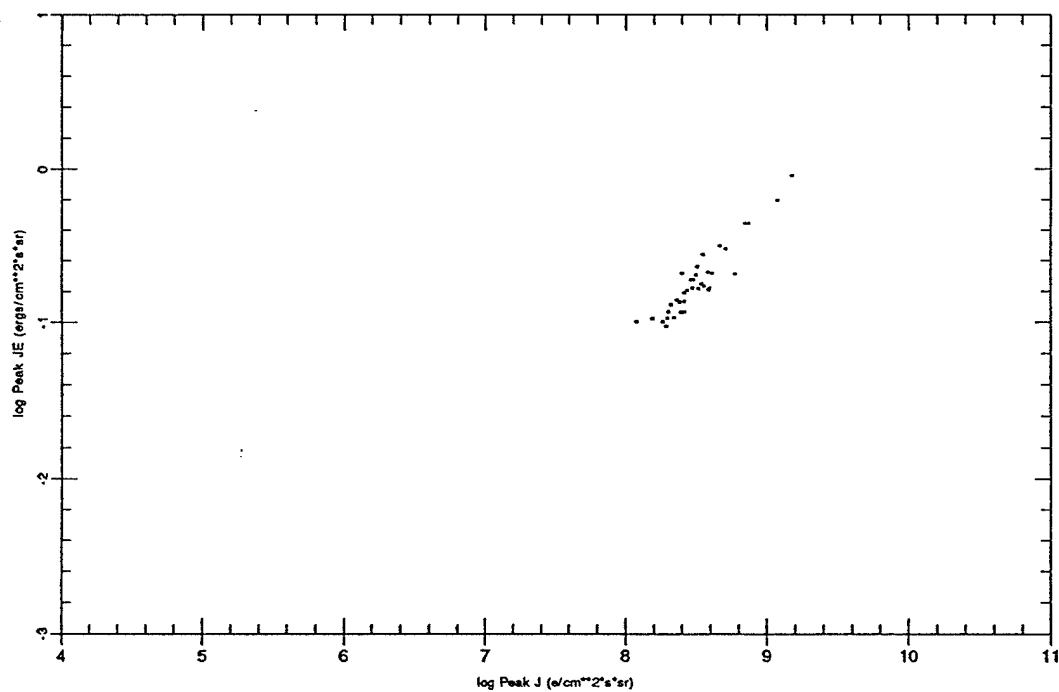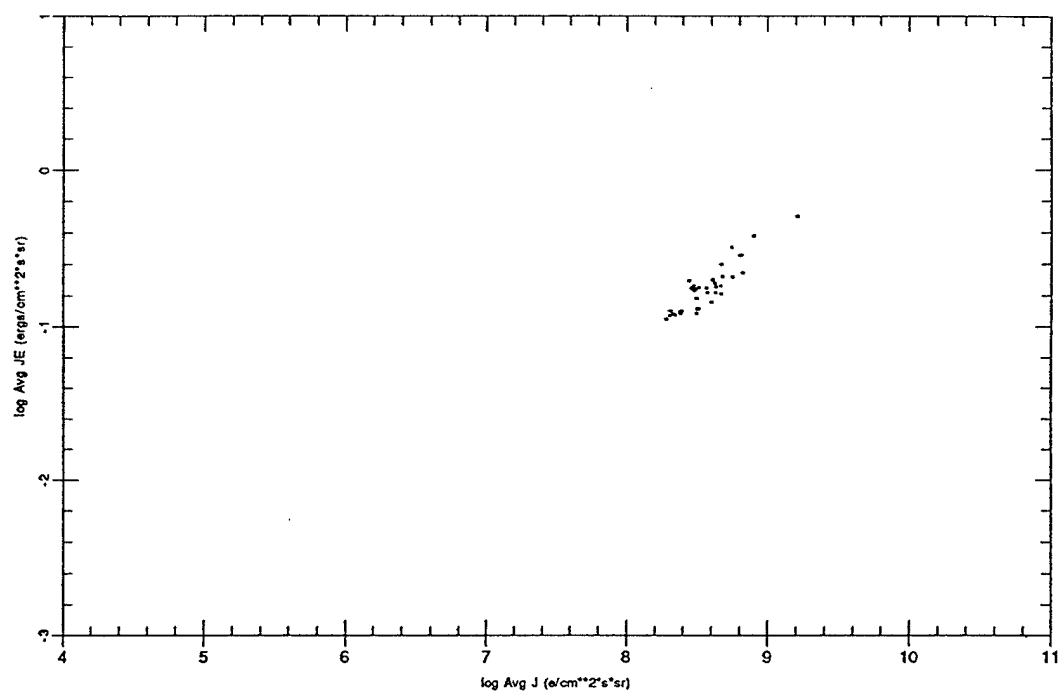
Threshold 0.0400 Peak Ch 8 Bz +
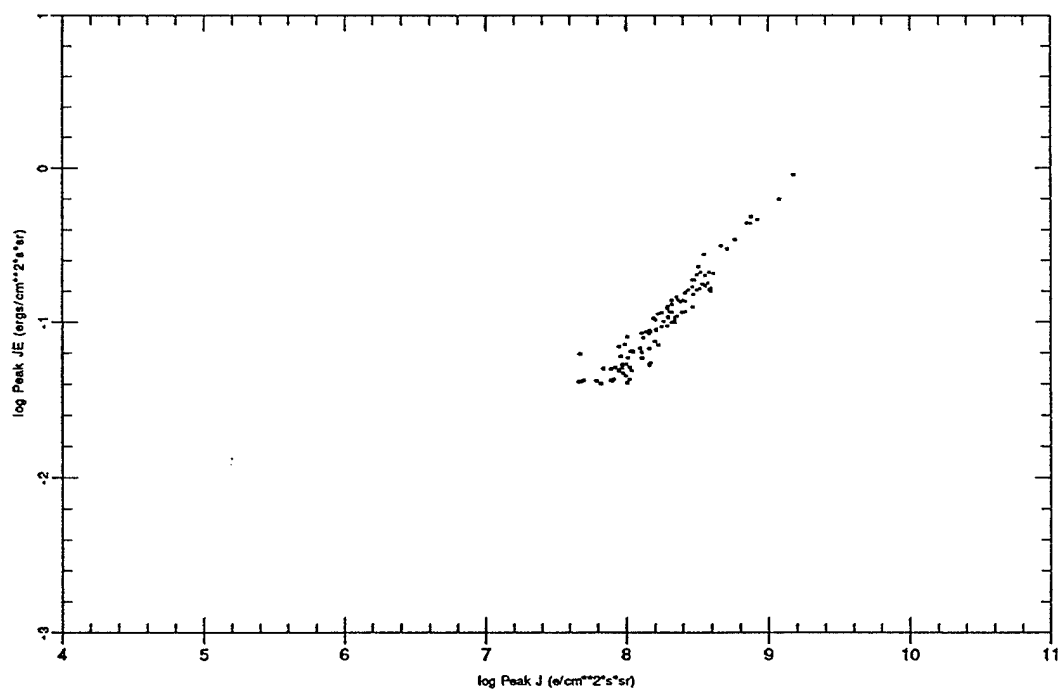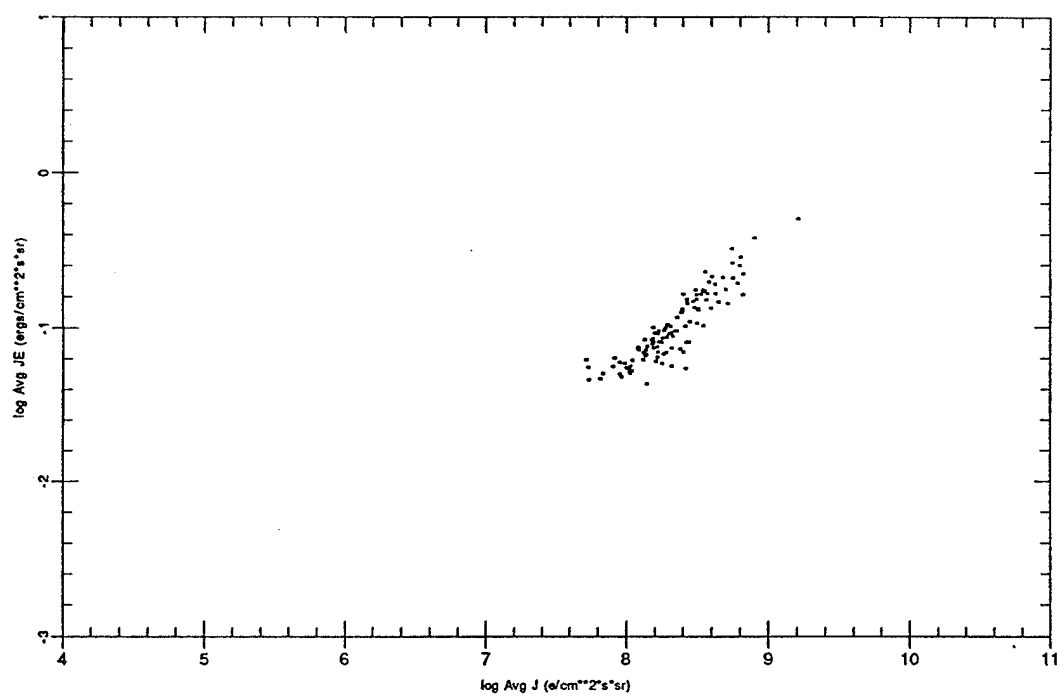
Threshold 0.0200 Peak Ch 8 Bz +
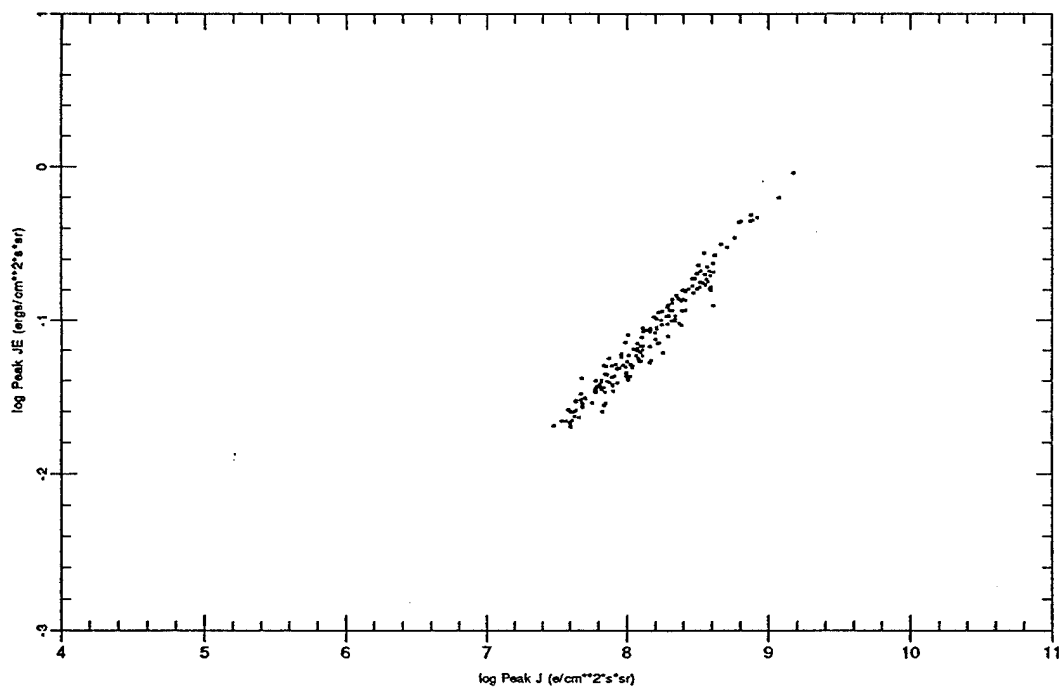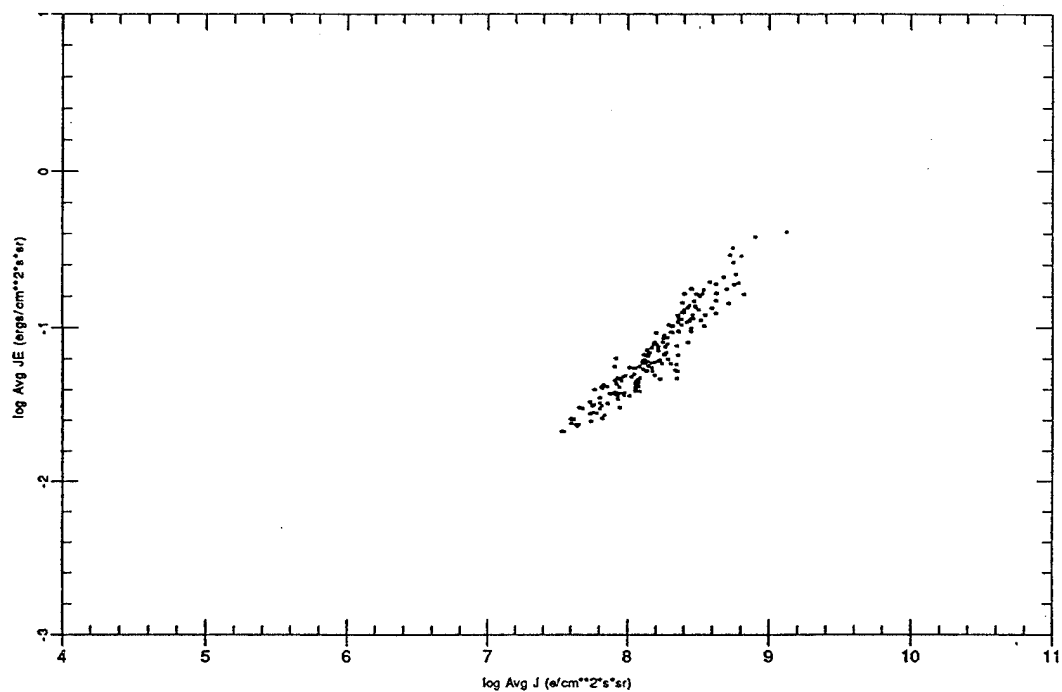
Threshold 0.0100 Peak Ch 8 Bz +
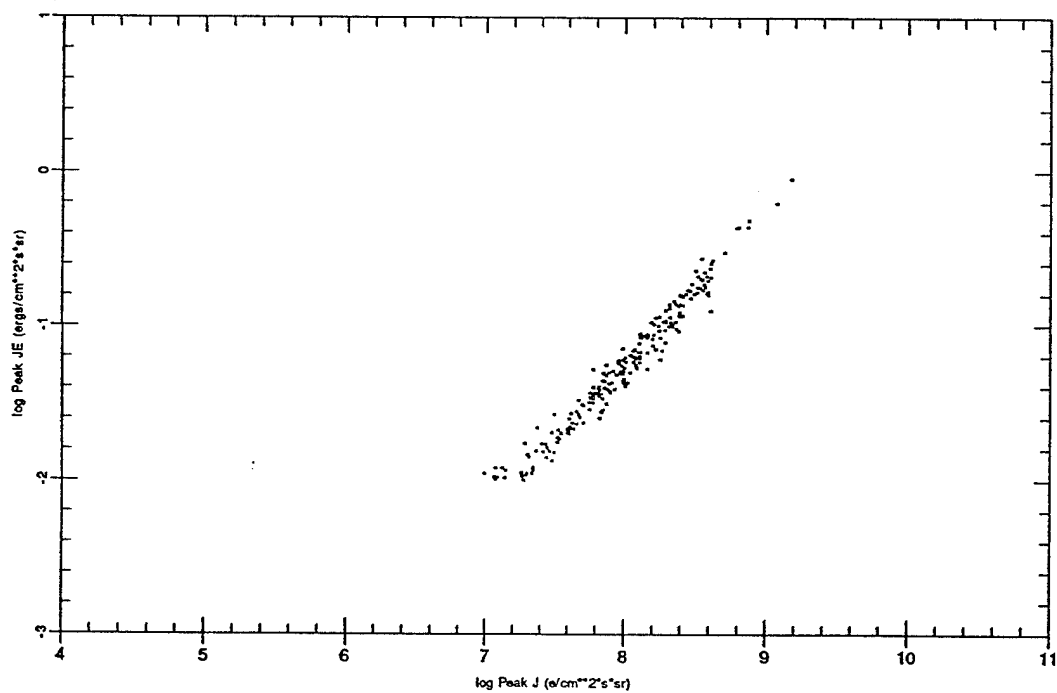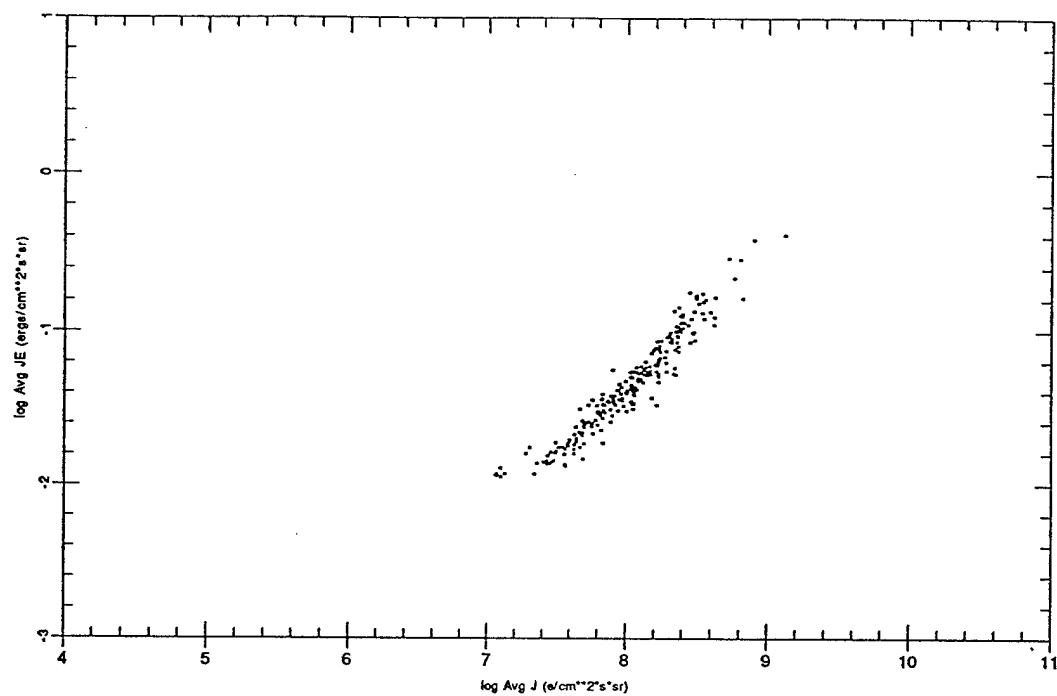
Threshold 0.0050 Peak Ch 8 Bz +

109

Threshold 0.0025 Peak Ch 8 Bz +

log Avg JE (ergs/cm**2*s*sr) vs log Avg J (e/cm**2*s*sr)

log Peak JE (ergs/cm**2*s*sr) vs log Peak J (e/cm**2*s*sr)
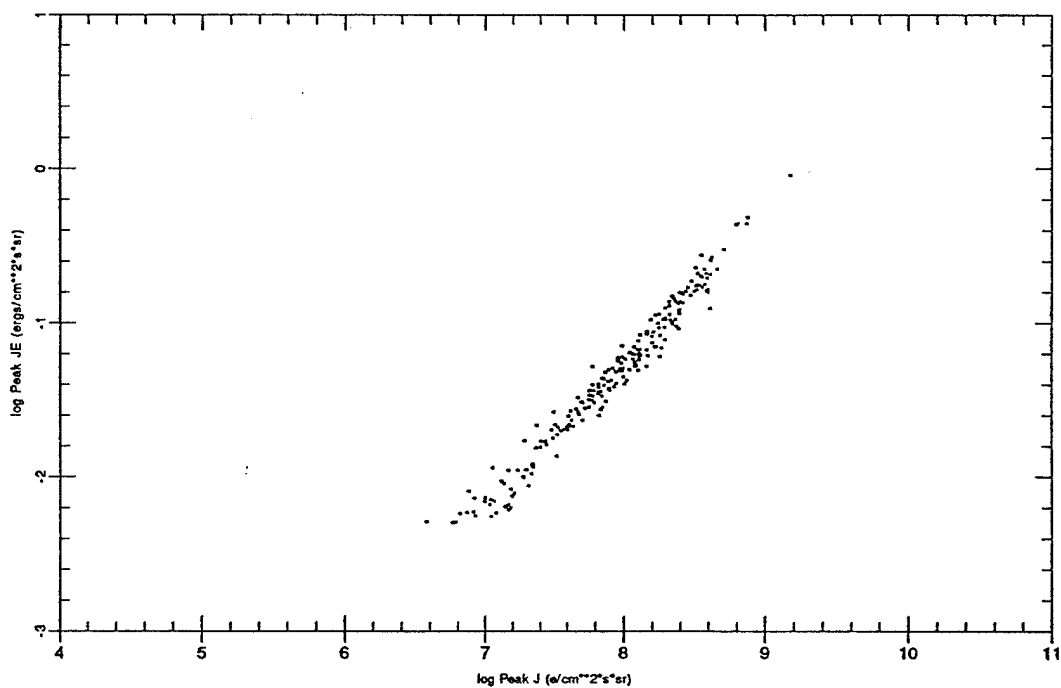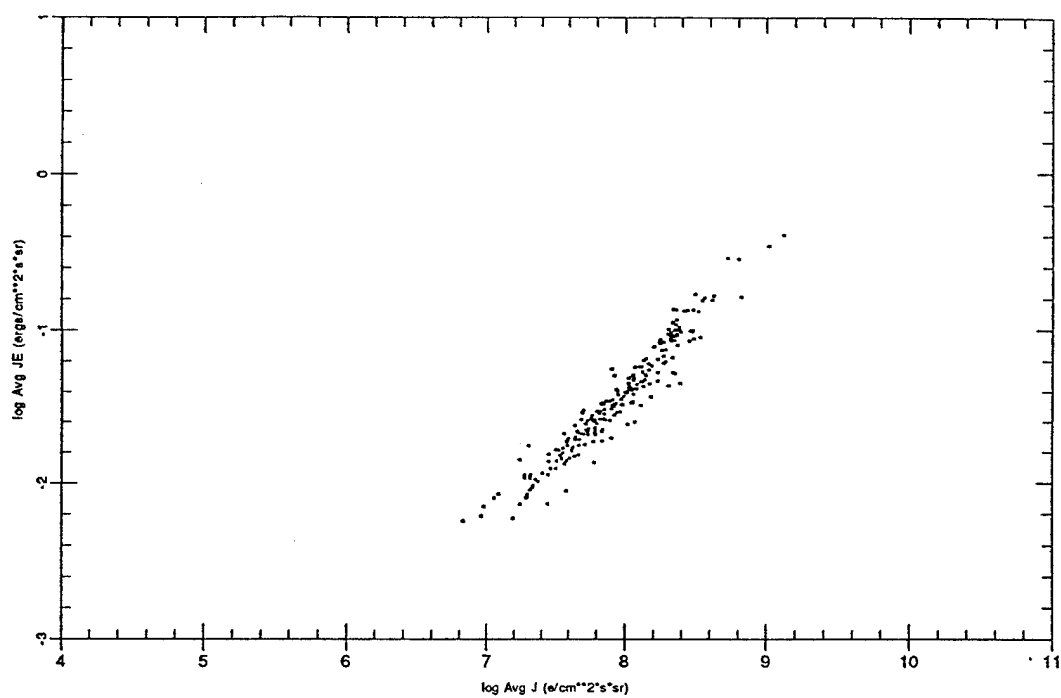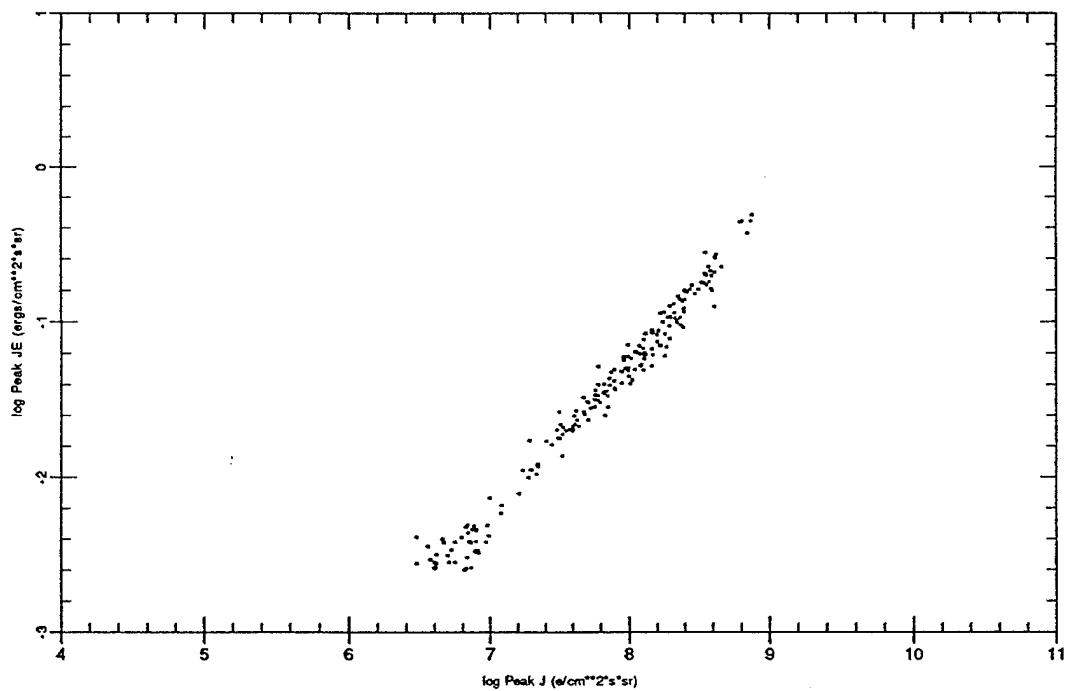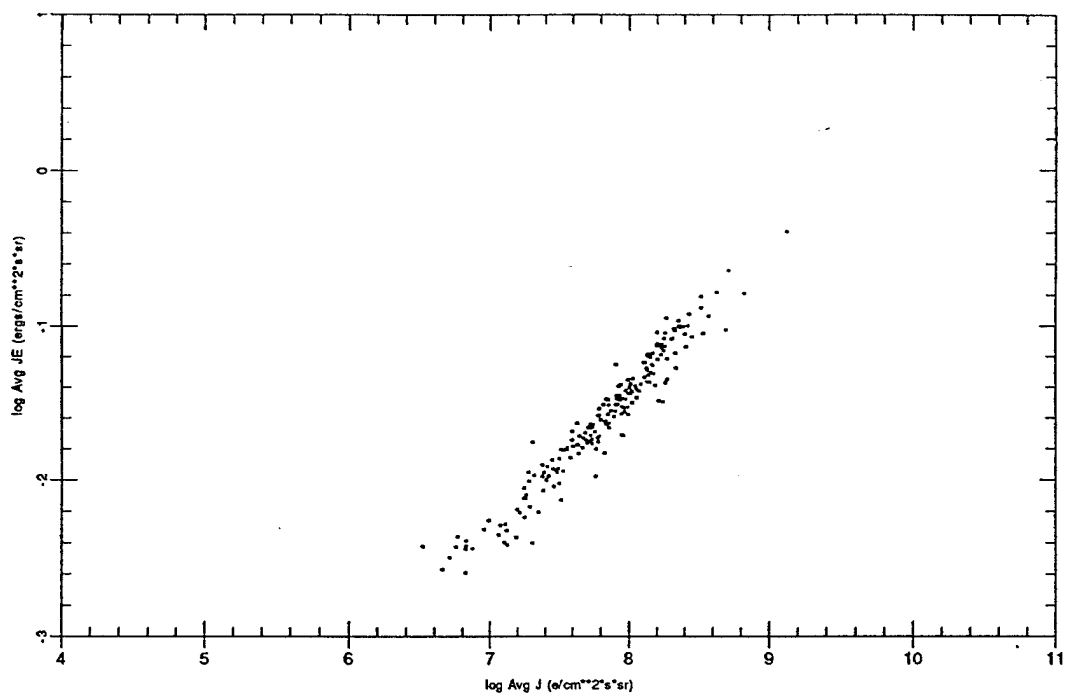
Threshold 0.1600 Peak Ch 7 Bz +
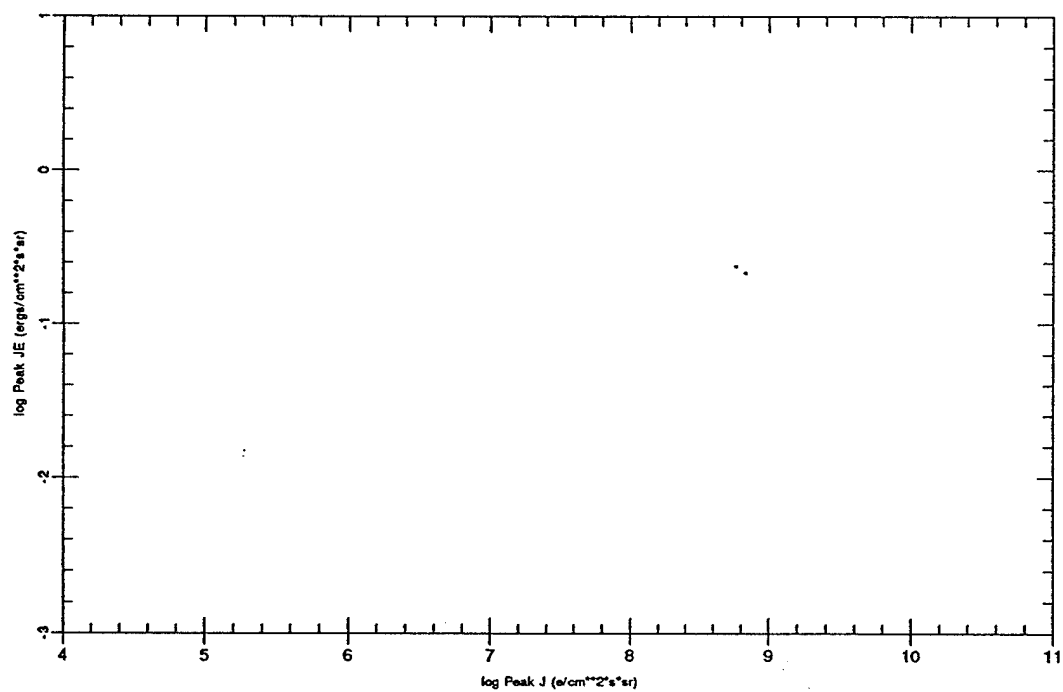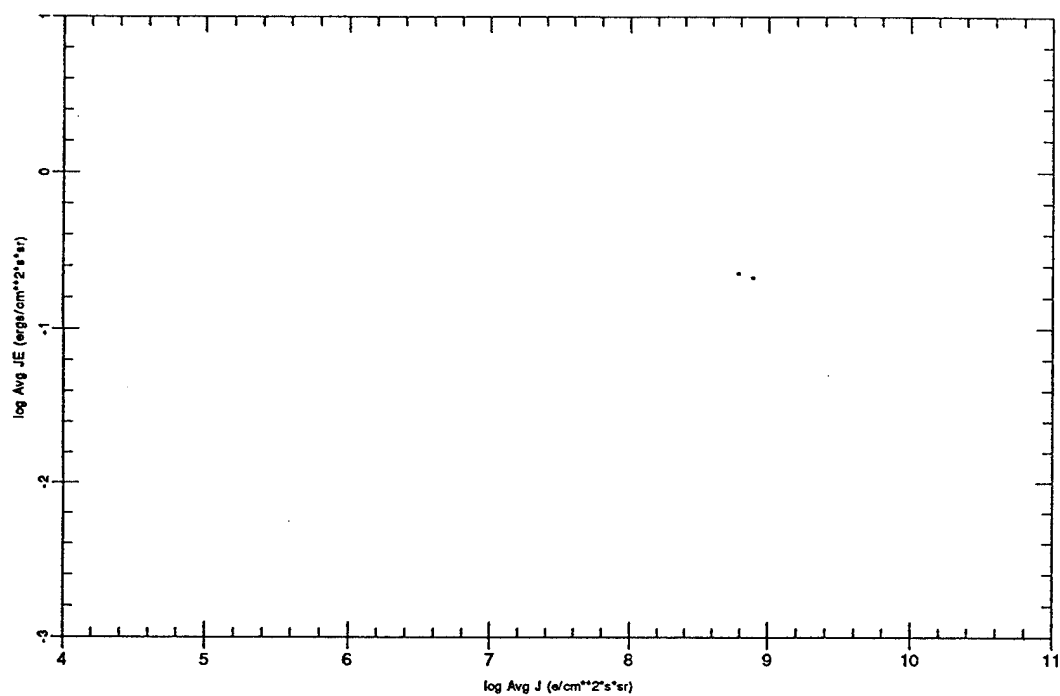
Threshold 0.0800 Peak Ch 7 Bz +
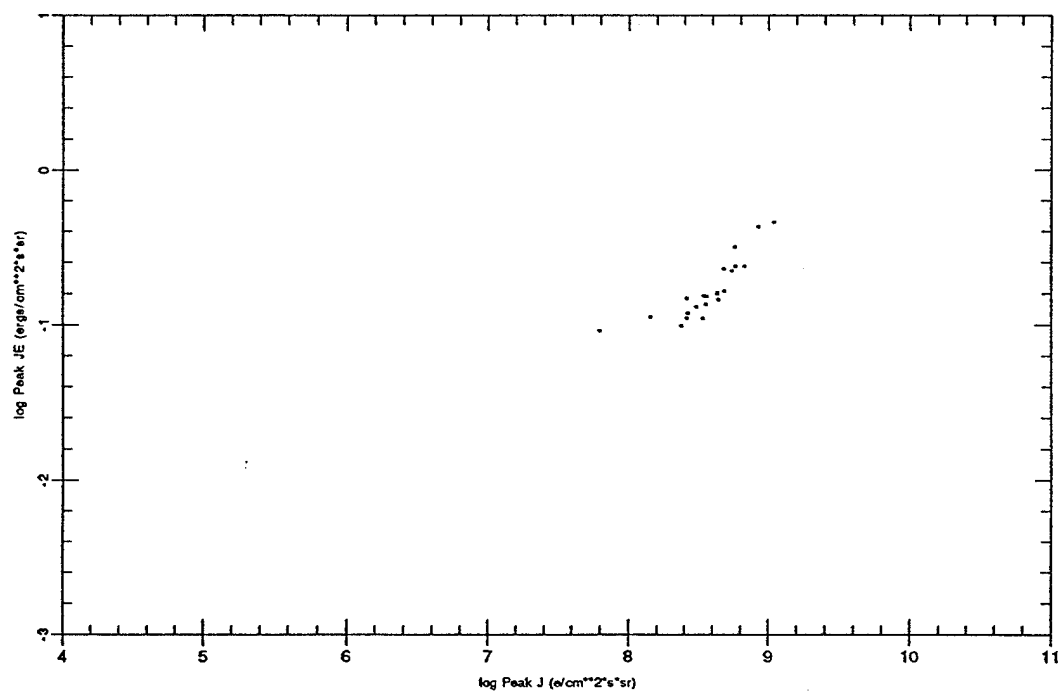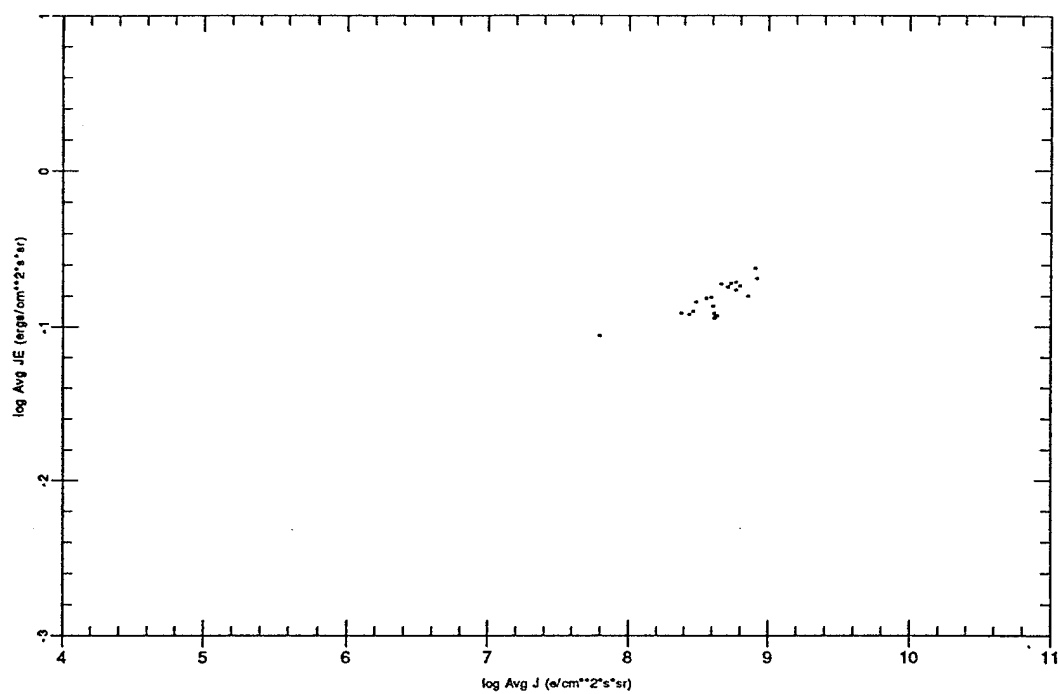
Threshold 0.0400 Peak Ch 7 Bz +
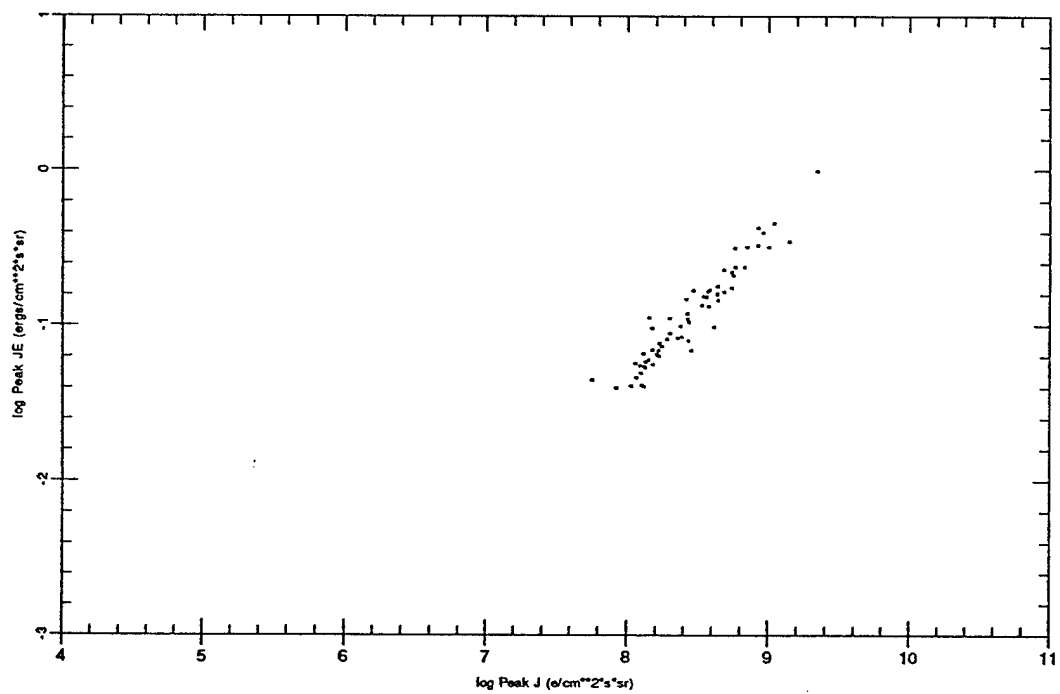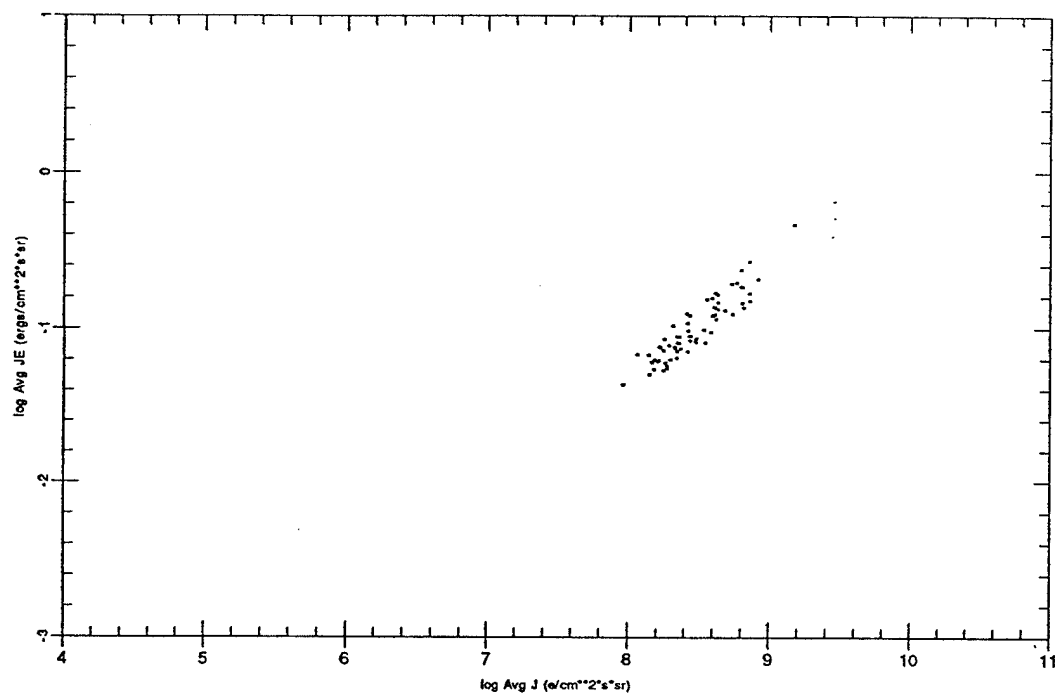
Threshold 0.0200 Peak Ch 7 Bz +
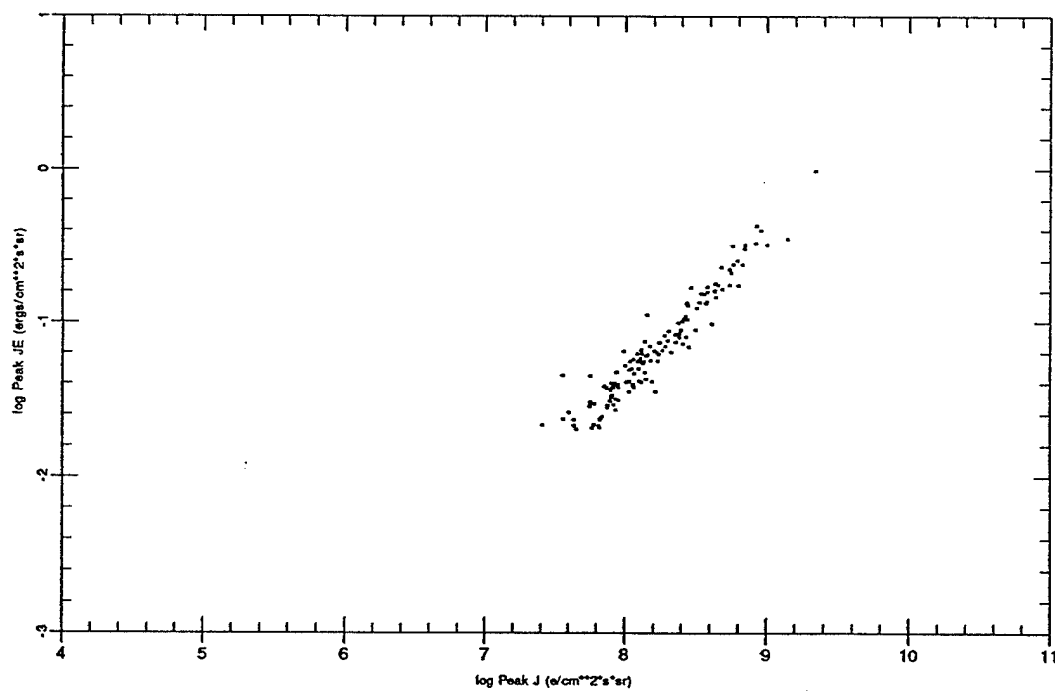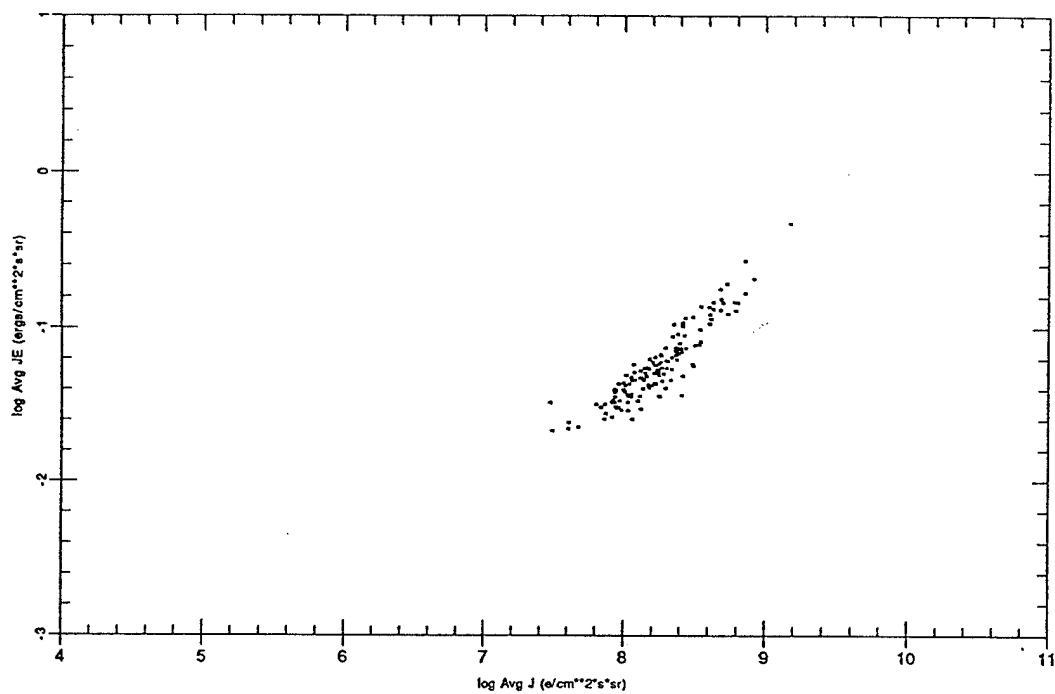
Threshold 0.0100 Peak Ch 7 Bz +
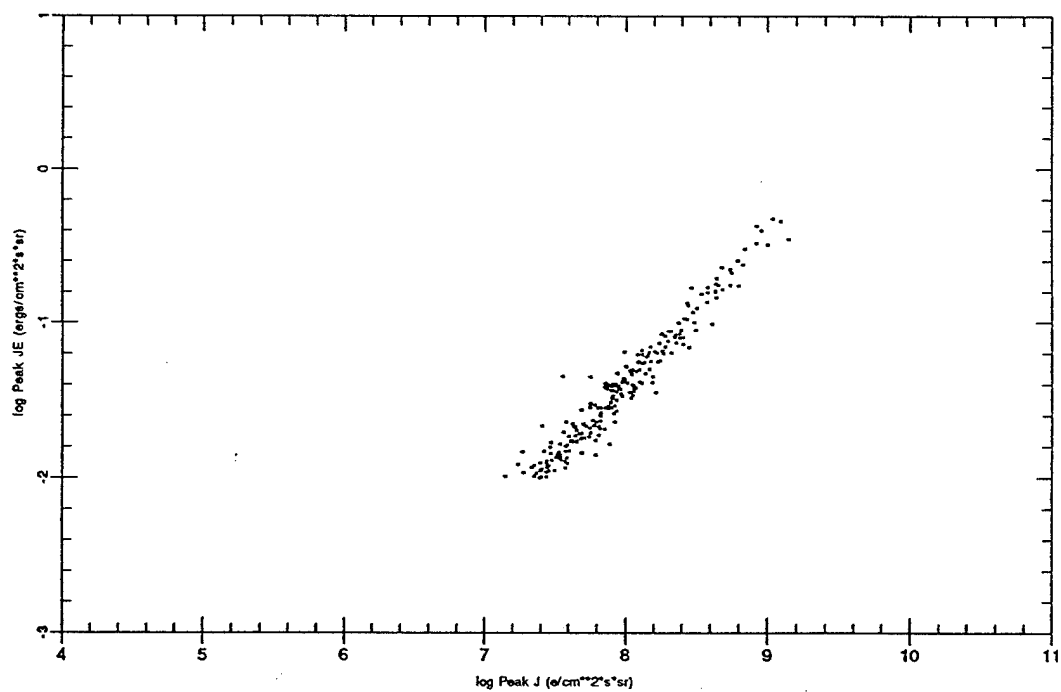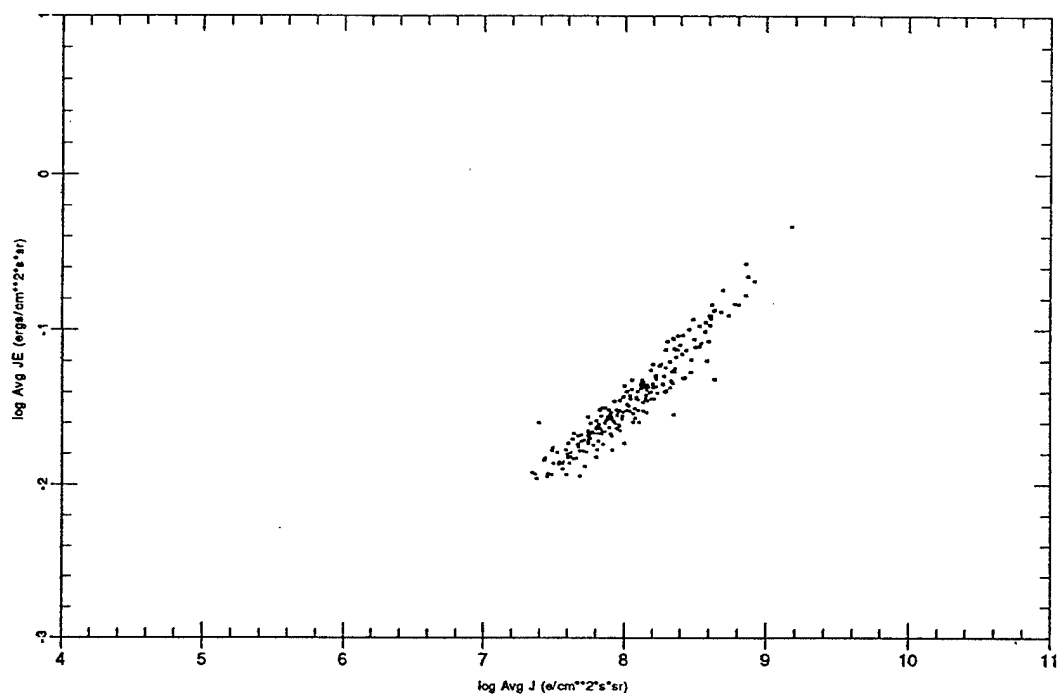
Threshold 0.0050 Peak Ch 7 Bz +
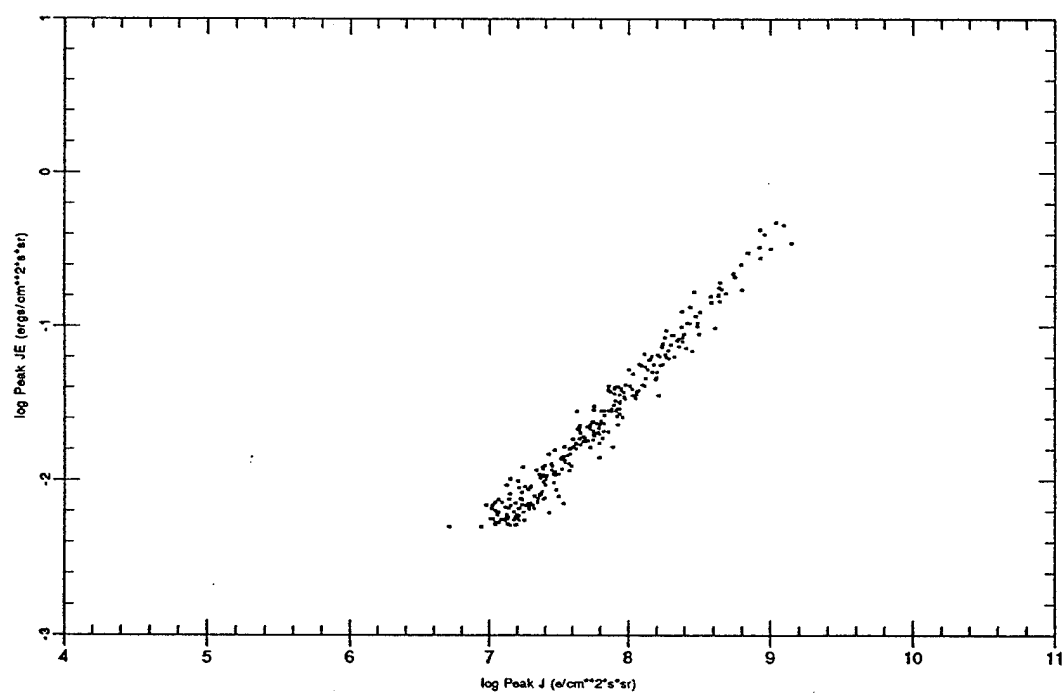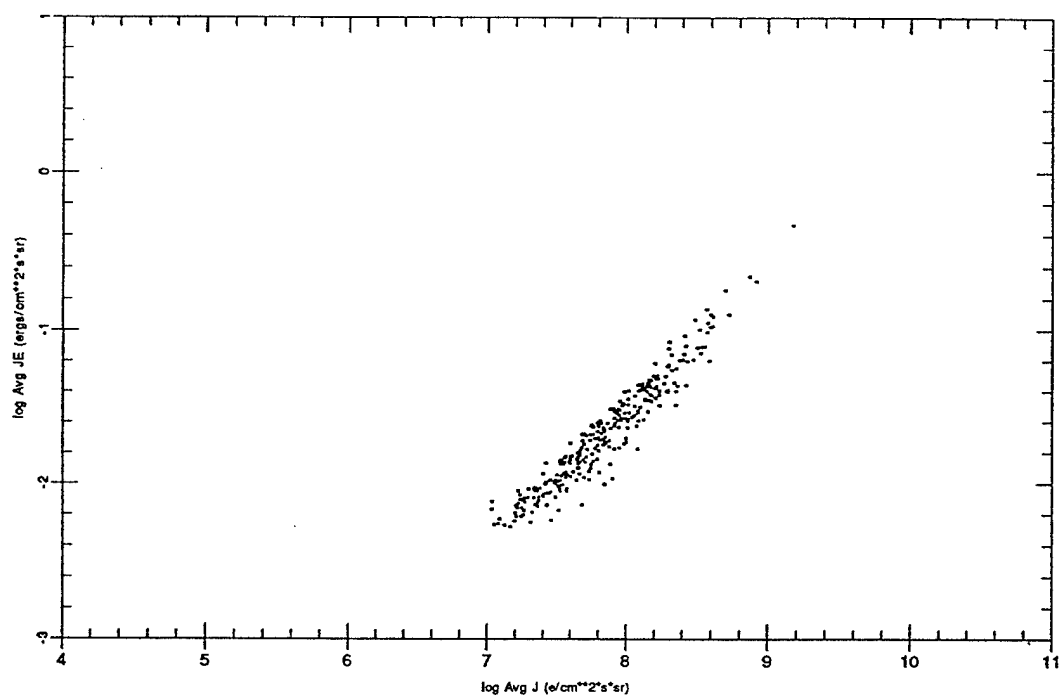
Threshold 0.0025 Peak Ch 7 Bz +
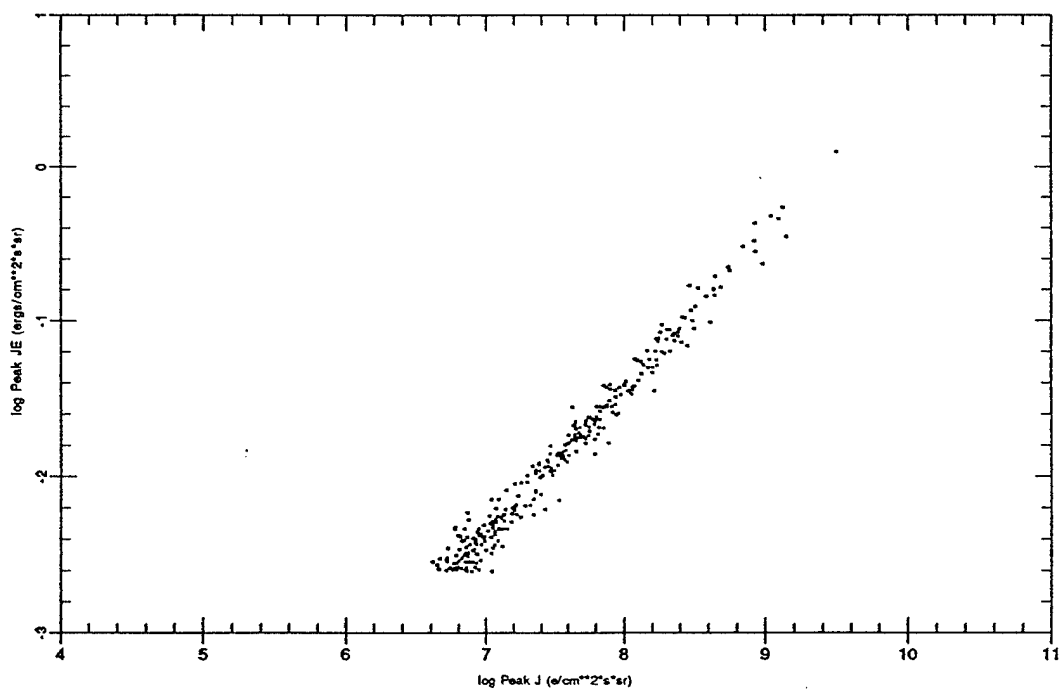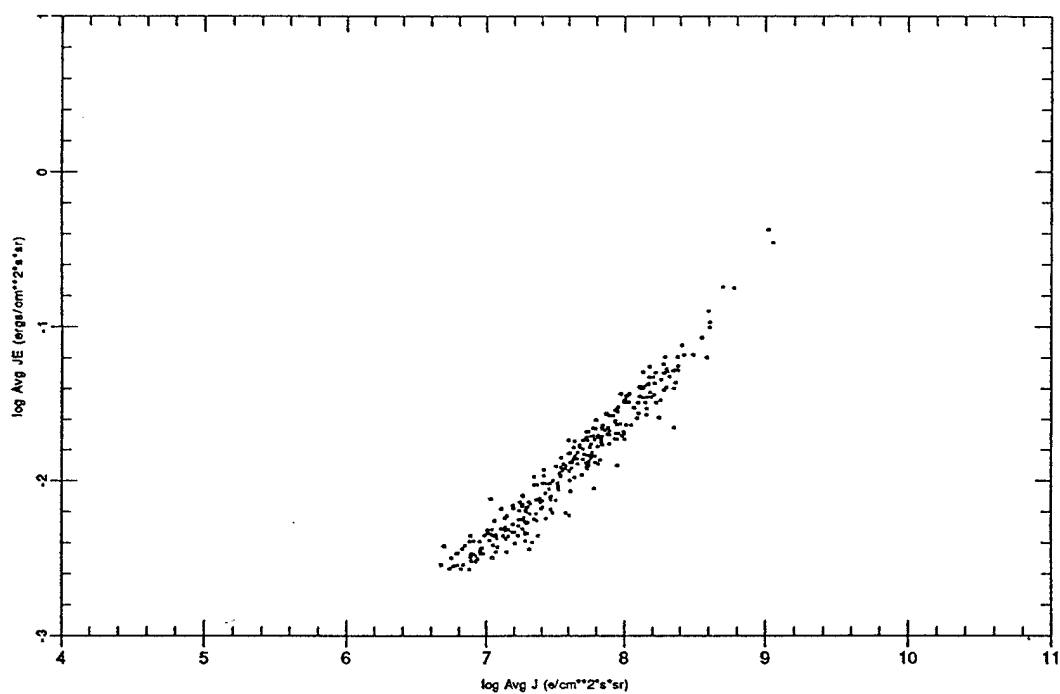
Threshold 0.0800 Peak Ch 6 Bz +
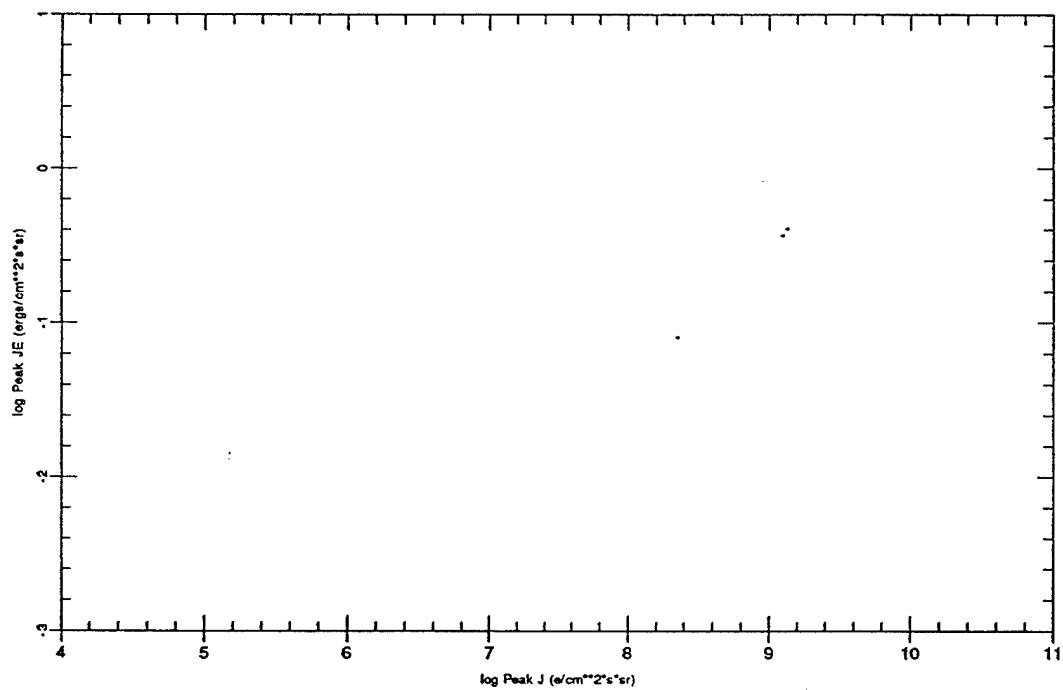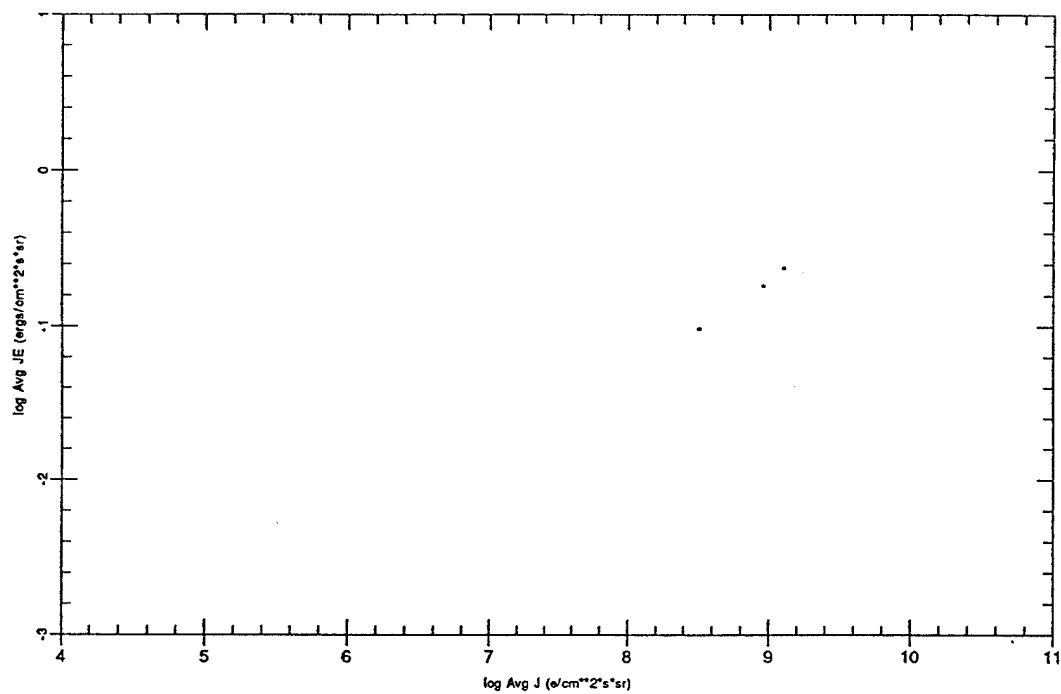
Threshold 0.0400 Peak Ch 6 Bz +
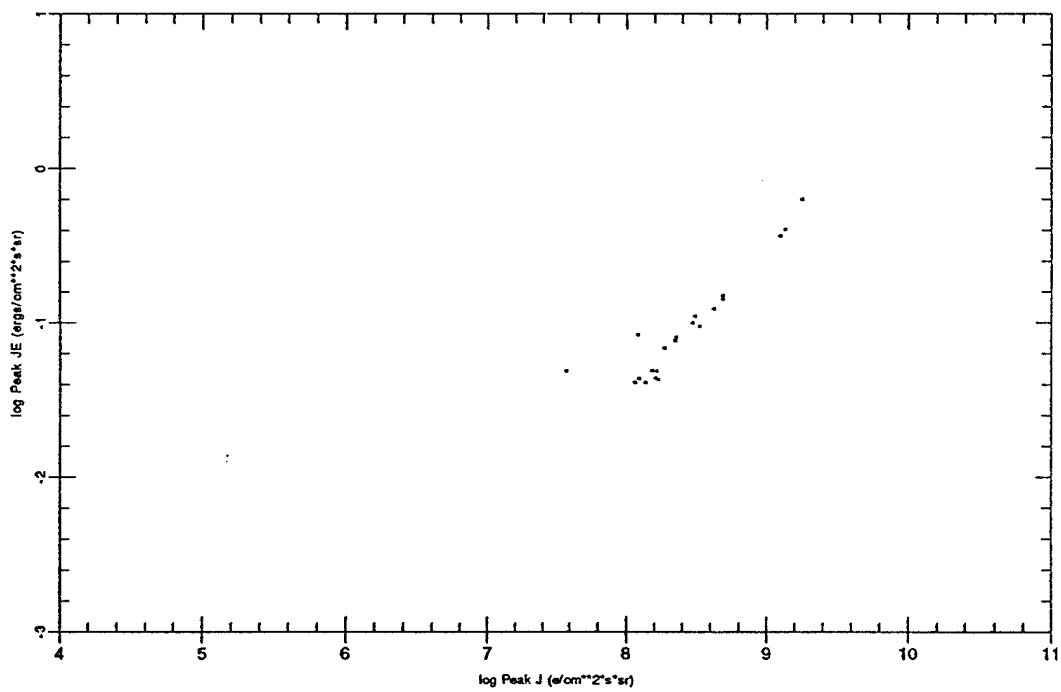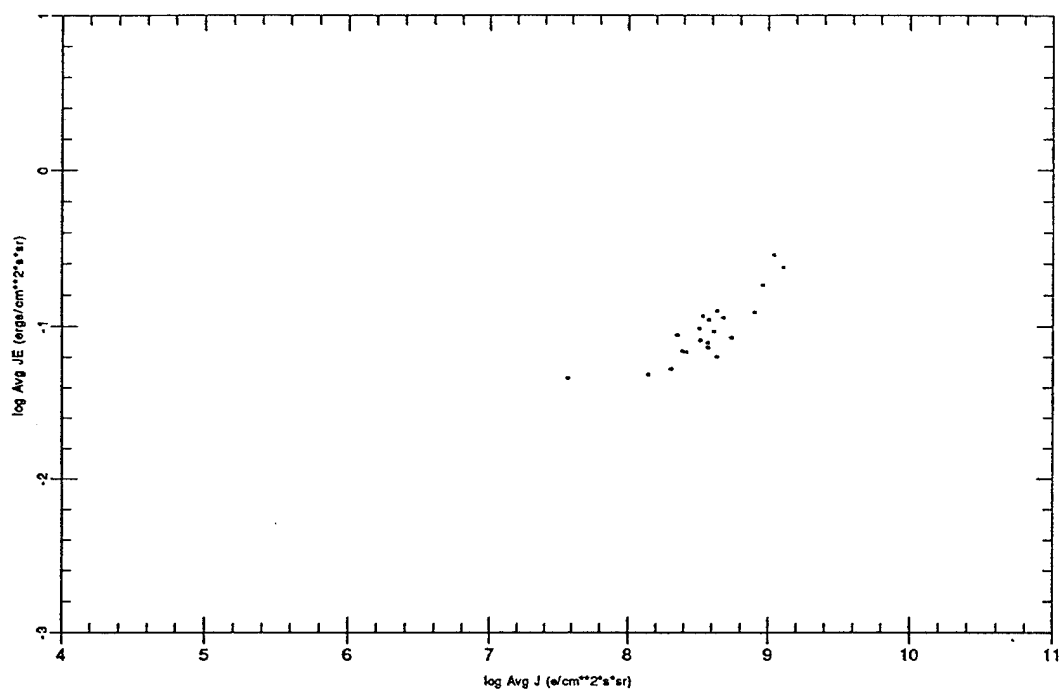
Threshold 0.0200 Peak Ch 6 Bz +
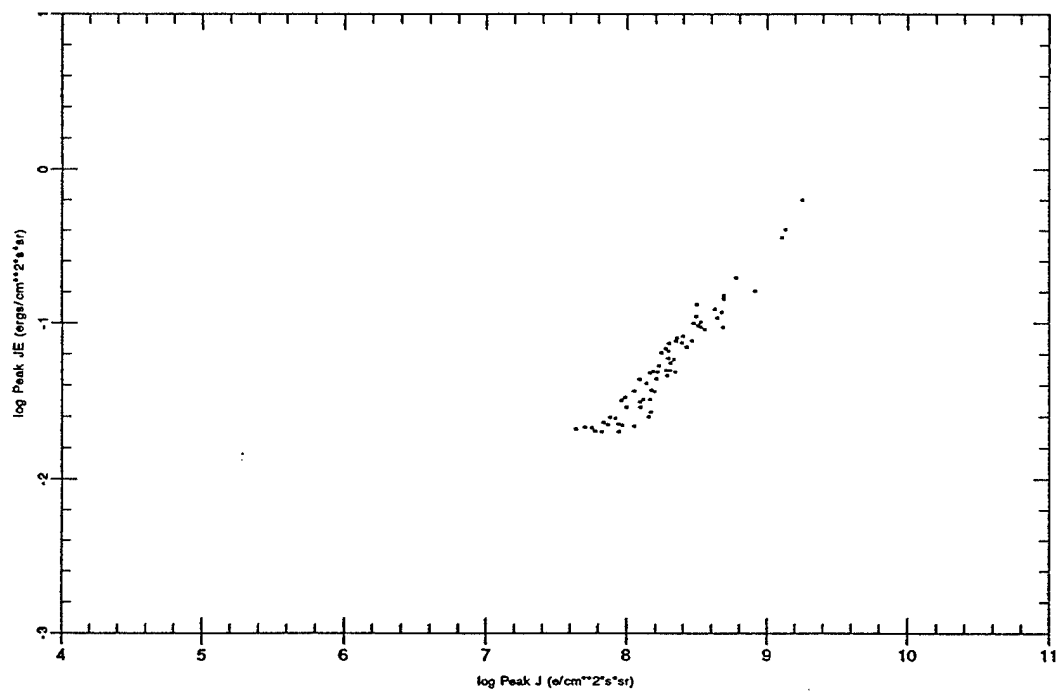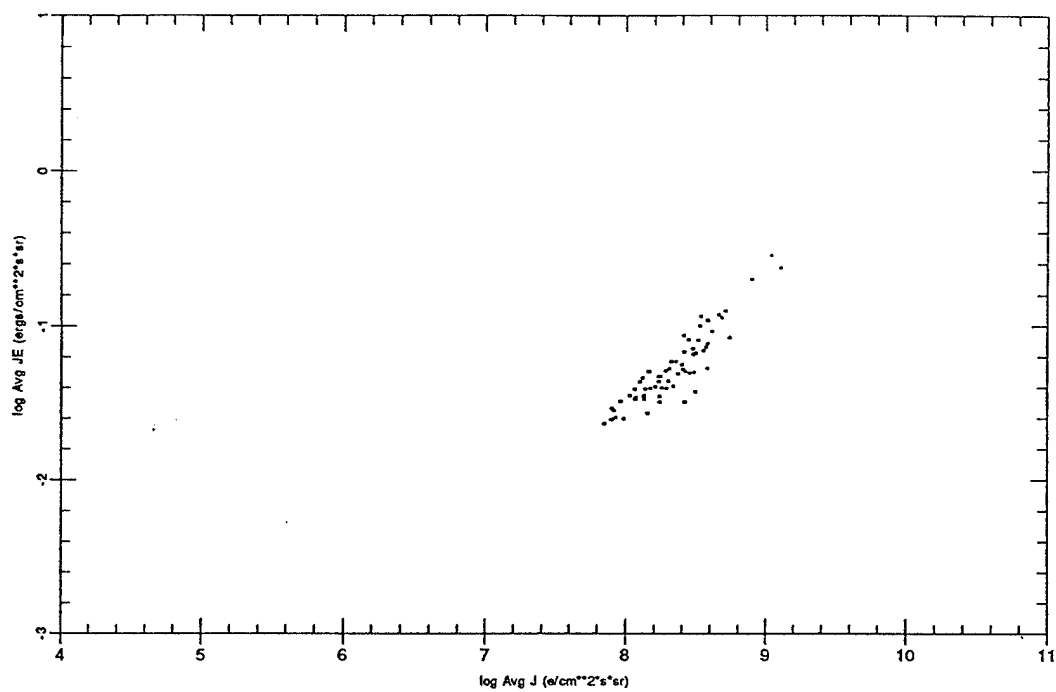
Threshold 0.0100 Peak Ch 6 Bz +
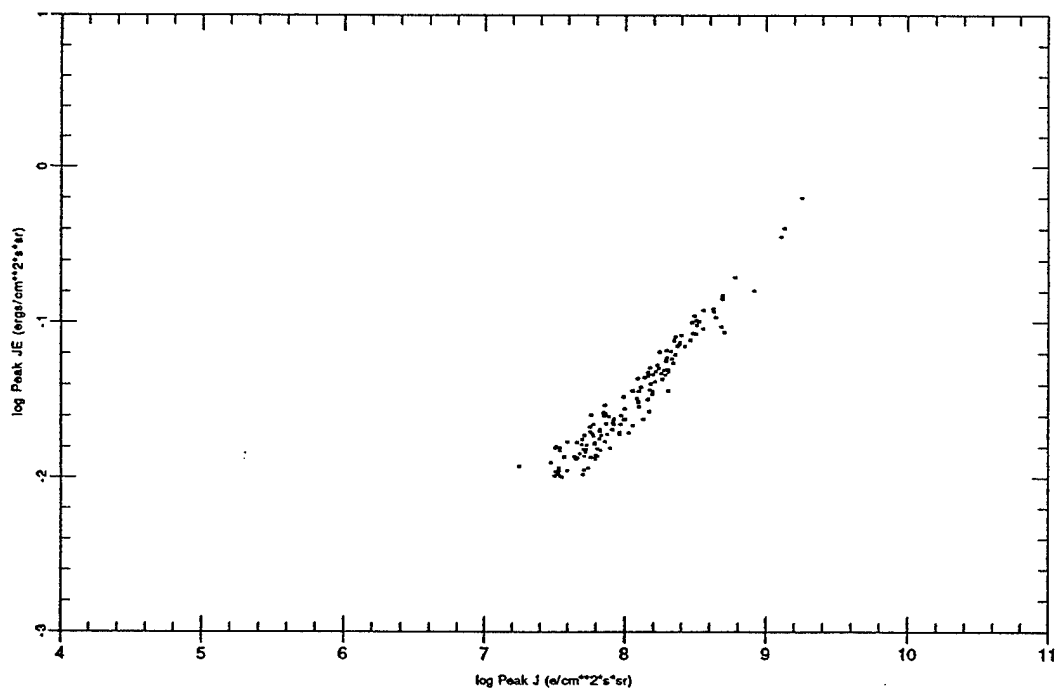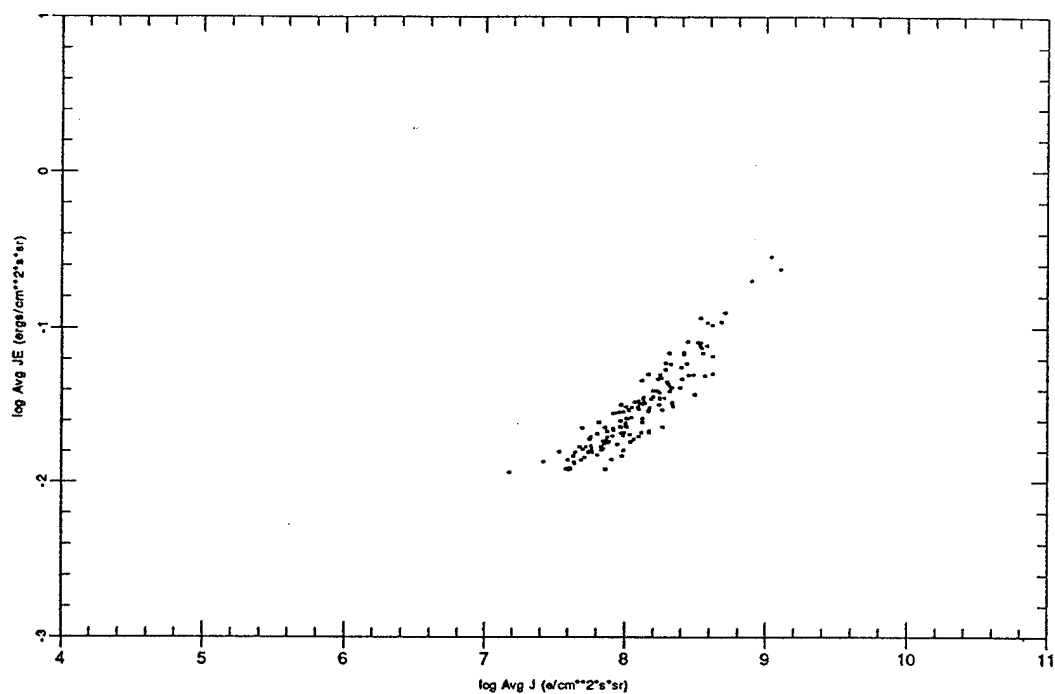
Threshold 0.0025 Peak Ch 6 Bz +
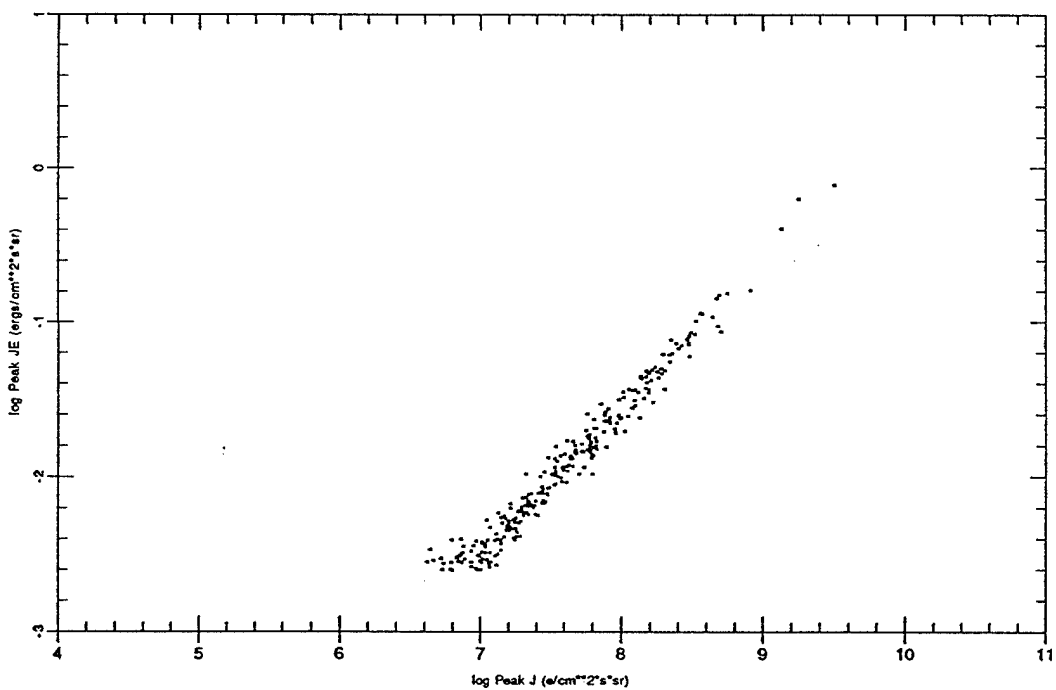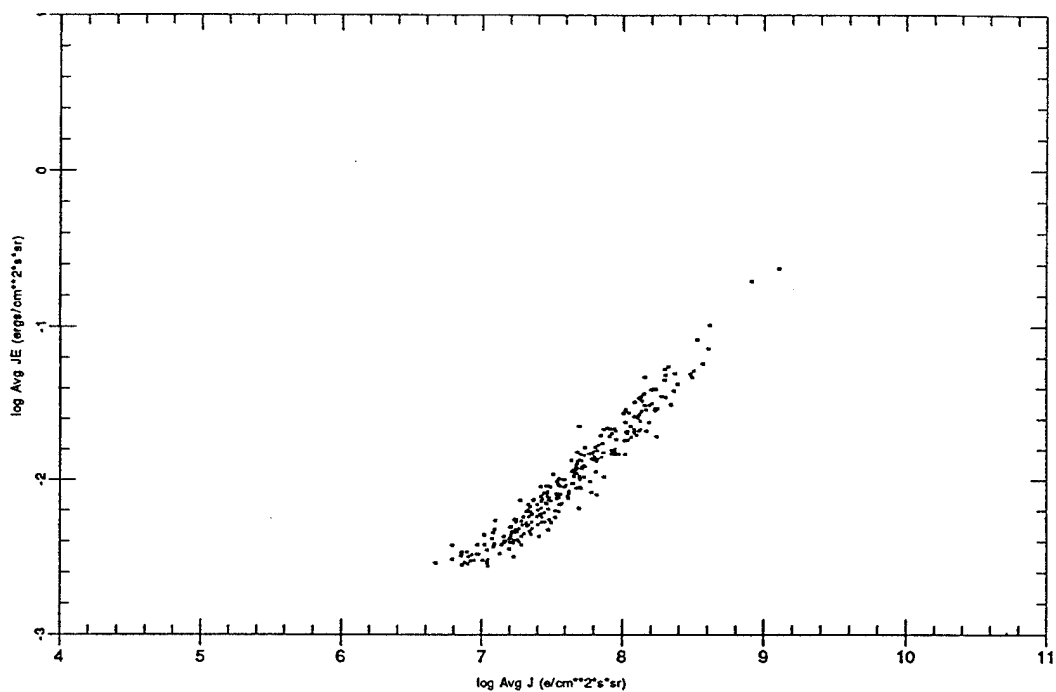
Threshold 0.0050 Peak Ch 6 Bz +

Threshold 0.0400 Peak Ch 5 Bz +

log Avg JE (ergs/cm**2*s*sr) vs log Avg J (e/cm**2*s*sr)

log Peak JE (ergs/cm**2*s*sr) vs log Peak J (e/cm**2*s*sr)

Threshold 0.0200 Peak Ch 5 Bz +

log Avg JE (erga/cm**2*s*sr)

log Avg J (e/cm**2*s*sr)

log Peak JE (erga/cm**2*s*sr)

log Peak J (e/cm**2*s*sr)
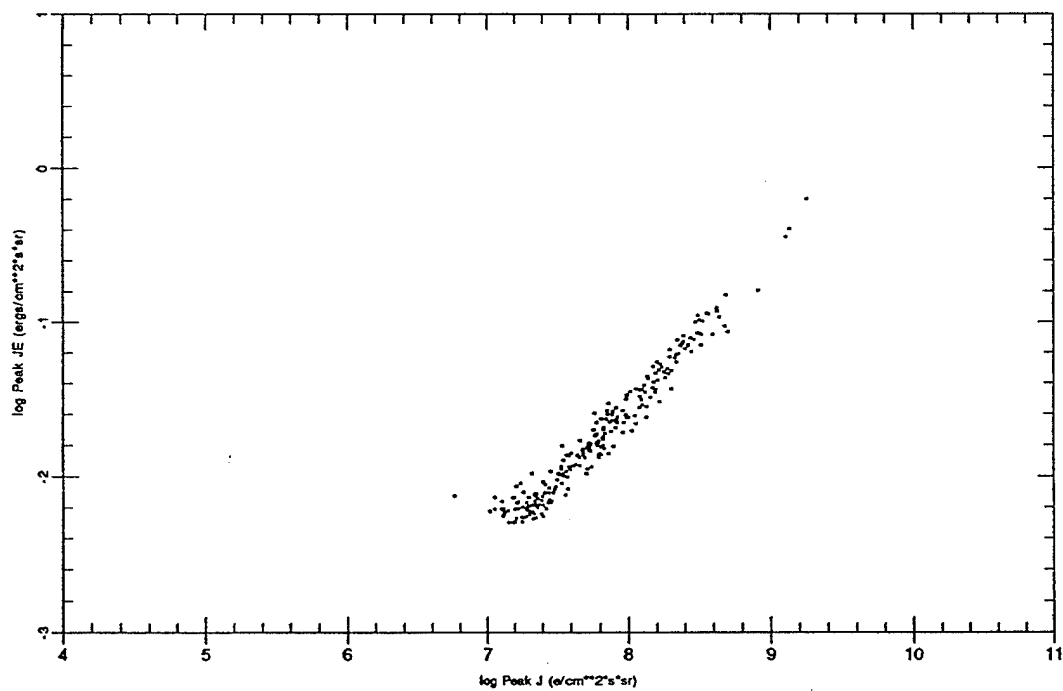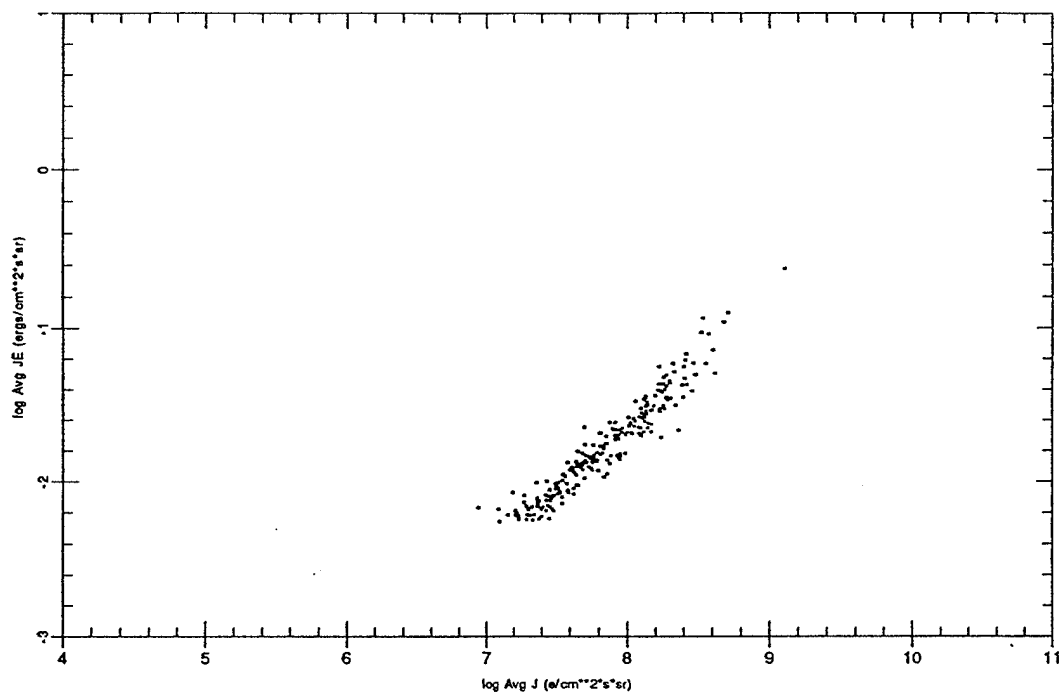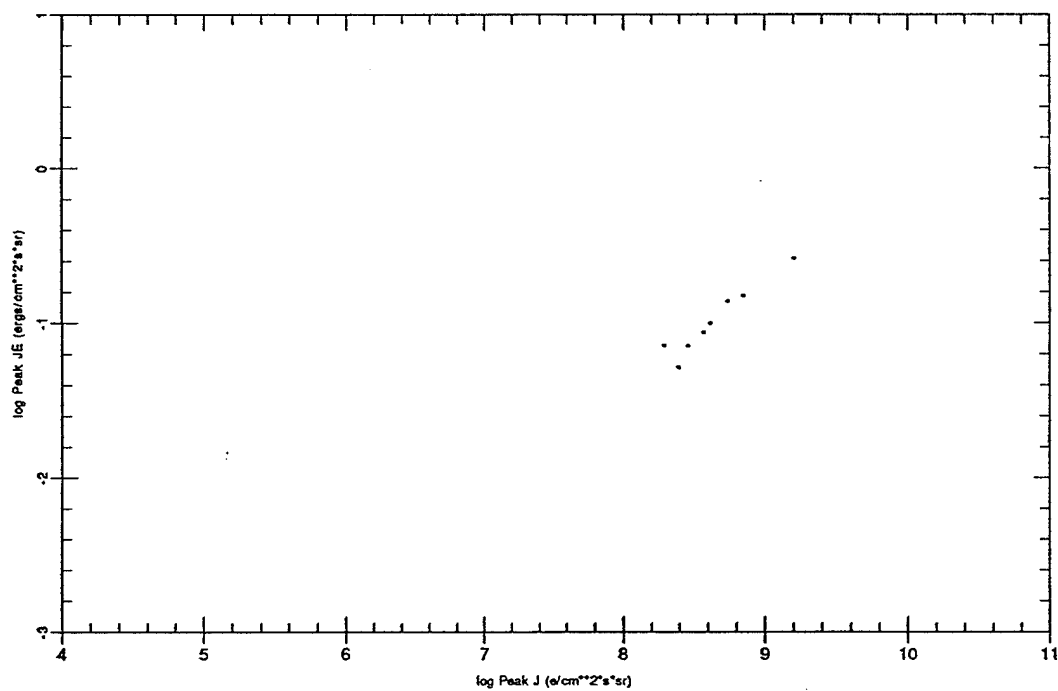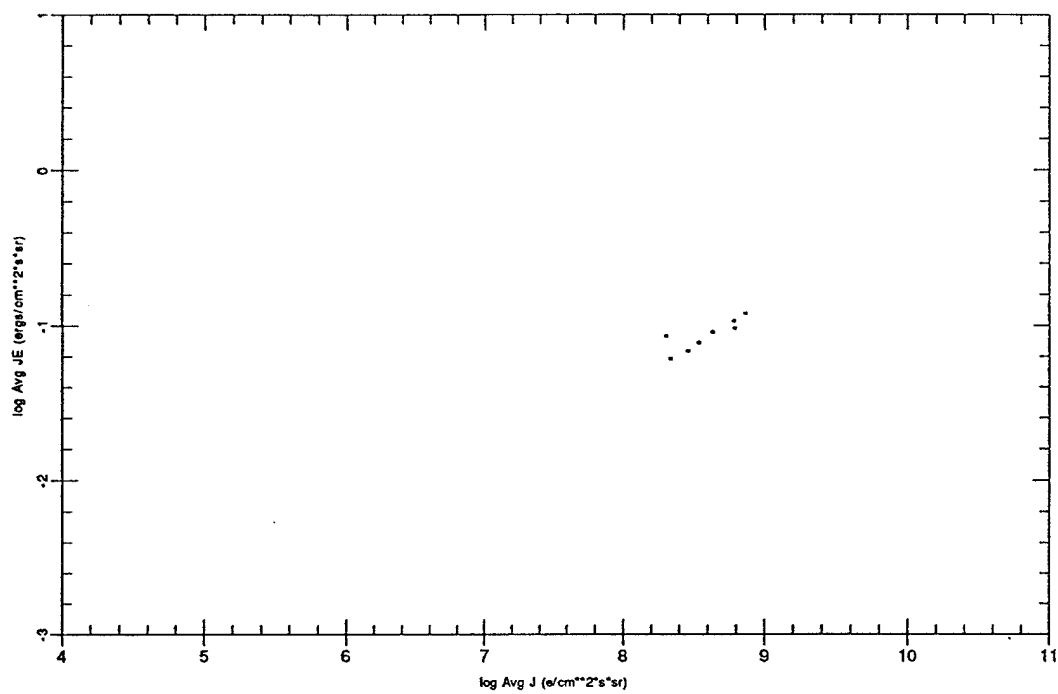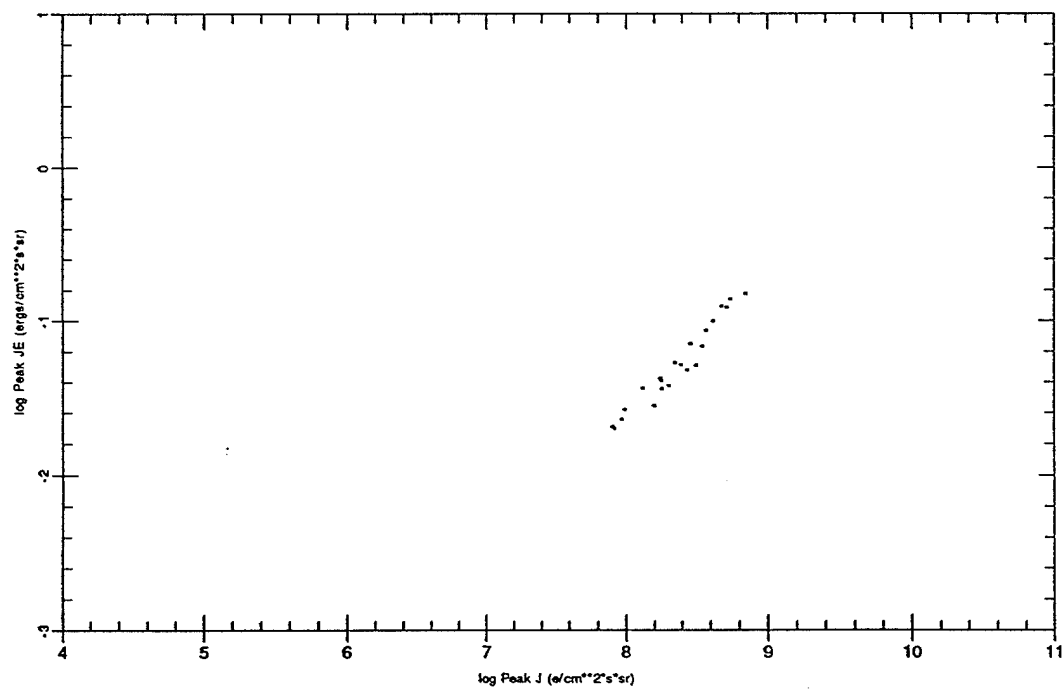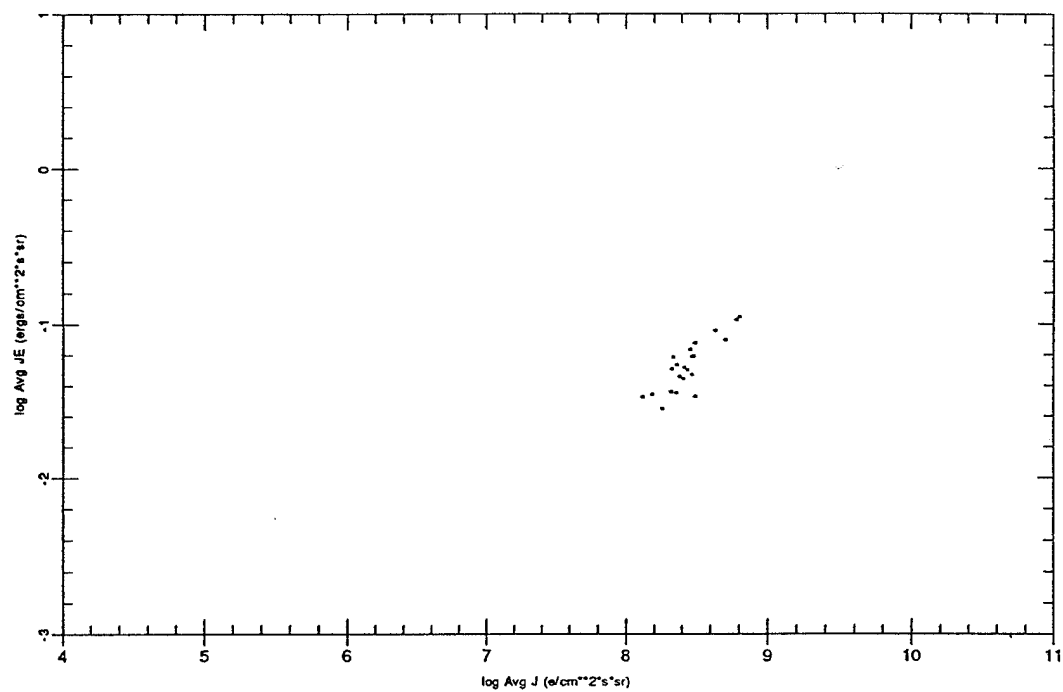
Threshold 0.0100 Peak Ch 5 Bz +
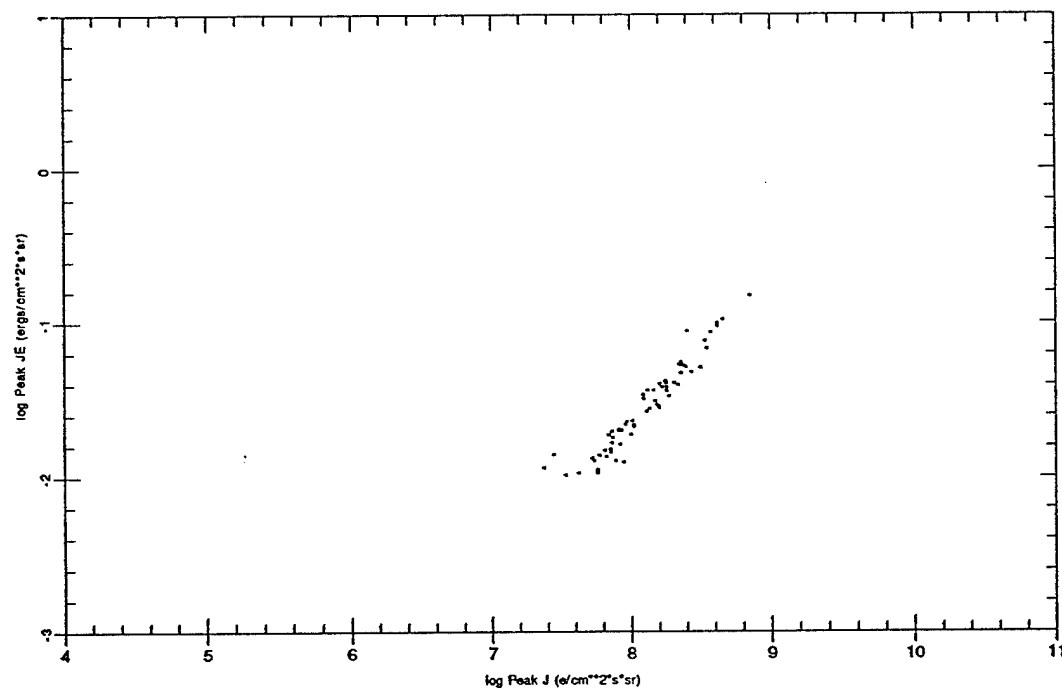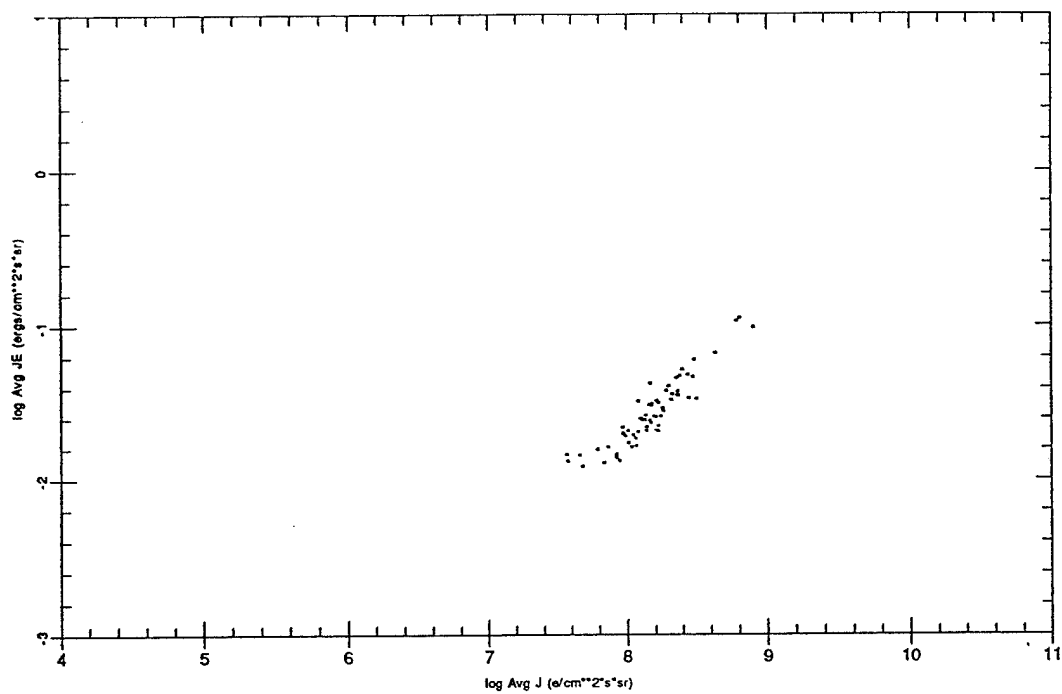
Threshold 0.0050 Peak Ch 5 Bz +
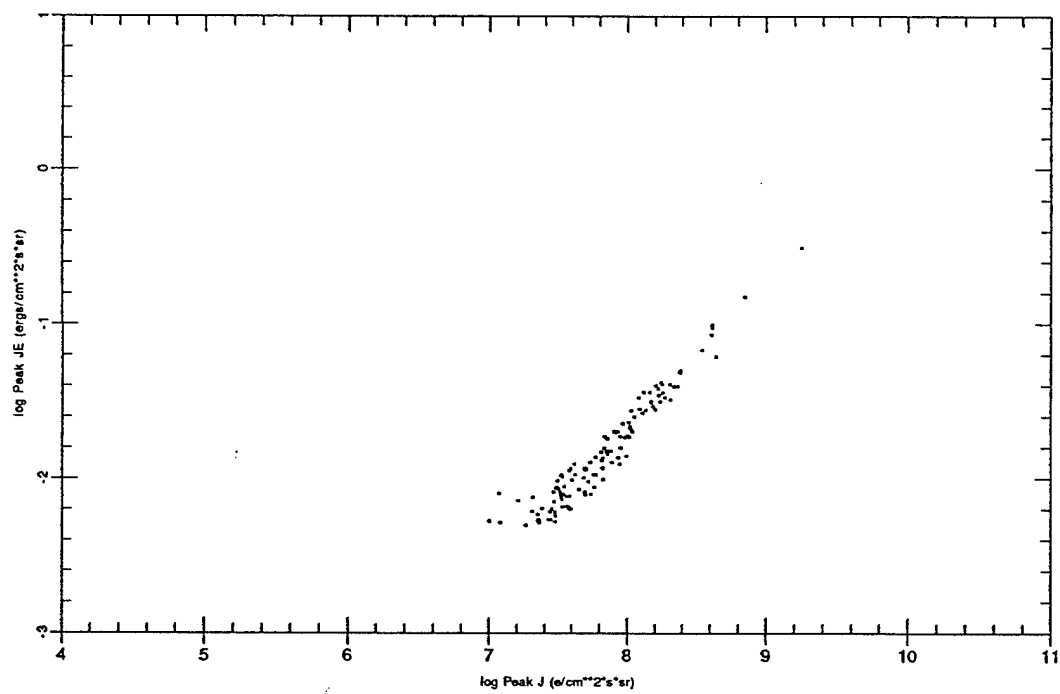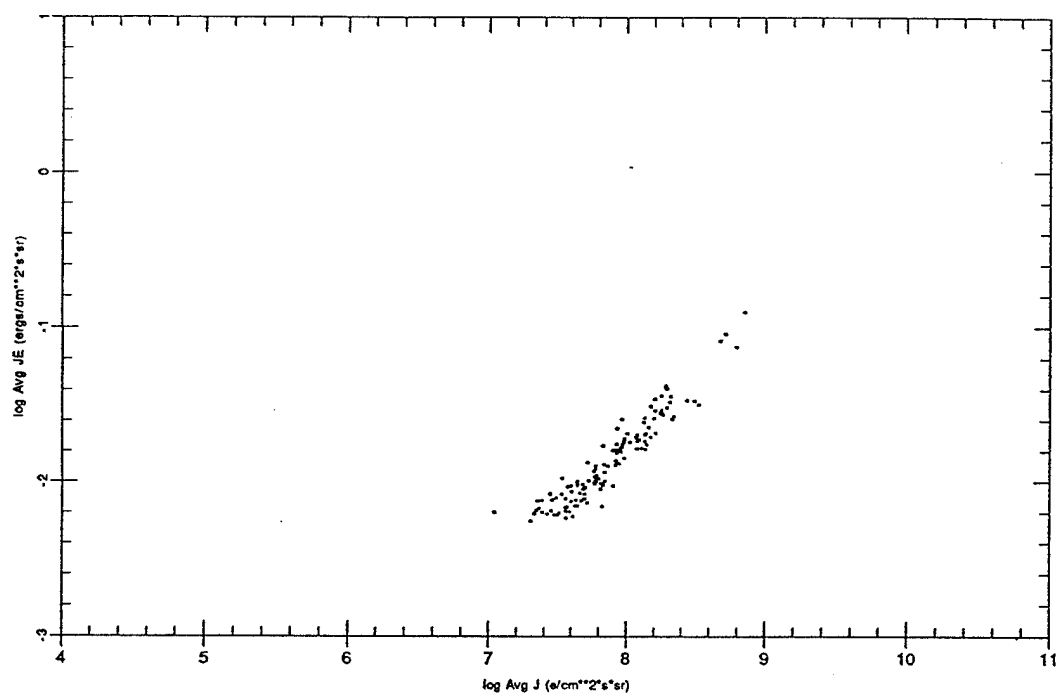
Threshold 0.0025 Peak Ch 5 Bz +
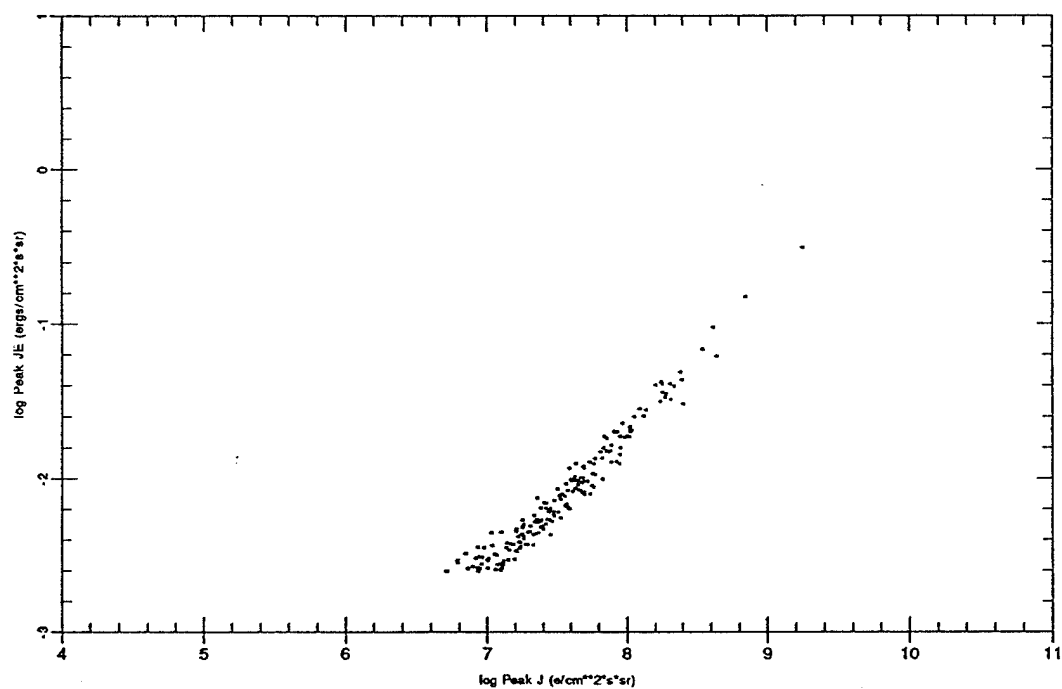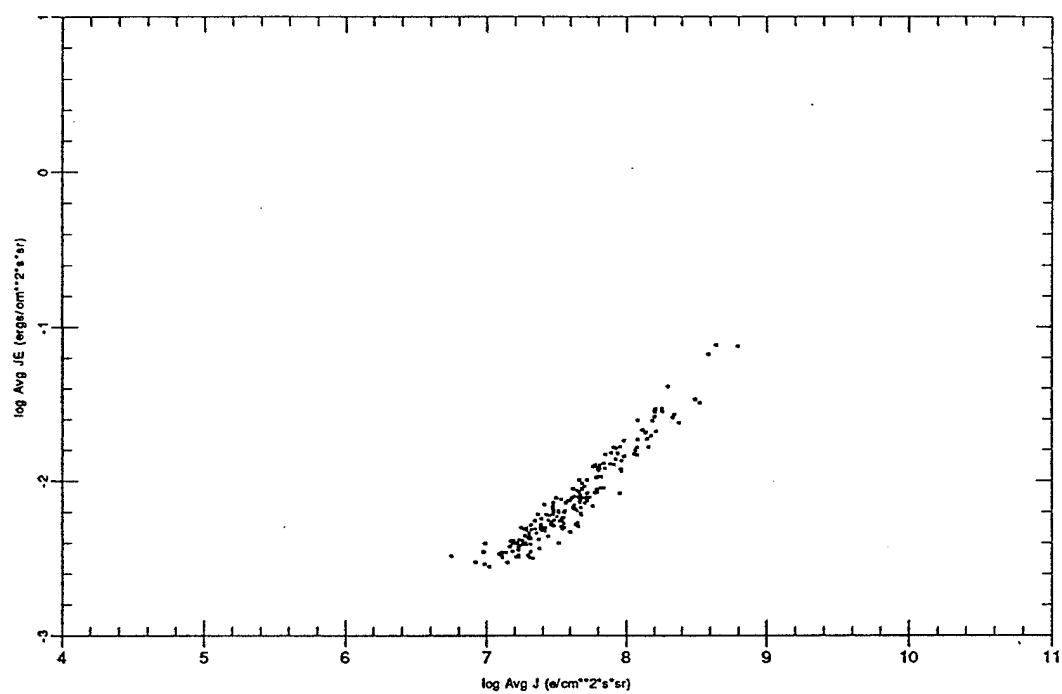
Threshold 0.0200 Peak Ch 4 Bz +
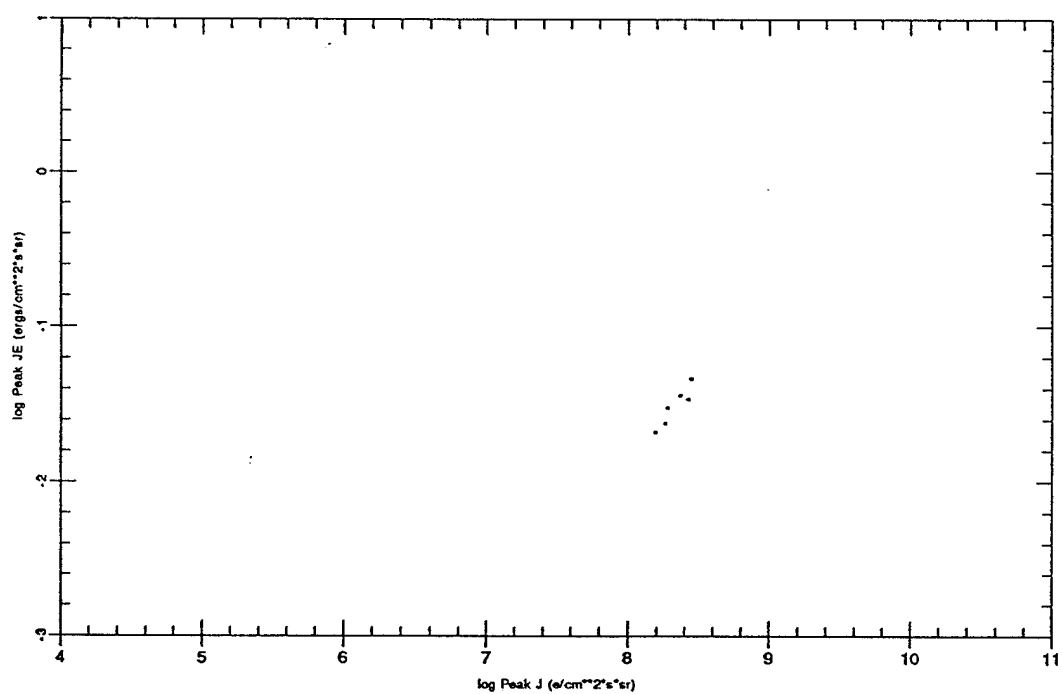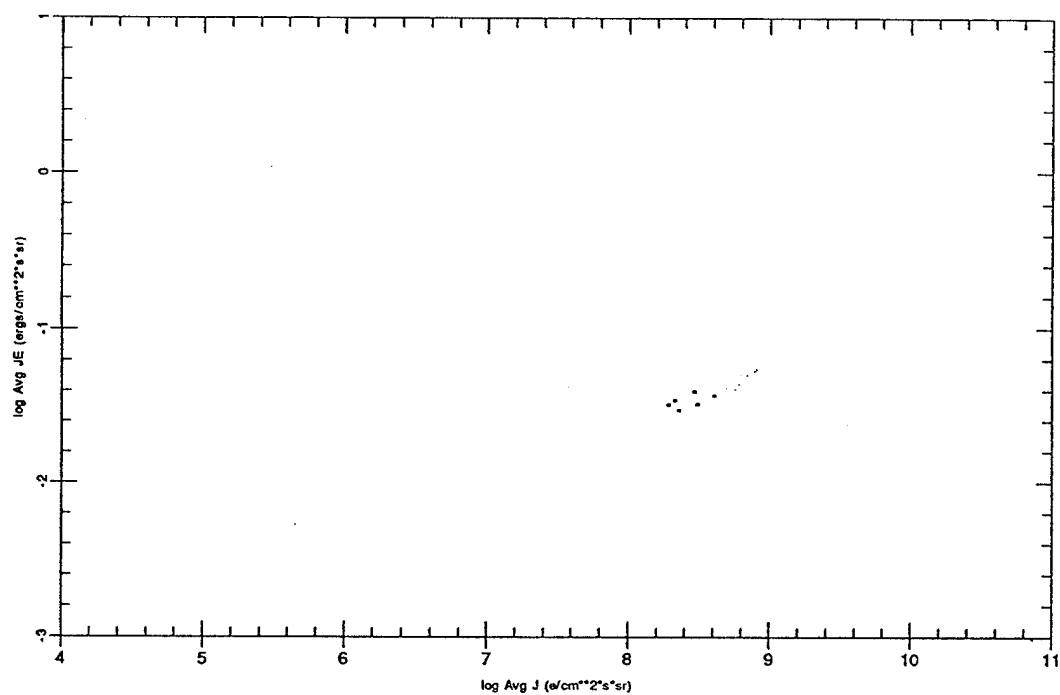
Threshold 0.0100 Peak Ch 4 Bz +
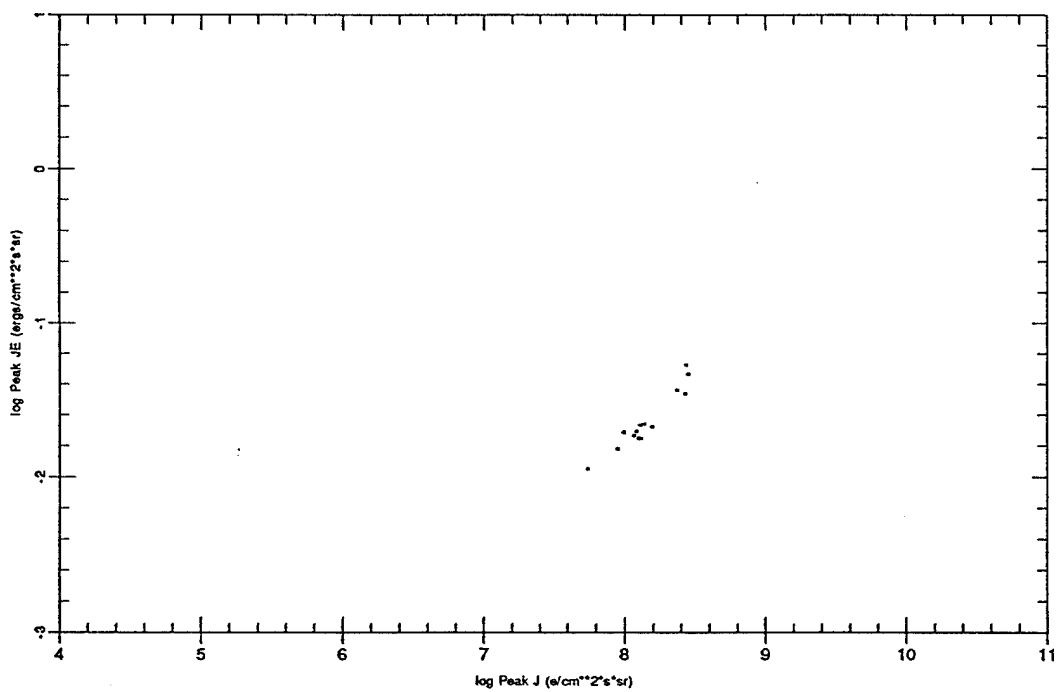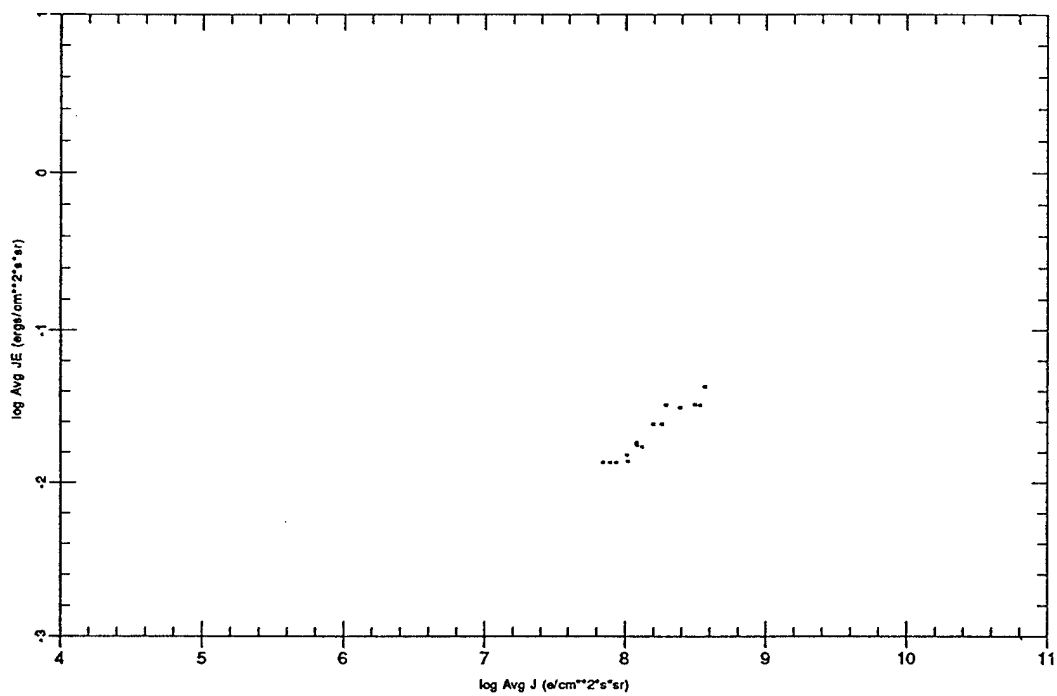
Threshold 0.0050 Peak Ch 4 Bz +
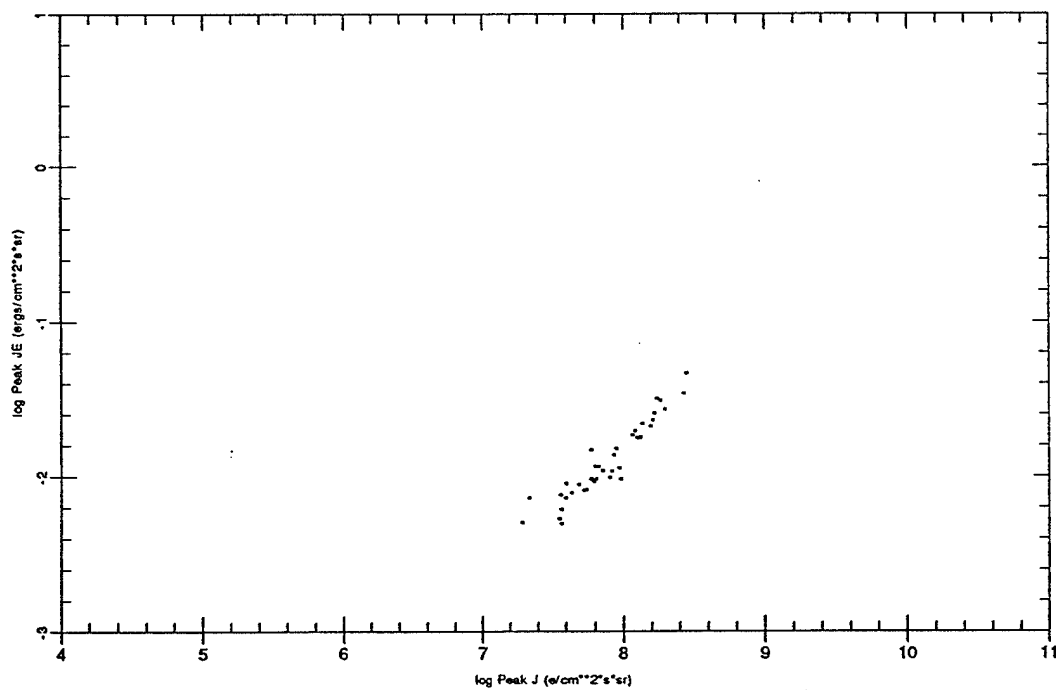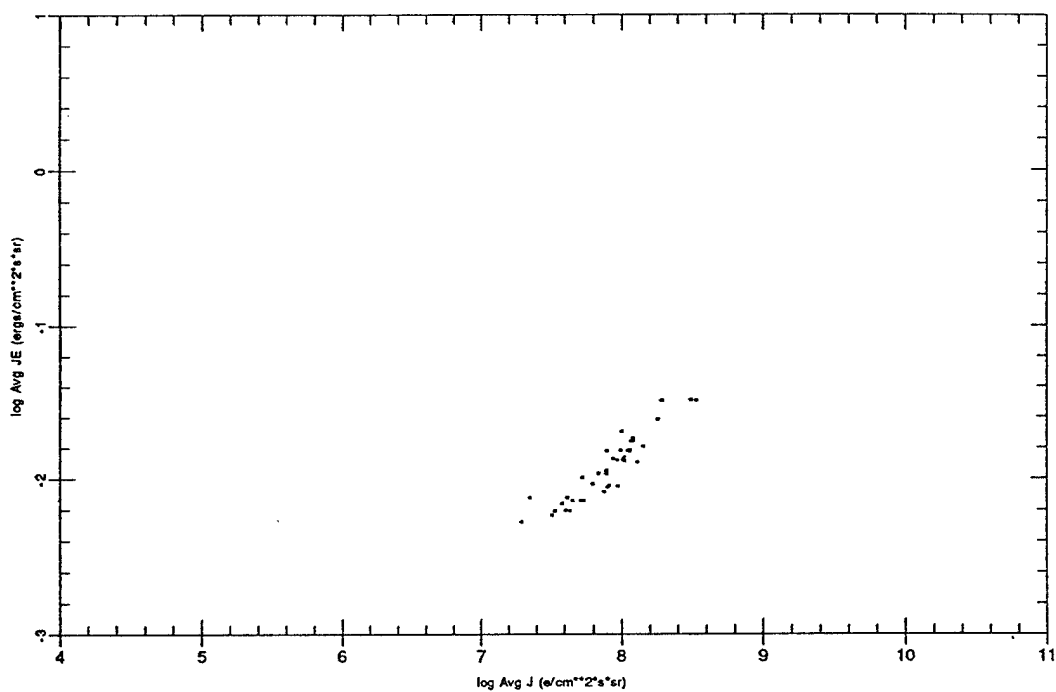
Threshold 0.0025 Peak Ch 4 Bz +
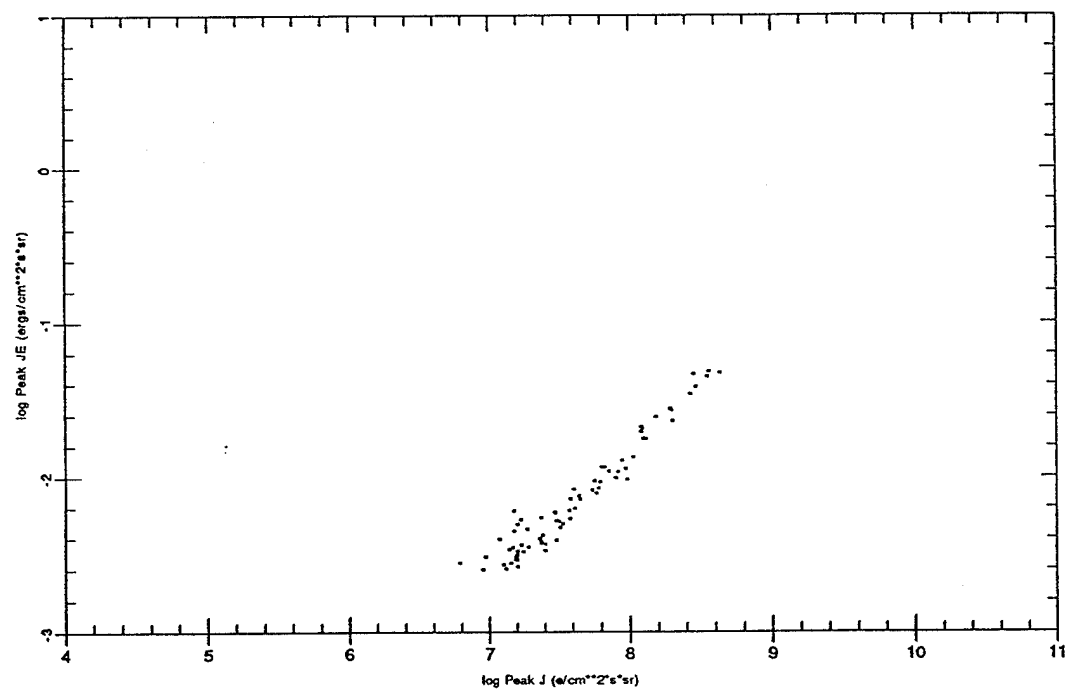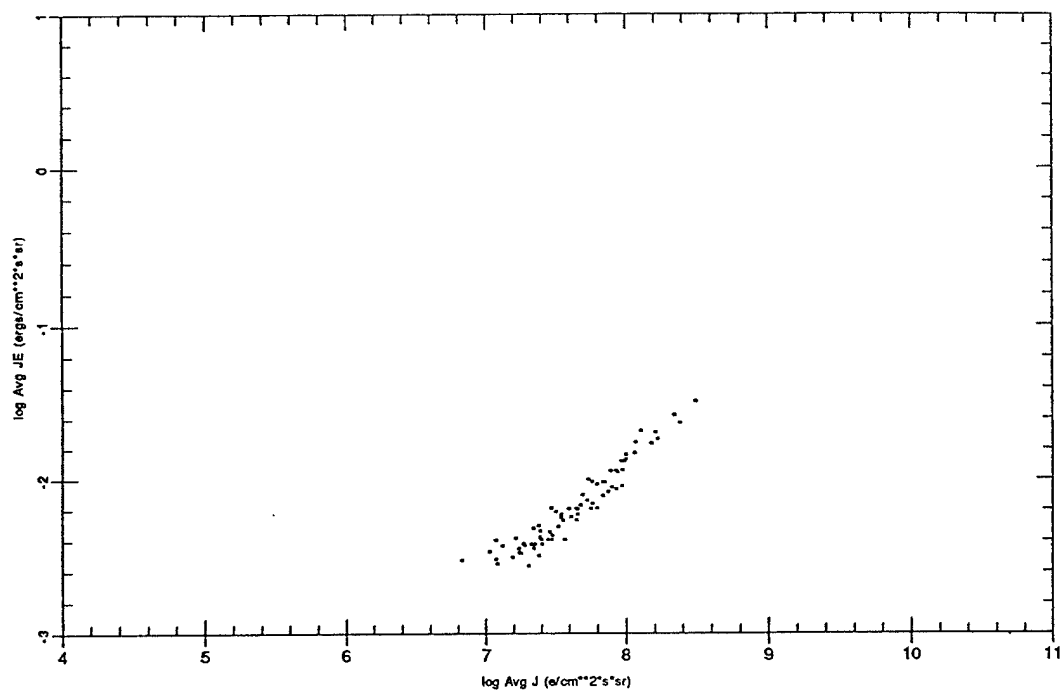
Threshold 0.0200 Peak Ch 3 Bz +
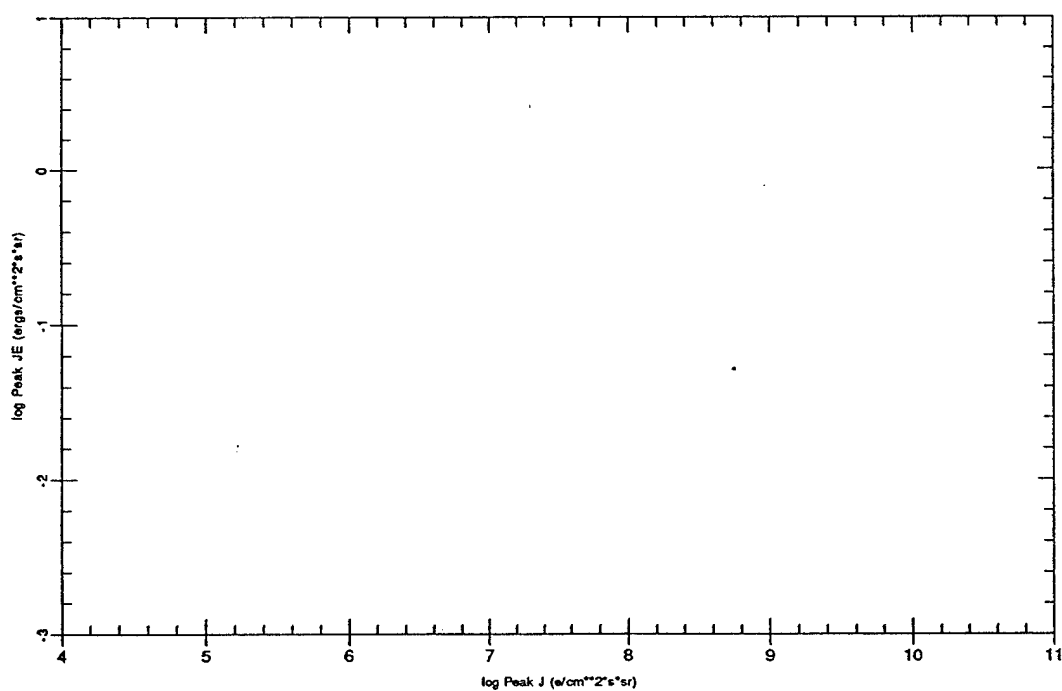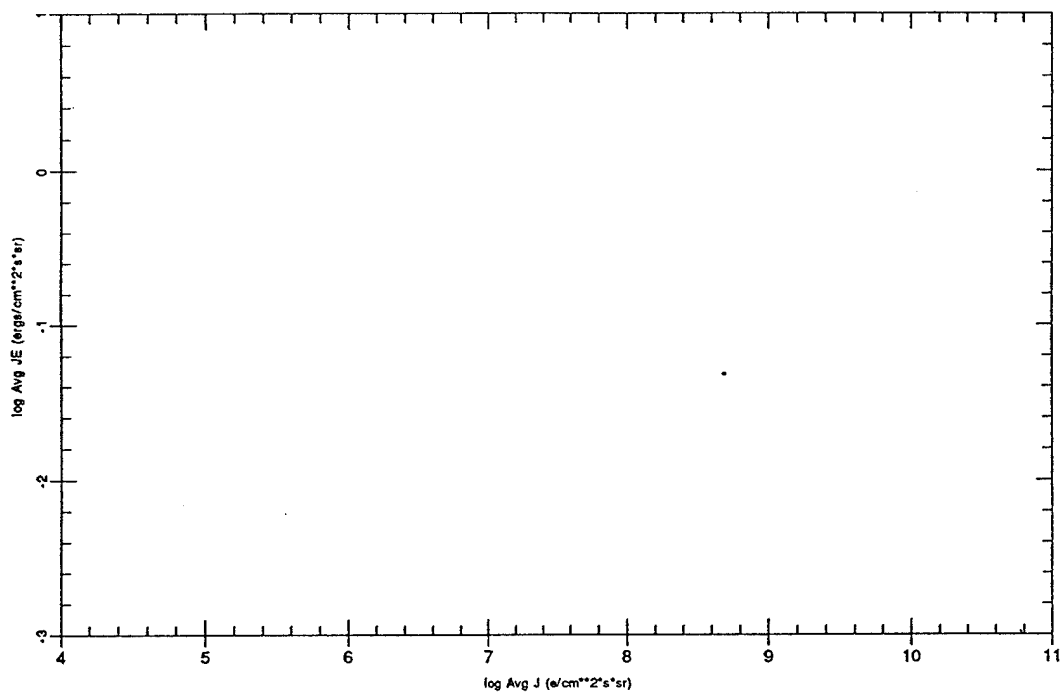
Threshold 0.0100 Peak Ch 3 Bz +
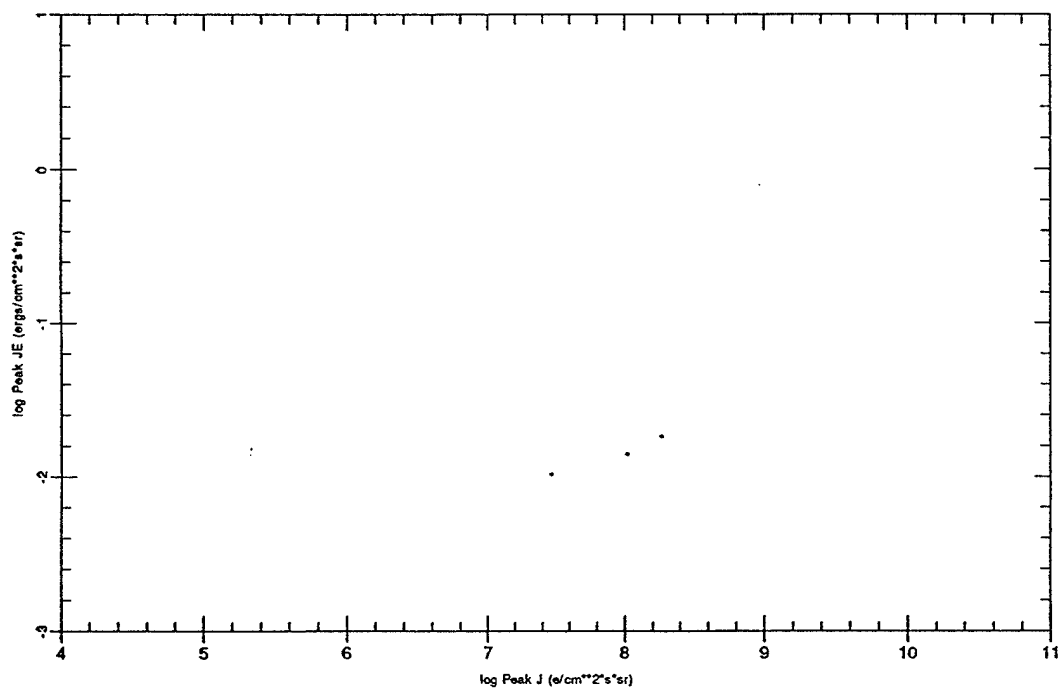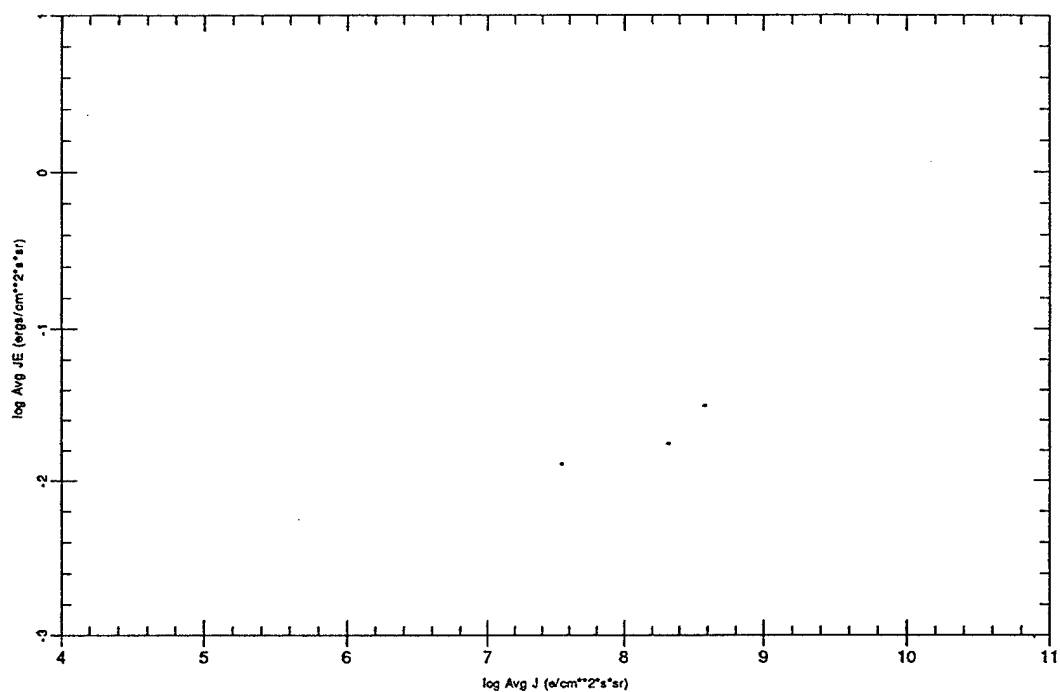
Threshold 0.0050 Peak Ch 3 Bz +
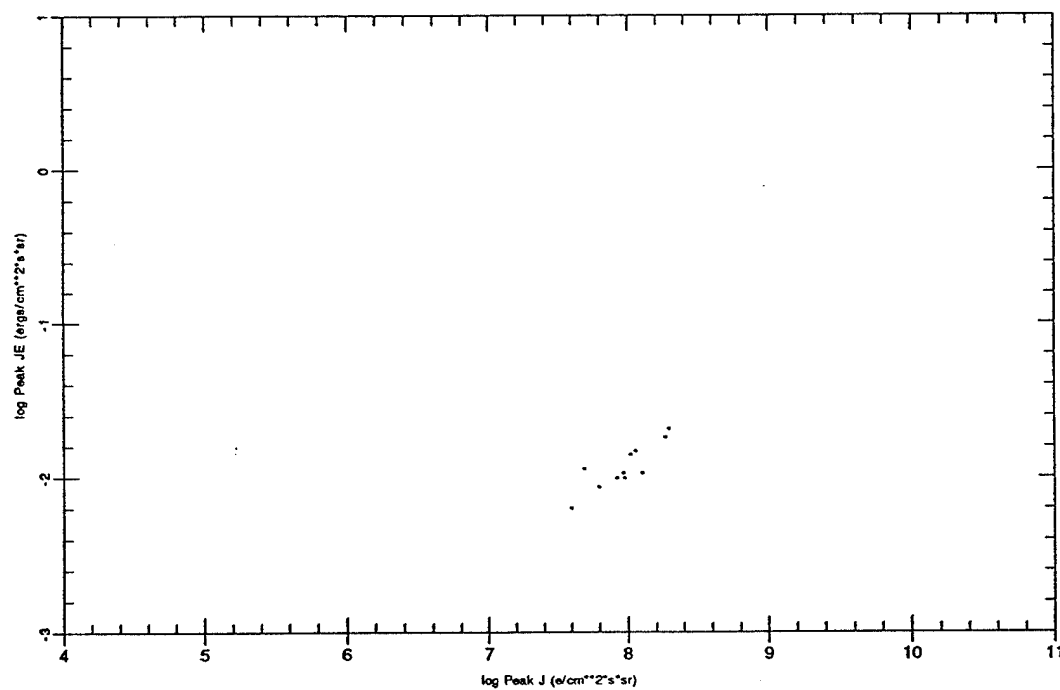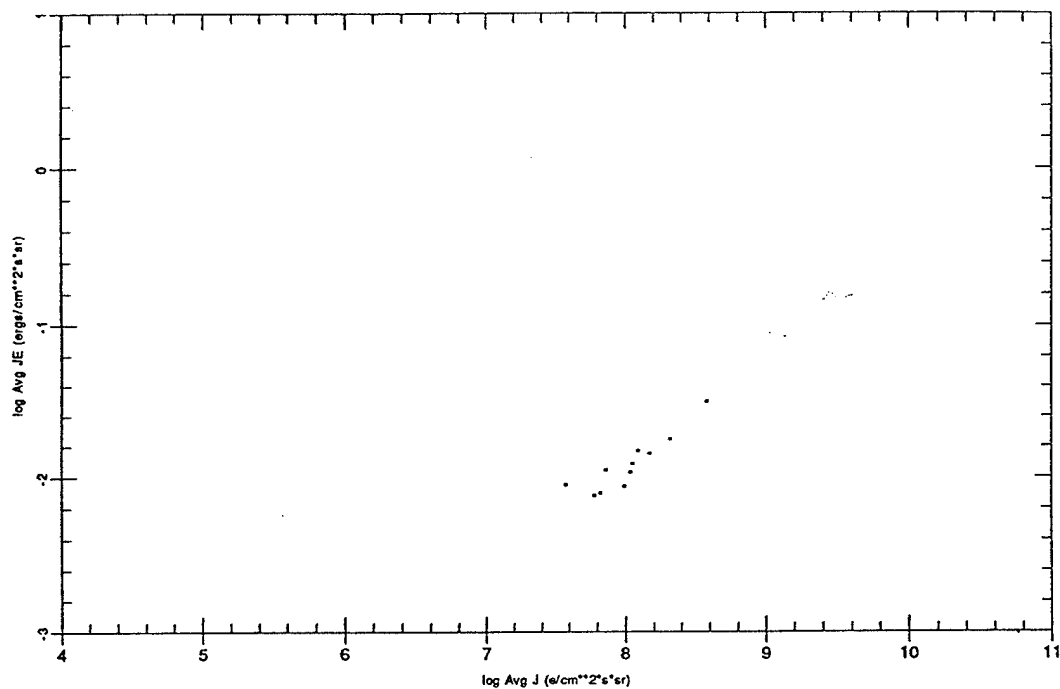
Threshold 0.0025 Peak Ch 3 Bz +
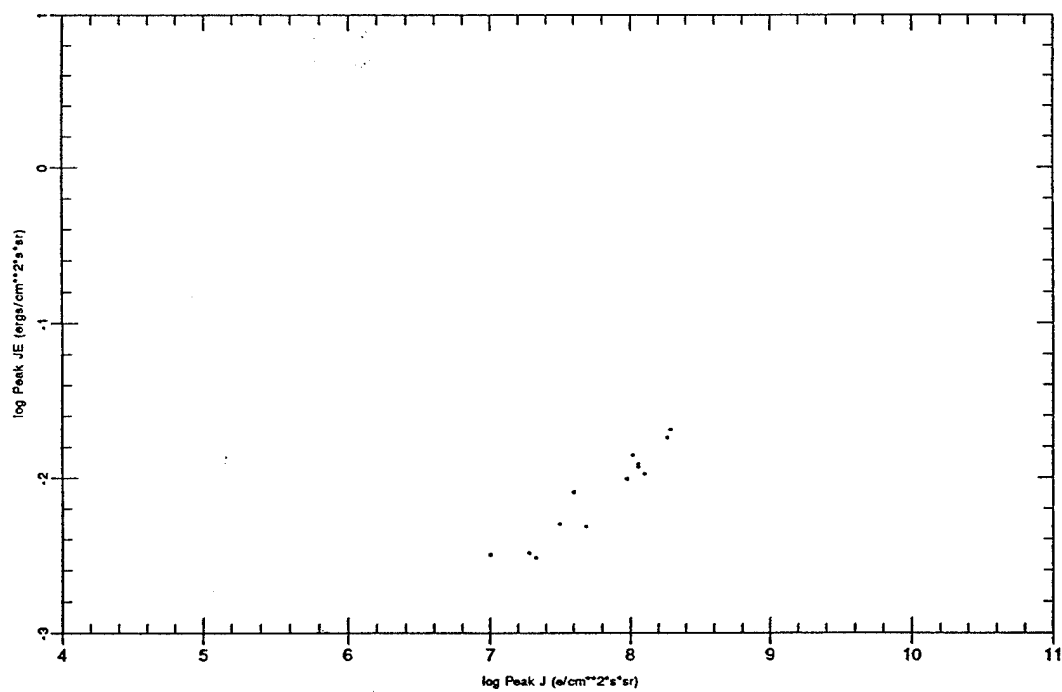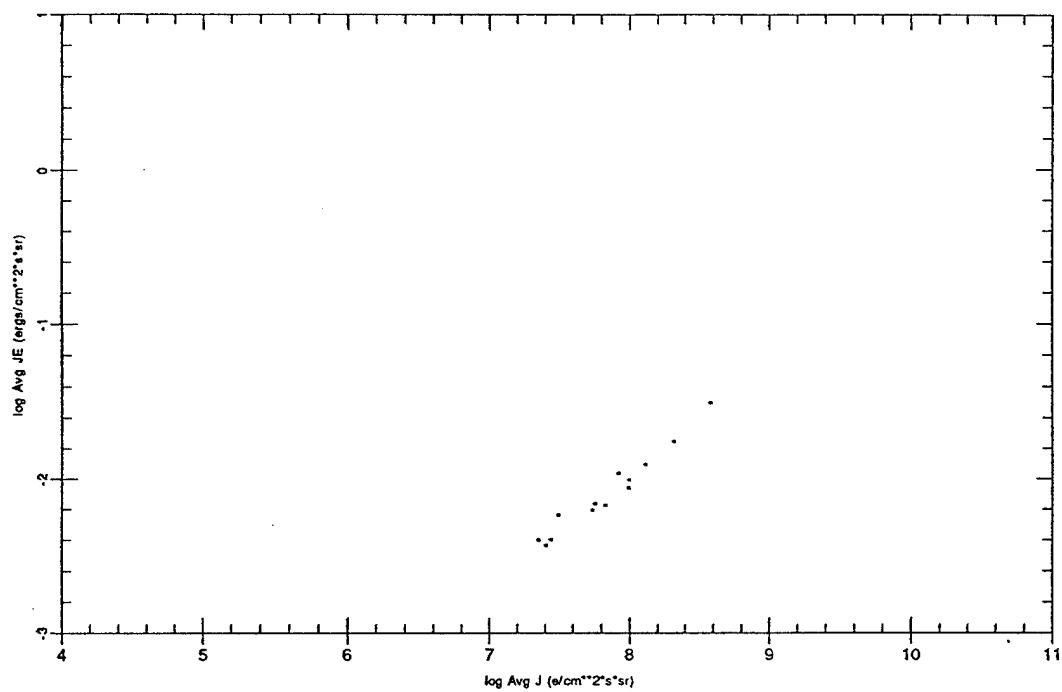
APPENDIX B: Histograms for All Channels and Thresholds

This appendix contains the histograms associated with all the peak JE versus peak J plots shown in Appendix A. The histograms are occurrence frequency versus peak JE. The order of the histograms is the same as the order of the plots in Appendix A. Thresholds are found in the output file name at the top of each histogram. For example, levelp1600ch14_6.out would indicate a threshold of 0.1600 ergs/cm^2·sec·ster in channel 14.

Histogram for file levelp1600ch14_6.out

Peak JE (erg/cm**2*s*sr)
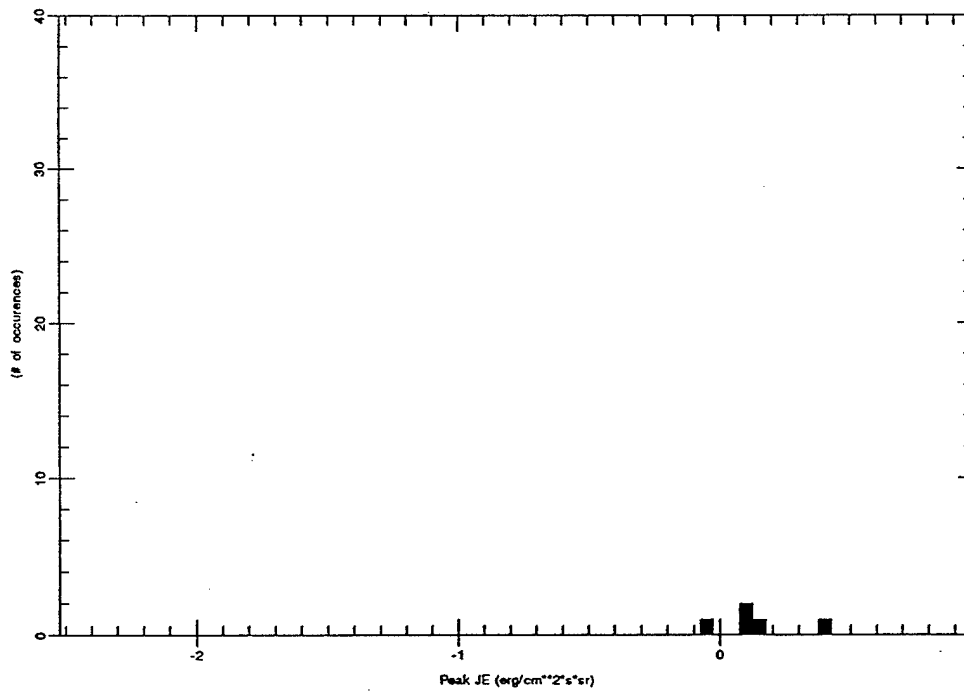
Histogram for file levelp0800ch14_6.out

Peak JE (erg/cm**2*s*sr)
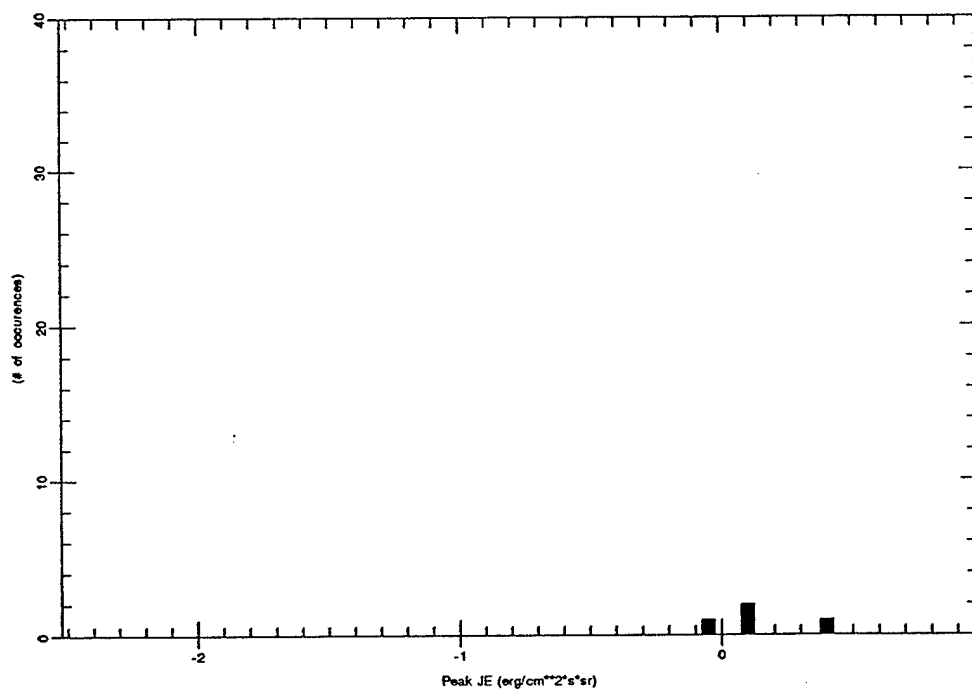
Histogram for file levelp0400ch14_6.out
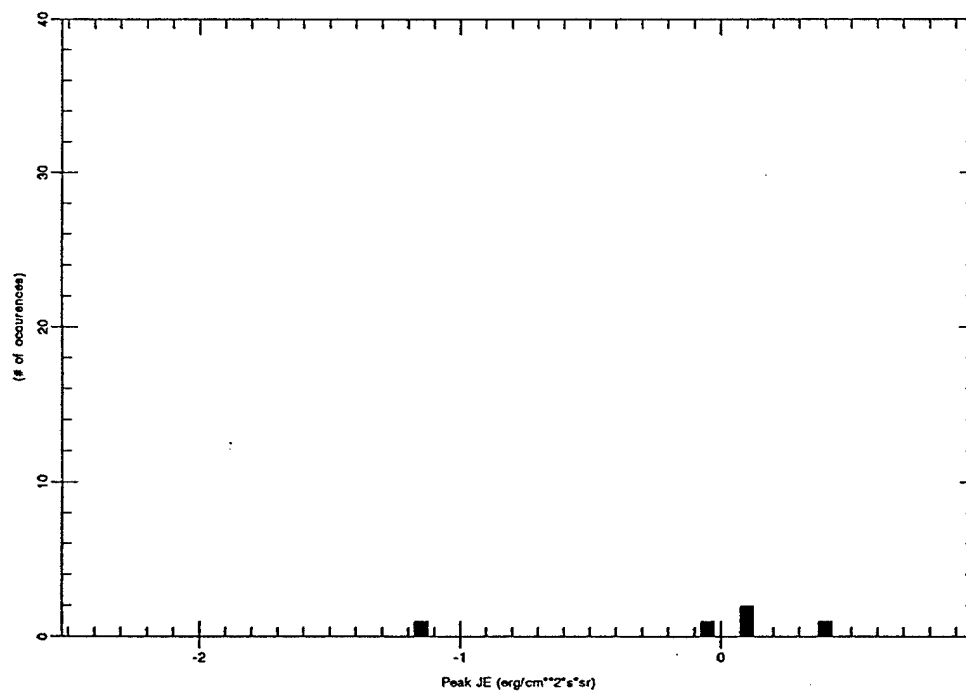
Histogram for file levelp0200ch14_6.out

Peak JE (erg/cm**2*s*sr)
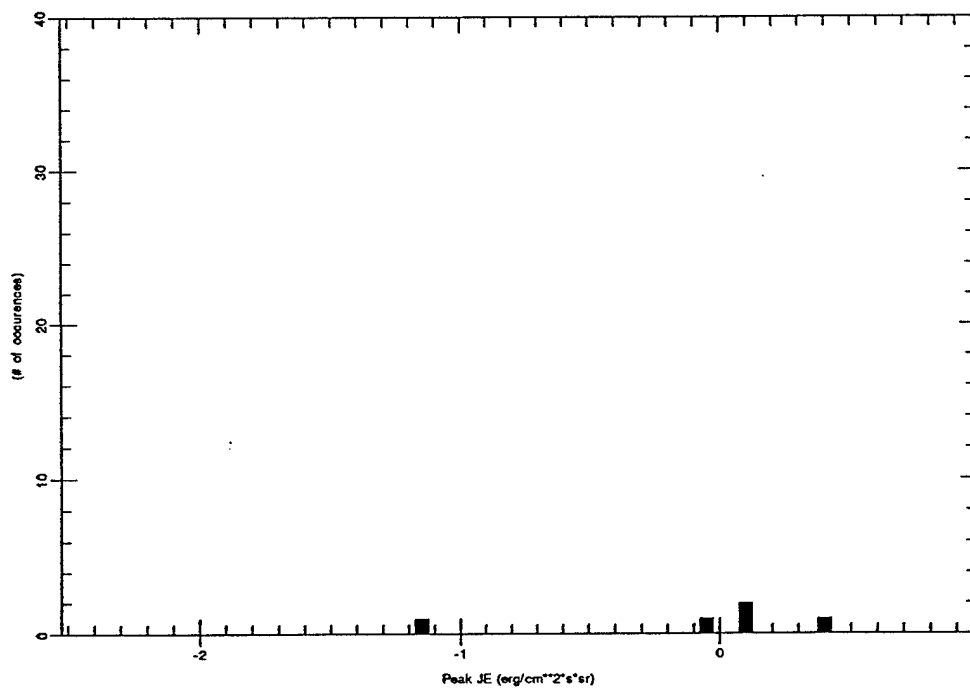
Histogram for file levelp0100ch14_6.out

142
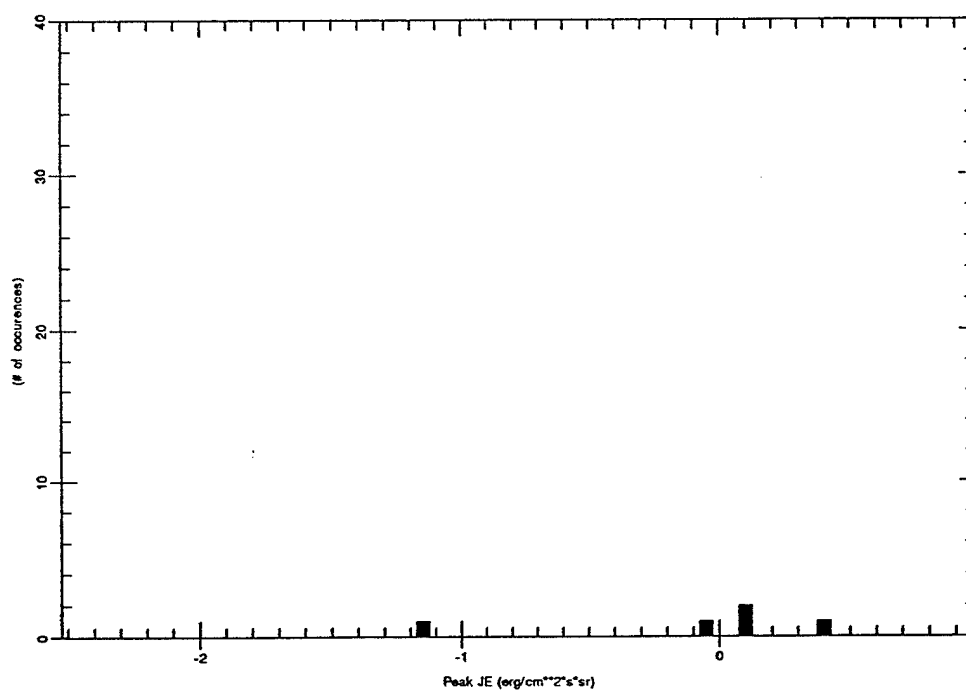
Histogram for file levelp0050ch14_6.out
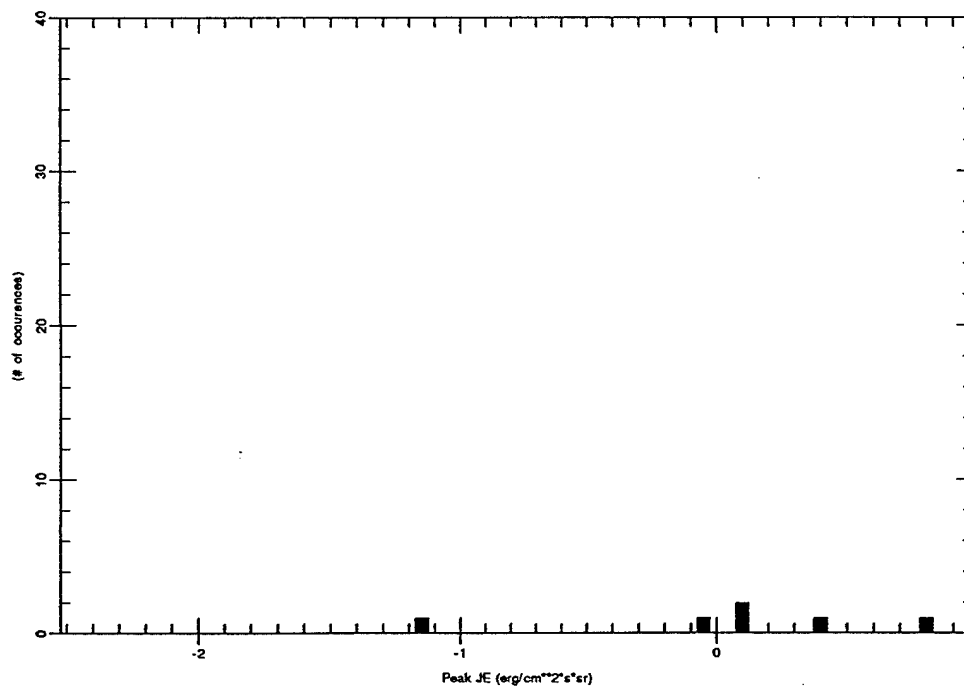
Histogram for file levelp0025ch14_6.out
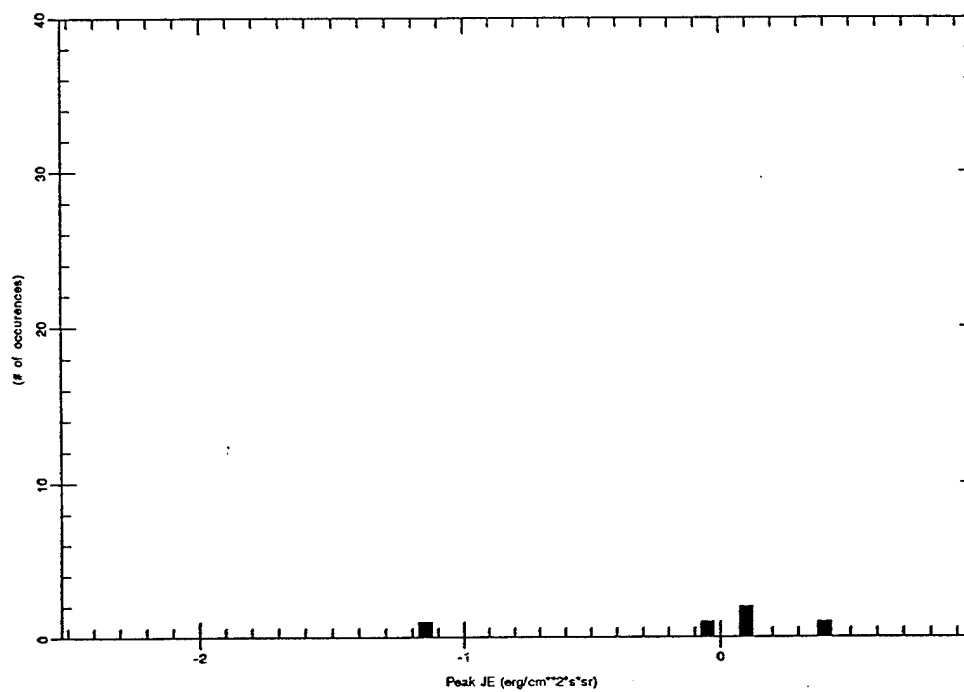
Histogram for file levelp1600ch13_6.out
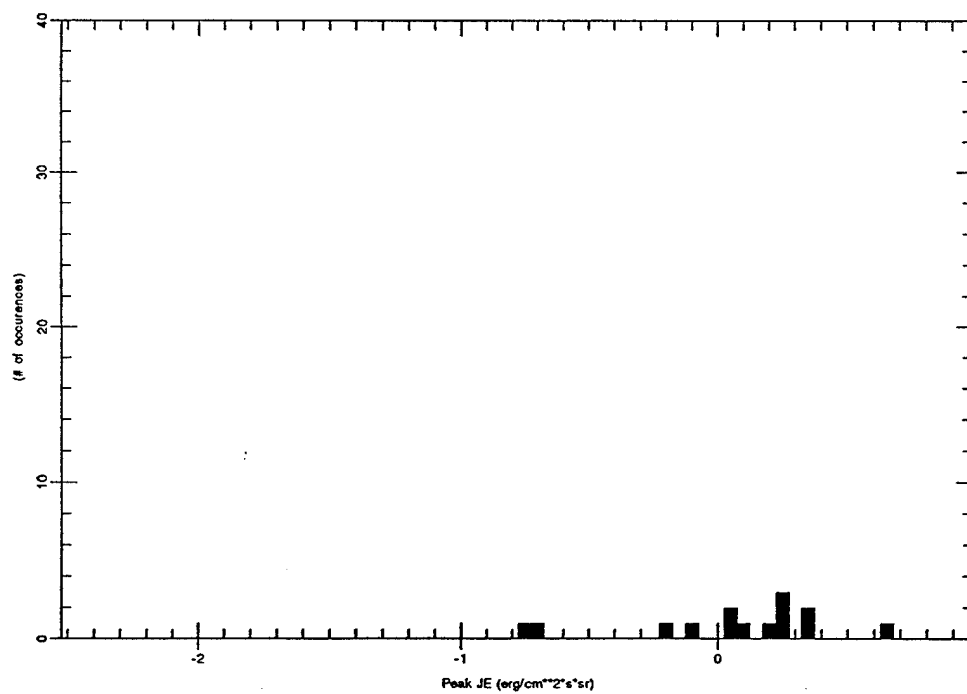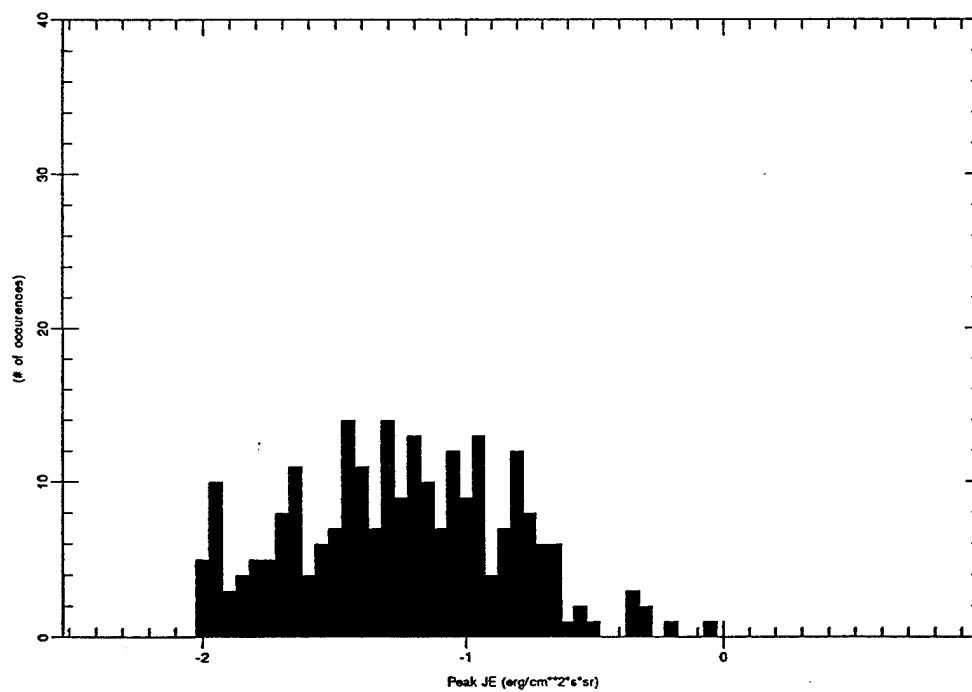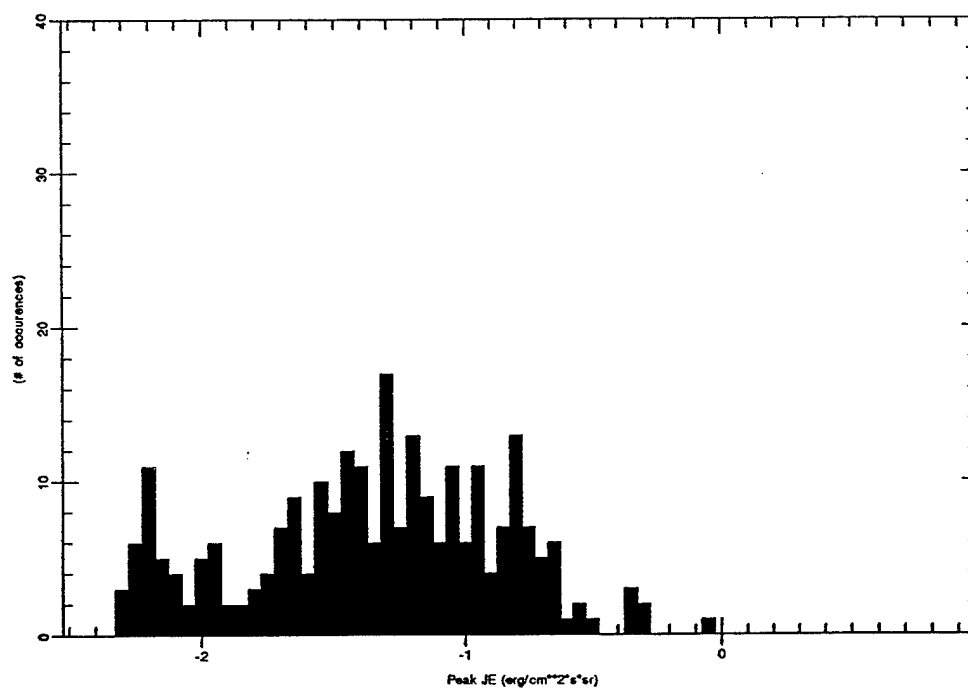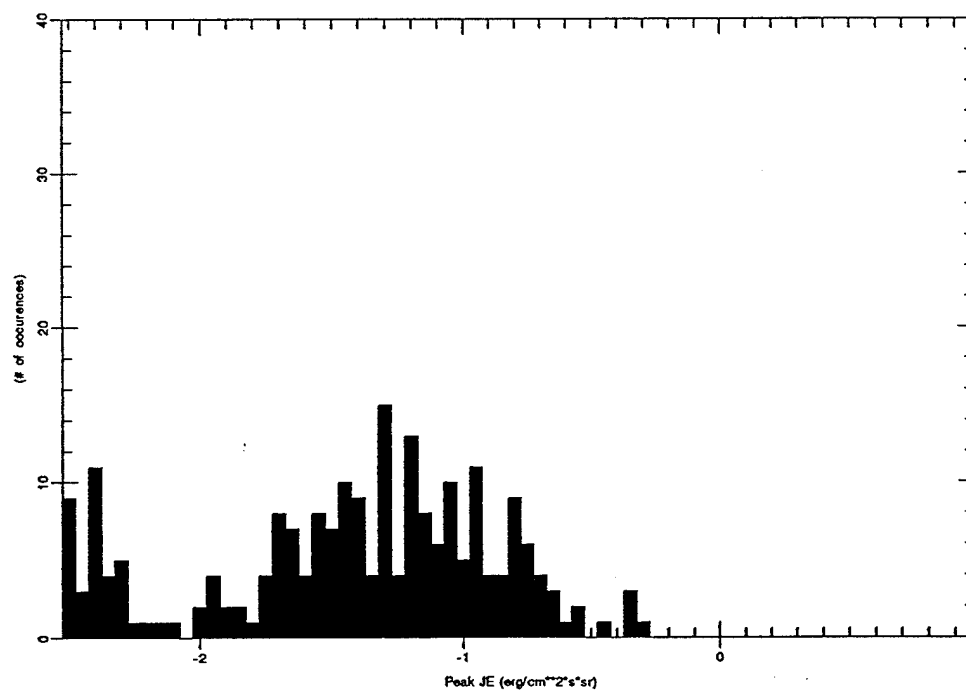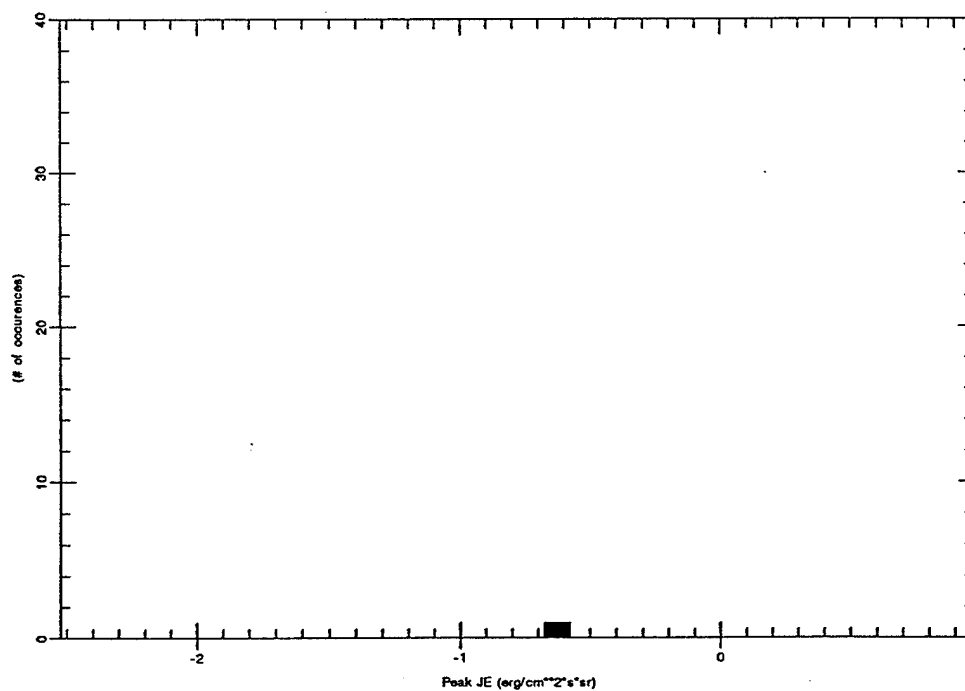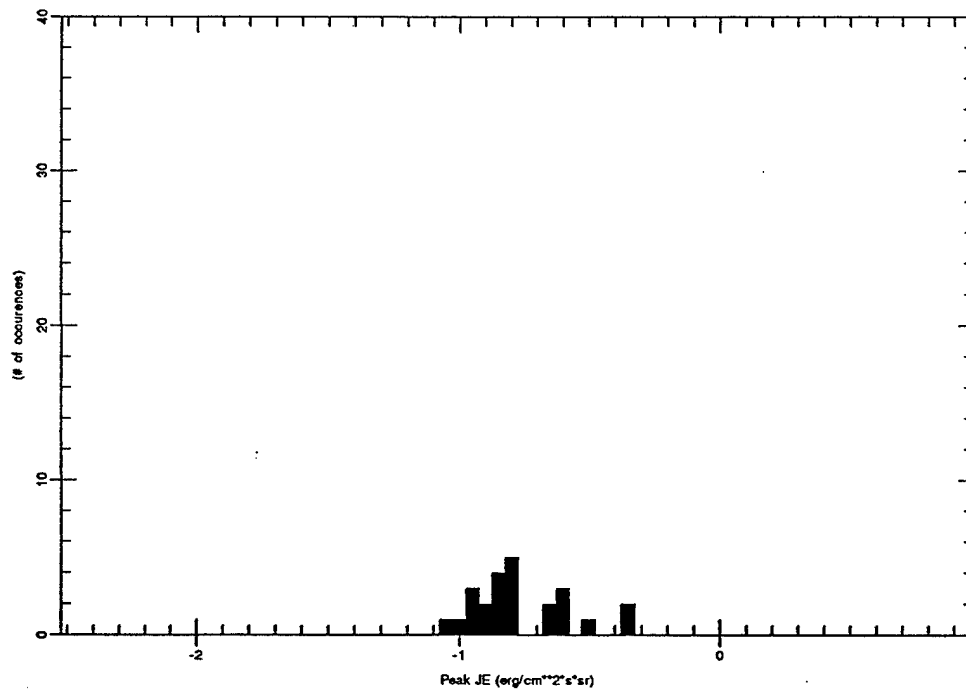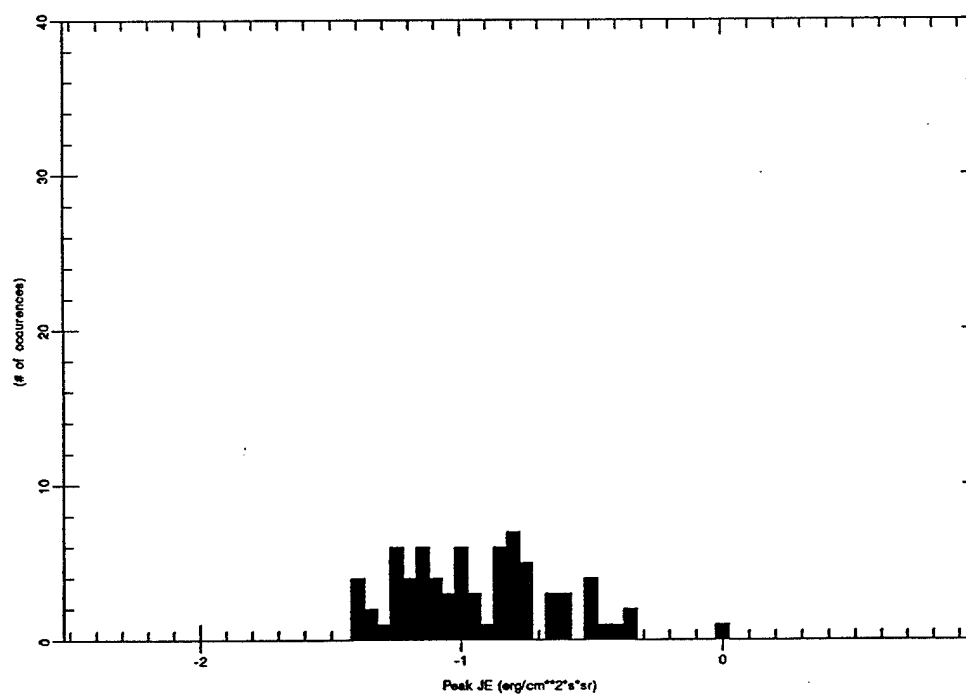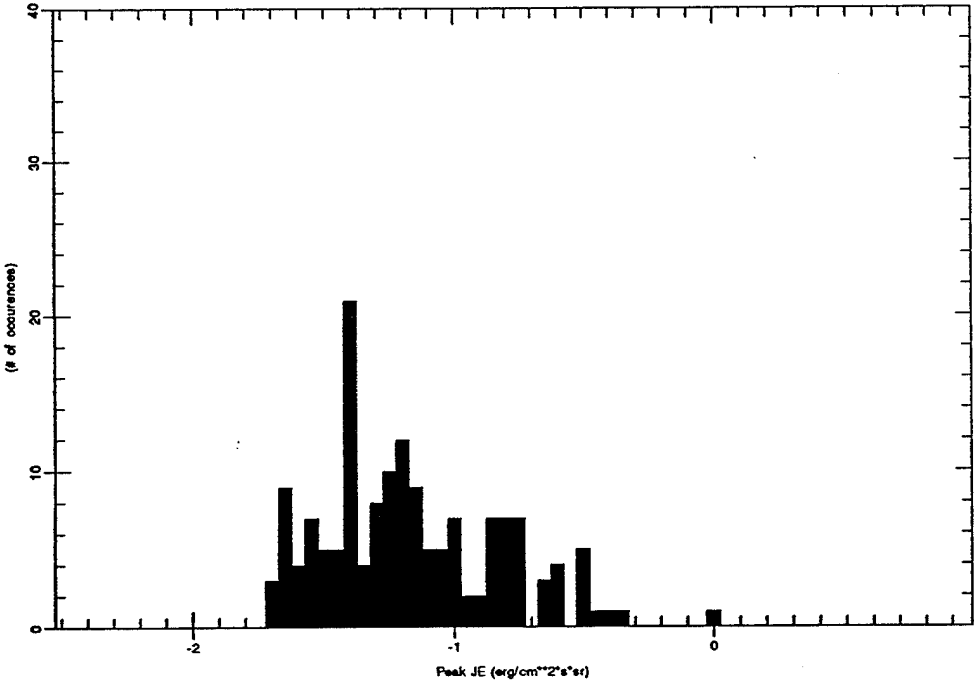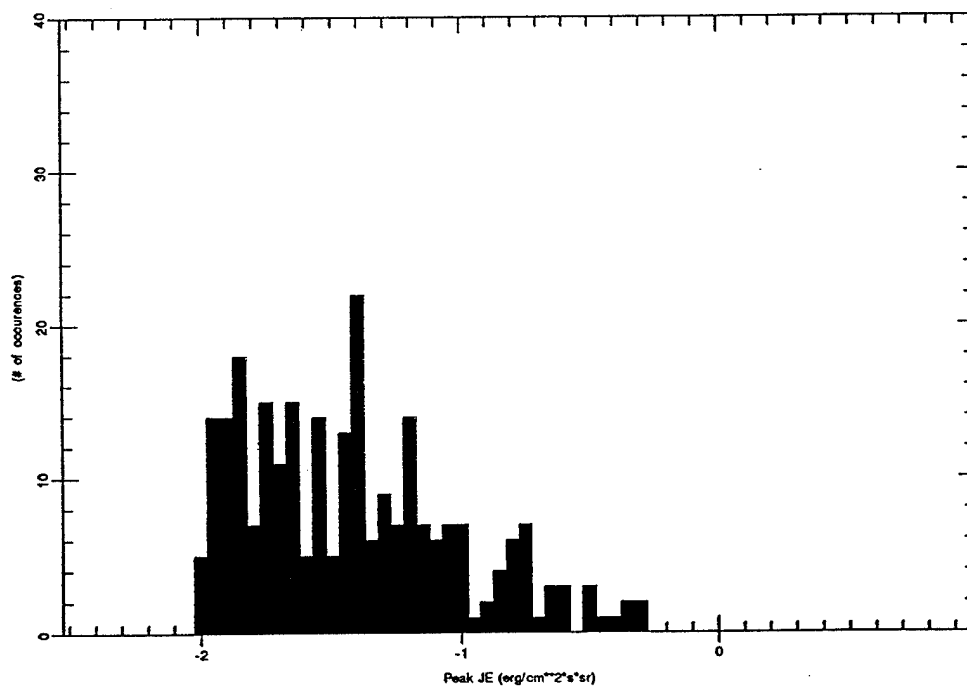
Histogram for file levelp0800ch13_6.out
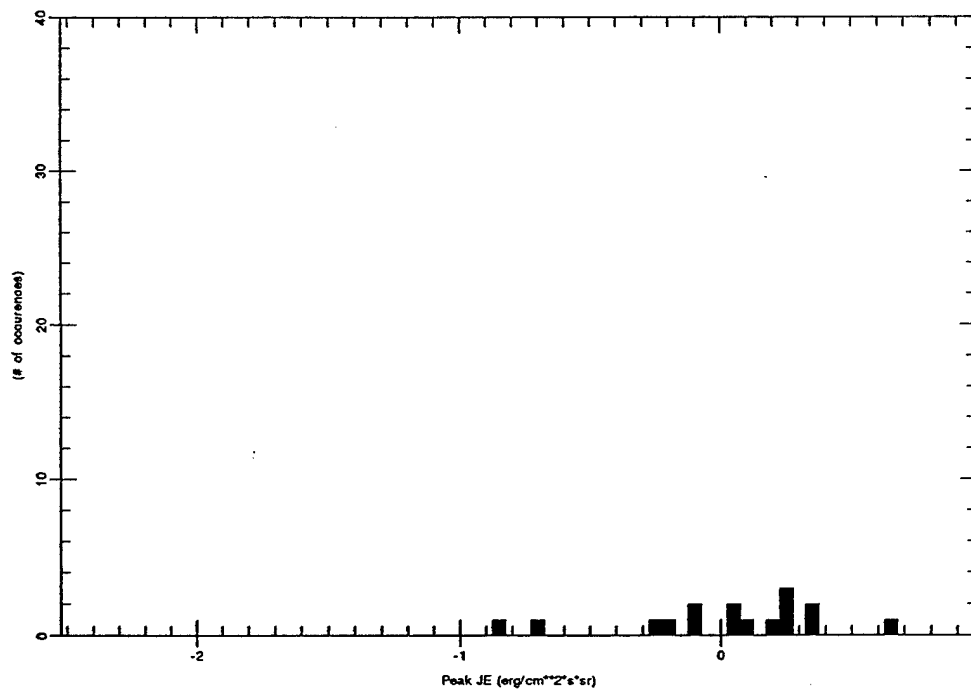
Histogram for file levelp0400ch13_6.out
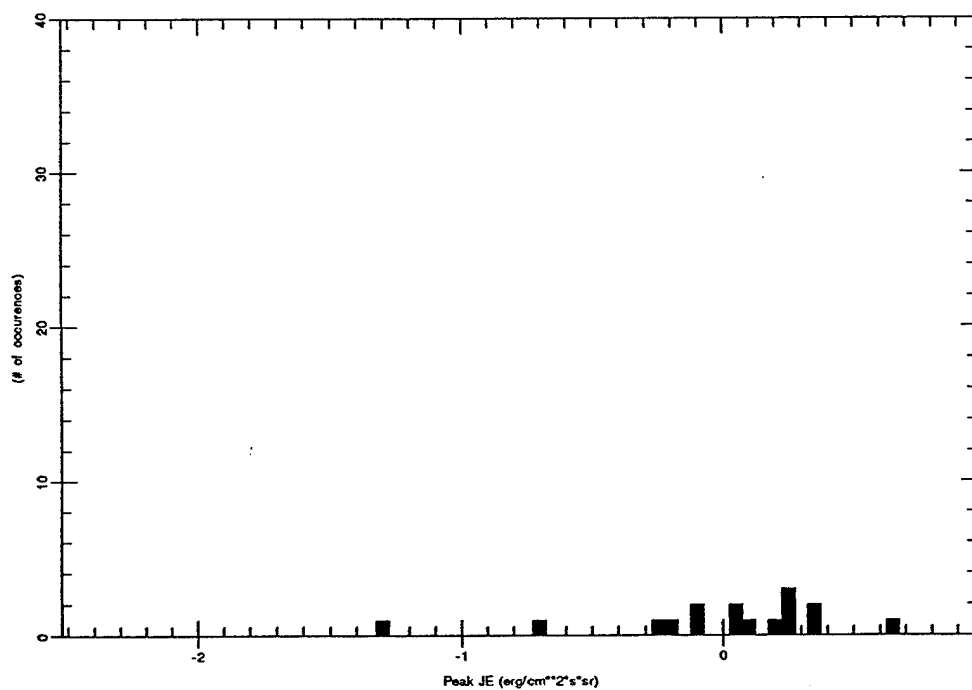
Histogram for file levelp0200ch13_6.out

Peak JE (erg/cm**2*s*sr)
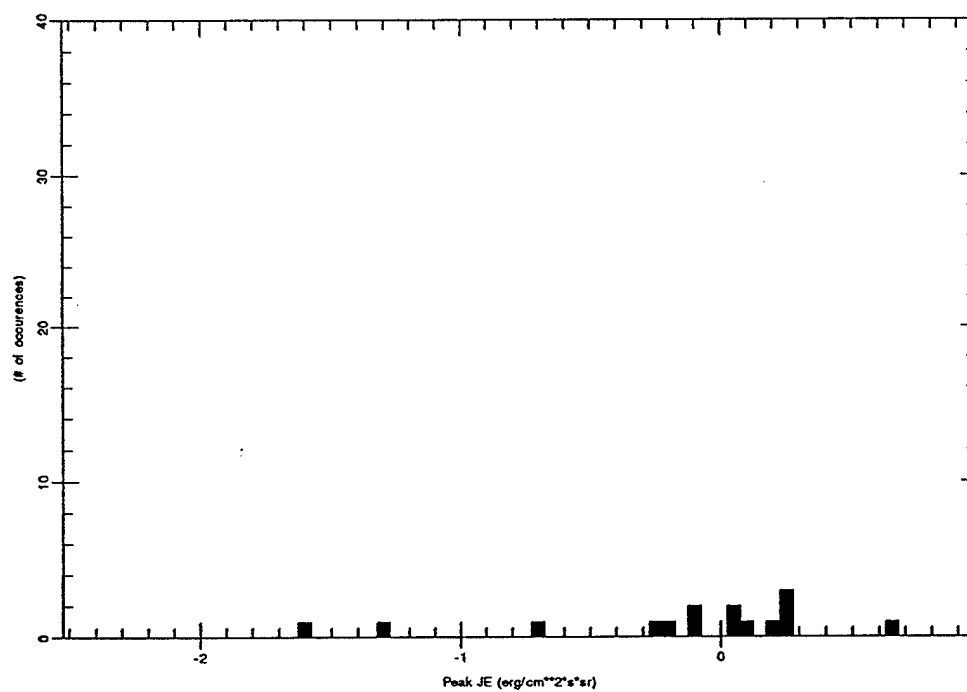
Histogram for file levelp0100ch13_6.out

Peak JE (erg/cm**2*s*sr)
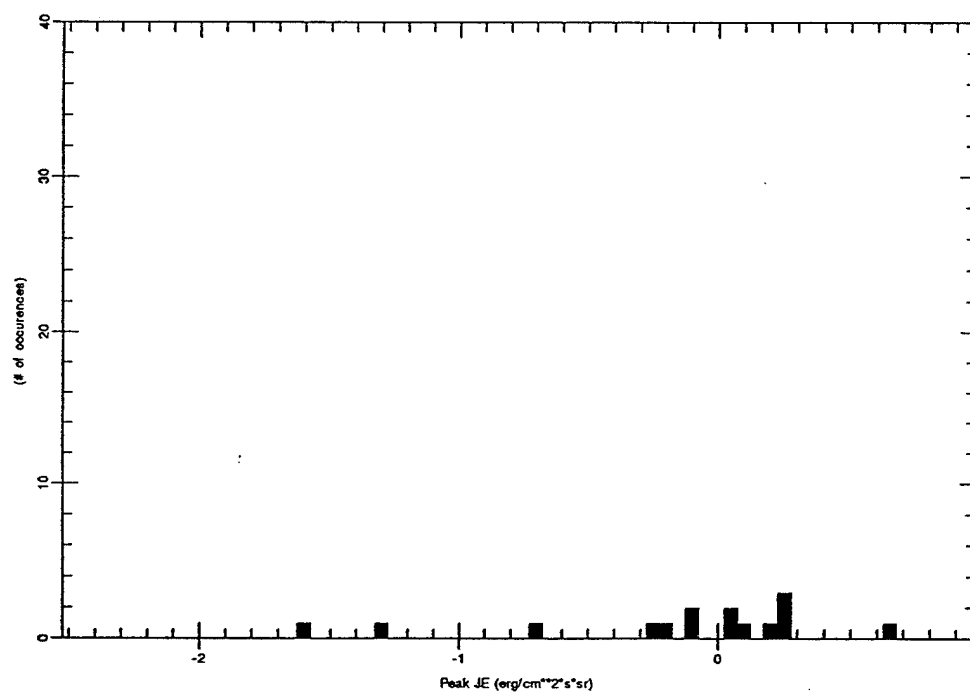
Histogram for file levelp0050ch13_6.out
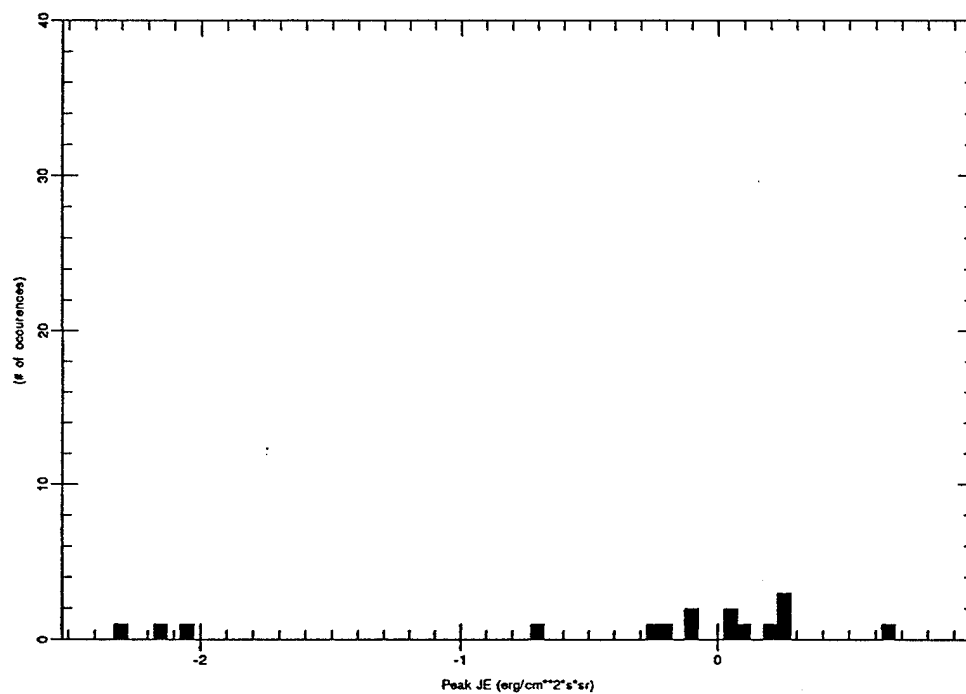
Histogram for file levelp0025ch13_6.out
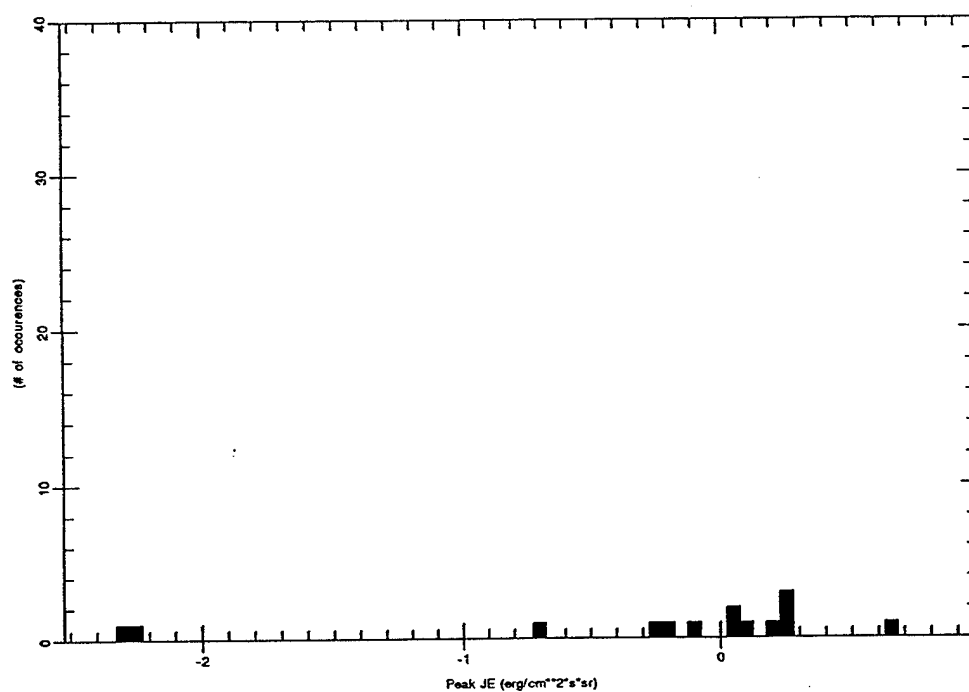
Histogram for file levelp1600ch12_6.out
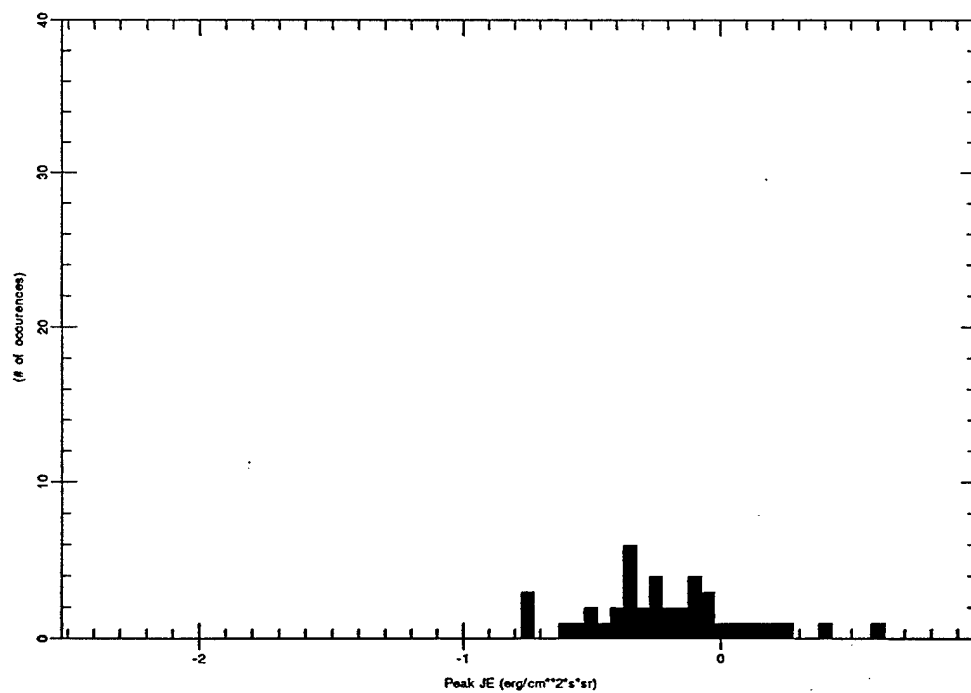
Histogram for file levelp0800ch12_6.out
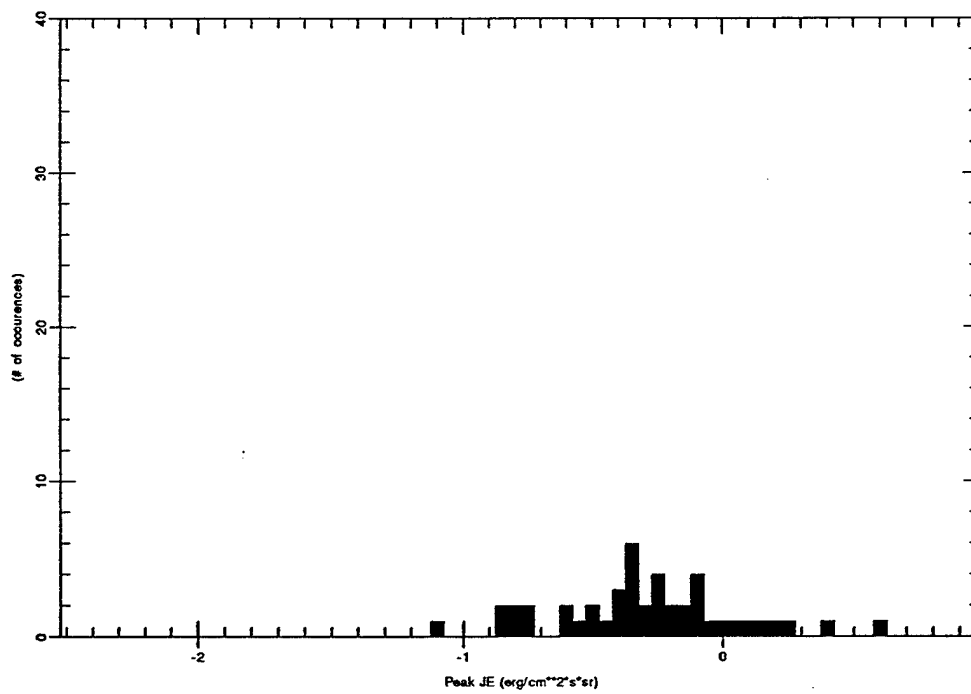
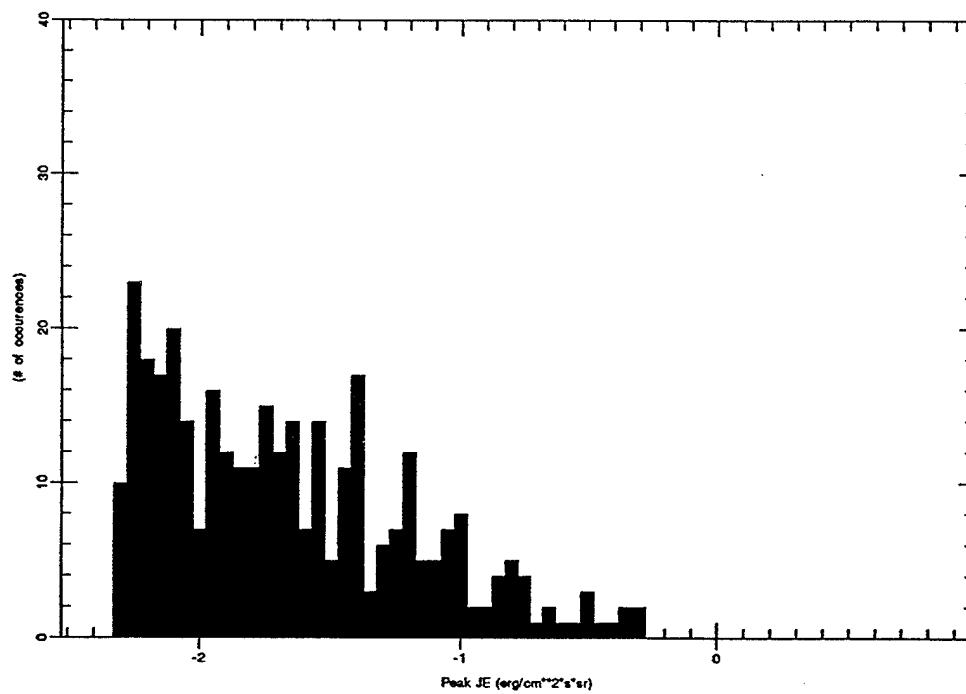Histogram for file levelp0400ch12_6.out
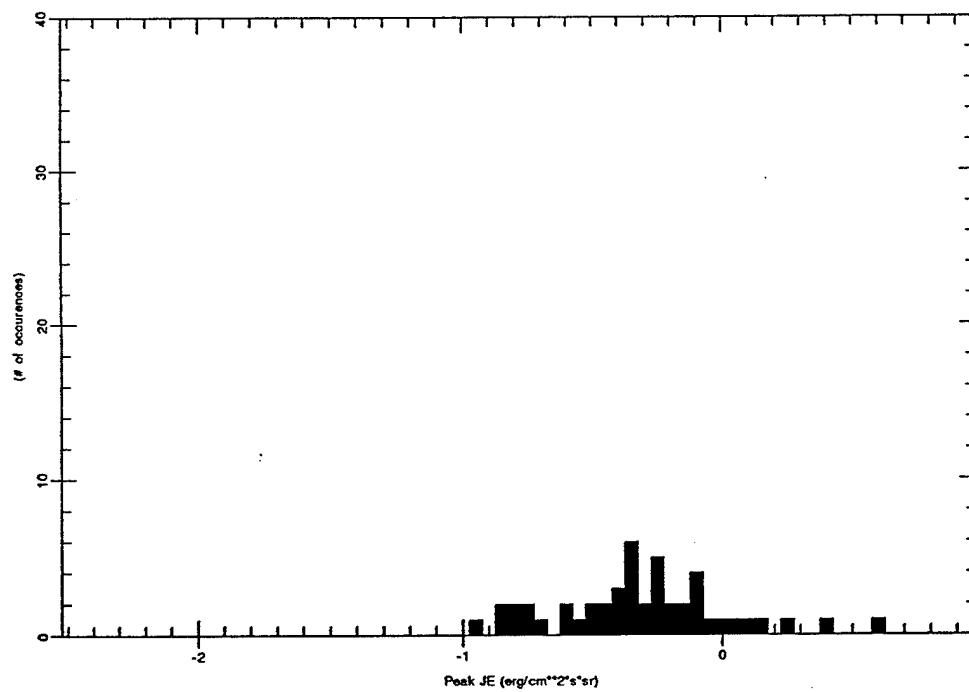
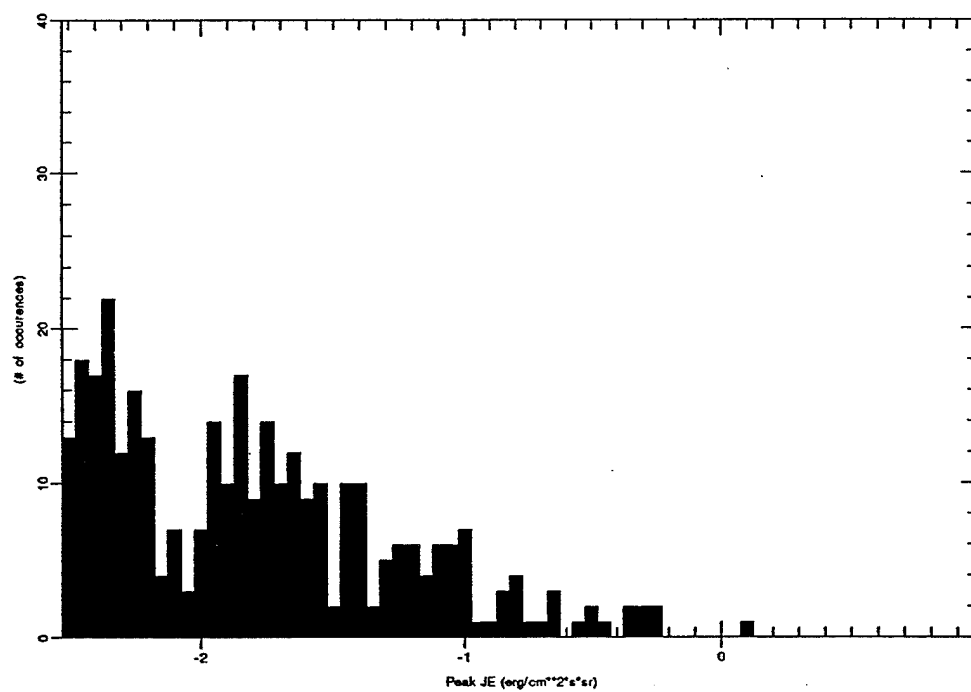Histogram for file levelp0200ch12_6.out

155
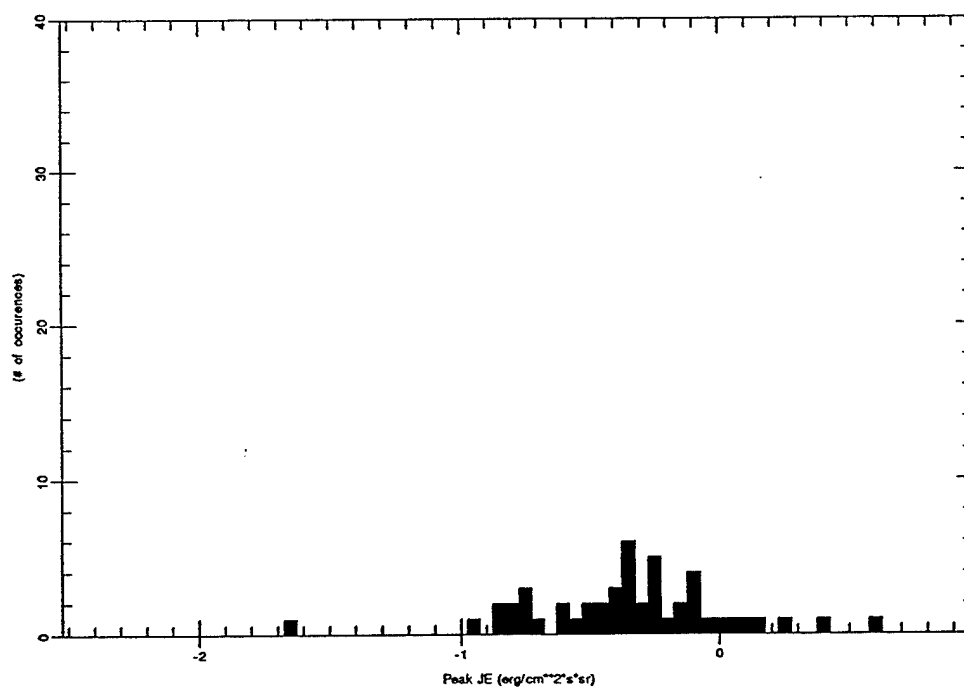
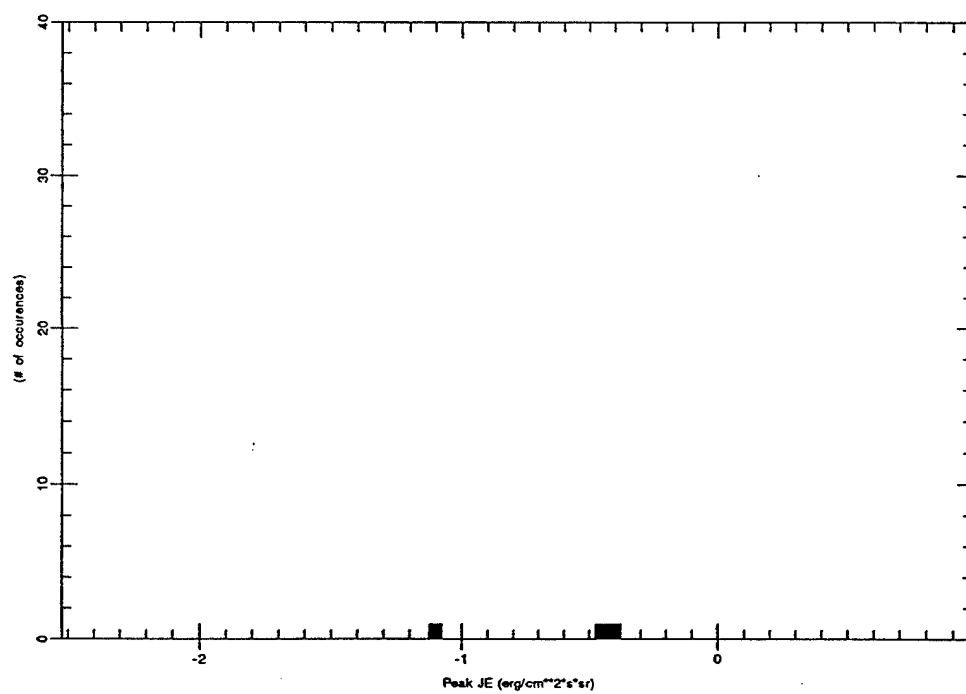Histogram for file levelp0100ch12_6.out

Peak JE (erg/cm**2*s*sr)
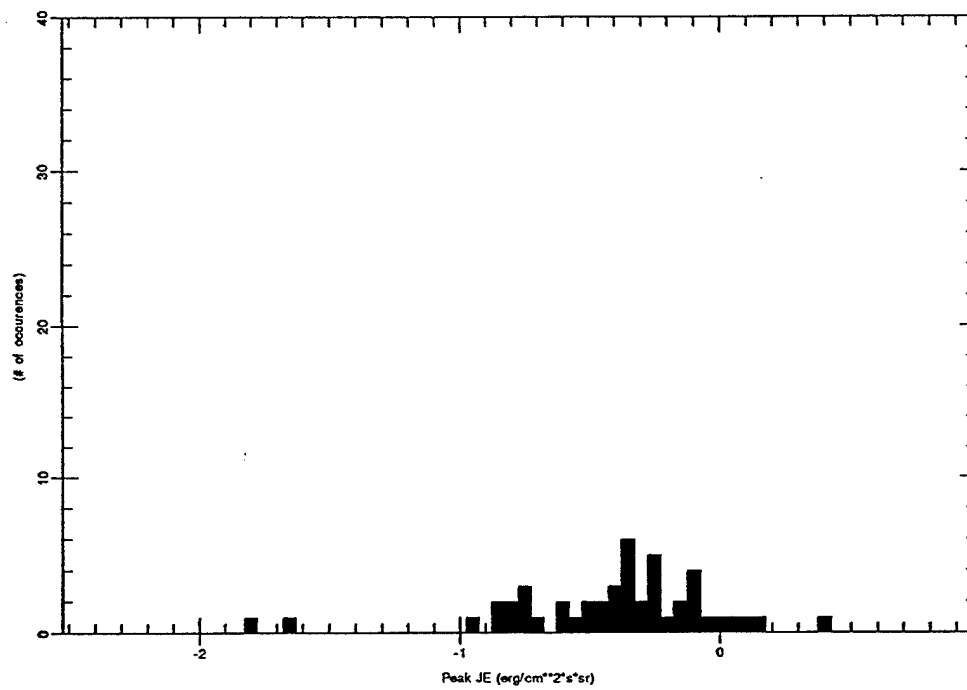
Histogram for file levelp0050ch12_6.out
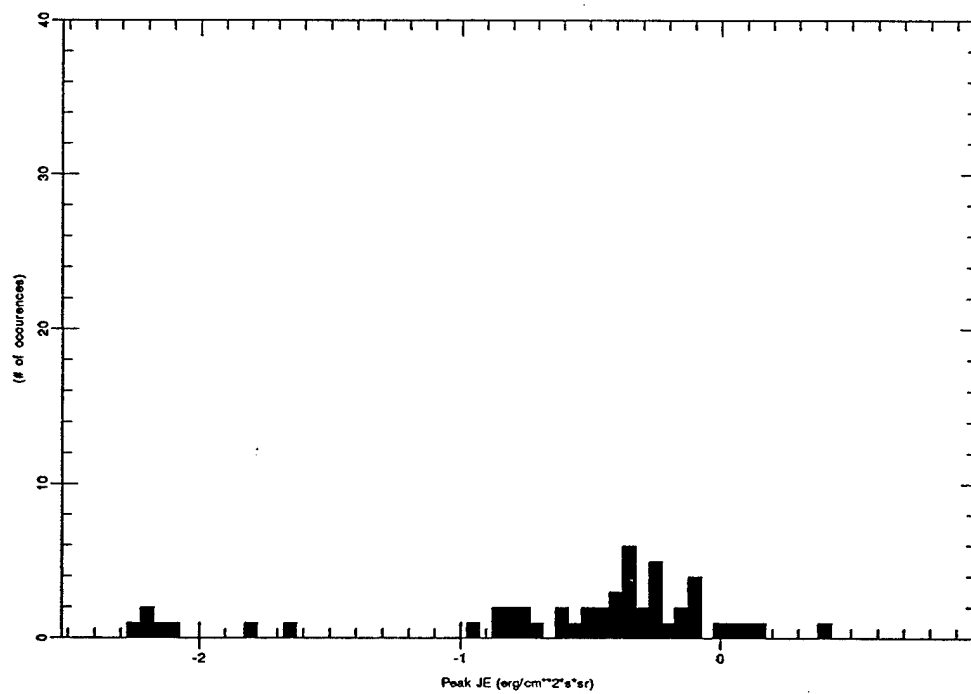
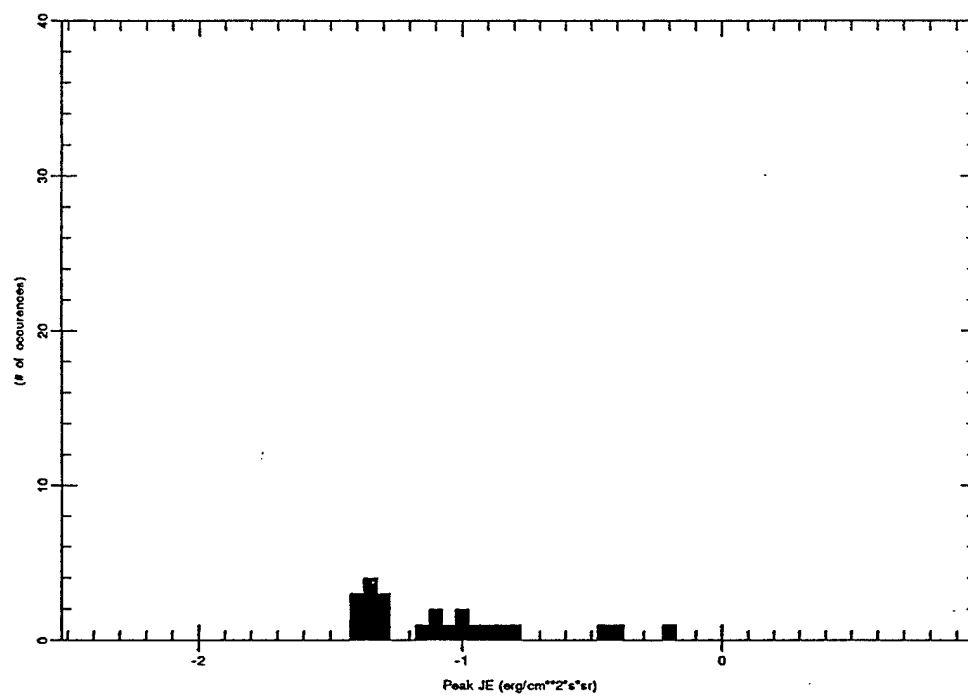Histogram for file levelp0025ch12_6.out
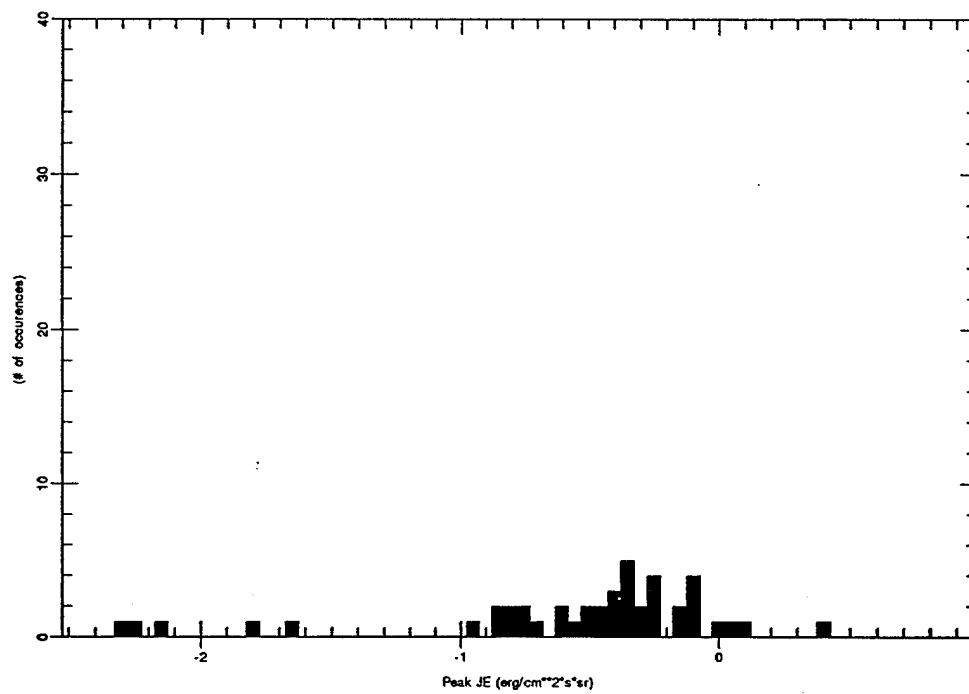
Histogram for file levelp1600ch11_6.out
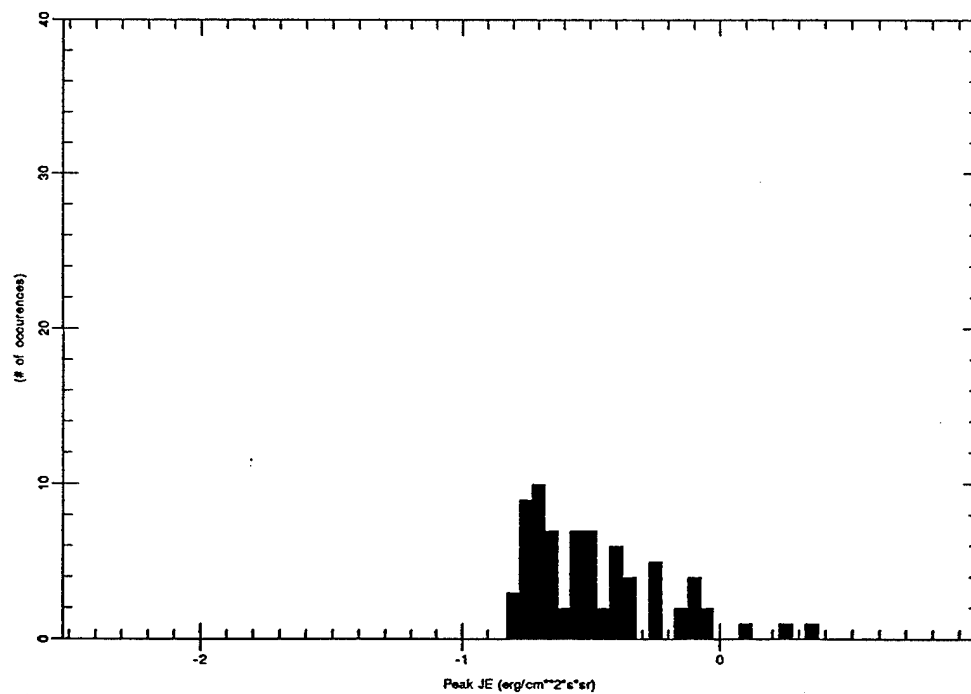
Histogram for file levelp0800ch11_6.out
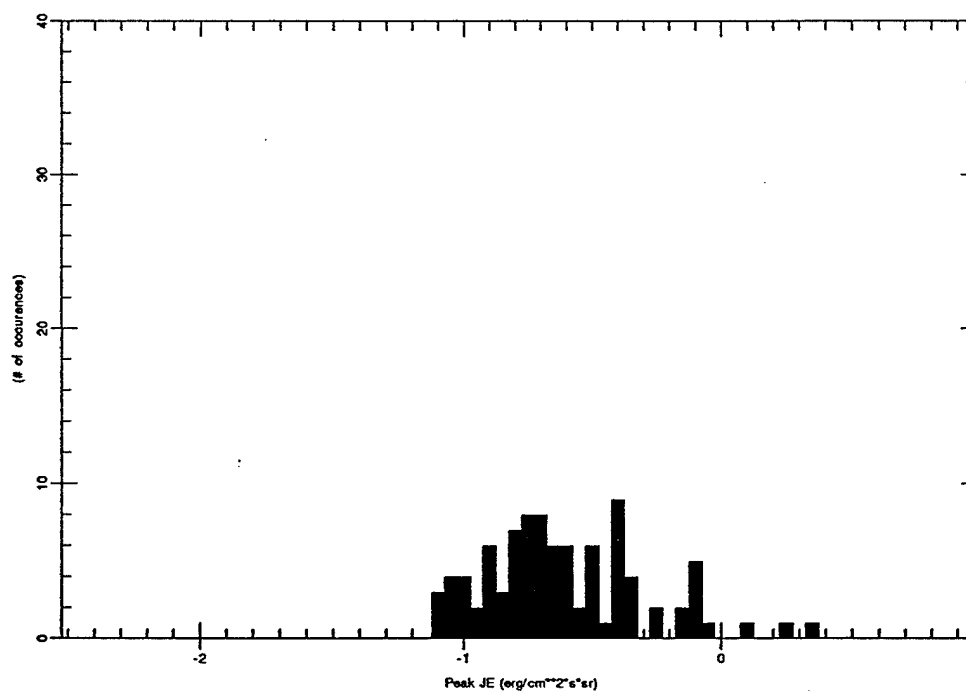
Histogram for file levelp0400ch11_6.out
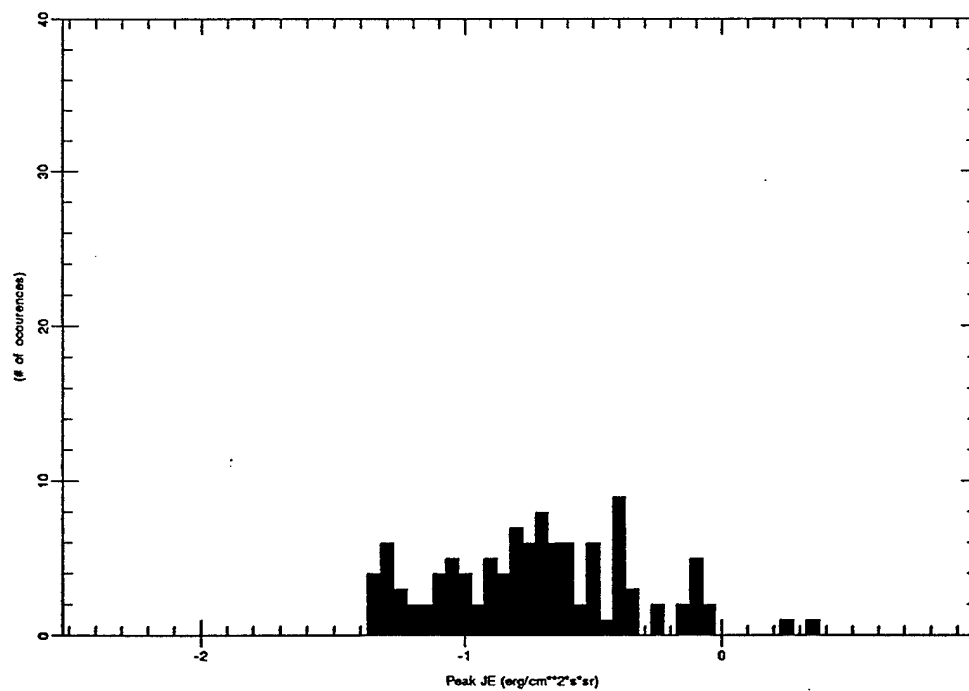
Histogram for file levelp0200ch11_6.out
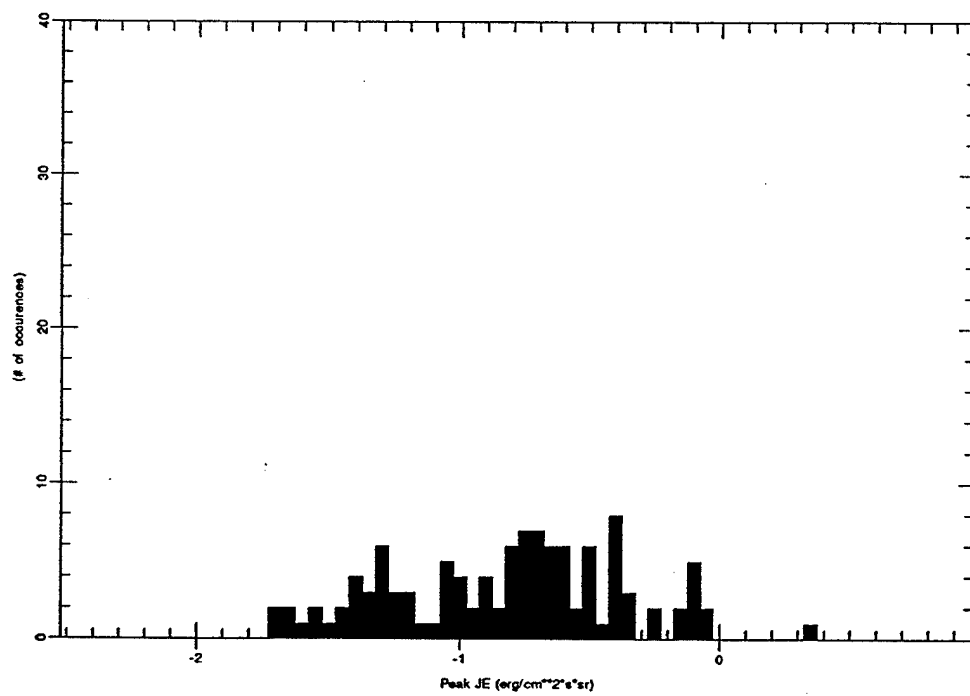
Histogram for file levelp0100ch11_6.out

Peak JE (erg/cm**2*s*sr)
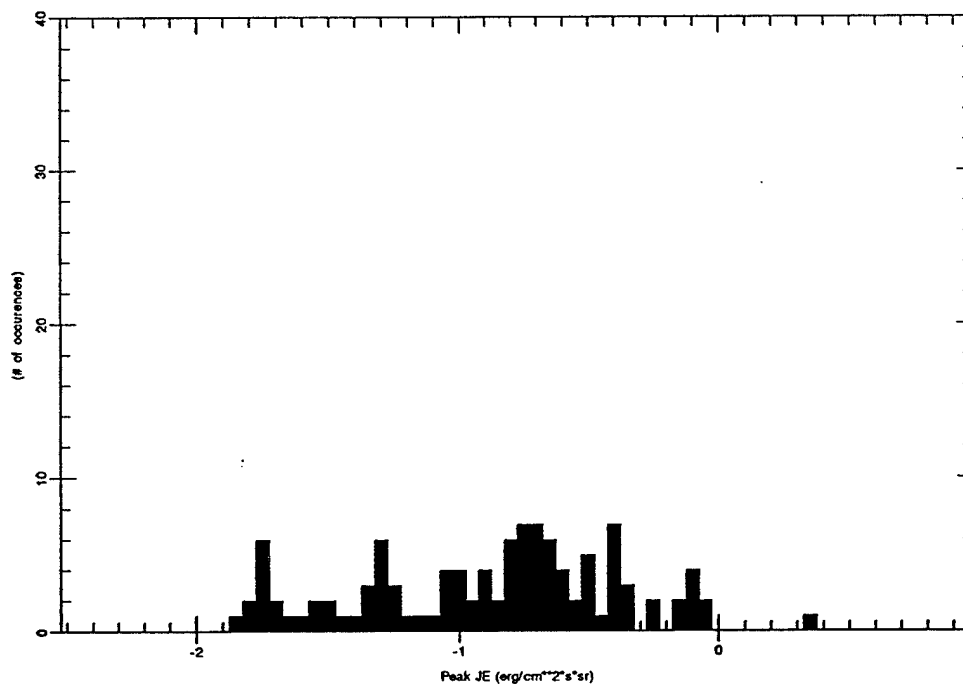
Histogram for file levelp0050ch11_6.out
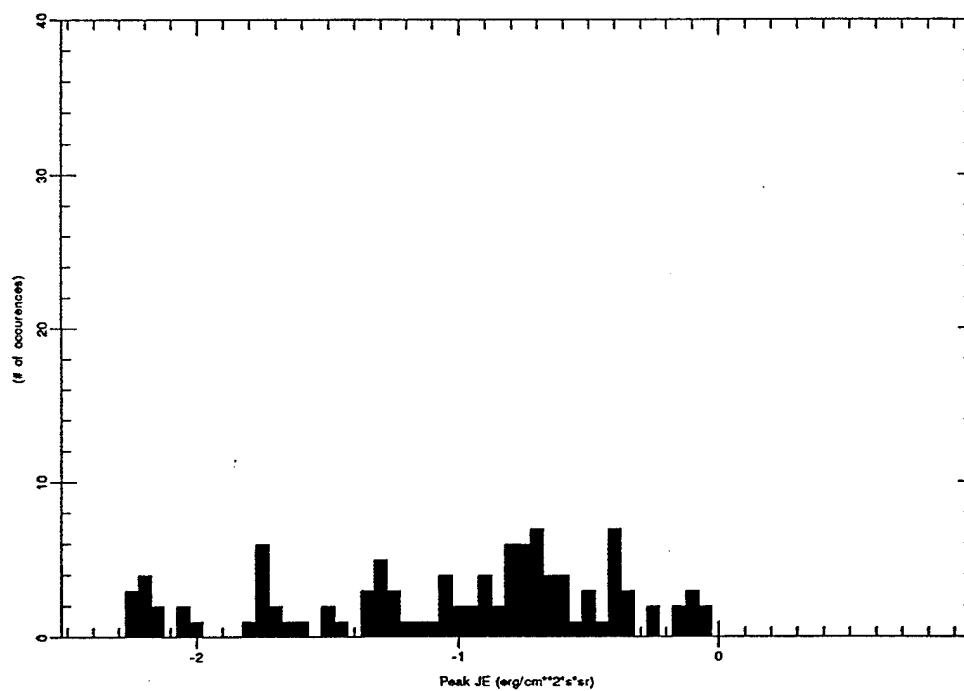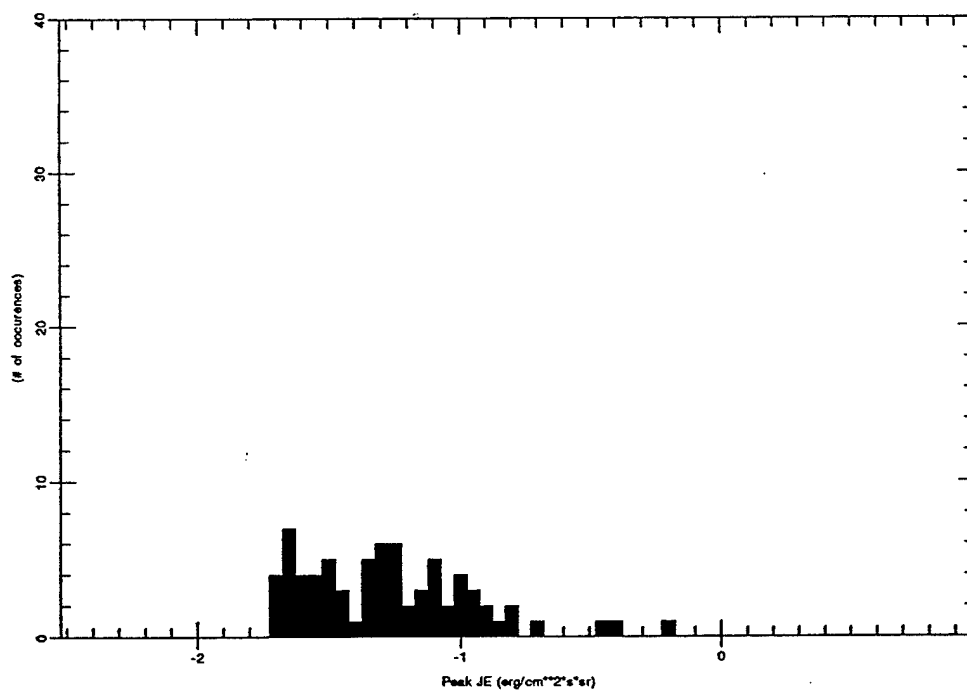
Histogram for file levelp0025ch11_6.out
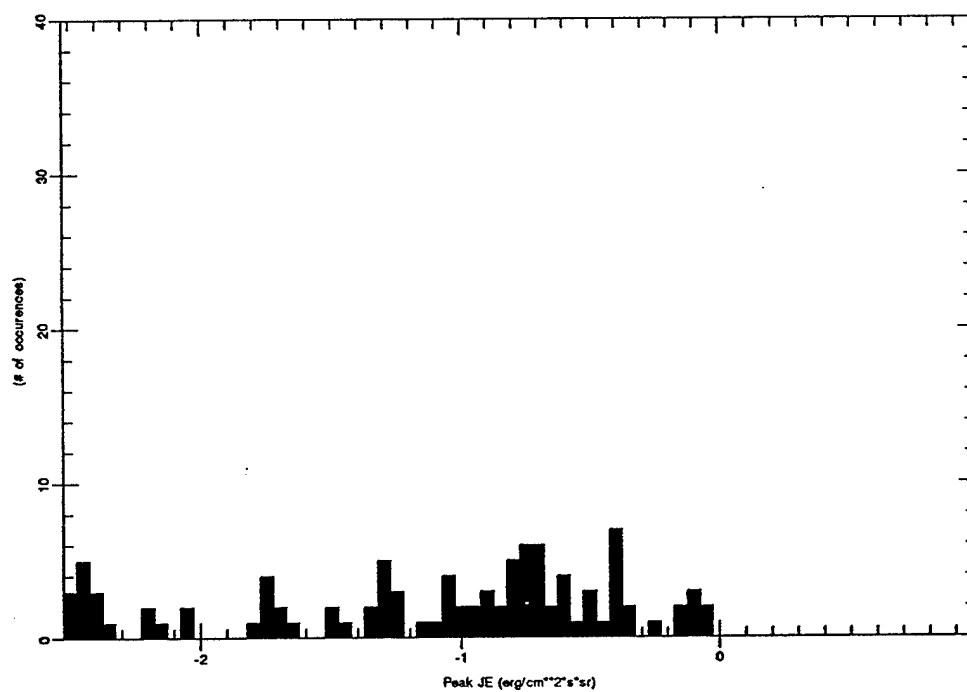
Histogram for file levelp1600ch9_6.out
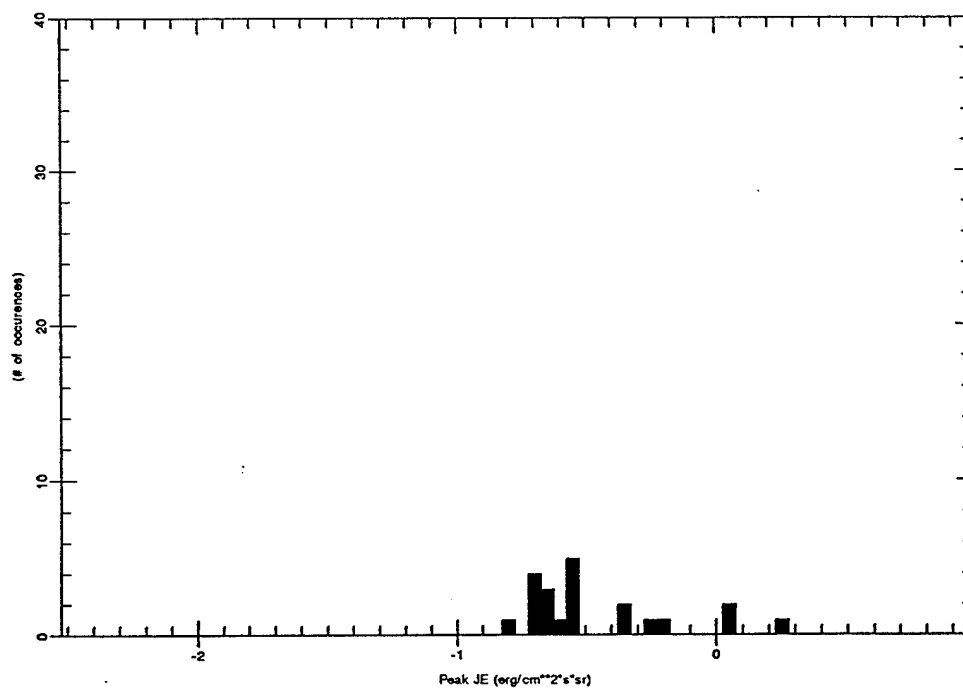
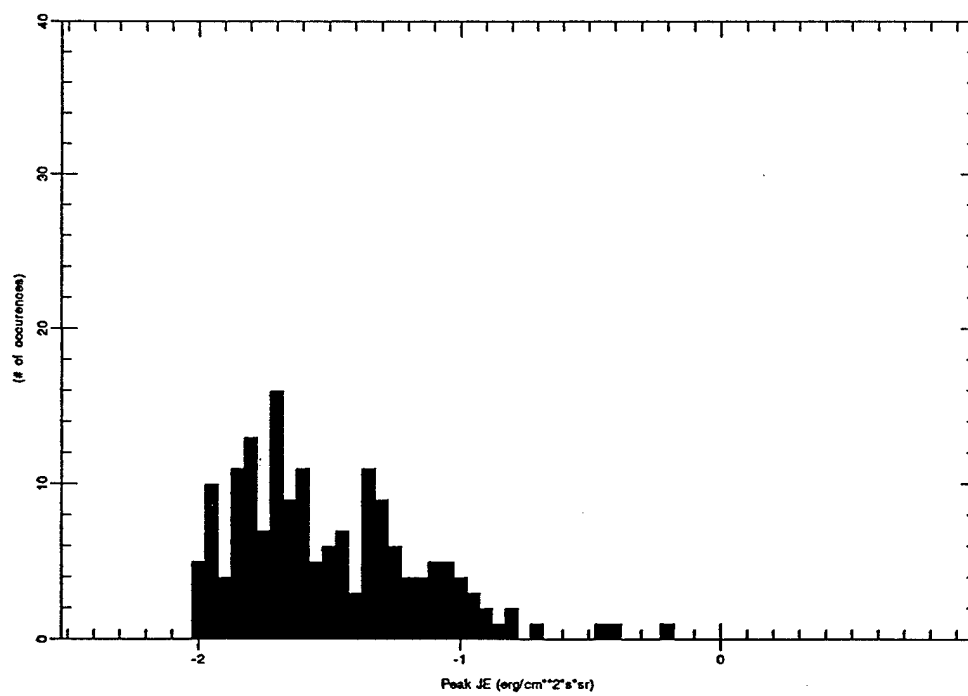Histogram for file levelp0800ch9_6.out
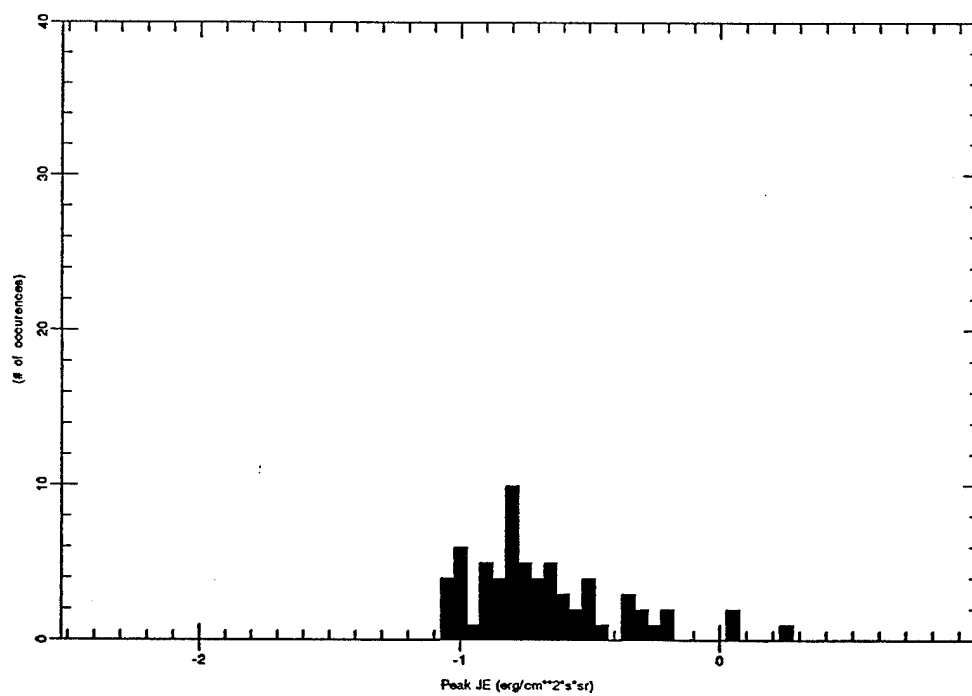
Histogram for file levelp0400ch9_6.out

Peak JE (erg/cm**2*s*sr)

Histogram for file levelp0200ch9_6.out
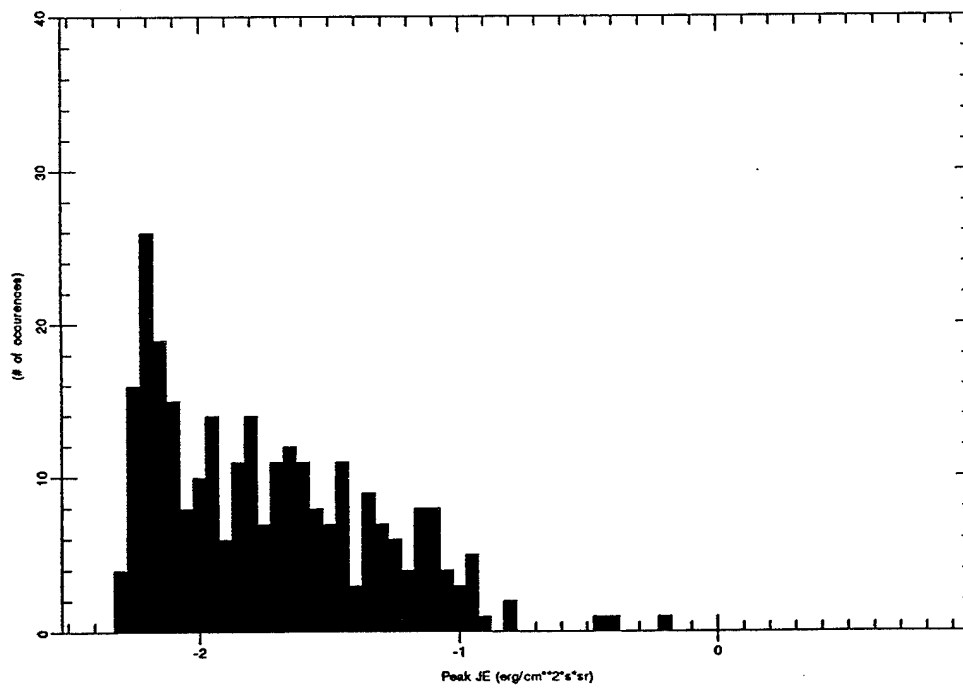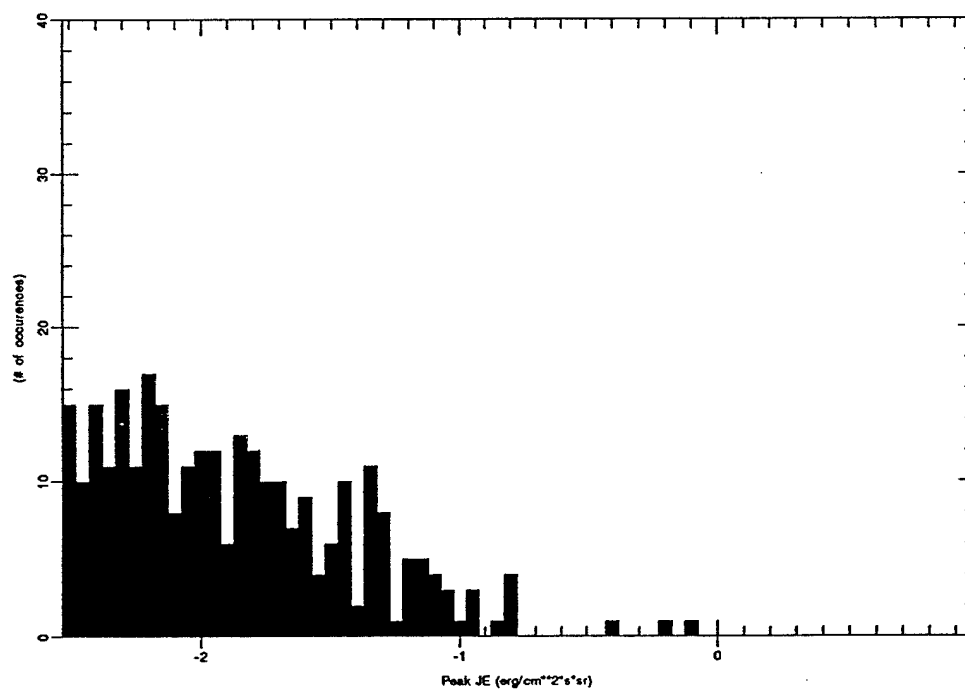

(# of occurences)

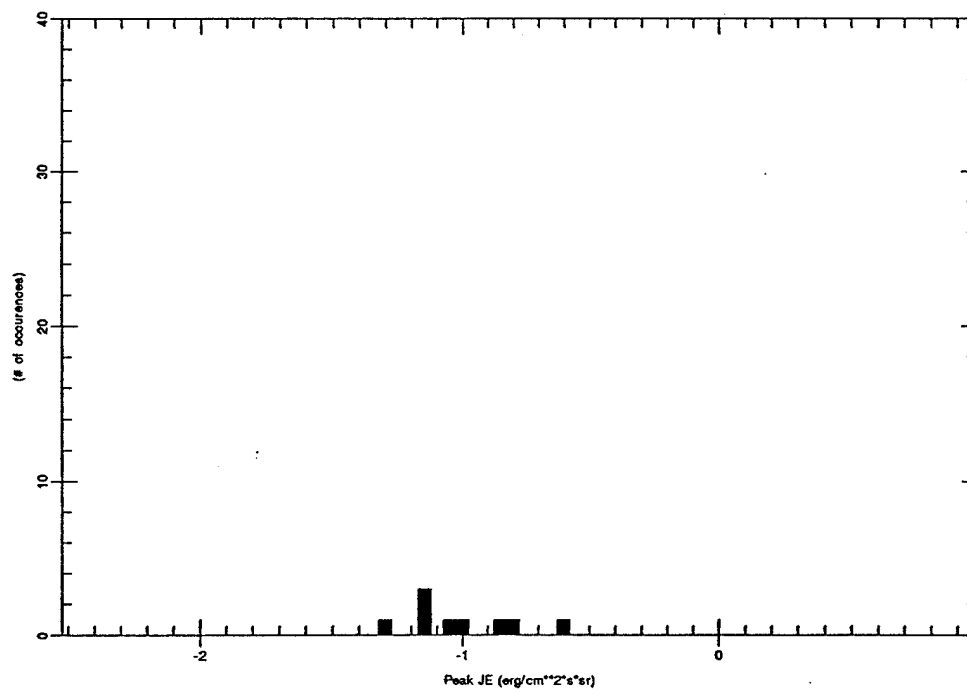Peak JE (erg/cm**2*s*sr)
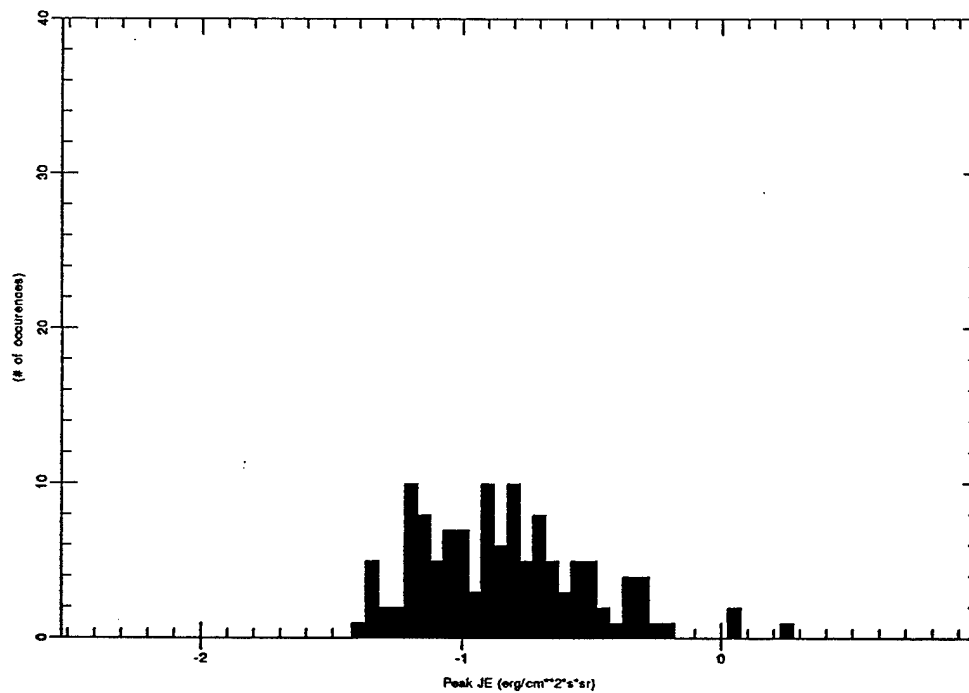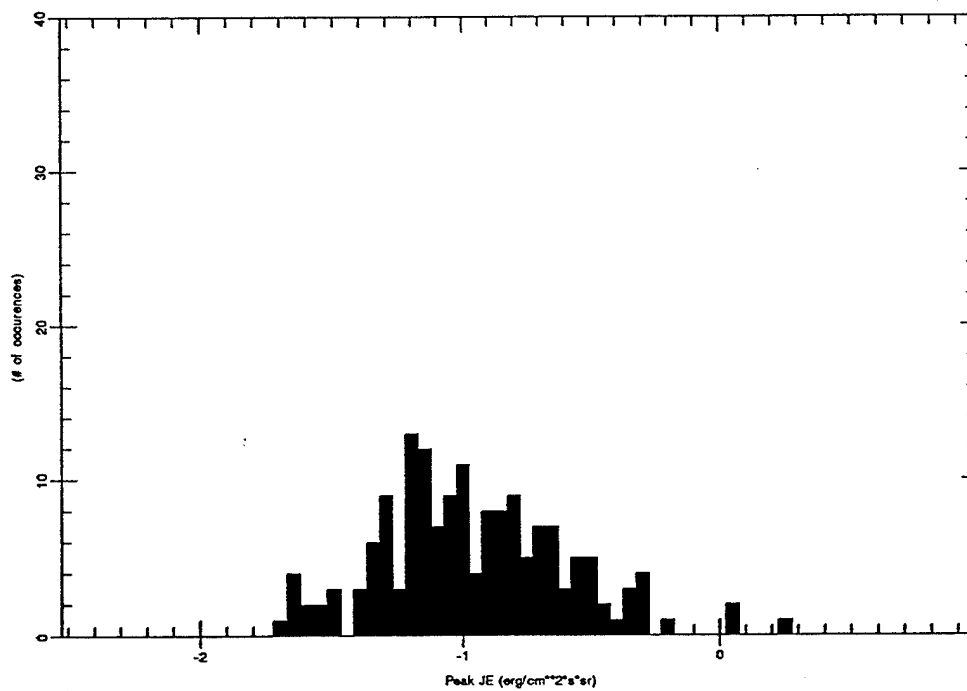
Histogram for file levelp0100ch9_6.out
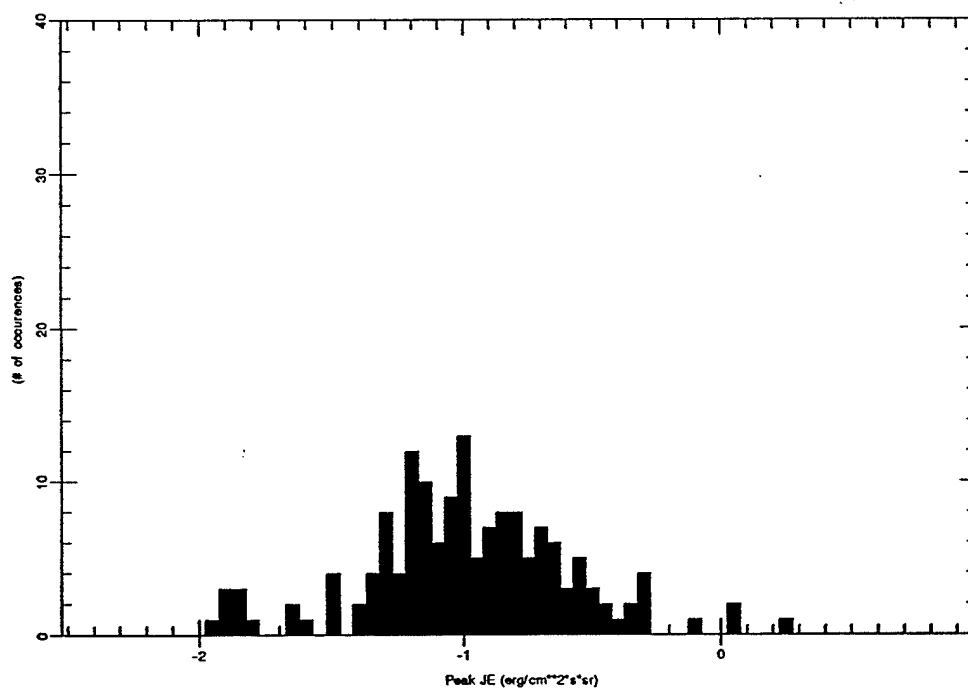
Histogram for file levelp0050ch9_6.out
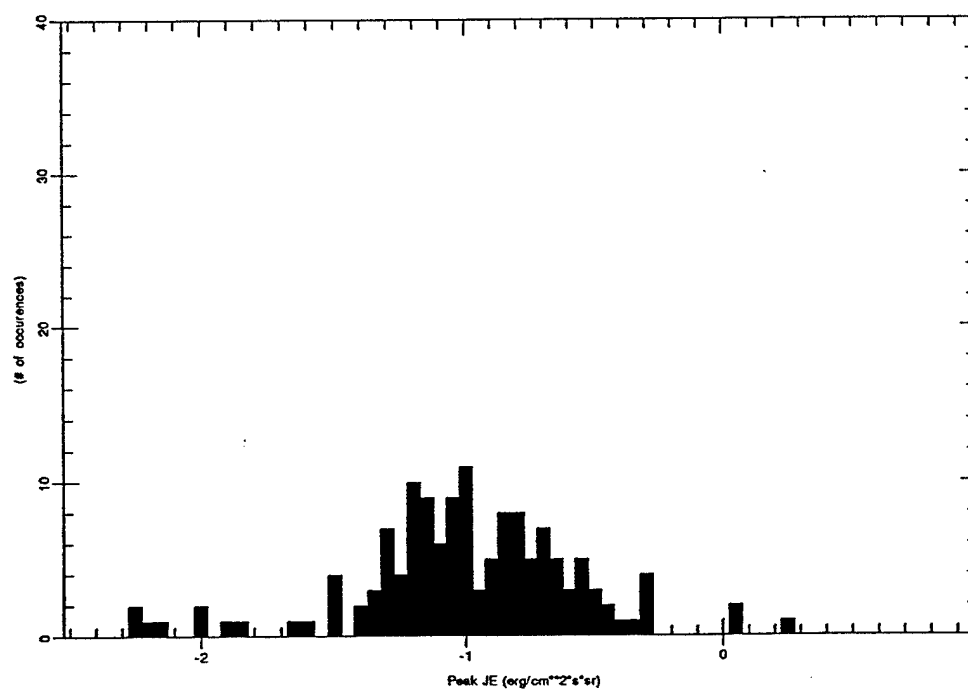
Histogram for file levelp0025ch9_6.out
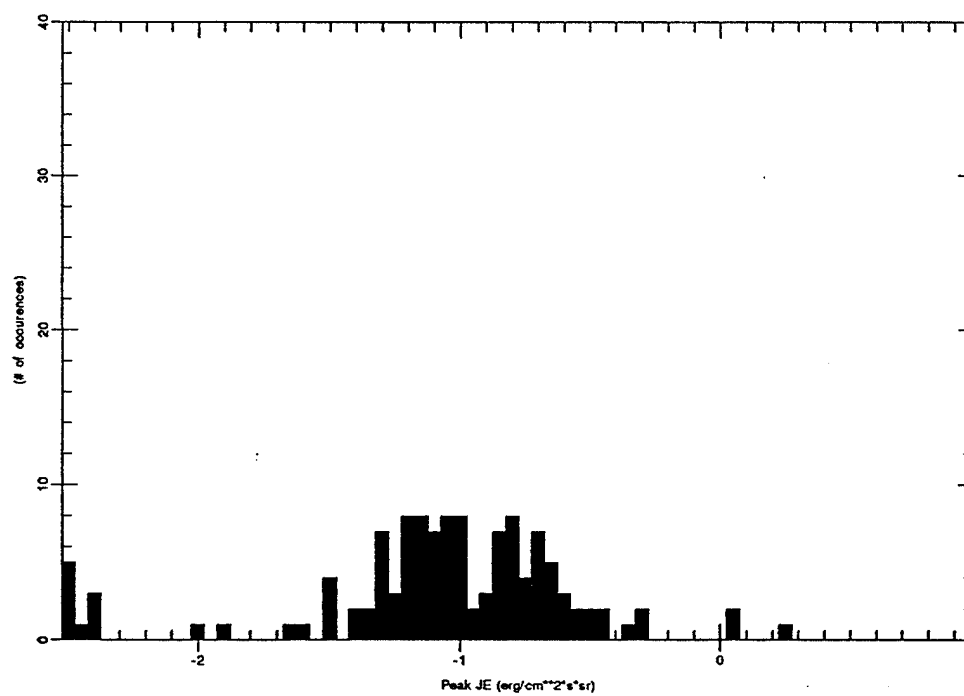
Histogram for file levelp1600ch8_6.out
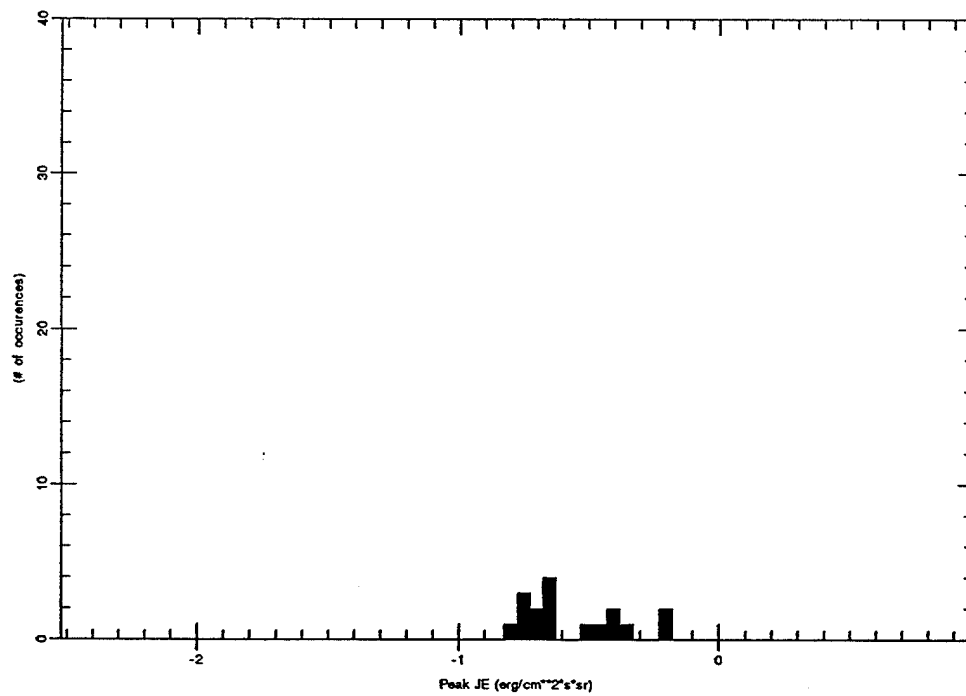
Histogram for file levelp0800ch8_6.out
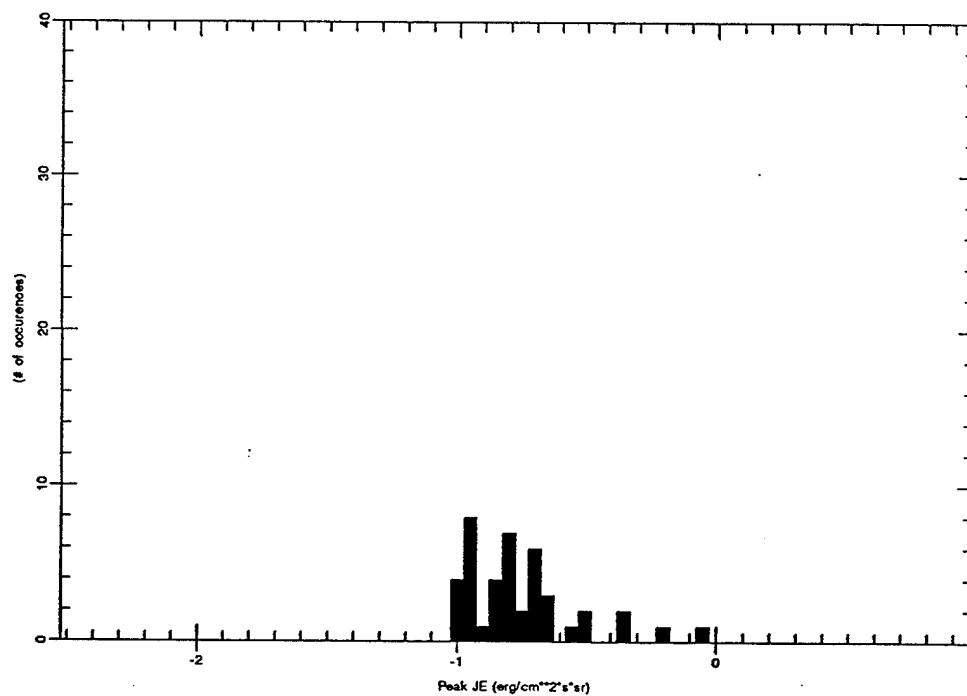
Histogram for file levelp0400ch8_6.out
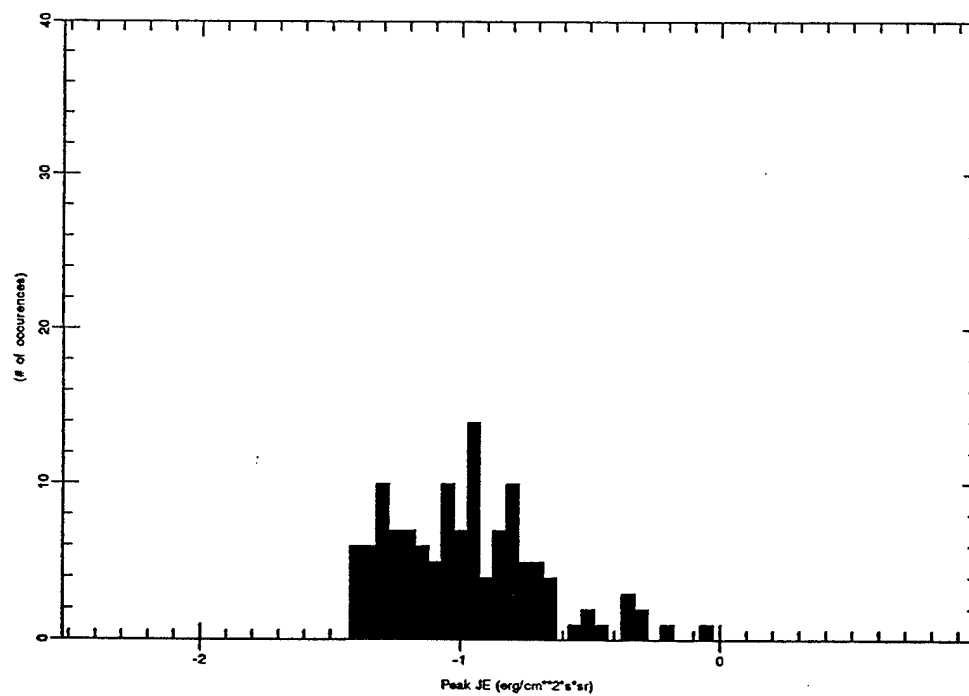
Histogram for file levelp0200ch8_6.out

Peak JE (erg/cm**2*s*sr)
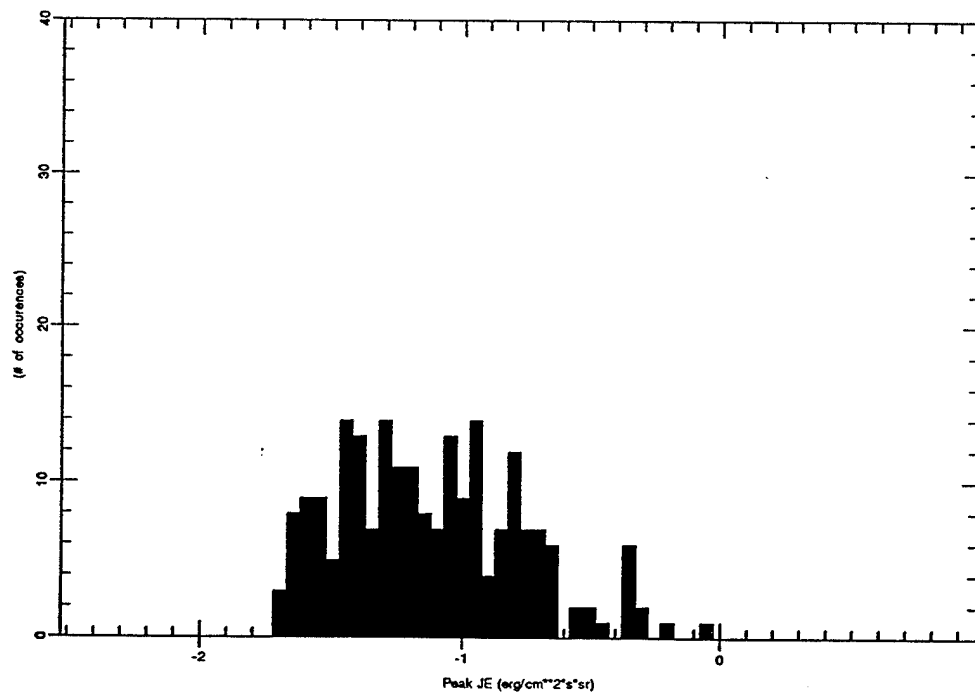
Histogram for file levelp0100ch8_6.out

Histogram for file levelp0050ch8_6.out

Peak JE (erg/cm**2*s*sr)

Histogram for file levelp0025ch8_6.out

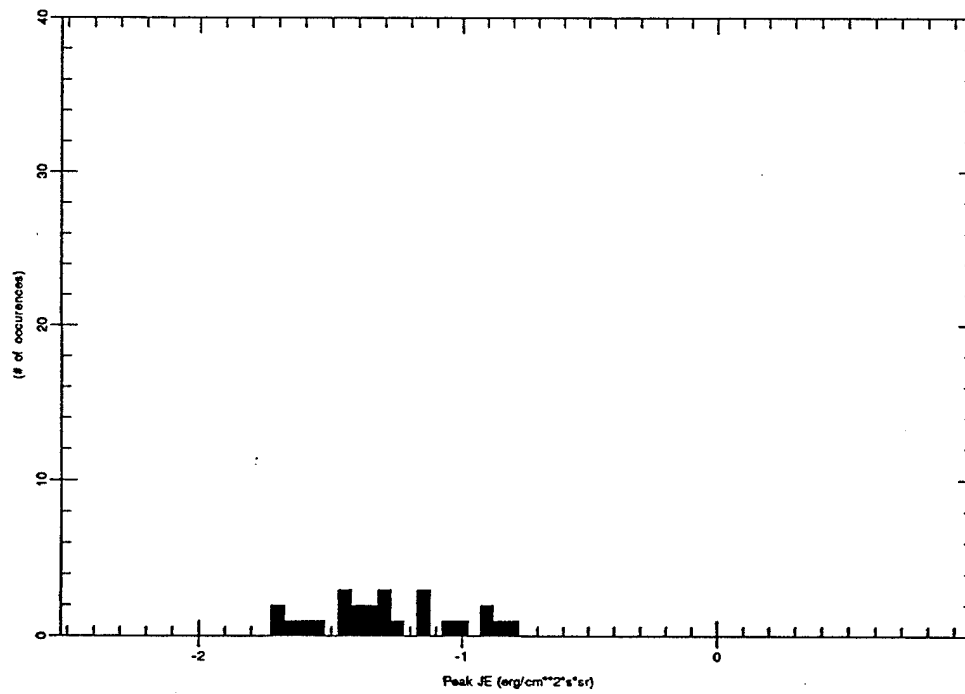Histogram for file levelp1600ch7_6.out

Peak JE (erg/cm**2*s*sr)

Histogram for file levelp0800ch7_6.out

Histogram for file levelp0400ch7_6.out

Histogram for file levelp0200ch7_6.out

Peak JE (erg/cm**2*s*sr)

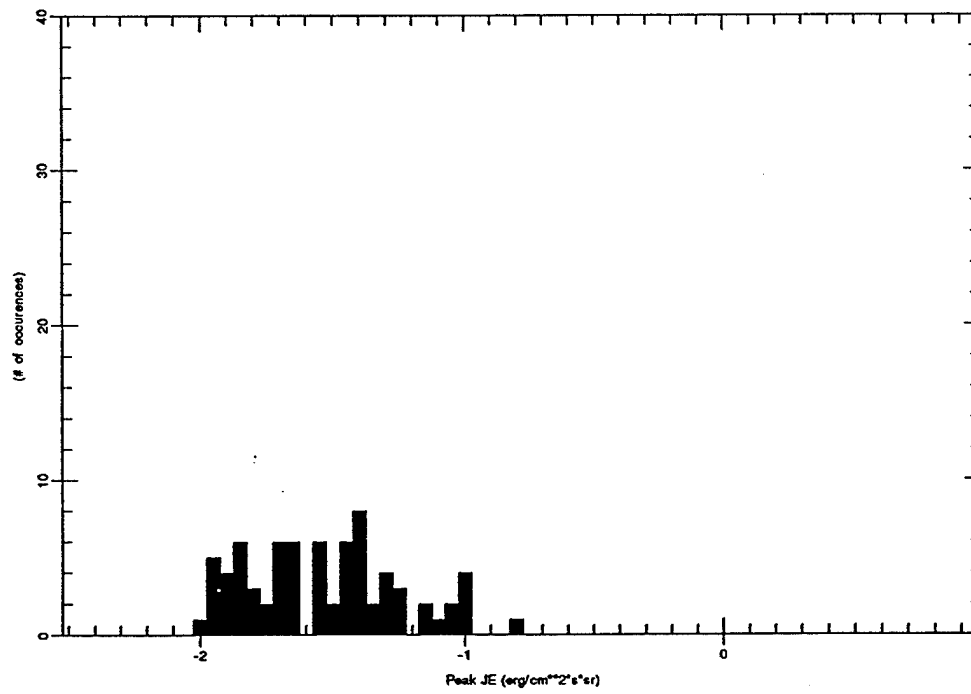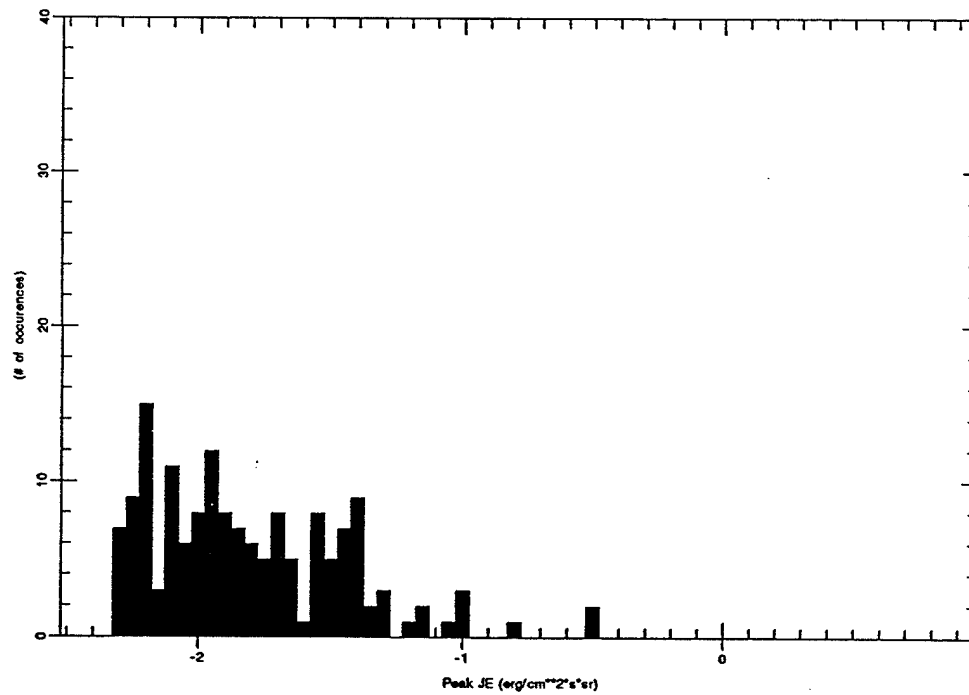Histogram for file levelp0100ch7_6.out

Peak JE (erg/cm**2*s*sr)

Histogram for file levelp0050ch7_6.out

Histogram for file levelp0025ch7_6.out

Histogram for file levelp0800ch6_6.out

Histogram for file levelp0400ch6_6.out

(# of occurrences)

Peak JE (erg/cm**2*s*sr)

188

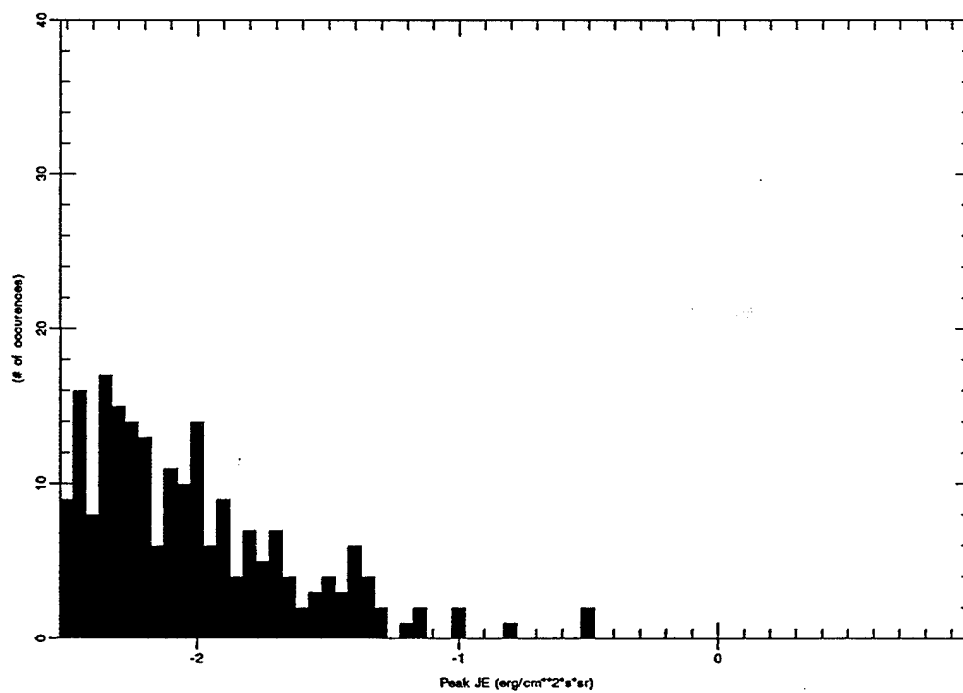Histogram for file levelp0200ch6_6.out

Peak JE (erg/cm**2*s*sr)

Histogram for file levelp0100ch6_6.out

Histogram for file levelp0050ch6_6.out

Histogram for file levelp0025ch6_6.out

Peak JE (erg/cm**2*s*sr)

Histogram for file levelp0400ch5_6.out

Histogram for file levelp0200ch5_6.out

Histogram for file levelp0100ch5_6.out
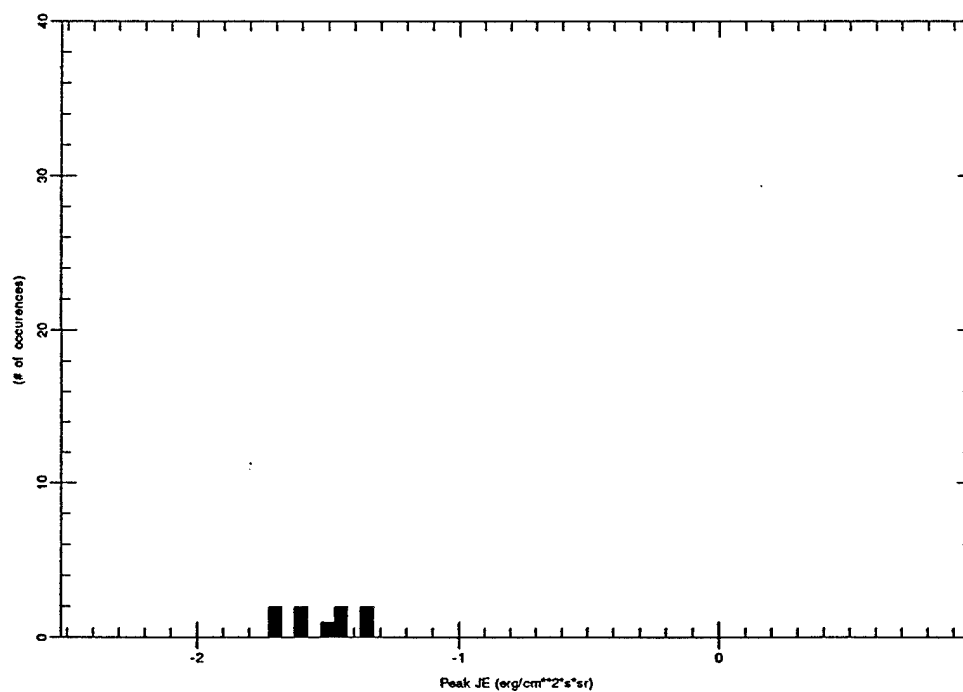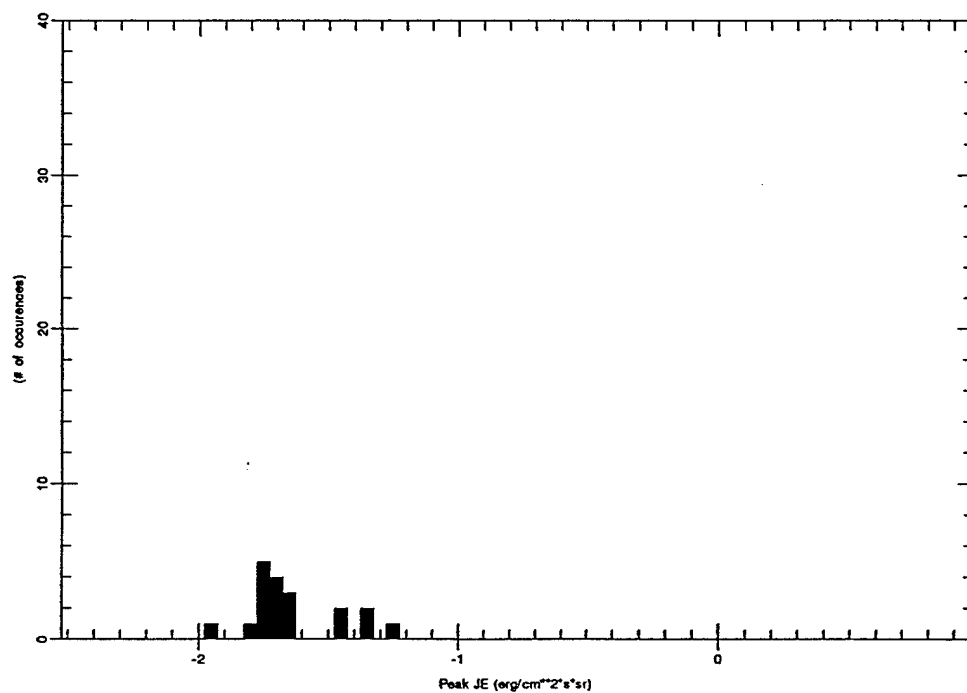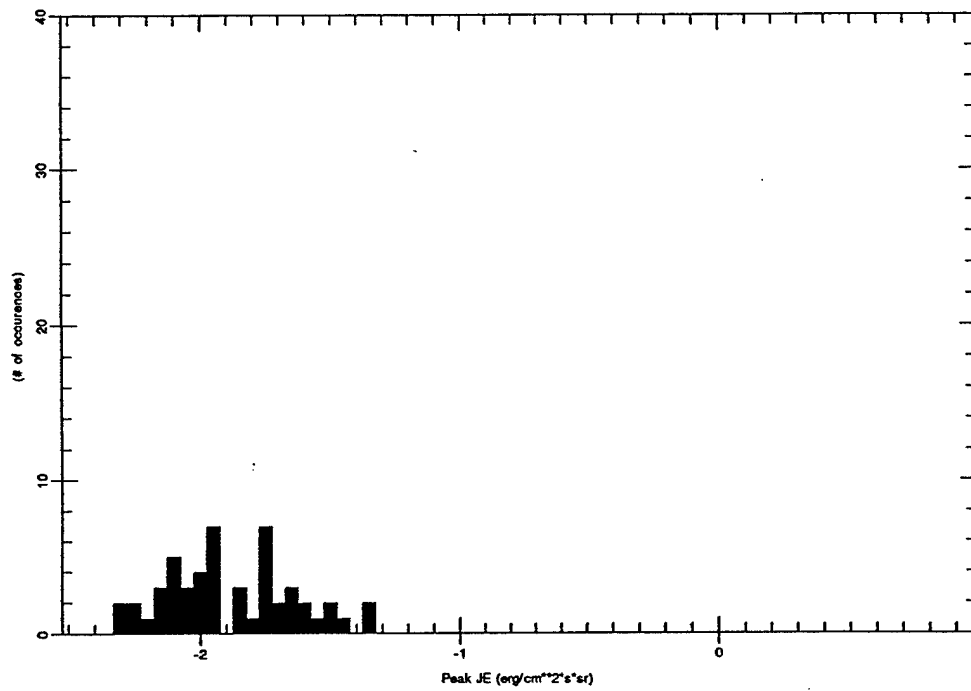
Histogram for file levelp0050ch5_6.out

Peak JE (erg/cm**2*s*sr)

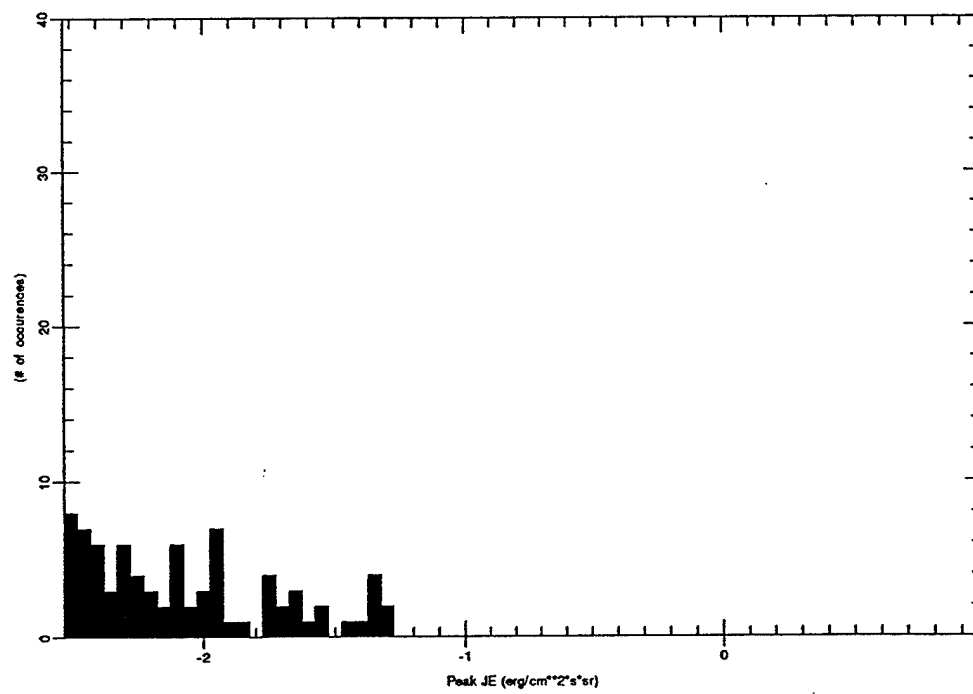Histogram for file levelp0025ch5_6.out

Peak JE (erg/cm**2*s*sr)

Histogram for file levelp0200ch4_6.out

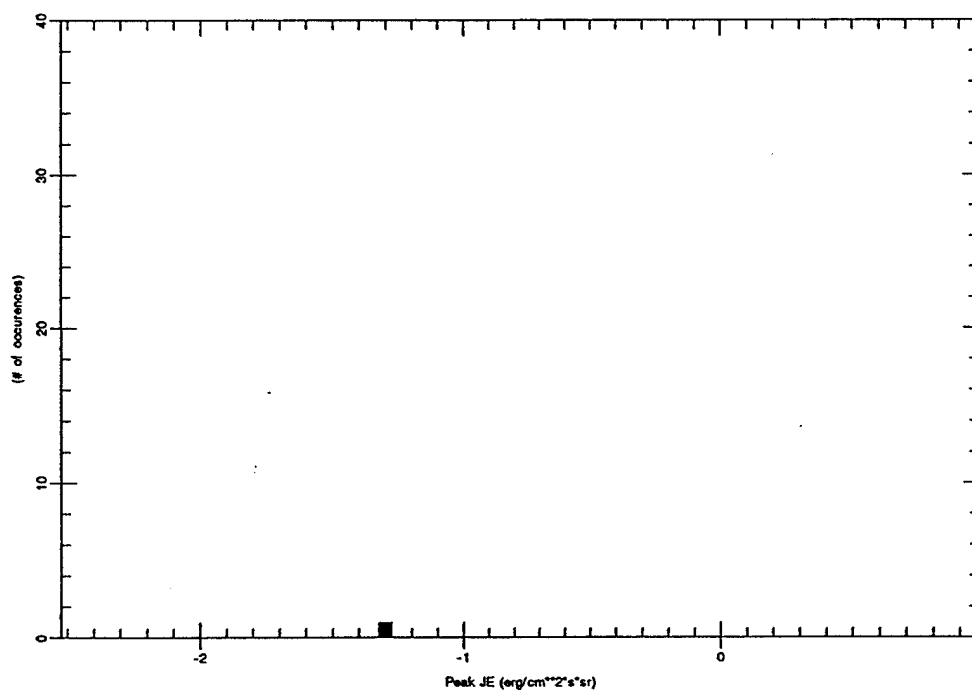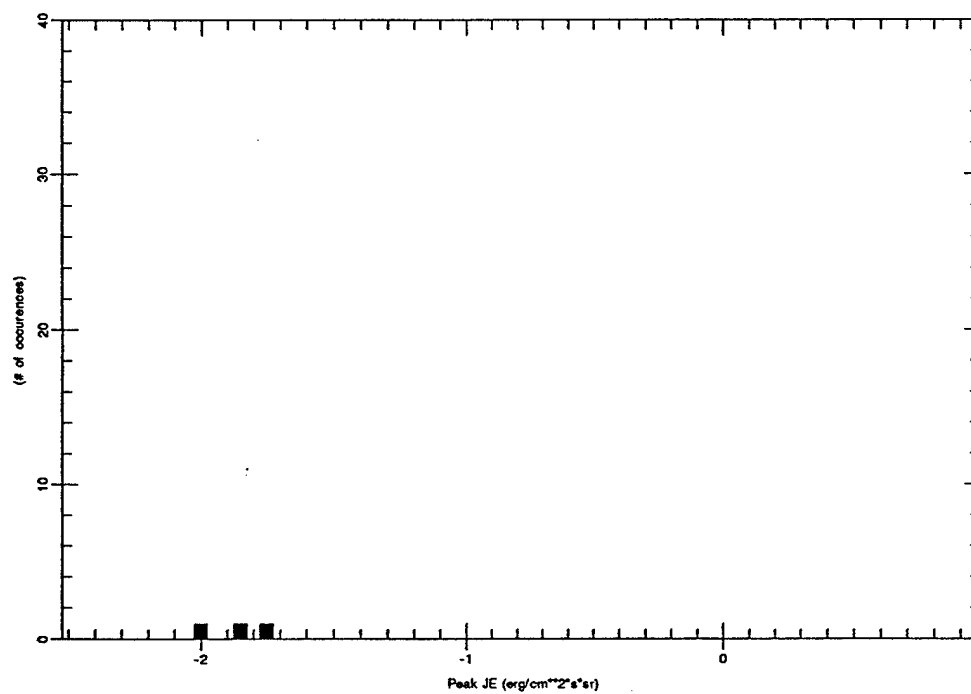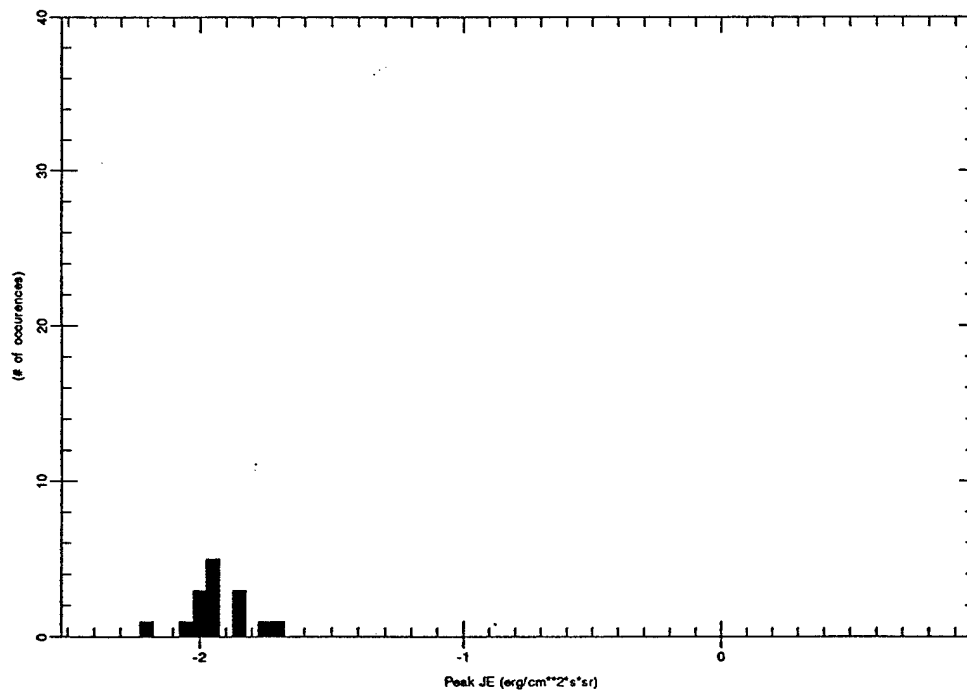Histogram for file levelp0100ch4_6.out

Histogram for file levelp0050ch4_6.out

Peak JE (erg/cm**2*s*sr)

Histogram for file levelp0025ch4_6.out

Peak JE (erg/cm**2*s*sr)

Histogram for file levelp0200ch3_6.out

Histogram for file levelp0100ch3_6.out

Peak JE (erg/cm**2*s*sr)

Histogram for file levelp0050ch3_6.out

Peak JE (erg/cm**2*s*sr)

Histogram for file levelp0025ch3_6.out

Peak JE (erg/cm**2*s*sr)